Spring 1-1-2017

Finite Strain Micromorphic Elasticity, Elastoplasticity, and Dynamics for Multiscale Finite Element Analysis

Farhad Shahabi
University of Colorado at Boulder, farhad.shahabi@colorado.edu

Finite Strain Micromorphic Elasticity, Elastoplasticity, and Dynamics for Multiscale Finite Element Analysis

by

Farhad Shahabi

B.S., Shahid Bahonar University of Kerman, 2009

M.S., Iran University of Science and Technology, 2011

A thesis submitted to the

Faculty of the Graduate School of the

University of Colorado in partial fulfillment

of the requirements for the degree of

Doctor of Philosophy

Department of Civil, Environmental, and Architectural Engineering

2017

This thesis entitled:
Finite Strain Micromorphic Elasticity, Elastoplasticity, and Dynamics for Multiscale Finite Element Analysis
written by Farhad Shahabi
has been approved for the Department of Civil, Environmental, and Architectural Engineering

Assoc. Prof. Richard A. Regueiro

Prof. Ronald Y. S. Pak

Date

The final copy of this thesis has been examined by the signatories, and we find that both the content and the form meet acceptable presentation standards of scholarly work in the above mentioned discipline.

Farhad Shahabi, (Ph.D., Engineering Science)

Finite Strain Micromorphic Elasticity, Elastoplasticity, and Dynamics for Multiscale Finite Element Analysis

Thesis directed by Assoc. Prof. Richard A. Regueiro

This study stands as an attempt to consider the micro-structure of materials in a continuum framework by the aid of micromorphic continuum theory in the sense of Eringen. Since classical continuum mechanics do not account for the micro-structural characteristics of materials, they cannot be used to address the macroscopic mechanical response of all micro-structured materials. In the "representative volume element (RVE)" based methods, classical continuum mechanics may be applied to analyze mechanical deformation and stresses of materials at the relevant micro-structural length-scale (such as grains of a polycrystalline metal, or sand, or metal matrix composite, etc), but when applying standard homogenization methods, such lower length scale effects get smeared out at the continuum scale. The micromorphic continuum theory provides the ability to incorporate the micro-structural effects into the macroscopic mechanical behavior. Therefore, the micromorphic continuum is a tool for a higher resolution multi-scale material modeling through capturing the material's micro-structural physics via bridging to the direct numerical simulations (DNS) at the lower length scale. In the micromorphic continuum theory of Eringen, the fundamental assumption is that the material is made of "micro-elements" in such a way that the classical continuum mechanics balance equations and thermodynamics are valid within a micro-element. Note that micro-elements represent the material's micro-structure in a micromorphic continuum. The micro-element deformation with respect to the centroid of a macroscopic continuum point is governed by an independent micro-deformation tensor $\boldsymbol{\chi}$ which adds 9 additional degrees of freedom to the continuum model. The micromorphic additional degrees of freedom represent micro-stretch, micro-shear, and micro-rotation of the micro-elements. The macroscopic deformation (macro-element deformation) in the micromorphic continuum is handled through the deformation gradient tensor $\boldsymbol{F}$.

If the hypothesis of micromorphic continuum works, in a multi-scale modeling framework, assuming proper constitutive models can be formulated, and material parameters calibrated, micromorphic continuum theory may fill the gap between the RVE-micro-structural-length-scale models and the macroscopic continuum scale. The advantage of using micromorphic continuum is that it provides a chance of linking the macroscopic model to the lower length scale simulations (DNS) and reducing the computational cost by switching from DNS to the macro-scale finite element analysis or other numerical methods at the continuum scale. The linking is done through defining the overlap coupling region between the lower length scale analysis and micromorphic continuum to calibrate the material parameters and the micromorphic continuum model degrees of freedom. Therefore, in the framework of multi-scale modeling, micromorphic continuum can be used as a filter on top of the DNS simulations to capture underlying length scale and better inform the macroscopic model. This is done through the direct linking of the micromorphic continuum micro-elements to the material's micro-structure. The focus of this research is mainly on discussing the macroscopic mechanical behavior of micro-structured materials from the perspective of micromorphic continuum. This is done via developing a three dimensional finite strain finite element model for micromorphic elasticity, elastoplasticity and dynamics.

Dedication

To my parents, Mehri and Houshang, to my grandmother, Vahdat, and to my brothers, Mehrdad and Farzad, without whom none of my success would have been possible.

Acknowledgements

There simply not words to convey the gratitude I feel for the guidance and support I receive from Assoc. Prof. Richard Regueiro, who has given me a vast degree of encouragement throughout my PhD studies at the University of Colorado Boulder. He has been beyond what is required of an advisor. His help and friendship have made a huge difference in my knowledge and experience in both professional and personal life. I consider the opportunity of working with him as my best luck in my professional career.

I would like to express my deepest appreciation to Prof. Ronald Pak, for his excellent comments and novel ideas on my research. I would like to thank my committee members Assoc. Prof. Franck Vernerey, Asst. Prof. John Evans, and Asst. Prof. Jeong-Hoon Song for their valuable time, helpful suggestions, and great support on my dissertation.

I want to express my sincerest appreciation and love for my mother, my father, my grandmother and my brothers for providing me with endless support and opportunities throughout my life.

Last but not least, my best friends, Arash, Hamidreza, Romik, Azadeh, Maryam, Parisa, and Yasmin, in Boulder with whom I had the most memorable moments, during my PhD studies.

Contents

Chapter

Tables

Table

Figures

Figure

Chapter 1

Introduction

In this new technological era, for broadly employed materials such as polycrystalline ceramics, concrete, composites and granular materials, their heterogeneous particulate physics regulates their macroscopic mechanical response. There is of great interest in developing models to be able to capture the grain-scale physics as well as the macro-scale continuum mechanics. Approaches in the continuum framework are trying to reconcile the idea of micro-structure through envisioning materials as a collection of deformable bodies which possess physical properties. This study stands as an attempt to incorporate the micro-structure of materials in a continuum framework by aid of the micromorphic continuum theory in the sense of Eringen. The classical continuum mechanics is based on the notion that a material body is continuous (does not consider the micro-structure of materials) and the balance and the constitutive equations are valid throughout the body regardless of the material body size. Thus, the continuum equations are only functions of the spatial position vector $\boldsymbol{x}$ and time t. This assumption is acceptable for a majority of engineering applications for which the size of the considered solid/structure is large enough in comparison with the size of deformable sub-bodies (or "micro-element," according to Eringen and Suhubi [1964]). From this perspective, for generality, continuous media may be considered composed of deformable sub-bodies (e.g., atoms, molecules, grains, clusters of grains, etc) with various characteristic length scales. The characteristic length scale can be defined as the size of underlying sub-bodies or distances between sub-bodies and the centroid of a corresponding macroscopic continuum material point P (in the

reference configuration $\mathcal{B}_0$). External loads may also be associated with characteristic lengths, which may be prescribed such that the material within the area on which the distributed load is applied may be considered either homogeneous (classical) or heterogeneous (micromorphic). The approximations that are provided by a local continuum theory are reliable when the ratio of an external characteristic length scale λ is relatively large when compared to an internal characteristic length scale l such that $\lambda/l \gg 1$ [Eringen, 1968a]. On the other hand, when $\lambda/l \approx 1$, the loss of accuracy in classical continuum theory occurs as a result of the inherent motions of the sub-bodies which are now able to affect the total mechanical response. So far, several experiments have proved the effect of sub-body-assemblies on the macroscopic continuum response (e.g., Fleck et al. [1994], Stolken and Evans [1998]). Generalized continuum theories have been developed to account for the interaction, deformation, and motion of microscale sub-bodies, but within a single macroscopic continuum theory [E. Kröner, ed., 1968]. Therefore, it is assumed that a material body is composed of a number of deformable sub-bodies within a macro-element (macroscopic continuum material point P) which are able to influence the macroscopic response of the continuum. The micropolar theories are considered as a first-step-extension of classical continuum theories in this direction. In micropolar theories, sub-bodies are assumed to have three rigid directors (independent of the macroscale rotation tensor $\boldsymbol{R}$) which define the sub-body rotations. In the micromorphic continuum theory, a material point P carries three deformable directors to represent the general deformation of sub-bodies (micro-rotation, micro-stretch, and micro-shear). This introduces nine additional degrees of freedom (dofs) when compared to the classical continuum theory. When the directors are constrained to capture only stretch-like deformation of the sub-bodies, then the theory is called a micro-stretch continuum theory. The micro-stretch continuum has four additional dofs over the classical continuum theory. In the micropolar continuum theory, the sub-bodies are assumed to be rigid, and the three associated directors of a sub-body are responsible for its rotation. The history of the polar theories dates back to Cosserat and Cosserat [1909]. They assumed that the sub-bodies are rigid. Therefore, they defined the directors of the sub-bodies in a way to be able to handle their rotational degrees of freedom. They were pioneers in proposing a kinematics framework for

generalized continuum theory [E. Kröner, ed., 1968]. Their theory has been developed by other researchers over time via defining the balance equations, kinematic relations, and constitutive equations. Mindlin [1964] developed a theory of small strain elasticity based upon the physical picture that each macro-element of a material is composed of deformable particles. He defined the kinematics to be able to account for the resulting displacements and strain measures associated with the macro and micro elements at small strain. He provided graphical interpretation of the higher order stress tensor, micro-deformation tensor, and gradient of micro-deformation tensor. Eringen and Suhubi [1964] formulated the basic field equations, boundary conditions, thermodynamics, and constitutive equations for what they called "simple micro-elastic solids" or "micromorphic continua" for large deformations. They defined a micro-elastic solid as a material body whose properties and its behavior are affected by the deformable sub-bodies. Suhubi and Eringen [1964] introduced strain measures and free energies to be able to specify the constitutive equations for isotropic micro-elastic materials. Germain [1973] derived the micromorphic equations of motion based upon the virtual power approach. They investigated micromorphic dynamics by introducing a micro-inertia tensor for deformable sub-bodies. These three methods [Mindlin, 1964, Eringen and Suhubi, 1964, Germain, 1973] constitute a basis for "modern" microcontinuum field theory by introducing higher order stress tensors and microstress tensors within their balance equations. The resulting balance equations of these three methods are different due to the differences in the kinematics or the differences related to the definitions of stress tensors. It is beyond the scope of this research to discuss the similarities and differences between the three approaches. This research follows the approach of Eringen and Suhubi [1964] because of the physical interpretation that their approach provides for each of the new micro-field variables (stress, strain, ...) and mathematically proves that they exist as a result of deformable micro-elements. They wrote balance equations for a micro-element, and then through a variational approach by integral-averaging, they obtained the balance equations for a macro-element. In the following, we describe more recent research on micromorphic continua. Neff et al. [2014] formulated what they called "relaxed linear micromorphic continuum" with the symmetric Cauchy stress in the absent of the coupling terms of the classical micromorphic contin-

uum by Eringen and Suhubi [1964]. In addition, free energy function of the relaxed micromorphic model is not uniformly pointwise positive definite. Their relaxed model is still able to capture the micro-scale deformation. This simplification is helpful for better understanding of the micromorphic continuum as well as reducing the number of elastic constants of the constitutive equations. Their model has been extended via the wave propagation analysis in the meta-materials by Madeo et al. [2015]. Through investigating the dispersion relation for the relaxed micromorphic media, a frequency range is predicted for which waves are not able to travel in the media. Chen and Lan [2009] discussed the modeling of granular materials as a micromorphic continuum through defining macro-elements as RVE's which contain a number of deformable micro-elements. They derived all the balance equations including mass, linear and angular momentum, and energy in the discrete format assigned to the material's particles. Finally, they transformed the discrete balance equations into their corresponding continuum scale macro-element. Note that in their modeling they considered the dynamics of particles through incorporating the velocity and acceleration associated with particles. Berezovski et al. [2015] studied the reflection and the transmission of elastic waves at the interface region of two micromorphic continua. This is done to illustrate that the reflection and transmission of waves are dependent on the micro-structural properties. Note that their model incorporates the micro-structural effects through the internal variables of state unlike the method of Eringen and Suhubi [1964] which is developed based upon incorporating the additional degrees of freedom. Dingreville et al. [2013] proposed what they called "multiresolution material modeling" to simulate the wave propagation in heterogeneous media. They performed a comparison between a modeling done via a direct numerical simulation (DNS) and that of the upscaled micromorphic continuum. The meso-scale DNS is used to inform the micromorphic continuum to be able to capture the underlying physics without explicitly touching the micro-structural features via a fewer number of degrees of freedom than the full DNS model. Note that they followed the micromorphic continuum in the sense of Germain [1973]. Rapti et al. [2016] used the micro-dilation model to study the effect of regularization on the mesh dependency in the shear band analysis under dynamic conditions. Note that the micro-dilation model describes only the volumetric deformation

at the micro-scale through a single additional degree of freedom. Sansour [1998] reformulated the micromorphic continuum field equations with new strain measures. He extended his model to finite strain micromorphic viscoplasticity based upon a multiplicative decomposition of the microstretch tensor. He used the integral-averaging-approach similar to Eringen and his co-workers to be able to obtain the macro-element field equations. Vernerey et al. [2007] proposed a multi-scale continuum theory which is able to capture the deformations at various scales. They also used the method of virtual power method [Germain, 1973] to derive a system of coupled equations to be able to represent the effects of each length-scale on macroscopic continuum behavior. They studied inelastic behavior by defining multiple yield functions, each representing the yielding at a specific microstructural length-scale. They compared their theory with the direct numerical simulation (DNS) for a specimen under tension. They observed that their model is successful in capturing the major length-scale dependent physics with less computational cost. Lee and Chen [2003] developed a constitutive equation for micromorphic thermoplasticity analysis. They used the kinematics and balance equations in the sense of Eringen and Suhubi [1964]. It is to be noted that they did not use a multiplicative decomposition of deformation gradient to formulate their elastoplasticity model. Forest and Sievert [2003] used the virtual power method of Germain [1973] to propose a framework for elastoviscoplastic analysis of the generalize continuum theories. In their derivations, they used different invariants of deformation measures in comparison with that of Eringen and Suhubi [1964]. Forest and Sievert [2006] discussed the hierarchy of higher order continuum theories in terms of degrees of freedom. They introduced the microstrain theory with six additional degrees of freedom to represent the deformation of sub-bodies. They provided some guidelines for the selection of a proper higher order continuum model. Based upon what they expressed in their research, microdilation theory with only one additional degree of freedom is an appropriate model to simulate significant microvolume change. The micropolar (or Cosserat) continuum theories are suitable only for materials with independently-rotating sub-bodies. The microstrain theory is good for capturing strain localization effects. Forest [2009] proposed a micromorphic approach for elasticity, viscoplasticity, and damage for micro-structured materials. They expressed that their micromorphic approach is

capable of providing the generalized balance equations that offers an anisotropic nonlinear constitutive relations between the generalized strain and stress tensors. The objective of their paper is to illustrate that the strain gradient theories can be related to the higher order continuum mechanics (or micromorphic continuum in general). Sansour et al. [2010] extended their previous work [Sansour, 1998] to a micromorphic continuum at finite inelastic strain. In order to illustrate their new model, they simplified their previous model by reducing the additional degrees of freedom and the associated material parameters. They conducted finite element (FE) simulations to illustrate the scale-effects which can be captured by their new model. Li and Tong [2015] developed multiscale micromorphic molecular dynamics which is a concurrent three-scale dynamics model that builds a bridge between (Andersen)-Parrinello-Rahman molecular dynamics to mesoscale micromorphic dynamics and continuum scale. Zhang et al. [2011b] studied wedge indentation of a thin film on a substrate based upon small strain micromorphic plasticity. They investigated that the predictions of the indentation hardness will be affected by internal length scale, film hardening modulus, and film thickness. Zhang et al. [2011a] investigated the size effect, Bauschinger effect, ratcheting effect, and plastic shakedown phenomenon in materials with deformable sub-bodies. For this purpose, they formulated small strain micromorphic elastoplasticity with isotropic/kinematic hardening in a 2D finite element framework. Grammenoudis et al. [2009] formulated micromorphic plasticity theory based upon a multiplicative decomposition of the macro-deformation gradient and the micro-deformation tensor. They illustrated coupling of isotropic damage to micromorphic plasticity model. Isbuga and Regueiro [2011] implemented a three-dimensional finite element analysis of finite deformation micromorphic isotropic elasticity in the sense of Eringen and Suhubi [1964]. They noticed that boundary conditions on the additional micromorphic degrees of freedom together with the elastic material parameters of micromorphic constitutive equations have significant affect on the total macroscopic behavior. Regueiro and Isbuga [2011] presented the formulation of a micromorphic continuum in the reference and current configurations. It is to be noted that their implementation is a full Total Lagrangian three-dimensional hexahedral finite element model. They demonstrated the effect of length scales by simulating a three-dimensional micro-indentation exam-

ple. Regueiro [2009] formulated finite strain micromorphic pressure-sensitive elastoplasticity model based upon a multiplicative decomposition of the deformation gradient and micro-deformation tensor. They assumed the isotropic linear elasticity and non-associative Drucker-Prager plasticity with cohesion hardening/softening for the constitutive equations. They formulated the plastic evolution equations in three levels: 1) evolution equation for the plastic part of deformation gradient $\boldsymbol{F}^p$; 2) evolution equations for the plastic part of micro-deformation tensor $\boldsymbol{\chi}^p$; 3) evolution equation for the plastic part of the gradient of micro-displacement tensor $\bar{\nabla}\boldsymbol{\chi}^p$. It is to be noted that the model was formulated in the current configuration. Regueiro [2010] expressed finite strain micromorphic elastoplasticity model in the intermediate configuration which can be implemented via the Total Lagrangian finite element analysis. He used a semi-implicit time integration method to integrate the constitutive equations in rate form. This research is following the micromorphic continuum approach by Eringen and Suhubi [1964] and the elasticity implementation by Isbuga and Regueiro [2011] and finite strain elastoplasticity approach proposed by Regueiro [2010]. This approach is one of the most general higher order continuum theories which is able to take into account the effect of underlying sub-bodies behavior. One of the main advantages of this approach is that it can be fit into a multi-scale modeling framework in which bridging/coupling is required between the different length scales to the macro-scale model of interest. The bridging of underlying microstructure to the macro-continuum of interest can be described as a transferring of the essential information out of the mechanical behavior of the microstructure to the macro-continuum to provide a high resolution simulation. Another advantage of the [Eringen and Suhubi, 1964] approach for the micromorphic continuum is that the derivations start with writing the balance equations for the micro-elements and then through using the variational approach and the integral averaging method the macro-continuum field equations will be derived. By this procedure, this approach provides a physical insight for all the additional microcontinuum parameters and mathematically proves that all these new parameters exist. Index notation will be used wherever needed to clarify the presentation. Cartesian coordinates are assumed, so all indices are subscripts, and a spatial partial derivative is the same as a covariant derivative [Eringen, 1962]. Some symbolic/direct notation is also given,

such that $(\boldsymbol{a}\cdot\boldsymbol{b})_{ik} = a_{ij}b_{jk}$, $(\boldsymbol{a}\otimes\boldsymbol{b})_{ijkl} = a_{ij}b_{kl}$. Boldface denotes a tensor or vector. Subscript $(\bullet)_{,i}$ implies a spatial partial derivative with respect to x_i. Superposed dot $\dot{(\square)} = D(\square)/Dt$ denotes a material time derivative. The symbols $\stackrel{\text{def}}{=}$ or $:=$ imply a definition. Quantities with $(\bullet)^{(\alpha)}$ live in the micro-elements and quantities with $(\bullet)_{\beta}$ are associated with the macro-elements.

Chapter 2

Finite Strain Micromorphic Elasticity

In this chapter, finite strain micromorphic elasticity proposed by Eringen and Suhubi [1964] will be presented in detail. We start with the micromorphic kinematics to illustrate how the deformation gradient $\boldsymbol{F}$ and the micro-deformation tensor $\boldsymbol{\chi}$ map the macro and micro elements from the reference configuration to the current configuration. Following the kinematics, the micromorphic balance equations and thermodynamics will be derived in the current configuration. The aim of this thesis is to implement micromorphic continuum in a total Lagrangian finite element framework. Therefore, the constitutive equations are defined in the reference configuration. Also, mapping of the current configuration tensor quantities to the reference configuration will be presented. The elastic parameters of the micromorphic constitutive equations need to be defined in such a way to ensure the positiveness of the strain energy function. Therefore, we discuss restrictions (proposed by Smith [1968]) on the elastic moduli of micromorphic continuum.

2.1 Kinematics

The kinematics of a micromorphic continuum can be expressed as follows: consider a macro-element continuum point P_β in the reference configuration with centroid C_β, such that its position vector $\boldsymbol{X}_\beta$ is attached to C_β (see Fig.2.1). The relative position vector $\boldsymbol{\Xi}^{(\alpha)}$ of sub-body α (micro-element) defines its centroid $C^{(\alpha)}$ with respect to the macro-element centroid C_β in the reference configuration $\mathcal{B}_0$. Note that in general, the macro element has a number of sub-bodies (micro-

elements) with their centroids determined through a family of position vectors $\boldsymbol{\Xi}^{(\alpha)}$ $(\alpha = 1, ..., N)$, where N is the number of sub-bodies for material point P_β. For simplicity of micromorphic continuum derivations, it is assumed that the family of relative position vectors $\boldsymbol{\Xi}^{(\alpha)}$ is not a function of the position vector $\boldsymbol{X}_\beta$ in the reference configuration $\mathcal{B}_0$ [Eringen, 1968a, 1999]. Note that subscript β is to denote that there is more than one macro-element over the continuum body $\mathcal{B}_0$. This is a fundamental assumption in the micromorphic theory to model materials with periodic micro-structure. Assuming $\boldsymbol{\Xi}^{(\alpha)}$ a function of $\boldsymbol{X}_\beta$, such that $\boldsymbol{\Xi}^{(\alpha)}(\boldsymbol{X}_\beta)$, we have a functionally graded micromorphic theory [Maugin, 2010]. A macro-element continuum point is, therefore, defined by its centroid and the relative position vector $\boldsymbol{\Xi}^{(\alpha)}$ in the reference configuration written as $P_\beta\left(\boldsymbol{X}_\beta, \boldsymbol{\Xi}^{(\alpha)}\right)$. In the current configuration, a macro-element continuum point and its relative position vector can be defined as $p_\beta\left(\boldsymbol{x}_\beta, \boldsymbol{\xi}^{(\alpha)}, t\right)$ with centroid c_β, and $\boldsymbol{\xi}^{(\alpha)}(\boldsymbol{X}_\beta, \boldsymbol{\Xi}^{(\alpha)}, t)$, respectively. Figure 2.1 illustrates the mapping of the macro-element and micro-element from the reference configuration to the current configuration through the deformation gradient $\boldsymbol{F}$ and micro-deformation tensor $\boldsymbol{\chi}$. Note that derivations in this thesis are done in Cartesian coordinates. The micro-element centroid position vector in the reference and current configurations can be expressed such that,

$$X_K^{(\alpha)} = X_{K(\beta)} + \Xi_K^{(\alpha)}\ , \quad x_k^{(\alpha)} = x_{k(\beta)}(\boldsymbol{X}_\beta, t) + \xi_k^{(\alpha)}(\boldsymbol{X}_\beta, \boldsymbol{\Xi}^{(\alpha)}, t) \tag{2.1}$$

An underlying assumption is that for "sufficiently small" sub-body relative position vectors through a MacLaurin series expansion about $\boldsymbol{\Xi}^{(\alpha)} = \boldsymbol{0}$ at C_β [Eringen and Suhubi, 1964], $\boldsymbol{\xi}^{(\alpha)}$ can be linearly related to $\boldsymbol{\Xi}^{(\alpha)}$ through the micro-deformation tensor $\boldsymbol{\chi}$, as follows,

$$\xi_k^{(\alpha)}(\boldsymbol{X}_\beta, \boldsymbol{\Xi}^{(\alpha)}, t) = \chi_{kK}(\boldsymbol{X}_\beta, t)\Xi_K^{(\alpha)} \tag{2.2}$$

This assumption dictates an affine deformation of the macro-element continuum point with respect to its independently-deforming sub-bodies (micro-elements) through $\boldsymbol{\chi}(\boldsymbol{X}_\beta, t)$, whereas the whole continuum body may experience inhomogeneous deformation through deformation gradient $\boldsymbol{F}(\boldsymbol{X}_\beta, t)$, micro-deformation $\boldsymbol{\chi}(\boldsymbol{X}_\beta, t)$, and micro-deformation gradient $\partial\boldsymbol{\chi}(\boldsymbol{X}_\beta, t)/\partial\boldsymbol{X}_\beta$. Substi-

tuting (2.2) into (2.1), we have the spatial position vector of the micro-element centroid as,

$$x_k^{(\alpha)} = x_{k(\beta)}(\boldsymbol{X}_\beta, t) + \chi_{kK}(\boldsymbol{X}_\beta, t)\Xi_K^{(\alpha)} \tag{2.3}$$

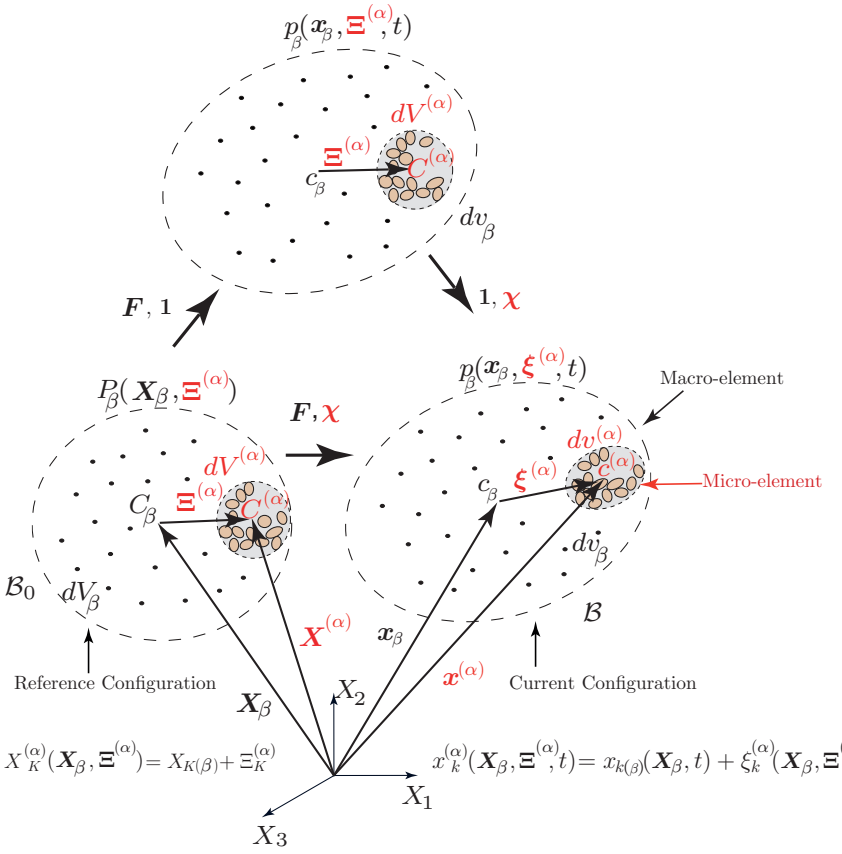

Figure 2.1. schematic of the mapping of the macro-element dV_β and micro-element $dV^{(\alpha)}$ from the reference configuration $\mathcal{B}_0$ to the current configuration $\mathcal{B}$ via the macro-deformation gradient $\boldsymbol{F}$ and micro-deformation tensor $\boldsymbol{\chi}$.

The spatial velocity of the micro-element relative position vector can be expressed as,

$$v_k^{(\alpha)} = \dot{x}_k^{(\alpha)} = \dot{x}_k + \dot{\xi}_k^{(\alpha)} = v_k + \nu_{kl}\xi_l^{(\alpha)} \tag{2.4}$$

where v_k is the velocity at c_β, and $\nu_{kl} = \dot{\chi}_{kK}\chi_{Kl}^{-1}$ is the gyration tensor. This is called gyration tensor because it describes the whirling motion of micro-element with respect to the centroid of macro-element c_β. The inverse motion of (2.2) is expressed as follows,

$$\Xi_K^{(\alpha)} = \chi_{Kl}^{-1}(\boldsymbol{x}_\beta, t)\xi_l^{(\alpha)} \tag{2.5}$$

Using (2.4) and (2.5), the gyration tensor ν_{kl} can be defined such that,

$$\dot{\xi}_k^{(\alpha)} = \dot{\chi}_{kK}\Xi_K^{(\alpha)} = \dot{\chi}_{kK}\chi_{Kl}^{-1}\xi_l^{(\alpha)} = \nu_{kl}\xi_l^{(\alpha)} \tag{2.6}$$

$$\nu_{kl} = \dot{\chi}_{kK}\chi_{Kl}^{-1} \tag{2.7}$$

Similarly, we can find the velocity gradient as,

$$v_{k,l} = \dot{F}_{kK}F_{Kl}^{-1} \tag{2.8}$$

If we take the partial spatial derivative of the micro-element position vector $x_k^{(\alpha)}$ in (2.3), with respect to the reference micro-element position vector $X_K^{(\alpha)}$, we can derive the micro-element deformation gradient $F_{kK}^{(\alpha)}$ such that,

$$\begin{aligned} F_{kK}^{(\alpha)} &= F_{kK}(\boldsymbol{X}_\beta, t) + \frac{\partial \chi_{kL}(\boldsymbol{X}_\beta, t)}{\partial X_{K(\beta)}}\Xi_L^{(\alpha)} \\ &\quad + \left(\chi_{kA}(\boldsymbol{X}_\beta, t) - F_{kA}(\boldsymbol{X}_\beta, t) - \frac{\partial \chi_{kM}(\boldsymbol{X}_\beta, t)}{\partial X_{A(\beta)}}\Xi_M^{(\alpha)}\right)\frac{\partial \Xi_A^{(\alpha)}}{\partial X_{K(\beta)}} \end{aligned} \tag{2.9}$$

By which the spatial micro-element differential line segment can then be formulated as follows,

$$dx_k^{(\alpha)} = F_{kK}^{(\alpha)}dX_K^{(\alpha)} \tag{2.10}$$

According to the micro-structural periodicity assumption, the relative position vector $\boldsymbol{\Xi}^{(\alpha)}$ is not a function of position vector $\boldsymbol{X}_\beta$. Therefore, the micro-element deformation gradient $F_{kK}^{(\alpha)}$ will be reduced such that,

$$F_{kK}^{(\alpha)}(\boldsymbol{X}_\beta, \boldsymbol{\Xi}^{(\alpha)}, t) \overset{\text{def}}{=} \frac{\partial x_k^{(\alpha)}}{\partial X_K^{(\alpha)}} = F_{kK}(\boldsymbol{X}_\beta, t) + \frac{\partial \chi_{kL}(\boldsymbol{X}_\beta, t)}{\partial X_{K(\beta)}}\Xi_L^{(\alpha)} \tag{2.11}$$

This is presented solely to illustrate a deformation gradient tensor that maps the reference configuration micro-element differential line segment $dX_K^{(\alpha)}$ to the current configuration micro-element differential line segment $dx_k^{(\alpha)}$, but it is not used directly (presently) in developing the constitutive equations. The micromorphic continuum theory of this thesis describes micro-element

deformations in terms of solving for micro-displacement tensor $\boldsymbol{\Phi}$ (rather than micro-element displacement vector $\boldsymbol{u}^{(\alpha)}$, explain later) and tracking changes in the length of the family of relative position vector $\boldsymbol{\Xi}^{(\alpha)}$. Deriving the micromorphic continuum constitutive equations based on the micro-element deformation gradient $F_{kK}^{(\alpha)}$ is very appealing in terms of solving for micro-element displacement vector $\boldsymbol{u}^{(\alpha)}$ and, obtaining better picture of micro-element deformation. However, it could be mathematically complicated to derive constitutive equations, micromorphic stress and strain tensors. From classical continuum mechanics, the deformation gradient of the macro-continuum can be expressed as,

$$F_{kK}(\boldsymbol{X}_{\beta}, t) = \frac{\partial x_{k(\beta)}(\boldsymbol{X}_{\beta}, t)}{\partial X_{K(\beta)}} = \delta_{kK} + \frac{\partial u_k(\boldsymbol{X}_{\beta}, t)}{\partial X_{K(\beta)}} \tag{2.12}$$

Similarly, for the micro-deformation tensor we have,

$$\chi_{kK}(\boldsymbol{X}_{\beta}, t) = \delta_{kK} + \Phi_{kK}(\boldsymbol{X}_{\beta}, t) \tag{2.13}$$

where Φ_{kK} is the "micro-displacement tensor". Note that Φ_{kK} is a displacement-gradient-like quantity, and it could be called "micro-displacement-gradient tensor". We choose to be consistent with Eringen's terminology [Eringen, 1968] for the micro-displacement tensor Φ_{kK}, but it should not be confused with the micro-element displacement vector $\boldsymbol{u}^{(\alpha)}$ (explain later). The micro-displacement tensor Φ_{kK} represents the deformation of the family of relative position vectors $\boldsymbol{\Xi}^{(\alpha)}$ such that,

$$\xi_k^{(\alpha)} = \chi_{kK}\Xi_K^{(\alpha)} = \delta_{kK}\Xi_K^{(\alpha)} + \Phi_{kK}\Xi_K^{(\alpha)} \tag{2.14}$$

where Φ_{kK} is the "micro-displacement tensor". Note that Φ_{kK} is a displacement gradient-like quantity which represents deformation of the relative position vector $\boldsymbol{\Xi}^{(\alpha)}$, which can be thought of as a moment arm. Sometimes it is difficult to interpret the micro-structural deformation just by investigating the micro-displacement tensor $\boldsymbol{\Phi}$. Clearer understanding of micro-structural deformation can be obtained through the micro-element displacement vector $\boldsymbol{u}^{(\alpha)}$ such that,

$$\boldsymbol{u}^{(\alpha)}(\boldsymbol{X}_{\beta}, \boldsymbol{\Xi}^{(\alpha)}, t) = \boldsymbol{u}(\boldsymbol{X}_{\beta}, t) + \boldsymbol{\Phi}(\boldsymbol{X}_{\beta}, t) \cdot \boldsymbol{\Xi}^{(\alpha)} \tag{2.15}$$

Note that micromorphic continuum theory deals with both the macro-element and micro-element continuum bodies. Therefore, the quantity $\boldsymbol{u}$ represents the displacement of the macro-element in the micromorphic continuum body. The quantity $\boldsymbol{u}^{(\alpha)}$ can be considered as a displacement of the micro-elements via explicitly involving the relative position vector $\boldsymbol{\Xi}^{(\alpha)}$ and the micro-displacement tensor $\boldsymbol{\Phi}$. The micro-displacement tensor $\boldsymbol{\Phi}$ can be related to the current configuration micro-displacement tensor $\boldsymbol{\phi}$ such that,

$$\phi_{kl} = \Phi_{kK}\chi^{-1}_{Kl} \tag{2.16}$$

The micro-element displacement vector in the current configuration is expressed as follows,

$$\boldsymbol{x}^{(\alpha)}(\boldsymbol{x}_\beta, \boldsymbol{\xi}^{(\alpha)}, t) - \boldsymbol{X}^{(\alpha)}(\boldsymbol{x}_\beta, \boldsymbol{\xi}^{(\alpha)}) = \boldsymbol{u}^{(\alpha)}(\boldsymbol{x}_\beta, \boldsymbol{\xi}^{(\alpha)}, t) = \boldsymbol{u}(\boldsymbol{x}_\beta, t) + \boldsymbol{\phi}(\boldsymbol{x}_\beta, t) \cdot \boldsymbol{\xi}^{(\alpha)} \tag{2.17}$$

The deformation measures for micromorphic continuum which are invariant under rigid body motion can be defined such that,

$$C_{KL} = F_{kK}F_{kL}, \qquad \boldsymbol{C} = \boldsymbol{F}^T \cdot \boldsymbol{F}, \tag{2.18}$$

$$\Psi_{KL} = F_{kK}\chi_{kL}, \qquad \boldsymbol{\Psi} = \boldsymbol{F}^T \cdot \boldsymbol{\chi}, \tag{2.19}$$

$$\Gamma_{KLM} = F_{kK}\chi_{kL,M}, \qquad \boldsymbol{\Gamma} = \boldsymbol{F}^T \cdot (\boldsymbol{\nabla}_0 \boldsymbol{\chi}) \tag{2.20}$$

Substituting (2.12, 2.14) into (2.18-2.20) we obtain the deformation measures as follows,

$$C_{KL} = \delta_{KL} + U_{K,L} + U_{L,K} + U_{M,K}U_{M,L} \tag{2.21}$$

$$\Psi_{KL} = \delta_{KL} + \Phi_{KL} + U_{L,K} + U_{M,K}\Phi_{ML} \tag{2.22}$$

$$\Gamma_{KLM} = \Phi_{KL,M} + U_{N,K}\chi_{NL,M} \tag{2.23}$$

where $U_K = \delta_{kK}u_k$, $\Phi_{KL} = \delta_{kK}\Phi_{kL}$, $\chi_{NL} = \delta_{nN}\chi_{nL}$, and $\chi_{NL,M} = \Phi_{NL,M}$, where δ_{kK} is the "shifter" in Cartesian coordinates [Eringen, 1962]. The Lagrangian strain tensor E_{KL}, material micro-strain tensor $\mathcal{E}_{KL}$, and the gradient deformation tensor Γ_{KLM} can be written such that

$$E_{KL} = \frac{1}{2}(C_{KL} - \delta_{KL}) \tag{2.24}$$

$$\mathcal{E}_{KL} = \Psi_{KL} - \delta_{KL} \tag{2.25}$$

$$\Gamma_{KLM} = F_{kK}\chi_{kL,M} \tag{2.26}$$

In the next section, the momentum balance equations and thermodynamics of a micromorphic continuum proposed by Eringen and Suhubi [1964] will be re-derived in detail, to be consistent with notation in this thesis and be complete with regard to derivation and future hierarchical upscaling through a "micromorphic filter" [Regueiro et al., 2014].

2.2 Micromorphic Balance Equations

In this section the weighted residual, integral averaging method, is used in the current configuration to derive balance equations and thermodynamics of a micromorphic continuum. Based upon Eringen and Suhubi [1964] (details also in Regueiro [2011]), we start with the local classical balance equations satisfied at centroid $c^{(\alpha)}$ of micro-element differential volume $dv^{(\alpha)}$ in the current configuration. By using the integral-averaging-method, we arrive at an integral form of the balance equations over the integrated macro-element differential volume dv_β.

2.2.1 Balance of Mass

The mass of micro-element differential volume $dv^{(\alpha)}$ is $\rho^{(\alpha)}dv^{(\alpha)}$, where $\rho^{(\alpha)}$ is the micro-element mass density. By integrating it over the macro-element volume dv_β, we can define the macro-element differential mass dm_β as follows,

$$dm_\beta \overset{\text{def}}{=} \int_{dv_\beta} \rho^{(\alpha)} dv^{(\alpha)} = \int_{dV_\beta} \rho_0^{(\alpha)} dV^{(\alpha)} \tag{2.27}$$

where assuming single phase conservation of mass $\rho_0^{(\alpha)} = \rho^{(\alpha)} J^{(\alpha)}$, $J^{(\alpha)} = \det \mathbf{F}^{(\alpha)}$. Then, we have the conservation of micro-element mass $m^{(\alpha)}$ over dv_β such that,

$$\begin{aligned}
\frac{D(dm_\beta)}{Dt} &= 0 && (2.28)\\
&= \frac{D}{Dt}\int_{dv_\beta} \rho^{(\alpha)} dv^{(\alpha)} && (2.29)\\
&= \frac{D}{Dt}\int_{dV_\beta} \rho^{(\alpha)} J^{(\alpha)} dV^{(\alpha)} \\
&= \int_{dV_\beta} \left(\frac{D\rho^{(\alpha)}}{Dt} J^{(\alpha)} + \rho^{(\alpha)} \frac{DJ^{(\alpha)}}{Dt} \right) dV^{(\alpha)} \\
&= \int_{dv_\beta} \left(\frac{D\rho^{(\alpha)}}{Dt} + \rho^{(\alpha)} \frac{\partial v_l^{(\alpha)}}{\partial x_l^{(\alpha)}} \right) dv^{(\alpha)} = 0
\end{aligned}$$

Thus, the localized balance of micro-element mass over dv_β is

$$\frac{D\rho^{(\alpha)}}{Dt} + \rho^{(\alpha)} \frac{\partial v_l^{(\alpha)}}{\partial x_l^{(\alpha)}} = 0 \tag{2.30}$$

Considering the mass density $\rho_\beta = dm_\beta / dv_\beta$ at c_β, applying the integral-average definition of differential mass over the macro-element,

$$\rho_\beta dv_\beta = dm_\beta \overset{\text{def}}{=} \int_{dv_\beta} \rho^{(\alpha)} dv^{(\alpha)} \tag{2.31}$$

The total mass m of the body $\mathcal{B}$ is then expressed as:

$$m = \int_{\mathcal{B}} \rho_\beta dv_\beta = \int_{\mathcal{B}} \left[\int_{dv_\beta} \rho^{(\alpha)} dv^{(\alpha)} \right] = \int_{\mathcal{B}_0} \left[\int_{dV_\beta} \rho^{(\alpha)} J^{(\alpha)} dV^{(\alpha)} \right] \tag{2.32}$$

The conservation of mass over the body $\mathcal{B}$ is expressed as:

$$\begin{aligned}
\frac{Dm}{Dt} &= \int_{\mathcal{B}_0} \left[\int_{dV_\beta} \frac{D\left(\rho^{(\alpha)} J^{(\alpha)}\right)}{Dt} dV^{(\alpha)} \right] \\
&= \int_{\mathcal{B}} \left[\int_{dv_\beta} \left(\underbrace{\frac{D\rho^{(\alpha)}}{Dt} + \rho^{(\alpha)} \frac{\partial v_l^{(\alpha)}}{\partial x_l^{(\alpha)}}}_{=0} \right) dv^{(\alpha)} \right] = 0 && (2.33)
\end{aligned}$$

Then, the balance of mass in $\mathcal{B}$ is such that,

$$\begin{aligned}\frac{Dm}{Dt} &= \frac{D}{Dt}\int_{\mathcal{B}}\rho_\beta dv_\beta = 0 \\ &= \int_{\mathcal{B}_0}\frac{D\left(\rho_\beta J_\beta\right)}{Dt}dV_\beta \\ &= \int_{\mathcal{B}}\left(\frac{D\rho_\beta}{Dt}+\rho_\beta\frac{\partial v_{l(\beta)}}{\partial x_{l(\beta)}}\right)dv_\beta = 0\end{aligned} \tag{2.34}$$

where localizing the integral form of the balance of mass, we arrive at the balance of mass similar to that of classical continuum theory such that,

$$\frac{D\rho_\beta}{Dt}+\rho_\beta\frac{\partial v_{l\beta}}{\partial x_{l(\beta)}} = 0 \tag{2.35}$$

2.2.2 Balance of micro-inertia

In order to derive the balance of micro-inertia, we start with the fact that all the micro-elements within a macro-element are in equilibrium with respect to the momentum. Therefore, the first mass moment about the centroid C_β will be zero as follows,

$$\int_{dV_\beta}\rho_0^{(\alpha)}\Xi_K^{(\alpha)}dV^{(\alpha)} = 0 \tag{2.36}$$

The second mass moment is not zero, such that the micro-inertia $I_{KL(\beta)}$ in the reference configuration $\mathcal{B}_0$ is defined as

$$\rho_{0(\beta)}I_{KL(\beta)}dV_\beta \overset{\text{def}}{=} \int_{dV_\beta}\rho_0^{(\alpha)}\Xi_K^{(\alpha)}\Xi_L^{(\alpha)}dV^{(\alpha)} \tag{2.37}$$

where $\boldsymbol{I}_\beta$ is the micro-inertia tensor in the reference configuration. Following the assumption of periodic micro-structure, the family of relative position vectors $\boldsymbol{\Xi}^{(\alpha)}$ is not a function of the position vector $\boldsymbol{X}_\beta$. Therefore, the relative position vector can be pulled out of the integral over the macro-element volume in the reference configuration dV_β such that,

$$\rho_{0(\beta)}I_{KL(\beta)}dV_\beta \overset{\text{def}}{=} \Xi_K^{(\alpha)}\Xi_L^{(\alpha)}\int_{dV_\beta}\rho_0^{(\alpha)}dV^{(\alpha)} \tag{2.38}$$

According to (2.38), for homogenous materials with periodic micro-structure, the micro-inertia tensor $\boldsymbol{I}_\beta$ is constant. This paper deals with the total Lagrangian finite element implementation of micromorphic continuum. Therefore, the balance of micro-inertia in the reference configuration $\mathcal{B}_0$ is satisfied. The material time derivative of the micro-inertia term in the reference configuration $\mathcal{B}_0$ is as follows,

$$\frac{D}{Dt}\int_{\mathcal{B}_0}\rho_{0(\beta)}I_{KL(\beta)}dV_\beta=\int_{\mathcal{B}_0}\rho_{0(\beta)}\frac{DI_{KL(\beta)}}{Dt}dV_\beta=0 \tag{2.39}$$

Likewise, a micro-inertia $i_{kl(\beta)}$ in the spatial configuration $\mathcal{B}$ and its mapping to the reference configuration $\mathcal{B}_0$ can be expressed as

$$\begin{aligned}\rho_\beta i_{kl(\beta)}dv_\beta &\overset{\text{def}}{=} \int_{dv_\beta}\rho^{(\alpha)}\xi_k^{(\alpha)}\xi_l^{(\alpha)}dv^{(\alpha)} \qquad (2.40)\\ &= \int_{dv_\beta}\rho^{(\alpha)}\chi_{kK}\Xi_K^{(\alpha)}\chi_{lL}\Xi_L^{(\alpha)}dv^{(\alpha)}\\ &= \chi_{kK}\chi_{lL}\int_{dV_\beta}\rho_0^{(\alpha)}\Xi_K^{(\alpha)}\Xi_L^{(\alpha)}dV^{(\alpha)}\\ &= \chi_{kK}\chi_{lL}\rho_{0(\beta)}I_{KL(\beta)}dV_\beta=\chi_{kK}\chi_{lL}\rho_\beta I_{KL(\beta)}dv_\beta\\ &\quad\Longrightarrow I_{KL(\beta)}=\chi^{-1}_{Kk}\chi^{-1}_{Ll}i_{kl(\beta)} \qquad (2.41)\end{aligned}$$

The balance of micro-inertia in the current configuration is derived such that,

$$\begin{aligned}\frac{D}{Dt}\int_{\mathcal{B}_0}\rho_{0(\beta)}I_{KL(\beta)}dV_\beta &= \int_{\mathcal{B}_0}\rho_{0(\beta)}\frac{D(I_{KL(\beta)})}{Dt}dV_\beta=0 \qquad (2.42)\\ &\quad \frac{DI_{KL(\beta)}}{Dt}=\chi^{-1}_{Kk}\chi^{-1}_{Ll}\left(\frac{D(i_{kl(\beta)})}{Dt}-\nu_{ka}i_{al(\beta)}-\nu_{la}i_{ak(\beta)}\right)\\ &= \int_{\mathcal{B}}\rho_\beta\chi^{-1}_{Kk}\chi^{-1}_{Ll}\left(\frac{D(i_{kl(\beta)})}{Dt}-\nu_{ka}i_{al(\beta)}-\nu_{la}i_{ak(\beta)}\right)dv_\beta=0\end{aligned}$$

and,

$$\frac{D(i_{kl(\beta)})}{Dt}-\nu_{ka}i_{al(\beta)}-\nu_{la}i_{ak(\beta)}=0 \tag{2.43}$$

Note that the balance of micro-inertia in the current configuration is presented for the purpose of being used for future work of implementing updated Lagrangian finite element analysis of micromorphic continuum.

2.2.3 Balance of Linear Momentum, Angular Momentum, and First Moment of Momentum

In the following, we derive the balance of linear momentum, angular momentum, and first moment of momentum for micromorphic continuum theory. Based upon the approach by Eringen and Suhubi [1964], we start with the localized balance of linear and angular momenta in the micro-element differential volume $dv^{(\alpha)}$ as follows,

$$\sigma^{(\alpha)}_{lk,l} + \rho^{(\alpha)}(f^{(\alpha)}_k - \ddot{u}^{(\alpha)}_k) = 0 \tag{2.44}$$

$$\sigma^{(\alpha)}_{lk} = \sigma^{(\alpha)}_{kl} \tag{2.45}$$

where the micro-element Cauchy stress tensor $\sigma^{(\alpha)}_{kl}$ is symmetric by way of angular momentum being conserved within $dv^{(\alpha)}$. $\rho^{(\alpha)}$ is the micro-element mass density, $\boldsymbol{f}^{(\alpha)}$ is the micro-element body force vector per unit mass, and $\ddot{\boldsymbol{u}}^{(\alpha)}$ is the micro-element acceleration vector. By using a weighted-residual approach, and selecting a smooth weighting function $\phi^{(\alpha)}$, the balance of momenta over $\mathcal{B}$ (depending on choice of $\phi^{(\alpha)}$) can be expressed as,

$$\int_{\mathcal{B}} \left\{ \int_{dv_\beta} \phi^{(\alpha)} \left[\sigma^{(\alpha)}_{lk,l} + \rho^{(\alpha)}(f^{(\alpha)}_k - \ddot{u}^{(\alpha)}_k) \right] dv^{(\alpha)} \right\} = 0 \tag{2.46}$$

where $(\bullet)^{(\alpha)}_{,l} = \partial(\bullet)^{(\alpha)}/\partial x^{(\alpha)}_l$. Applying the chain rule and divergence theorem, we can rewrite (2.46) as,

$$\int_{\mathcal{B}} \left\{ \int_{dv_\beta} \left[(\phi^{(\alpha)} \sigma_{lk}^{(\alpha)})_{,l} - \phi_{,l}^{(\alpha)} \sigma_{lk}^{(\alpha)} + \rho^{(\alpha)} \phi^{(\alpha)} (f_k^{(\alpha)} - \ddot{u}_k^{(\alpha)}) \right] dv^{(\alpha)} \right\} = 0 \tag{2.47}$$

$$\int_{\partial\mathcal{B}} \left\{ \int_{da_\beta} (\phi^{(\alpha)} \sigma_{lk}^{(\alpha)}) n_l^{(\alpha)} da^{(\alpha)} \right\} +$$

$$\int_{\mathcal{B}} \left\{ \int_{dv_\beta} \left[-\phi_{,l}^{(\alpha)} \sigma_{lk}^{(\alpha)} + \rho^{(\alpha)} \phi^{(\alpha)} (f_k^{(\alpha)} - \ddot{u}_k^{(\alpha)}) \right] dv^{(\alpha)} \right\} = 0 \tag{2.48}$$

Assuming three different weighting functions for $\phi^{(\alpha)}$, we can derive the balance of linear momentum, angular momentum, and first moment of momentum on $\mathcal{B}$ for micromorphic continuum: (1) $\phi^{(\alpha)} = 1$, balance of linear momentum; (2) $\phi^{(\alpha)} = e_{nmk} x_m^{(\alpha)}$, balance of angular momentum (e_{nmk} is the permutation tensor); (3) $\phi^{(\alpha)} = x_m^{(\alpha)}$, balance of first moment of momentum. Substituting these three choices for $\phi^{(\alpha)}$ into (2.48), we can derive the respective micromorphic balance equations on $\mathcal{B}$ as follows.

2.2.3.1 Balance of Linear Momentum: ($\phi^{(\alpha)} = 1$)

The balance of linear momentum can be expressed as,

$$\int_{\partial\mathcal{B}} \left\{ \int_{da_\beta} \sigma_{lk}^{(\alpha)} n_l^{(\alpha)} da^{(\alpha)} \right\} + \int_{\mathcal{B}} \left\{ \int_{dv_\beta} \left[\rho^{(\alpha)} (f_k^{(\alpha)} - \ddot{u}_k^{(\alpha)}) \right] dv^{(\alpha)} \right\} = 0 \tag{2.49}$$

where we have the following definition,

$$\sigma_{lk} n_l da_\beta \overset{\text{def}}{=} \int_{da_\beta} \sigma_{lk}^{(\alpha)} n_l^{(\alpha)} da^{(\alpha)} \tag{2.50}$$

$$\rho f_k dv_\beta \overset{\text{def}}{=} \int_{dv_\beta} \rho^{(\alpha)} f_k^{(\alpha)} dv^{(\alpha)} \tag{2.51}$$

$$\rho \ddot{u}_k dv_\beta \overset{\text{def}}{=} \int_{dv_\beta} \rho^{(\alpha)} \ddot{u}_k^{(\alpha)} dv^{(\alpha)} \tag{2.52}$$

where we drop the subscript β denoting macro-element variables at c_β (for example, macro-element mass density ρ_β and ρ are the same vaiable at c_β), unless needed for clarification, σ_{lk} is the unsymmetric macroscopic Cauchy stress tensor, f_k is the macroscopic body force vector per unit

mass, ρ is the macroscopic mass density, and $\ddot{u}_k$ is the macroscopic acceleration vector. From (2.49), (2.50-2.52), we have

$$\int_{\partial\mathcal{B}} \sigma_{lk} n_l da_\beta + \int_{\mathcal{B}} \rho(f_k - \ddot{u}_k) dv_\beta = 0 \tag{2.53}$$

$$\int_{\mathcal{B}} \left[\sigma_{lk,l} + \rho(f_k - \ddot{u}_k)\right] dv_\beta = 0 \tag{2.54}$$

The localized expression for micromorphic balance of linear momentum at spatial position $\boldsymbol{x}_\beta$ can then be written as,

$$\sigma_{lk,l} + \rho(f_k - \ddot{u}_k) = 0 \tag{2.55}$$

The balance of linear momentum for the micromorphic continuum is similar to that of the classical continuum theory, except that the macroscopic Cauchy stress tensor σ_{lk} may be unsymmetric.

2.2.3.2 Balance of Angular Momentum: $(\phi^{(\alpha)} = e_{nmk} x_m^{(\alpha)})$

The balance of angular momentum can be derived as follows,

$$\begin{aligned}
&\int_{\partial\mathcal{B}} \left\{ \int_{da_\beta} e_{nmk} (x_m^{(\alpha)} \sigma_{lk}^{(\alpha)}) n_l^{(\alpha)} da^{(\alpha)} \right\} + \\
&\int_{\mathcal{B}} \left\{ \int_{dv_\beta} e_{nmk} \left[-x_{m,l}^{(\alpha)} \sigma_{lk}^{(\alpha)} + \rho^{(\alpha)} x_m^{(\alpha)} (f_k^{(\alpha)} - \ddot{u}_k^{(\alpha)}) \right] dv^{(\alpha)} \right\} = 0 \\
&\int_{\partial\mathcal{B}} \left\{ \int_{da_\beta} e_{nmk} (x_{m(\beta)} + \xi_m^{(\alpha)}) \sigma_{lk}^{(\alpha)} n_l^{(\alpha)} da^{(\alpha)} \right\} \\
&\qquad + \int_{\mathcal{B}} \left\{ \int_{dv_\beta} e_{nmk} \left[-\sigma_{mk}^{(\alpha)} + \rho^{(\alpha)} (x_{m(\beta)} + \xi_m^{(\alpha)}) (f_k^{(\alpha)} - \ddot{u}_k^{(\alpha)}) \right] dv^{(\alpha)} \right\} = 0
\end{aligned} \tag{2.56}$$

where $x_{m,l}^{(\alpha)} = \partial x_m^{(\alpha)} / \partial x_l^{(\alpha)} = \delta_{ml}$. The acceleration of the micro-element centroid and the acceleration of the relative position vector can be expressed as

$$\ddot{u}_k^{(\alpha)} = \ddot{u}_k + \ddot{\xi}_k^{(\alpha)} \tag{2.57}$$

$$\ddot{\xi}_k^{(\alpha)} = (\dot{\nu}_{kc} + \nu_{kb}\nu_{bc}) \xi_c^{(\alpha)} \tag{2.58}$$

Inserting (2.57, 2.58) into (2.56), we have,

$$\begin{aligned}
\int_{\partial\mathcal{B}} \left\{ \int_{da_\beta} e_{nmk}((x_{m(\beta)} + \xi_m^{(\alpha)})\sigma_{lk}^{(\alpha)}) n_l^{(\alpha)} da^{(\alpha)} \right\} &= \int_{\partial\mathcal{B}} \left\{ e_{nmk} x_{m(\beta)} \underbrace{\int_{da_\beta} \sigma_{lk}^{(\alpha)} n_l^{(\alpha)} da^{(\alpha)}}_{\stackrel{\text{def}}{=} \sigma_{lk} n_l da_\beta} \right\} \\
&\quad + \int_{\partial\mathcal{B}} \left\{ e_{nmk} \underbrace{\int_{da_\beta} \sigma_{lk}^{(\alpha)} \xi_m^{(\alpha)} n_l^{(\alpha)} da^{(\alpha)}}_{\stackrel{\text{def}}{=} m_{lkm} n_l da_\beta} \right\} \\
&= e_{nmk} \int_{\partial\mathcal{B}} \left[x_{m(\beta)} \sigma_{lk} n_l + m_{lkm} n_l \right] da_\beta \\
&= e_{nmk} \int_{\mathcal{B}} \left[\sigma_{mk} + x_{m(\beta)} \sigma_{lk,l} + m_{lkm,l} \right] dv_\beta \qquad (2.59) \\
\int_{\mathcal{B}} \left\{ \int_{dv_\beta} e_{nmk} \left[-\sigma_{mk}^{(\alpha)} \right] dv^{(\alpha)} \right\} &= -e_{nmk} \int_{\mathcal{B}} \underbrace{\int_{dv_\beta} \sigma_{mk}^{(\alpha)} dv^{(\alpha)}}_{\stackrel{\text{def}}{=} s_{mk} dv_\beta} \\
&= -e_{nmk} \int_{\mathcal{B}} s_{mk} dv_\beta \qquad (2.60) \\
\int_{\mathcal{B}} \left\{ \int_{dv_\beta} e_{nmk} \left[\rho^{(\alpha)} (x_{m(\beta)} + \xi_m^{(\alpha)}) f_k^{(\alpha)} \right] dv^{(\alpha)} \right\} &= \\
\int_{\mathcal{B}} \left\{ e_{nmk} x_{m(\beta)} \underbrace{\int_{dv_\beta} \rho^{(\alpha)} f_k^{(\alpha)} dv^{(\alpha)}}_{\stackrel{\text{def}}{=} \rho f_k dv_\beta} \right\} &+ \int_{\mathcal{B}} \left\{ e_{nmk} \underbrace{\int_{dv_\beta} \rho^{(\alpha)} f_k^{(\alpha)} \xi_m^{(\alpha)} dv^{(\alpha)}}_{\stackrel{\text{def}}{=} \rho \ell_{km} dv_\beta} \right\} \\
&= e_{nmk} \int_{\mathcal{B}} \left(x_{m(\beta)} \rho f_k + \rho \ell_{km} \right) dv_\beta \qquad (2.61)
\end{aligned}$$

$$
\begin{aligned}
&\int_{\mathcal{B}} \left\{ \int_{dv_\beta} e_{nmk} \left[\rho^{(\alpha)} (x_{m(\beta)} + \xi_m^{(\alpha)})(-\ddot{u}_k^{(\alpha)}) \right] dv^{(\alpha)} \right\} \\
&= -e_{nmk} \int_{\mathcal{B}} \left\{ \int_{dv_\beta} \rho^{(\alpha)} (x_{m(\beta)} \ddot{u}_k + x_{m(\beta)} \ddot{\xi}_k^{(\alpha)} + \xi_m^{(\alpha)} \ddot{u}_k + \xi_m^{(\alpha)} \ddot{\xi}_k^{(\alpha)}) dv^{(\alpha)} \right\} \\
&= -e_{nmk} \int_{\mathcal{B}} \Bigg[x_{m(\beta)} \ddot{u}_k \underbrace{\int_{dv_\beta} \rho^{(\alpha)} dv^{(\alpha)}}_{\stackrel{\text{def}}{=} \rho dv_\beta} + x_{m(\beta)} (\dot{\nu}_{kc} + \nu_{kb}\nu_{bc}) \underbrace{\int_{dv_\beta} \rho^{(\alpha)} \xi_c^{(\alpha)} dv^{(\alpha)}}_{=0} \\
&+ \ddot{u}_k \underbrace{\int_{dv_\beta} \rho^{(\alpha)} \xi_m^{(\alpha)} dv^{(\alpha)}}_{=0} + \underbrace{\int_{dv_\beta} \rho^{(\alpha)} \ddot{\xi}_k^{(\alpha)} \xi_m^{(\alpha)} dv^{(\alpha)}}_{\stackrel{\text{def}}{=} \rho \omega_{km} dv_\beta} \Bigg] \\
&= -e_{nmk} \int_{\mathcal{B}} \left[x_{m(\beta)} \rho \ddot{u}_k + \rho \omega_{km} \right] dv_\beta
\end{aligned} \tag{2.62}
$$

where $\int_{dv_\beta} \rho^{(\alpha)} \xi_k^{(\alpha)} dv^{(\alpha)} = 0$ because $\xi_k^{(\alpha)}$ is mass-centered on dv_β, m_{lkm} is the higher order (couple) stress defined through relative position vector $\xi_m^{(\alpha)}$, s_{mk} is the symmetric micro-stress, ℓ_{km} is the body force couple, and ω_{km} is the micro-spin inertia. Combining terms, we have

$$
\begin{aligned}
&e_{nmk} \int_{\mathcal{B}} \left[x_{m(\beta)} \underbrace{(\sigma_{lk,l} + \rho(f_k - \ddot{u}_k))}_{=0} + \sigma_{mk} - s_{mk} + m_{lkm,l} + \rho(\ell_{km} - \omega_{km}) \right] dv_\beta = 0 \\
&e_{nmk} \int_{\mathcal{B}} \left[\sigma_{mk} - s_{mk} + m_{lkm,l} + \rho(\ell_{km} - \omega_{km}) \right] dv_\beta = 0
\end{aligned} \tag{2.63}
$$

Upon localizing the integral at $\boldsymbol{x}_\beta$,

$$
e_{nmk} \left[\sigma_{mk} - s_{mk} + m_{lkm,l} + \rho(\ell_{km} - \omega_{km}) \right] = 0 \tag{2.64}
$$

$$
e_n \left[\sigma_{[mk]} - \underbrace{s_{[mk]}}_{=0} + m_{l[km],l} + \rho(\ell_{[km]} - \omega_{[km]}) \right] = 0 \tag{2.65}
$$

where e_n is a coefficient such that $e_n = 1$ for $n = 1, 2, 3$ $(n \neq m \neq k)$, and we have,

$$
\sigma_{[mk]} + m_{l[km],l} + \rho(\ell_{[km]} - \omega_{[km]}) = 0 \tag{2.66}
$$

For $n = 1, 2, 3$ where the antisymmetric definition is $\sigma_{[mk]} = (\sigma_{mk} - \sigma_{km})/2$. It is to be noted that (2.66) provides 3 equations through the balance of angular momentum to solve for the micro-rotation vector φ_k (discussed later) and thus the balance of angular momentum does not provide enough equations if we consider micro-shear and micro-stretch. Therefore, we need six additional equations to be able to solve for all of the 9 additional micromorphic dofs Φ_{kK} (or ϕ_{kl}). This is done via the **balance of first moment of momentum**.

2.2.3.3 balance of first moment of momentum: $(\phi^{(\alpha)} = x_m^{(\alpha)})$

Similar to the procedure we followed for the balance of angular momentum, the balance of first moment of momentum is derived without multiplying by the permutation tensor e_{nmk}. Thus, we may write directly equation (2.64) without the permutation tensor e_{nmk} as,

$$\sigma_{mk} - s_{mk} + m_{lkm,l} + \rho(\ell_{km} - \omega_{km}) = 0 \tag{2.67}$$

This equation provides 9 equations to solve for the 9 components of the micro-displacement tensor Φ_{kK} through the definition $\chi_{kK} = \delta_{kK} + \Phi_{kK}$ (and later a Total Langrangian FE formulation). Based upon these equations it can be seen that the macroscopic Cauchy stress σ_{lk} may not be symmetric (if the couple stress is non-zero and not divergence free, and/or the body couple and micro-spin inertia are non-zero).

2.3 Thermodynamics

In the following, we derive the first and second laws of thermodynamics for a micromorphic continuum, as well as the Clasisus-Duhem inequality.

2.3.1 Balance of Energy:

The macro-element balance of energy equation with respect to micro-element $dv^{(\alpha)}$ can be written in integral form over dv_β such that,

$$\int_{dv_\beta} \rho^{(\alpha)} \dot{e}^{(\alpha)} dv^{(\alpha)} = \int_{dv_\beta} \left[\sigma_{kl}^{(\alpha)} v_{l,k}^{(\alpha)} + q_{k,k}^{(\alpha)} + \rho^{(\alpha)} r^{(\alpha)} \right] dv^{(\alpha)} \tag{2.68}$$

where $\dot{e}^{(\alpha)}$ is the micro-internal energy rate per unit mass, $q_k^{(\alpha)}$ is the micro-heat flux, and $r^{(\alpha)}$ the micro-heat source per unit mass. In this equation, it is assumed that the classical balance of energy in localized form is valid within the micro-element differential volume $dv^{(\alpha)}$. By integrating over the whole body $\mathcal{B}$, we have

$$\int_{\mathcal{B}} \left\{ \int_{dv_\beta} \rho^{(\alpha)} \dot{e}^{(\alpha)} dv^{(\alpha)} \right\} = \int_{\mathcal{B}} \left\{ \int_{dv_\beta} \left[\sigma_{kl}^{(\alpha)} v_{l,k}^{(\alpha)} + q_{k,k}^{(\alpha)} + \rho^{(\alpha)} r^{(\alpha)} \right] dv^{(\alpha)} \right\} \tag{2.69}$$

Further derivation of the above equation, term by term, leads to (again leaving off, subscript β on macro-element variables at $\boldsymbol{x}_\beta$, unless needed for clarification),

$$\begin{aligned}
\int_{dv_\beta} \rho^{(\alpha)}\dot{e}^{(\alpha)}dv^{(\alpha)} &= \int_{dV_\beta} \rho_0^{(\alpha)}\dot{e}^{(\alpha)}dV^{(\alpha)} = \frac{D}{Dt}\underbrace{\int_{dV_\beta} \rho_0^{(\alpha)}e^{(\alpha)}dV^{(\alpha)}}_{\stackrel{\text{def}}{=}\rho_0 e dV_\beta = \rho e dv_\beta} \\
&= \frac{D}{Dt}(\rho_0 e dV_\beta) = \rho_0 \dot{e} dV_\beta = \rho \dot{e} dv_\beta \qquad (2.70) \\
\int_{dv_\beta} \sigma_{kl}^{(\alpha)} v_{l,k}^{(\alpha)} dv^{(\alpha)} &= \int_{dv_\beta} \left[(\sigma_{kl}^{(\alpha)} v_l^{(\alpha)})_{,k} - \sigma_{kl,k}^{(\alpha)} v_l^{(\alpha)} \right] dv^{(\alpha)} \qquad (2.71) \\
&= \int_{da_\beta} \sigma_{kl}^{(\alpha)} v_l^{(\alpha)} n_k^{(\alpha)} da^{(\alpha)} - \int_{dv_\beta} \sigma_{kl,k}^{(\alpha)} v_l^{(\alpha)} dv^{(\alpha)} \\
&= \int_{da_\beta} \sigma_{kl}^{(\alpha)} (v_l + \nu_{lm}\xi_m^{(\alpha)}) n_k^{(\alpha)} da^{(\alpha)} - \int_{dv_\beta} \rho^{(\alpha)} (\ddot{u}_l^{(\alpha)} - f_l^{(\alpha)})(v_l + \nu_{lm}\xi_m^{(\alpha)}) dv^{(\alpha)} \\
&= v_l \underbrace{\int_{da_\beta} \sigma_{kl}^{(\alpha)} n_k^{(\alpha)} da^{(\alpha)}}_{\stackrel{\text{def}}{=}\sigma_{kl} n_k da_\beta} + \nu_{lm} \underbrace{\int_{da_\beta} \sigma_{kl}^{(\alpha)} \xi_m^{(\alpha)} n_k^{(\alpha)} da^{(\alpha)}}_{\stackrel{\text{def}}{=} m_{klm} n_k da_\beta} \\
&\quad - v_l \underbrace{\int_{dv_\beta} \rho^{(\alpha)} \ddot{u}_l^{(\alpha)} dv^{(\alpha)}}_{\stackrel{\text{def}}{=}\rho \ddot{u}_l dv_\beta} + v_l \underbrace{\int_{dv_\beta} \rho^{(\alpha)} f_l^{(\alpha)} dv^{(\alpha)}}_{\stackrel{\text{def}}{=}\rho f_l dv_\beta} \\
&\quad - \nu_{lm}\ddot{u}_l \underbrace{\int_{dv_\beta} \rho^{(\alpha)} \xi_m^{(\alpha)} dv^{(\alpha)}}_{=0} - \nu_{lm} \underbrace{\int_{dv_\beta} \rho^{(\alpha)} \ddot{\xi}_l^{(\alpha)} \xi_m^{(\alpha)} dv^{(\alpha)}}_{\stackrel{\text{def}}{=}\rho \omega_{lm} dv_\beta} \\
&\quad + \nu_{lm} \underbrace{\int_{dv_\beta} \rho^{(\alpha)} f_l^{(\alpha)} \xi_m^{(\alpha)} dv^{(\alpha)}}_{\stackrel{\text{def}}{=}\rho \ell_{lm} dv_\beta}
\end{aligned}$$

$$\int_{dv_\beta} q_{k,k}^{(\alpha)} dv^{(\alpha)} = \int_{da_\beta} q_k^{(\alpha)} n_k^{(\alpha)} da^{(\alpha)} \stackrel{\text{def}}{=} q_k n_k da_\beta \qquad (2.72)$$

$$\int_{dv_\beta} \rho^{(\alpha)} r^{(\alpha)} dv^{(\alpha)} \stackrel{\text{def}}{=} \rho r dv_\beta \qquad (2.73)$$

Substituting these terms back into equation (2.69), we have

$$\begin{aligned}\int_{\mathcal{B}}\rho\dot{e}dv_\beta &= \int_{\partial\mathcal{B}}(v_l\sigma_{kl}n_k+\nu_{lm}m_{klm}n_k)da_\beta-\int_{\mathcal{B}}v_l\rho(a_l-f_l)dv_\beta-\int_{\mathcal{B}}\nu_{lm}\rho(\omega_{lm}-\ell_{lm})dv_\beta \\ &\quad+\int_{\partial\mathcal{B}}q_kn_kda_\beta+\int_{\mathcal{B}}\rho rdv_\beta \qquad (2.74)\\ &= \int_{\mathcal{B}}\Bigg[v_l(\underbrace{\sigma_{kl,k}+\rho(f_l-\ddot{u}_l)}_{=0})+\nu_{lm}(\underbrace{m_{klm,k}+\rho(\ell_{lm}-\omega_{lm})}_{=s_{ml}-\sigma_{ml}}) \\ &\quad+v_{l,k}\sigma_{kl}+\nu_{lm,k}m_{klm}+q_{k,k}+\rho r\Bigg]dv_\beta\end{aligned}$$

The localized balance of energy over $\mathcal{B}$ becomes,

$$\rho\dot{e}=\nu_{lm}(s_{ml}-\sigma_{ml})+v_{l,k}\sigma_{kl}+\nu_{lm,k}m_{klm}+q_{k,k}+\rho r \qquad (2.75)$$

2.3.2 Second Law of Thermodynamics and Clausius-Duhem Inequality:

It is assumed that the classical second law of thermodynamics is valid within the micro-element differential volume $dv^{(\alpha)}$. By using the integral-averaging-method, the second law of thermodynamics over dv_β can be written as,

$$\underbrace{\frac{D}{Dt}\int_{dv_\beta}\rho^{(\alpha)}\eta^{(\alpha)}dv^{(\alpha)}}_{\int_{dv_\beta}\rho^{(\alpha)}\dot{\eta}^{(\alpha)}dv^{(\alpha)}\stackrel{\text{def}}{=}\rho\dot{\eta}dv_\beta}-\underbrace{\int_{da_\beta}\frac{1}{\theta}q_k^{(\alpha)}n_k^{(\alpha)}da^{(\alpha)}}_{\int_{dv_\beta}\left(\frac{q_k^{(\alpha)}}{\theta}\right)_{,k}dv^{(\alpha)}\stackrel{\text{def}}{=}\left(\frac{q_k}{\theta}\right)_{,k}dv_\beta}-\underbrace{\int_{dv_\beta}\frac{\rho^{(\alpha)}r^{(\alpha)}}{\theta}dv^{(\alpha)}}_{\stackrel{\text{def}}{=}\frac{\rho r}{\theta}dv_\beta}\geq 0 \qquad (2.76)$$

Note that there is no micro-temperature $\theta^{(\alpha)}$ in the model [Eringen, 1999], only macro-temperature θ as a simplifying assumption in the thesis. The localized form of the second law at spatial position $\boldsymbol{x}_\beta$ can be expressed as,

$$\int_{\mathcal{B}}\rho\dot{\eta}dv_\beta-\int_{\mathcal{B}}\left(\frac{1}{\theta}q_{k,k}-\frac{q_k}{\theta^2}\theta_{,k}\right)dv_\beta-\int_{\mathcal{B}}\frac{\rho r}{\theta}dv_\beta\geq 0 \qquad (2.77)$$

$$\rho\theta\dot{\eta}-q_{k,k}+\frac{1}{\theta}q_k\theta_{,k}-\rho r\geq 0 \qquad (2.78)$$

The macroscale Helmholtz free energy per unit mass ψ, and its material time derivative can be written as,

$$\psi = e - \theta\eta \tag{2.79}$$

$$\dot{\psi} = \dot{e} - \dot{\theta}\eta - \theta\dot{\eta} \tag{2.80}$$

Inserting the above equations into (2.75), the Clausius-Duhem inequality for micromorphic continuum can be written as,

$$-\rho(\dot{\psi} + \eta\dot{\theta}) + \sigma_{kl}(v_{l,k} - \nu_{lk}) + s_{kl}\nu_{lk} + m_{klm}\nu_{lm,k} + \frac{1}{\theta}q_k\theta_{,k} \geq 0 \tag{2.81}$$

Summary of Balance Equations The equations are now summarized over the current configuration $\mathcal{B}$ at macro-element β with centroid c_β at spatial position vector $\boldsymbol{x}_\beta$ as,

$$
\begin{cases}
\text{balance of mass}: & \dfrac{D\rho}{Dt} + \rho v_{k,k} = 0 \\
& \rho dv_\beta \overset{\text{def}}{=} \int_{dv_\beta} \rho^{(\alpha)} dv^{(\alpha)} \\
\text{balance of micro}-\text{inertia}: & \dfrac{Di_{kl(\beta)}}{Dt} - \nu_{km} i_{ml(\beta)} - \nu_{lm} i_{mk(\beta)} = 0 \\
& \rho i_{kl(\beta)} dv_\beta \overset{\text{def}}{=} \int_{dv_\beta} \rho^{(\alpha)} \xi_k^{(\alpha)} \xi_l^{(\alpha)} dv^{(\alpha)} \\
\text{balance of linear momentum}: & \sigma_{lk,l} + \rho(f_k - a_k) = 0 \\
& \sigma_{lk} n_l da_\beta \overset{\text{def}}{=} \int_{da_\beta} \sigma_{lk}^{(\alpha)} n_l^{(\alpha)} da^{(\alpha)} \\
& \rho f_k dv_\beta \overset{\text{def}}{=} \int_{dv_\beta} \rho^{(\alpha)} f_k^{(\alpha)} dv^{(\alpha)} \\
& \rho \ddot{u}_k dv_\beta \overset{\text{def}}{=} \int_{dv_\beta} \rho^{(\alpha)} \ddot{u}_k^{(\alpha)} dv^{(\alpha)} \\
\text{balance of first moment of momentum}: & \sigma_{ml} - s_{ml} + m_{klm,k} + \rho(\ell_{lm} - \omega_{lm}) = 0 \\
& s_{ml} dv_\beta \overset{\text{def}}{=} \int_{dv_\beta} \sigma_{ml}^{(\alpha)} dv^{(\alpha)} \\
& m_{klm} n_k da_\beta \overset{\text{def}}{=} \int_{da_\beta} \sigma_{kl}^{(\alpha)} \xi_m^{(\alpha)} n_k^{(\alpha)} da^{(\alpha)} \\
& \rho \ell_{lm} dv_\beta \overset{\text{def}}{=} \int_{dv_\beta} \rho^{(\alpha)} f_l^{(\alpha)} \xi_m^{(\alpha)} dv^{(\alpha)} \\
& \rho \omega_{lm} dv_\beta \overset{\text{def}}{=} \int_{dv_\beta} \rho^{(\alpha)} \ddot{\xi}_l^{(\alpha)} \xi_m^{(\alpha)} dv^{(\alpha)} \\
\text{balance of energy}: & \rho \dot{e} = (s_{kl} - \sigma_{kl}) \nu_{lk} + \sigma_{kl} v_{l,k} \\
& + m_{klm} \nu_{lm,k} + q_{k,k} + \rho r \\
& \rho \dot{e} dv_\beta \overset{\text{def}}{=} \int_{dv_\beta} \rho^{(\alpha)} \dot{e}^{(\alpha)} dv^{(\alpha)} \\
& \rho r dv_\beta \overset{\text{def}}{=} \int_{dv_\beta} \rho^{(\alpha)} r^{(\alpha)} dv^{(\alpha)} \\
& q_k n_k da_\beta \overset{\text{def}}{=} \int_{da_\beta} q_k^{(\alpha)} n_k^{(\alpha)} da^{(\alpha)} \\
\text{Clausius}-\text{Duhem inequality}: & -\rho(\dot{\psi} + \eta \dot{\theta}) + \sigma_{kl}(v_{l,k} - \nu_{lk}) + s_{kl} \nu_{lk} \\
& + m_{klm} \nu_{lm,k} + \dfrac{1}{\theta} q_k \theta_{,k} \geq 0
\end{cases}
\tag{2.82}
$$

In this section, the governing equations of micromorphic continuum and the procedure of applying the integral-averaging-method have been presented in detail. Next, constitutive equations are presented to relate the various stresses to deformations in order to close the micromorphic elastic theory.

2.4 Constitutive Equations and Constraints on Elastic Parameters

The Clausius-Duhem inequality for isothermal problems in the current configuration can be written such that,

$$-\rho_0\dot{\psi} + J\sigma_{kl}(v_{l,k} - \nu_{lk}) + Js_{kl}\nu_{lk} + Jm_{klm}\nu_{lm,k} \geq 0 \tag{2.83}$$

The Helmholtz free energy function and its rate in terms of the deformation gradient $\boldsymbol{F}$, micro-deformation tensor $\boldsymbol{\chi}$ and gradient of micro-deformation tensor $\nabla_0\boldsymbol{\chi}$ can be expressed as

$$\rho_0\psi(F_{kK}, \chi_{kK}, \chi_{kK,L}) \tag{2.84}$$

$$\rho_0\dot{\psi} = \frac{\partial(\rho_0\psi)}{\partial F_{kK}}\dot{F}_{kK} + \frac{\partial(\rho_0\psi)}{\partial \chi_{kK}}\dot{\chi}_{kK} + \frac{\partial(\rho_0\psi)}{\partial \chi_{lK,L}}\dot{\chi}_{lK,L} \tag{2.85}$$

where $\dot{\rho}_0 = 0$ for conservation of mass. Substituting (2.85) into (2.83) and expanding other kinematical terms, we have

$$\begin{aligned} &-\left(\frac{\partial(\rho_0\psi)}{\partial F_{lK}}\dot{F}_{lK} + \frac{\partial(\rho_0\psi)}{\partial \chi_{lK}}\dot{\chi}_{lK} + \frac{\partial(\rho_0\psi)}{\partial \chi_{lK,L}}\dot{\chi}_{lK,L}\right) + J\sigma_{kl}\left(\dot{F}_{lK}F^{-1}_{Kk} - \dot{\chi}_{lK}\chi^{-1}_{Kk}\right) \\ &+Js_{kl}\dot{\chi_{lK}}\chi^{-1}_{Kk} + Jm_{klm}\left(\dot{\chi_{lK,L}}\chi^{-1}_{Km}F^{-1}_{Lk} + \dot{\chi}_{lK}\dot{\chi^{-1}_{lK,L}}F^{-1}_{Lk}\right) \geq 0 \end{aligned} \tag{2.86}$$

Note that the macroscopic Cauchy stress σ_{kl}, the micro stress s_{kl}, and the higher order couple stress tensors m_{klm} are in the current configuration $\mathcal{B}$. Since we want to derive the constitutive equations in the reference configuration $\mathcal{B}_0$, we need to pull back the micromorphic stress tensors to their corresponding pseudo-stresses in $\mathcal{B}_0$ via the Piola transforms as follows

$$\sigma_{kl} = \frac{1}{J} F_{kK} S_{KL} F_{lL} \tag{2.87}$$

$$s_{kl} = \frac{1}{J} F_{kK} \Sigma_{KL} F_{lL} \tag{2.88}$$

$$m_{klm} = \frac{1}{J} F_{kK} F_{lL} M_{KLM} \chi_{mM} \tag{2.89}$$

The pseudo-stress tensors in the reference configuration $\mathcal{B}_0$ with respect to the Helmholtz free energy function per unit reference volume ($\rho_0 \psi$) where ψ is the Helmholtz energy per unit mass, are derived via thermodynamics (e.g., following [Coleman and Noll, 1963]) as,

$$S_{KL} = \frac{\partial(\rho_0 \psi)}{\partial F_{kK}} F^{-1}_{Lk} \tag{2.90}$$

$$\begin{aligned} \Sigma_{KL} &= \frac{\partial(\rho_0 \psi)}{\partial F_{kK}} F^{-1}_{Lk} + F^{-1}_{Kc} \chi_{cA} \frac{\partial(\rho_0 \psi)}{\partial \chi_{aA}} F^{-1}_{La} \\ &+ F^{-1}_{Kd} \chi_{dM,E} \frac{\partial(\rho_0 \psi)}{\partial \chi_{fM,E}} F^{-1}_{Lf} \end{aligned} \tag{2.91}$$

$$M_{KLM} = \frac{\partial(\rho_0 \psi)}{\partial \chi_{fM,E}} F^{-1}_{Lf} \tag{2.92}$$

where S_{KL} is the second Piola Kirchhoff stress tensor, Σ_{KL} is the pseudo-micro-stress in $\mathcal{B}_0$, and M_{KLM} is the pseudo-couple-stress in $\mathcal{B}_0$. Assuming a quadratic form of the Helmholtz free energy function in the reference configuration $\mathcal{B}_0$ in terms of the Lagrangian strain E_{KL}, micro-strain $\mathcal{E}_{KL}$, and gradient deformation Γ_{KLM} we have,

$$\begin{aligned} \rho_0 \psi &= \frac{1}{2} E_{KL} A_{KLMN} E_{MN} + \frac{1}{2} \mathcal{E}_{KL} B_{KLMN} \mathcal{E}_{MN} \\ &+ \frac{1}{2} \Gamma_{KLM} C_{LMKNPQ} \Gamma_{NPQ} + E_{KL} D_{KLMN} \mathcal{E}_{MN} \end{aligned} \tag{2.93}$$

where the elastic material moduli tensors A_{KLMN}, B_{KLMN}, D_{KLMN} and C_{LMKNPQ} may be written [Suhubi and Eringen, 1964],

$$
\begin{aligned}
A_{KLMN} &= \lambda\delta_{KL}\delta_{MN} + \mu\left(\delta_{KM}\delta_{LN} + \delta_{KN}\delta_{LM}\right) && (2.94)\\
B_{KLMN} &= \left(\eta - \tau\right)\delta_{KL}\delta_{MN} + \left(\kappa - \sigma\right)\left(\delta_{KM}\delta_{LN}\right) + \left(\nu - \sigma\right)\left(\delta_{KN}\delta_{LM}\right) && (2.95)\\
C_{LMKNPQ} &= \tau_1\left(\delta_{LM}\delta_{KN}\delta_{PQ} + \delta_{LQ}\delta_{MK}\delta_{NP}\right) + \tau_2\left(\delta_{LM}\delta_{KP}\delta_{NQ} + \delta_{LK}\delta_{MQ}\delta_{NP}\right)\\
&+ \tau_3\delta_{LM}\delta_{KQ}\delta_{NP} + \tau_4\delta_{LN}\delta_{MK}\delta_{PQ} + \tau_5\left(\delta_{LK}\delta_{MN}\delta_{PQ} + \delta_{LP}\delta_{MK}\delta_{NQ}\right)\\
&+ \tau_6\delta_{LK}\delta_{MP}\delta_{NQ} + \tau_7\delta_{LN}\delta_{MP}\delta_{KQ} + \tau_8\left(\delta_{LP}\delta_{MQ}\delta_{KN} + \delta_{LQ}\delta_{MN}\delta_{KP}\right)\\
&+ \tau_9\delta_{LN}\delta_{MQ}\delta_{KP} + \tau_{10}\delta_{LP}\delta_{MN}\delta_{KQ} + \tau_{11}\delta_{LQ}\delta_{MP}\delta_{KN} && (2.96)\\
D_{KLMN} &= \tau\delta_{KL}\delta_{MN} + \sigma\left(\delta_{KN}\delta_{LM} + \delta_{LN}\delta_{KM}\right) && (2.97)
\end{aligned}
$$

where δ_{KL} is the Kronecker-delta operator; λ, μ, ν, τ, κ, σ, and ν are elastic moduli (units Pa) for the Second Piola-Kirchhoff stress $\boldsymbol{S}$ and micro-stress $\boldsymbol{\Sigma}$, and $\tau_1, \ldots, \tau_{11}$ are elastic moduli (units Pa.m^2) for the higher order couple stress $\boldsymbol{M}$. By using the Helmholtz free energy function per unit reference volume in (2.93), from (2.92) the micromorphic stress tensors in $\mathcal{B}_0$ can be written as follows,

$$
\begin{aligned}
S_{KL} &= A_{KLMN}E_{MN} + D_{KBMN}\mathcal{E}_{MN}\\
&+ \left(D_{KBMN}E_{MN} + B_{KBMN}\mathcal{E}_{MN}\right)\left[C^{-1}_{LA}\left(\mathcal{E}_{AB} + \delta_{AB}\right)\right]\\
&+ C_{KBCNPQ}\Gamma_{NPQ}C^{-1}_{LQ}\Gamma_{QBC} && (2.98)\\
\Sigma_{KL} &= A_{KLMN}E_{MN} + D_{KBMN}\mathcal{E}_{MN}\\
&+ 2sym\left(D_{KLMN}E_{MN} + B_{KBMN}\mathcal{E}_{MN}\right)\left[C^{-1}_{LA}\left(\mathcal{E}_{AB} + \delta_{AB}\right)\right]\\
&+ C_{KBCNPQ}\Gamma_{NPQ}C^{-1}_{LQ}\Gamma_{QBC} && (2.99)\\
M_{KLM} &= C_{LMKNPQ}\Gamma_{NPQ} && (2.100)
\end{aligned}
$$

Assuming small elastic strains (but potentially large rotations, which will be valid when we extend the FE implementation to micromorphic elastoplasticity at finite strain [Regueiro, 2009, 2010]), the micromorphic stress tensors can be simplified to,

$$
\begin{aligned}
S_{KL} &= (\lambda+\tau)\,E_{MM}\delta_{KL} + 2\,(\mu+\sigma)\,E_{KL} + \eta\mathcal{E}_{MM}\delta_{KL} + \kappa\mathcal{E}_{KL} + \nu\mathcal{E}_{LK} && (2.101)\\
\Sigma_{KL} &= (\lambda+2\tau)\,E_{MM}\delta_{KL} + 2\,(\mu+2\sigma)\,E_{KL} + (2\eta-\tau)\,\mathcal{E}_{MM}\delta_{KL}\\
&+ (\nu+\kappa-\sigma)\,(\mathcal{E}_{KL}+\mathcal{E}_{LK}) && (2.102)\\
M_{KLM} &= \tau_1\,(\delta_{LM}\Gamma_{KPP} + \delta_{MK}\Gamma_{PPL}) + \tau_2\,(\delta_{LM}\Gamma_{NKN} + \delta_{LK}\Gamma_{PPM}) + \tau_3\delta_{LM}\Gamma_{NNK}\\
&+ \tau_4\delta_{MK}\Gamma_{LPP} + \tau_5\,(\delta_{LK}\Gamma_{MPP} + \delta_{MK}\Gamma_{NLN}) + \tau_6\delta_{LK}\Gamma_{NMN} + \tau_7\Gamma_{LMK}\\
&+ \tau_8\,(\Gamma_{KLM} + \Gamma_{MKL}) + \tau_9\Gamma_{LKM} + \tau_{10}\Gamma_{MLK} + \tau_{11}\Gamma_{KML} && (2.103)
\end{aligned}
$$

The next section is devoted to the positiveness of micromorphic strain energy (Helmholtz free energy without temperature terms) function and defining constraints on elastic parameters of the constitutive equations.

2.4.1 Constraints on Elastic Parameters of the Micromorphic Constitutive Equations

In this section, constraints on elastic parameters of the micromorphic constitutive equations are presented. Note that the study on positiveness of micromorphic strain energy in the sense of Suhubi and Eringen [1964] was presented first by Smith [1968] for micromorphic linear isotropic elasticity at small strain. Details on the derivations of the proposed restrictions on elastic material moduli can be found in Smith [1968] and Isbuga and Regueiro [2011]. These constraints are defined in such a way that guarantees the positiveness of the strain energy function, or Helmholtz free energy function in our case. The constraints on the elastic parameters of the macroscopic Cauchy stress σ_{kl} and micro-stress tensor s_{kl} are as follows,

$$
\begin{aligned}
\lambda &> 0 \\
\kappa + \nu &> 2\sigma \\
(\kappa + \nu - 2\sigma)\,\mu &> 2\sigma^2 \\
3\lambda + 2\mu &> 0 \\
\kappa + \nu + 3\eta &> 3\tau + 2\sigma \\
(\kappa + \nu + 2\eta - 3\tau - 2\sigma)\,(3\lambda + 2\mu) &> (3\tau + 2\sigma)^2 \\
\kappa - \nu &> 0 \\
4\mu\,(\kappa + \nu - 2\sigma) &> 2\sigma
\end{aligned}
\tag{2.104}
$$

In order to determine the restrictions on τ_i of the couple stress, Smith [1968] proposed a matrix $\boldsymbol{T}$ as follows

$$
\boldsymbol{T} = \begin{bmatrix}
\tau_1 + \tau_2 + 3\tau_3 + \tau_7 + \tau_{10} & 3\tau_1 + \tau_4 + 3\tau_5 + \tau_8 + \tau_{11} & 3\tau_2 + \tau_5 + \tau_6 + \tau_8 + \tau_9 \\
3\tau_1 + \tau_2 + \tau_3 + \tau_8 + \tau_{11} & \tau_1 + 3\tau_4 + \tau_5 + \tau_7 + \tau_9 & \tau_2 + 3\tau_5 + \tau_6 + \tau_8 + \tau_{10} \\
\tau_1 + 3\tau_2 + \tau_3 + \tau_8 + \tau_9 & \tau_1 + \tau_4 + 3\tau_5 + \tau_8 + \tau_{10} & \tau_2 + \tau_5 + 3\tau_6 + \tau_7 + \tau_{11}
\end{bmatrix}
\tag{2.105}
$$

The constraints on τ_i are such that,

$$
\begin{aligned}
\tau_7 + 2\tau_8 &> |\tau_9 + \tau_{10} + \tau_{11}| \\
\tau_7 - \tau_8 &> \frac{1}{\sqrt{2}} \left| (\tau_9 - \tau_{10})^2 + (\tau_{10} - \tau_{11})^2 + (\tau_{11} - \tau_9)^2 \right|^{1/2} \\
tr\,(\mathbf{T}) &> 0 \\
tr\,(\mathbf{coT}) &> 0 \\
det\,(\mathbf{T}) &> 0
\end{aligned}
\tag{2.106}
$$

Note that $tr(\mathbf{T})$ denotes the trace of $\boldsymbol{T}$, and $\mathbf{coT}$ represents for the cofactor of $\boldsymbol{T}$. It can be seen that there is no constraint on any of the material parameters individually, except that $\lambda > 0$. Therefore, some of the parameters can be either positive or negative, but they must satisfy Smith's conditions

(2.104) and (2.106) to be able to be selected as valid micromorphic elastic material parameters. So far, in this chapter, the kinematics, balance equations, thermodynamics, and constitutive equations for the micromorphic continuum have been presented. Following the approach of Eringen, the mathematical derivations of each new variable (higher order stress, microstress, micro-inertia, and so forth) have been shown to provide insight into the micromorphic continuum.

2.5 Comparison of Micromorphic and Micropolar Elasticity

In this section, a simplification from micromorphic continuum theory to micropolar theory is presented. This is done for the purpose of comparing micromorphic theory with micropolar theory for quasi-static linear elastic isotropic materials. In the results section, several examples are presented to compare micromorphic and micropolar elasticity theories. This is done to illustrate the effect of micromorphic additional dofs which makes this theory able to consider micro-shear and micro-stretch deformations of the micro-elements, in addition to micro-rotation which is the only micro-element deformation captured by micropolar continuum theory. One of the challenges of comparing micromorphic and micropolar elasticity theories is that the material parameters for each theory are different. The finite element code that is written in Tahoe (`tahoe.sourceforge.net`) is specifically developed for micromorphic continuum equations, and cannot be simplified to simulate a micropolar continuum (this requires a separate FE implementation). This means that constraint $\phi_k = -\frac{1}{2} e_{klm}\phi_{lm}$ (for small strains) cannot be applied directly onto micromorphic dofs within the finite element model in Tahoe. Eringen [1999] proposed a procedure for simplifying the micromorphic kinematics, balance equations and constitutive equations to microstretch and micropolar theories for small strain problems. But the proposed approach cannot be applied to simulations in this thesis, since it requires that we apply the constraint of skew-symmetry on the micro-displacement tensor, $\boldsymbol{\Phi} = -\boldsymbol{\Phi}^T$. In the following the micropolar balance equations and constitutive equations will be presented.

2.5.1 Micropolar Balance and Constitutive Equations

The differences in the kinematics of micromorphic and micropolar continuum theories is mainly related to their interpretation of the deformation of the micro-elements. In micromorphic continuum, the micro-displacement tensor $\boldsymbol{\Phi}(\boldsymbol{X}, t)$ has 9 components to capture micro-shear, micro-stretch, and micro-rotation. The micro-displacement tensor $\boldsymbol{\Phi}(\boldsymbol{X}, t)$ for micropolar theory [Eringen, 1968a], is written such that,

$$\Phi_{kK} = -e_{kKM}\Phi_M^{\text{rot}}, \qquad \Phi_M^{\text{rot}} = -\frac{1}{2}e_{MkK}\Phi_{kK} \tag{2.107}$$

where $\boldsymbol{\Phi}^{\text{rot}}$ is the independent micro-rotation vector of the micro-elements. The balance of mass and linear momentum for a micropolar continuum theory are similar to those of a micromorphic continuum. To derive the balance of angular momentum for micropolar continuum, we start with the balance of angular momentum for micromorphic continuum such that,

$$e_{nmk}\left[\sigma_{mk} - s_{mk} + m_{lkm,l} + \rho(\ell_{km} - \omega_{km})\right] = 0 \tag{2.108}$$

$$e_n\left[\sigma_{[mk]} - \underbrace{s_{[mk]}}_{=0} + m_{l[km],l} + \rho(\ell_{[km]} - \omega_{[km]})\right] = 0 \tag{2.109}$$

where e_n is a coefficient such that $e_n = 1$ for $n = 1, 2, 3$ $(n \neq m \neq k)$, and we have,

$$e_n\left[\sigma_{[mk]} + m_{l[km],l} + \rho(\ell_{[km]} - \omega_{[km]})\right] = 0 \tag{2.110}$$

where the antisymmetric definition is $\sigma_{[mk]} = (\sigma_{mk} - \sigma_{km})/2$. It is to be noted that (2.110) provides 3 equations to solve for the micro-rotation vector φ_k. Thus, the micro-rotation vector of a micropolar continuum can be solved from the balance of angular momentum (2.110) such that,

$$t_k + m_{lk,l} + \rho(\ell_k - \omega_k) = 0 \tag{2.111}$$

where,

$$t_k \overset{\text{def}}{=} e_k \sigma_{[mn]} \tag{2.112}$$

$$m_{lk,l} \overset{\text{def}}{=} e_{kmn} m_{lnm,l} = e_k m_{l[nm],l} \tag{2.113}$$

$$\ell_k \overset{\text{def}}{=} e_k \ell_{[nm]} \tag{2.114}$$

$$\omega_k \overset{\text{def}}{=} e_k \omega_{[nm]} \tag{2.115}$$

$$\tag{2.116}$$

where t_k is the antisymmetric part of the micropolar Cauchy stress, m_{lk} is the couple stress, ℓ_k is the body force couple, and ω_k is micro-spin inertia. The micro-rotation vector $\boldsymbol{\varphi}$ of micropolar theory can be solved through the balance of angular momentum. Therefore, micropolar theory does not involve the balance of first moment of momentum. Recalling from the previous section, the integral form of the balance of energy for micromorphic theory can be written as,

$$\begin{aligned}
\int_{\mathcal{B}} \rho \dot{e} dv_\beta &= \int_{\partial\mathcal{B}} (v_l \sigma_{kl} n_k + \nu_{lm} m_{klm} n_k) da_\beta - \int_{\mathcal{B}} v_l \rho(\ddot{u}_l - f_l) dv_\beta - \int_{\mathcal{B}} \nu_{lm} \rho(\omega_{lm} - \ell_{lm}) dv_\beta \\
&\quad + \int_{\partial\mathcal{B}} q_k n_k da_\beta + \int_{\mathcal{B}} \rho r dv_\beta \\
&= \int_{\mathcal{B}} \Bigg[v_l \underbrace{(\sigma_{kl,k} + \rho(f_l - \ddot{u}_l))}_{=0} + \nu_{lm} \underbrace{(m_{klm,k} + \rho(\ell_{lm} - \omega_{lm}))}_{=s_{ml} - \sigma_{ml}} \\
&\quad + v_{l,k} \sigma_{kl} + \nu_{lm,k} m_{klm} + q_{k,k} + \rho r \Bigg] dv_\beta
\end{aligned} \tag{2.117}$$

The balance of energy for micropolar continuum is then derived as follows, where we substitute for micro-gyration tensor ν_{lm} the micropolar gyration vector ν_n, such that $\nu_{lm} = -e_{lmn}\nu_n$, and

$$\begin{aligned}
\int_{\mathcal{B}} \rho \dot{e} dv_\beta &= \int_{\partial\mathcal{B}} (v_l \sigma_{kl} n_k - e_{lmn} \nu_n m_{klm} n_k) da_\beta - \int_{\mathcal{B}} v_l \rho(\ddot{u}_l - f_l) dv + \int_{\mathcal{B}} e_{lmn} \nu_n \rho(\omega_{lm} - \ell_{lm}) dv_\beta \\
&\quad + \int_{\partial\mathcal{B}} q_k n_k da + \int_{\mathcal{B}} \rho r dv_\beta \\
&= \int_{\mathcal{B}} \Bigg[v_l \underbrace{(\sigma_{kl,k} + \rho(f_l - \ddot{u}_l))}_{=0} + \nu_l \underbrace{(m_{kl,k} + \rho(\ell_l - \omega_l))}_{=-e_{lmn}\sigma_{mn}} \\
&\quad + v_{l,k} \sigma_{kl} + \nu_{l,k} m_{kl} + q_{k,k} + \rho r \Bigg] dv_\beta
\end{aligned} \tag{2.118}$$

Thus, the localized balance of energy at spatial position $\boldsymbol{x}_\beta$ for a micropolar continuum is as follows,

$$\rho\dot{e} = \sigma_{ml}(v_{l,m} + \nu_{lm}) + \nu_{l,k}m_{kl} + q_{k,k} + \rho r \tag{2.119}$$

where $\sigma_{ml}\nu_{lm}$ for a micropolar continuum can be written such that,

$$\sigma_{ml}\nu_{lm} = -\sigma_{ml}e_{lmn}\nu_n = -\sigma_{[ml]}e_n\nu_n \tag{2.120}$$

The Clausius-Duhem inequality for a micropolar continuum can be derived by substituting the micropolar balance of energy (2.119) into the micromorphic Clausius-Duhem inequality (2.81) such that,

$$-\rho(\dot{\psi} + \eta\dot{\theta}) - \sigma_{[kl]}e_n\nu_n + \sigma_{kl}v_{l,k} + m_{kl}\nu_{l,k} + \frac{1}{\theta}q_k\theta_{,k} \geq 0 \tag{2.121}$$

As mentioned earlier in this section, Eringen [1999] proposed a procedure to simplify micromorphic continuum to micropolar continuum. This procedure has been explained for the micropolar balance equations. The key part of this simplification is to apply the constraint $\boldsymbol{\Phi} = -\boldsymbol{\Phi}^T$ on the micro-displacement tensor $\boldsymbol{\Phi}$. Note that we are not able to apply such a constraint on the micro-displacement tensor $\boldsymbol{\Phi}$ of our FE micromorphic model in Tahoe. Therefore, in this thesis the material parameters of micromorphic continuum are selected in such a way to make the micromorphic constitutive equations to be similar to the micropolar ones. The constitutive equations of micropolar continuum given by Eringen [1999] (for small elastic strains, but potentially large rotations) are as follows,

$$S_{KL} = (\lambda)\,\bar{\bar{E}}_{MM}\delta_{KL} + (\bar{\mu} + \bar{\eta})\,\bar{\bar{E}}_{KL} + (\bar{\mu})\,\bar{\bar{E}}_{LK} \tag{2.122}$$

$$M_{KL} = \alpha\bar{\bar{\Gamma}}_{MM}\,(\delta_{KL}) + \beta\bar{\bar{\Gamma}}_{KL} + \gamma\bar{\bar{\Gamma}}_{LK} \tag{2.123}$$

where M_{KL} is the second order pseudo couple stress tensor in $\mathcal{B}_0$, $\bar{\bar{E}}_{KL} = F^T_{kK}\chi^{-1}_{Lk} - \delta_{KL}$, and $\bar{\bar{\Gamma}}_{KL} = \frac{1}{2}e_{KMN}\chi_{KN}\chi_{kM,L}$. Where $\bar{\lambda}$, $\bar{\mu}$, $\bar{\eta}$, $\bar{\alpha}$, $\bar{\beta}$, and $\bar{\gamma}$ are micropolar material parameters. The

constitutive equations of micromorphic and micropolar theories at small strain are written as,

$$\begin{aligned} \sigma_{kl} &= (\lambda+\tau)\, e_{mm}\delta_{kl} + 2\,(\mu+\sigma)\, e_{kl} \\ &+ \eta\varepsilon_{mm}\delta_{kl} + \kappa\varepsilon_{kl} + \nu\varepsilon_{lk} \quad \text{(micromorphic)} \end{aligned} \tag{2.124}$$

$$\sigma_{kl} = \bar{\lambda}\varepsilon_{mm}\delta_{kl} + (\bar{\mu}+\bar{\eta})\,\varepsilon_{kl} + \bar{\mu}\varepsilon_{lk} \quad \text{(micropolar)} \tag{2.125}$$

where the linearized strain measures for micromorphic continuum are given such that,

$$e_{kl} = \frac{1}{2}\left(u_{k,l} + u_{l,k}\right), \quad \varepsilon_{kl} = \phi_{kl} + u_{l,k} \tag{2.126}$$

Inserting (2.126) into the micromorphic constitutive equations (2.124) we have,

$$\begin{aligned} \sigma_{kl} &= \underbrace{(\lambda+\tau+\eta)\, u_{m,m}\delta_{kl} + (\mu+\sigma+\kappa)\, u_{k,l} + (\mu+\sigma+\nu)\, u_{l,k}}_{\text{macroscopic part}} \\ &+ \underbrace{\eta\phi_{mm}\delta_{kl} + \kappa\phi_{kl} + \nu\phi_{lk}}_{\text{microscopic part}} \end{aligned} \tag{2.127}$$

The linear strain measure for micropolar theory and the constitutive equation for Cauchy stress are given as,

$$\varepsilon_{kl} = e_{lkj}\phi_j + u_{l,k} \tag{2.128}$$

$$\sigma_{kl} = \underbrace{\bar{\lambda}u_{m,m}\delta_{kl} + (\bar{\mu}+\bar{\eta})\, u_{l,k} + \bar{\mu}u_{k,l}}_{\text{macroscopic part}} + \underbrace{\bar{\eta}e_{lkj}\phi_j}_{\text{microscopic part}} \tag{2.129}$$

An interesting feature of the micromorphic and micropolar constitutive equations at small strain is that they can be separated into a macroscopic part (terms related to the macroscopic displacement u_i) and microscopic part (terms related to the micro-displacement tensor ϕ_{ij}, for small strain). It is evident that the constitutive equations of a micromorphic continuum have more terms involving micro-scale deformation than does the micropolar theory. In the examples, the micromorphic material parameters are selected such that the macroscopic part of (2.127) is equivalent to that of (2.129). In the micropolar theory, the symmetric micro-stress still exists, but it will not contribute to the balance of angular momentum (2.109), since it is written in terms of the anti-symmetric part of the stresses. Therefore, in micropolar theory there is no constitutive equation required for

the symmetric micro-stress. Eringen [1999] proposed a relation between the micromorphic couple stress and that of the micropolar theory such that,

$$m_{kl} = e_{lmp}m_{kpm} = \bar{\alpha}\phi_{r,r}\delta_{kl} + \bar{\beta}\phi_{k,l} + \bar{\gamma}\phi_{l,k} + \bar{\alpha_0}e_{klp}\phi^{\text{str}}_{,p} \tag{2.130}$$

$$\phi_{kl} = \phi^{\text{str}}\delta_{kl} \tag{2.131}$$

where ϕ^{str} is the micro-stretch term coefficient. Note that in microstretch theory it is assumed that micro-stretch components are equal in all directions. The relations of $\bar{\alpha}$, $\bar{\beta}$, $\bar{\gamma}$, and $\bar{\alpha}_0$ with $\tau_1, \tau_2, ..., \tau_{11}$ are as follows,

$$\begin{aligned} \bar{\alpha} &= 2\tau_8 - \tau_9 - \tau_{11}, \quad \bar{\beta} = -\tau_4 + 2\tau_5 - \tau_6 \\ \bar{\gamma} &= \tau_4 - 2\tau_5 + \tau_6 + 2\tau_7 - 2\tau_8 + \tau_9 - 2\tau_{10} + \tau_{11} \\ \bar{\alpha}_0 &= 3\tau_1 - 3\tau_2 + \tau_4 + \tau_6 - \tau_9 + \tau_{11} \end{aligned} \tag{2.132}$$

To compare the micromorphic and micropolar theories, τ_i are selected such that $\bar{\alpha}$,$\bar{\beta}$, and $\bar{\gamma}$ given through (2.132) are equal to the micropolar material parameters. Note that $\bar{\alpha}_0 e_{klp}\phi^{\text{str}}_{,p}$ is not part of the micropolar couple stress constitutive equation, but it appears in (2.130) as a result of simplifying micromorphic to micropolar theory. Eringen [1968a] defined a micro-rotation vector $\mathbf{\Phi}^{\text{rot}}$ in terms of the micro-displacement tensor $\mathbf{\Phi}$ such that,

$$skw\left(\mathbf{\Phi}\right)_{kK} = \left[\frac{1}{2}\left(\mathbf{\Phi} - \mathbf{\Phi}^T\right)_{kK}\right] = \left[-e_{kKM}\Phi^{\text{rot}}_M\right] \tag{2.133}$$

$$= \frac{1}{2}\begin{bmatrix} 0 & \Phi_{12} - \Phi_{21} & \Phi_{13} - \Phi_{31} \\ \Phi_{21} - \Phi_{12} & 0 & \Phi_{23} - \Phi_{32} \\ \Phi_{31} - \Phi_{13} & \Phi_{32} - \Phi_{23} & 0 \end{bmatrix} \tag{2.134}$$

$$= -\begin{bmatrix} 0 & e_{123}\Phi^{\text{rot}}_3 & e_{132}\Phi^{\text{rot}}_2 \\ e_{213}\Phi^{\text{rot}}_3 & 0 & e_{231}\Phi^{\text{rot}}_1 \\ e_{312}\Phi^{\text{rot}}_2 & e_{321}\Phi^{\text{rot}}_1 & 0 \end{bmatrix} \tag{2.135}$$

where we can write the rotation vector $\boldsymbol{\Phi}^{\text{rot}}$ for micropolar theory such that,

$$\boldsymbol{\Phi}^{\text{rot}} = \begin{bmatrix} \Phi_1^{\text{rot}} \\ \Phi_2^{\text{rot}} \\ \Phi_3^{\text{rot}} \end{bmatrix} = \begin{bmatrix} \frac{1}{2}\left(\Phi_{32} - \Phi_{23}\right) \\ \frac{1}{2}\left(\Phi_{13} - \Phi_{31}\right) \\ \frac{1}{2}\left(\Phi_{21} - \Phi_{12}\right) \end{bmatrix} \tag{2.136}$$

We use (2.136) to calculate the rotation vector from the micromorphic dofs in order to compare with that of the micropolar theory in the numerical examples. We can also apply BCs on the shear terms of $\boldsymbol{\Phi}$ to apply associated rotations $\boldsymbol{\Phi}^{\text{rot}}$.

2.6 Total Lagrangian Finite Element Formulation for Micromorphic Continuum and Time Integration for Implicit Dynamics

For the finite element formulation, the coupled strong form (S) of the micromorphic balance of momenta in the current configuration are presented such that,

$$(S)\begin{cases} \text{Find } u_k(\boldsymbol{x},t) : \hat{\mathcal{B}} \times [0,t_{\text{final}}] \mapsto \mathbb{R}^3, \quad \text{and} \quad \phi_{kK}(\boldsymbol{x},t) : \hat{\mathcal{B}} \times [0,t_{\text{final}}] \mapsto \mathbb{R}^9, \text{such that} \\ \sigma_{lk,l} + \rho(f_k - \ddot{u}_k) = 0 \in \mathcal{B} \\ u_k(t) = g_k^u(t) \text{ on } \Gamma_g^u \\ \sigma_{lk} n_l(t) = t_k^\sigma(t) \text{ on } \Gamma_t \\ u_k(\boldsymbol{x},0) = u_{k0}(\boldsymbol{x}) \in \mathcal{B} \\ \sigma_{mk} - s_{mk} + m_{lkm,l} + \rho(\ell_{km} - \omega_{km}) = 0 \in \mathcal{B} \\ \phi_{kl}(t) = g_{kl}^\phi(t) \text{ on } \Gamma_g^\phi \\ m_{klm} n_k(t) = \mathcal{M}_{lm}(t) \text{ on } \Gamma_{\mathcal{M}} \\ \phi_{kl}(\boldsymbol{x},0) = \phi_{kl0}(\boldsymbol{x}) \in \mathcal{B} \end{cases} \tag{2.137}$$

where $\hat{\mathcal{B}} = \mathcal{B} \cup \Gamma$, and $\Gamma = \Gamma_g^u \cup \Gamma_t = \Gamma_g^\phi \cup \Gamma_{\mathcal{M}}$. The finite element formulation will be presented in the reference configuration $\mathcal{B}_0$ for a total Lagrangian implementation. Through the weighted residual method and integration by parts, the balance of linear momentum in the current configuration can

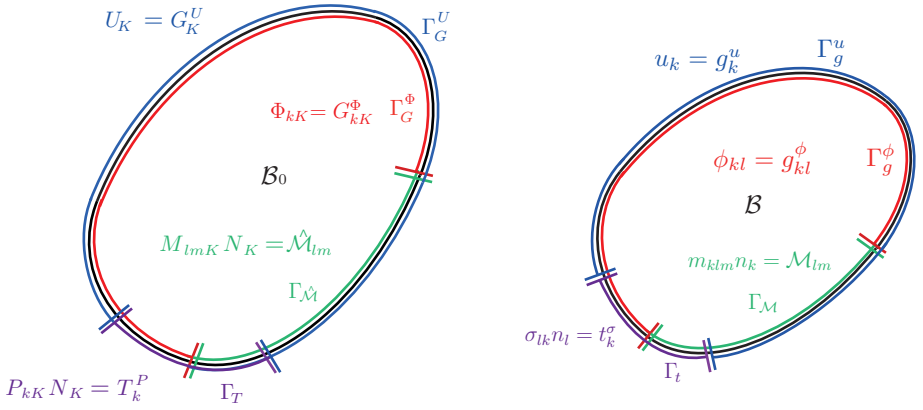

Figure 2.2. Schematic of Neumann and Dirichlet boundary conditions for the micromorphic continuum in the reference (left) and current (right) configurations.

be expressed as

$$\int_{\mathcal{B}} w_k \left[\sigma_{lk,l} + \rho \left(f_k - \ddot{u}_k\right)\right] dv_\beta = \int_{\partial\mathcal{B}} w_k \sigma_{lk} n_l da_\beta - \int_{\mathcal{B}} \left[w_{k,l}\sigma_{lk} + w_k \rho \left(f_k - \ddot{u}_k\right)\right] dv_\beta = 0 \tag{2.138}$$

where w_k is the weighting function for macro-scale displacement vector u_k. Applying the Piola transforms and mapping $P_{lL} = J\sigma_{lk}F_{Lk}^{-1}$ and $\sigma_{lk} = \dfrac{1}{J}F_{lL}S_{LK}F_{kK}$, and Nanson's formula to relate the area change $n_l da = JF_{Kl}^{-1}N_K dA$, the variational form of the balance of linear momentum can be written as,

$$\int_{\partial\mathcal{B}_0} w_k (P_{kK}N_K) dA_\beta - \int_{\mathcal{B}_0} \left[w_{k,l}(F_{lL}S_{LK}F_{kK}) + w_k \rho_0 \left(f_k - \ddot{u}_k\right)\right] dV_\beta = 0 \tag{2.139}$$

Similarly, the variational form of the balance of first moment of momentum in the current configuration $\mathcal{B}$ is such that,

$$\int_{\mathcal{B}} \eta_{ml} \left[\sigma_{ml} - s_{ml} + m_{lkm,l} + \rho \left(\lambda_{lm} - \omega_{lm}\right)\right] dV_\beta = 0 \tag{2.140}$$

where η_{ml} is the weighting function of the micro-displacement tensor ϕ_{ml} in the current configuration. Using (2.87)-(2.89), the variational form of the balance of first moment of momentum in the reference configuration $\mathcal{B}_0$ can be expressed such that,

$$\int_{\mathcal{B}_0} \eta_{ml} \left[F_{mM} S_{ML} F_{lL} - F_{mM} \Sigma_{ML} F_{lL} + \rho_0 \left(\lambda_{lm} - \omega_{lm} \right) \right] dV_\beta$$
$$- \int_{\mathcal{B}_0} \eta_{ml,k} F_{kK} F_{lL} M_{KLM} \chi_{mM} dV_\beta + \int_{\Gamma_{\hat{\mathcal{M}}}} \eta_{ml} \hat{\mathcal{M}}_{lm} dA_\beta = 0 \tag{2.141}$$

where λ_{lm} can be derived such that,

$$\rho_0 \lambda_{lm} dV_\beta = \chi_{mK} \int_{dV_\beta} \rho_0^{(\alpha)} f_l^{(\alpha)} \Xi_K^{(\alpha)} dV^{(\alpha)} \tag{2.142}$$

where the boundary couple-traction $\hat{\mathcal{M}}_{lm} = m_{klm} J F^{-1}_{Kk} N_K = \hat{M}_{lmK} N_K$. Thus, the coupled weak form for micromorphic elastodynamics in $\mathcal{B}_0$ may be stated as,

$$(W) \begin{cases} \text{Find } u_k(\boldsymbol{X}, t) \in \mathscr{S}^u \text{ and } \Phi_{kK}(\boldsymbol{X}, t) \in \mathscr{S}^\Phi \text{ such that} \\ \quad \int_{\mathcal{B}_0} \left[w_{k,l} (F_{lL} S_{LK} F_{kK}) + w_k \rho_0 f_k \right] dV_\beta - \int_{\Gamma_T} w_k (T_K^P) dA_\beta - \int_{\mathcal{B}_0} w_k \rho_0 \ddot{u}_k dV_\beta = 0 \\ \quad \int_{\mathcal{B}_0} \eta_{ml} \left[F_{mM} (S_{ML} - \Sigma_{ML}) F_{lL} + \rho_0 \lambda_{lm} \right] dV_\beta \\ \quad - \int_{\mathcal{B}_0} (\eta_{ml,k}) \left[F_{kK} F_{lL} M_{KLM} \chi_{mM} \right] dV_\beta + \int_{\Gamma_{\hat{\mathcal{M}}}} \eta_{ml} \hat{\mathcal{M}}_{lm} dA_\beta - \int_{\mathcal{B}_0} (\eta_{ml,k}) \rho_0 \omega_{lm} dV_\beta = 0 \\ \text{holds } \forall w_k(\boldsymbol{X}) \in \mathscr{V}^u \text{ and } \eta_{ml}(\boldsymbol{X}) \in \mathscr{V}^\Phi \\ \mathscr{S}^u = \{ u_k : \mathcal{B}_0 \times [0, t_{\text{final}}] \mapsto \mathbb{R}^3, u_k \in H^1, u_k(\boldsymbol{X}, t) = g_k^u(t) \text{ on } \Gamma_g^u, u_k(\boldsymbol{X}, 0) = u_{k0}(\boldsymbol{X}) \} \\ \mathscr{S}^\Phi = \{ \Phi_{kK} : \mathcal{B}_0 \times [0, t_{\text{final}}] \mapsto \mathbb{R}^9, \Phi_{kK} \in H^1, \Phi_{kK}(\boldsymbol{X}, t) = G_{kK}^\Phi(t) \text{ on } \Gamma_G^\Phi, \Phi_{kK}(\boldsymbol{X}, 0) = \Phi_{k0}(\boldsymbol{X}) \} \\ \mathscr{V}^u = \{ w_k : \mathcal{B}_0 \mapsto \mathbb{R}^3, w_k \in H^1, w_k = 0 \text{ on } \Gamma_g^u \} \\ \mathscr{V}^\Phi = \{ \eta_{ml} : \mathcal{B}_0 \mapsto \mathbb{R}^9, \eta_{ml} \in H^1, \eta_{ml} = 0 \text{ on } \Gamma_G^\Phi \} \end{cases} \tag{2.143}$$

where H^1 denotes the first Sobolev space [Hughes, 1987], and $\mathscr{S}^u$ and $\mathscr{S}^\Phi$ are the trial solution spaces, and $\mathscr{V}^u$ and $\mathscr{V}^\Phi$ the variation spaces.

Ignoring the boundary traction (T_K^P), body force ($\rho_0 f_k$), body couple ($\rho_0 \lambda_{lm}$), and boundary traction-couple terms ($\hat{\mathcal{M}}_{lm}$), we arrive at the following simplified coupled variational equations of the balance of linear momentum and first moment of momentum for micromorphic elastodynamics

as,

$$\mathcal{G} = \int_{\mathcal{B}_0} w_{k,l}(F_{lL}S_{LK}F_{kK})dV_\beta + \int_{\mathcal{B}_0} w_k\rho_0\ddot{u}_k dV_\beta = 0 \tag{2.144}$$

$$\begin{aligned}\mathcal{H} &= \int_{\mathcal{B}_0} \eta_{ml}F_{mM}\left(\Sigma_{ML} - S_{ML}\right)F_{lL}dV_\beta + \int_{\mathcal{B}_0} \eta_{ml,k}F_{kK}F_{lL}M_{KLM}\chi_{mM}dV_\beta \\ &+ \int_{\mathcal{B}_0} \eta_{ml}\rho_0\omega_{lm}dV_\beta = 0\end{aligned} \tag{2.145}$$

The linearization of $\mathcal{G}$ and $\mathcal{H}$ may be stated as,

$$\mathcal{L}\mathcal{G} = \mathcal{G} + \delta\mathcal{G} = 0\ ,\ \mathcal{L}\mathcal{H} = \mathcal{H} + \delta\mathcal{H} = 0 \tag{2.146}$$

where $\delta(\bullet)$ is the incremental operator with respect to a linearization procedure. We write,

$$\begin{aligned}\delta\mathcal{G} &= \int_{\mathcal{B}_0} \delta\left(w_{k,l}\right)F_{lL}S_{LK}F_{kK}dV_\beta + \int_{\mathcal{B}_0} w_{k,l}\left(\delta F_{lL}\right)S_{LK}F_{kK}dV_\beta \\ &+ \int_{\mathcal{B}_0} w_{k,l}F_{lL}\left(\delta S_{LK}\right)F_{kK}dV_\beta + \int_{\mathcal{B}_0} w_{k,l}F_{lL}S_{LK}\left(\delta F_{kK}\right)dV_\beta \\ &+ \int_{\mathcal{B}_0} w_k\rho_0\left(\delta\ddot{u}_k\right)dV_\beta = 0\end{aligned} \tag{2.147}$$

where

$$\delta F_{lK} = \left(\delta u_l\right)_{,K} \tag{2.148}$$

$$\delta\chi_{lK} = \delta\Phi_{lK} \tag{2.149}$$

$$\delta\left(w_{k,l}\right) = -w_{k,a}(\delta F_{aA})F^{-1}_{Al} \tag{2.150}$$

$$\delta E_{LK} = \frac{1}{2}\left[(\delta F_{iL})F_{iK} + F_{iL}(\delta F_{iK})\right] \tag{2.151}$$

$$\delta\mathcal{E}_{LK} = \left[(\delta F_{iL})\chi_{iK} + F_{iL}(\delta\chi_{iK})\right] \tag{2.152}$$

$$\begin{aligned}\delta S_{KL} &= \left(\lambda + \tau\right)(\delta E_{MM})\delta_{KL} + 2\left(\mu + \sigma\right)(\delta E_{KL}) \\ &+ \eta(\delta\mathcal{E}_{MM})\delta_{KL} + \kappa(\delta\mathcal{E}_{KL}) + \nu(\delta\mathcal{E}_{LK})\end{aligned} \tag{2.153}$$

and,

$$
\begin{aligned}
\delta\mathcal{H} &= \int_{\mathcal{B}_0} \eta_{ml}\left(\delta F_{mM}\right)\left(\Sigma_{ML}-S_{ML}\right)F_{lL}dV_\beta + \int_{\mathcal{B}_0} \eta_{ml}F_{mM}\delta\left(\Sigma_{ML}-S_{ML}\right)F_{lL}dV_\beta \\
&+ \int_{\mathcal{B}_0} \eta_{ml}F_{mM}\left(\Sigma_{ML}-S_{ML}\right)\left(\delta F_{lL}\right)dV_\beta + \int_{\mathcal{B}_0} \delta(\eta_{ml,k})F_{kK}F_{lL}M_{KLM}\chi_{mM}dV_\beta \\
&+ \int_{\mathcal{B}_0} \eta_{ml,k}\left(\delta F_{kK}\right)F_{lL}M_{KLM}\chi_{mM}dV_\beta + \int_{\mathcal{B}_0} \eta_{ml,k}F_{kK}\left(\delta F_{lL}\right)M_{KLM}\chi_{mM}dV_\beta \\
&+ \int_{\mathcal{B}_0} \eta_{ml,k}F_{kK}F_{lL}\delta\left(M_{KLM}\right)\chi_{mM}dV_\beta + \int_{\mathcal{B}_0} \eta_{ml,k}F_{kK}F_{lL}M_{KLM}\left(\delta\chi_{mM}\right)dV_\beta \\
&+ \int_{\mathcal{B}_0} \eta_{ml}\left(\delta\ddot{\chi}_{lK}\right)\chi_{mL}\rho_0 I_{KL(\beta)}dV_\beta + \int_{\mathcal{B}_0} \eta_{ml}\ddot{\chi}_{lK}\left(\delta\chi_{mL}\right)\rho_0 I_{KL(\beta)}dV_\beta
\end{aligned} \tag{2.154}
$$

where $\delta\left(\Sigma_{ML}-S_{ML}\right)$ and $\delta\left(M_{KLM}\right)$ are expressed such that,

$$
\begin{aligned}
\delta\left(\Sigma-S\right)_{KL} &= \tau(\delta E_{MM})\delta_{KL} + 2\sigma(\delta E_{KL}) + (\eta-\tau)\left(\delta\mathcal{E}_{MM}\right)\delta_{KL} \\
&+ (\nu-\sigma)\left(\delta\mathcal{E}_{KL}\right) + (\kappa-\sigma)\left(\delta\mathcal{E}_{LK}\right)
\end{aligned} \tag{2.155}
$$

$$
\begin{aligned}
\delta\left(M_{KLM}\right) &= \tau_1\left[\delta_{LM}\delta\left(\Gamma_{KPP}\right)+\delta_{MK}\delta\left(\Gamma_{PPL}\right)\right] + \tau_2\left[\delta_{LM}\delta\left(\Gamma_{NKN}\right)+\delta_{LK}\delta\left(\Gamma_{PPM}\right)\right] \\
&+\tau_3\delta_{LM}\delta\left(\Gamma_{NNK}\right) + \tau_4\delta_{MK}\delta\left(\Gamma_{LPP}\right) + \tau_5\left[\delta_{LK}\delta\left(\Gamma_{MPP}\right)+\delta_{MK}\delta\left(\Gamma_{NLN}\right)\right] \\
&+\tau_6\delta_{LK}\delta\left(\Gamma_{NMN}\right) + \tau_7\delta\left(\Gamma_{LMK}\right) + \tau_8\left[\delta\left(\Gamma_{KLM}\right)+\delta\left(\Gamma_{MKL}\right)\right] \\
&+\tau_9\delta\left(\Gamma_{LKM}\right) + \tau_{10}\delta\left(\Gamma_{MLK}\right) + \tau_{11}\delta\left(\Gamma_{KML}\right)
\end{aligned} \tag{2.156}
$$

$$
\delta\left(\Gamma_{KLM}\right) = \left(\delta F_{kK}\right)\chi_{lL,M} + F_{kK}\left(\delta\Phi_{iL}\right)_{,M} \tag{2.157}
$$

Upon applying the linearization of the balance of linear and first moment of momenta equations in (2.146), the coupled finite element equations can be constructed. Note that the terms involving $\delta\boldsymbol{u}$ and $\delta\boldsymbol{\Phi}$ in the balance of linear momentum are related to the $\boldsymbol{K}_{dd}$ and $\boldsymbol{K}_{d\phi}$ parts of the consistent tangent in (2.158). Similarly, the terms involving $\delta\boldsymbol{u}$ and $\delta\boldsymbol{\Phi}$ in the balance of first moment of momentum are related to $\boldsymbol{K}_{\phi d}$ and $\boldsymbol{K}_{\phi\phi}$ in the consistent tangent. The system of coupled finite element equations solved at each iteration for the incremental nodal macro-displacement vector $\delta\boldsymbol{d}$ and micro-displacement tensor $\delta\boldsymbol{\phi}$ as follows,

$$
\begin{bmatrix} \boldsymbol{M}_{dd} & \boldsymbol{M}_{d\phi} \\ \boldsymbol{M}_{\phi d} & \boldsymbol{M}_{\phi\phi} \end{bmatrix} \cdot \begin{Bmatrix} \delta\ddot{\boldsymbol{u}} \\ \delta\ddot{\boldsymbol{\Phi}} \end{Bmatrix} + \begin{bmatrix} \boldsymbol{K}_{dd} & \boldsymbol{K}_{d\phi} \\ \boldsymbol{K}_{\phi d} & \boldsymbol{K}_{\phi\phi} \end{bmatrix} \cdot \begin{Bmatrix} \delta\boldsymbol{u} \\ \delta\boldsymbol{\Phi} \end{Bmatrix} = \begin{Bmatrix} -\boldsymbol{R}_d \\ -\boldsymbol{R}_\phi \end{Bmatrix} \tag{2.158}
$$

where $\boldsymbol{R}_d$ and $\boldsymbol{R}_\phi$ are the residual vectors at the current iteration of the Newton-Raphson algorithm [Isbuga, 2012]. $\boldsymbol{K}_{dd}$, $\boldsymbol{K}_{d\phi}$ are the stiffness matrix components related to the balance of linear momentum involving $\delta\boldsymbol{u}$ and $\delta\boldsymbol{\Phi}$ respectively. $\boldsymbol{K}_{\phi d}$, $\boldsymbol{K}_{\phi\phi}$ are the stiffness matrix terms related to the balance of first moment of momentum involving $\delta\boldsymbol{u}$ and $\delta\boldsymbol{\Phi}$. Similarly we have $\boldsymbol{M}_{dd}$, $\boldsymbol{M}_{d\phi}$, and $\boldsymbol{M}_{\phi d}$, $\boldsymbol{M}_{\phi\phi}$ which are the components of mass matrix related to the balance of linear and the balance of first moment of momenta, respectively. Note that for the quasi-static analysis the terms related to the incremental nodal acceleration vector $\delta\ddot{\boldsymbol{d}}$ and acceleration of micro-displacement tensor $\delta\ddot{\boldsymbol{\phi}}$ will be zero. In this thesis, the Hilber-Hughes-Taylor (HHT) implicit time integration method has been used to construct temporally discretized equations of motion. Assuming the classical equation of motion, temporal discretization applying the HHT method is expressed as,

$$\boldsymbol{M}\cdot\ddot{\boldsymbol{u}}_{n+1} + (1+\alpha)\,\boldsymbol{K}\cdot\boldsymbol{u}_{n+1} - \alpha\boldsymbol{K}\cdot\boldsymbol{u}_n = \boldsymbol{R}\left(t_{n+1+\alpha}\right) \tag{2.159}$$

$$\boldsymbol{u}_{n+1} = \boldsymbol{u}_n + \Delta t\dot{\boldsymbol{u}}_n + \frac{\Delta t^2}{2}\left[(1-2\beta)\,\ddot{\boldsymbol{u}}_n + 2\beta\ddot{\boldsymbol{u}}_{n+1}\right] \tag{2.160}$$

$$\dot{\boldsymbol{u}}_{n+1} = \dot{\boldsymbol{u}}_n + \Delta t\left[(1-\gamma)\,\ddot{\boldsymbol{u}}_n + \gamma\ddot{\boldsymbol{u}}_{n+1}\right] \tag{2.161}$$

where $\alpha\in[-1/3,0]$, $\gamma=(1-2\alpha)/2$, and $\beta=(1-\alpha)^2/4$. Note that at $\alpha=0$, the HHT method returns the trapezoidal rule. For $\alpha<0$ the numerical dissipation will be involved in the dynamic analysis. The coupled micromorphic finite element equations can be written such that,

$$\begin{bmatrix} \boldsymbol{M}_{dd}+\beta\,(1+\alpha)\,\Delta t^2\boldsymbol{K}_{dd} & \boldsymbol{M}_{d\phi}+\beta\,(1+\alpha)\,\Delta t^2\boldsymbol{K}_{d\phi} \\ \boldsymbol{M}_{\phi d}+\beta\,(1+\alpha)\,\Delta t^2\boldsymbol{K}_{\phi d} & \boldsymbol{M}_{\phi\phi}+\beta\,(1+\alpha)\,\Delta t^2\boldsymbol{K}_{\phi\phi} \end{bmatrix}\cdot\begin{Bmatrix} \delta\ddot{\boldsymbol{u}} \\ \delta\ddot{\boldsymbol{\Phi}} \end{Bmatrix} = \begin{Bmatrix} -\boldsymbol{R}_d \\ -\boldsymbol{R}_\phi \end{Bmatrix} \tag{2.162}$$

where in (2.162), we can solve for $\delta\ddot{\boldsymbol{u}}$ and $\delta\ddot{\boldsymbol{\Phi}}$. Therefore, the acceleration of macroscopic displacement and the micro-displacement tensor can be found $\ddot{\boldsymbol{u}}^{k+1}_{n+1}=\ddot{\boldsymbol{u}}^{k}_{n+1}+\delta\ddot{\boldsymbol{u}}$, $\ddot{\boldsymbol{\Phi}}^{k+1}_{n+1}=\ddot{\boldsymbol{\Phi}}^{k}_{n+1}+\delta\ddot{\boldsymbol{\Phi}}$. Applying (2.160) and (2.161), the macro-element displacement vector $\boldsymbol{u}$ and micro-displacement tensor $\boldsymbol{\Phi}$, and their velocities can be obtained as follows,

$$\boldsymbol{u}_{n+1} = \boldsymbol{u}_n + \Delta t \dot{\boldsymbol{u}}_n + \frac{\Delta t^2}{2}\left[(1-2\beta)\,\ddot{\boldsymbol{u}}_n + 2\beta \ddot{\boldsymbol{u}}_{n+1}\right] \tag{2.163}$$

$$\dot{\boldsymbol{u}}_{n+1} = \dot{\boldsymbol{u}}_n + \Delta t\left[(1-\gamma)\,\ddot{\boldsymbol{u}}_n + \gamma \ddot{\boldsymbol{u}}_{n+1}\right] \tag{2.164}$$

$$\boldsymbol{\Phi}_{n+1} = \boldsymbol{\Phi}_n + \Delta t \dot{\boldsymbol{\Phi}}_n + \frac{\Delta t^2}{2}\left[(1-2\beta)\,\ddot{\boldsymbol{\Phi}}_n + 2\beta \ddot{\boldsymbol{\Phi}}_{n+1}\right] \tag{2.165}$$

$$\dot{\boldsymbol{\Phi}}_{n+1} = \dot{\boldsymbol{\Phi}}_n + \Delta t\left[(1-\gamma)\,\ddot{\boldsymbol{\Phi}}_n + \gamma \ddot{\boldsymbol{\Phi}}_{n+1}\right] \tag{2.166}$$

Chapter 3

Finite Strain Micromorphic Elastoplasticity

In this chapter, the finite strain micromorphic elasticity in the sense of Eringen and Suhubi [1964] will be extended to elastoplasticity which has been first developed by Regueiro [2009, 2010]. The formulation presented by Regueiro [2009, 2010] has several advantages over the other finite strain micromorphic elastoplastic models available in the literature. This formulation is based upon the micromorphic elasticity by Eringen and Suhubi [1964] in which the balance equations, thermodynamics relations, and, the constitutive equations are developed for the finite strain analysis. From the applicability perspective, this formulation provides an evident bridge between the microscopic scale structure and continuum scale deformation. Furthermore, this formulation fits well in the multi-scale hierarchical micro-structured material modeling framework when the bridging between the direct numerical simulation and the finite element analysis is desired. To the best of my knowledge, this formulation for the finite strain micromorphic elastoplasticity is the most general model in comparison with the available models in the literature. Note that in this chapter all expressions with a bar are defined in the intermediate configuration $\bar{\mathcal{B}}$. It is noteworthy to mention that the main reason for the elastoplasticity formulation in the intermediate configuration is that including material texture in the intermediate configuration is more straight forward in comparison with the elastoplasticity model developed in the current configuration.

3.1 Kinematics of finite strain micromorphic elastoplasticity

To involve the plasticity analysis within the finite strain framework, the deformation gradient tensor has to be decomposed into elastic and plastic parts. This decomposition is done via the multiplicative decomposition of the deformation gradient tensor which requires to define a new plastically deformed configuration named the intermediate configuration $\bar{\mathcal{B}}$. Figure 3.1 illustrates the schematic of the micromorphic kinematics. In the context of the micromorphic continuum, we have the deformation gradient and the micro-deformation tensor which have to be decomposed into elastic and plastic parts, such that

$$\begin{aligned} F_{kK} &= F^{e}_{k\bar{K}} F^{p}_{\bar{K}K} \\ \chi_{kK} &= \chi^{e}_{k\bar{K}} \chi^{p}_{\bar{K}K} \end{aligned} \tag{3.1}$$

Given the multiplicative decompositions of $\boldsymbol{F}$ and $\boldsymbol{\chi}$, the velocity gradient and micro-gyration tensors can be expressed as,

$$v_{l,k} = \dot{F}^{e}_{l\bar{A}} F^{e\,-1}_{\bar{A}k} + F^{e}_{l\bar{B}} \bar{L}^{p}_{\bar{B}\bar{C}} F^{e\,-1}_{\bar{C}k} = \ell^{e}_{lk} + \ell^{p}_{lk} \tag{3.2}$$

$$\bar{L}^{p}_{\bar{B}\bar{C}} = \dot{F}^{p}_{\bar{B}B} F^{p\,-1}_{B\bar{C}} \tag{3.3}$$

$$\nu_{lk} = \dot{\chi}^{e}_{l\bar{A}} \chi^{e\,-1}_{\bar{A}k} + \chi^{e}_{l\bar{B}} \bar{L}^{\chi,p}_{\bar{B}\bar{C}} \chi^{e\,-1}_{\bar{C}k} = \nu^{e}_{lk} + \nu^{p}_{lk} \tag{3.4}$$

$$\bar{L}^{\chi,p}_{\bar{B}\bar{C}} = \dot{\chi}^{p}_{\bar{B}B} \chi^{p\,-1}_{B\bar{C}} \tag{3.5}$$

where $\bar{\boldsymbol{L}}^{p}$ is the plastic velocity gradient in $\bar{\mathcal{B}}$ for F^{p}, and $\bar{\boldsymbol{L}}^{\chi,p}$ is the micro-scale plastic gyration tensor in $\bar{\mathcal{B}}$. The spatial derivative of the micro-gyration tensor can be written such that,

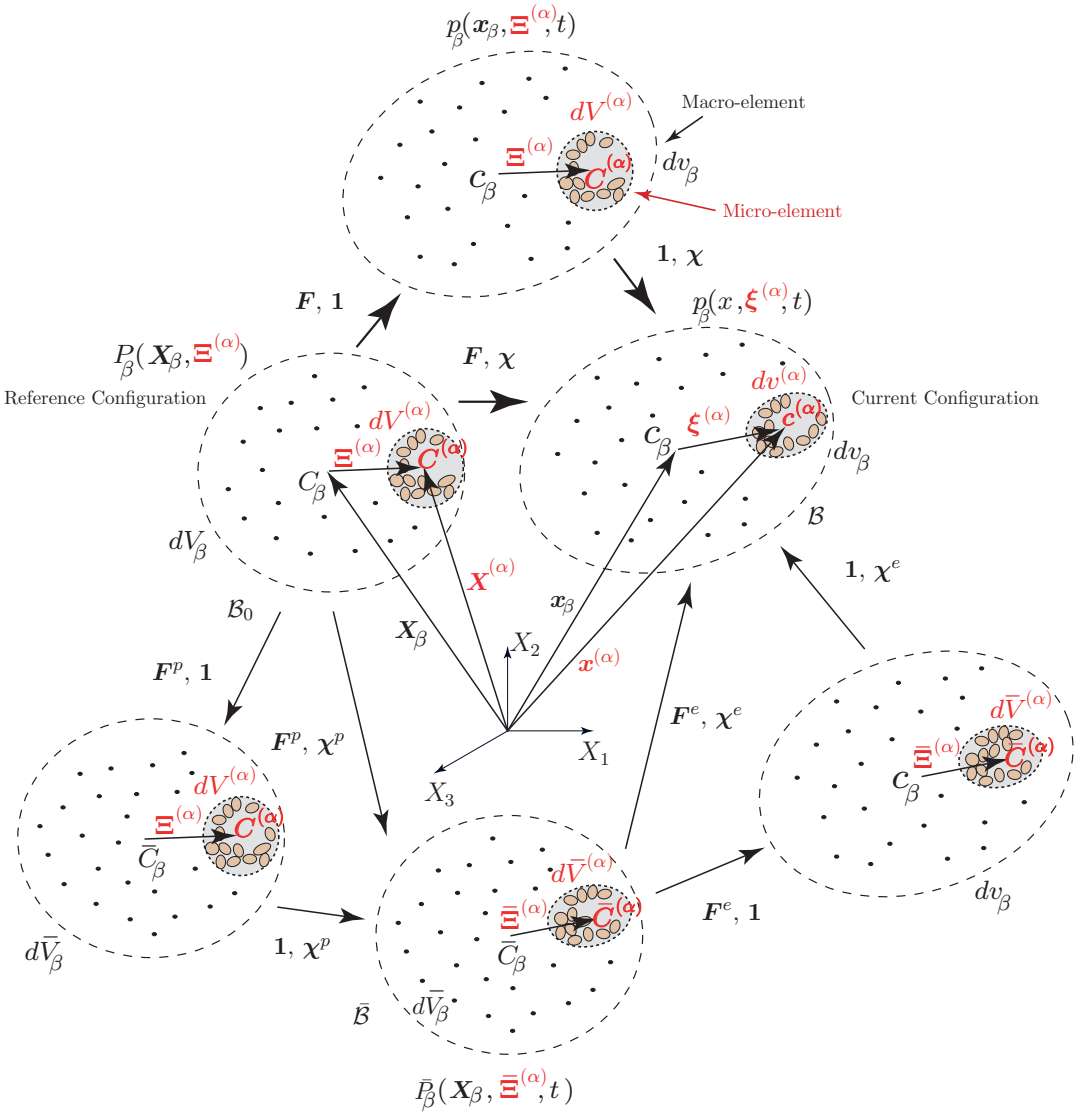

Figure 3.1. Multiplicative decomposition of deformation gradient $\boldsymbol{F}$ and micro-deformation tensor $\boldsymbol{\chi}$ into elastic and plastic parts, schematic of the mapping of the macro-element dV_β and the micro-element $dV^{(\alpha)}$ from the reference configuration $\mathcal{B}_0$ to the intermediate configuration $\bar{\mathcal{B}}$ and to the current configuration $\mathcal{B}$ via the elastic and plastic parts of the macro deformation gradient $\boldsymbol{F}^e$, $\boldsymbol{F}^p$ and the elastic and plastic parts of the micro-deformation tensor $\boldsymbol{\chi}^e$, $\boldsymbol{\chi}^p$.

$$
\begin{aligned}
\nu_{lm,k} &= \nu^e_{lm,k} + \nu^p_{lm,k} \\
\nu^e_{lm,k} &= \dot{\chi}^e_{l\bar{A},k}\chi^{e\,-1}_{\bar{A}m} - \nu^e_{ln}\chi^e_{n\bar{D},k}\chi^{e\,-1}_{\bar{D}m} \qquad (3.6)\\
\nu^p_{lm,k} &= \left(\chi^e_{l\bar{C},k}\,\dot{\chi}^p_{\bar{C}A} + \chi^e_{l\bar{E}}\,\dot{\chi}^p_{\bar{E}A,k} - \chi^e_{l\bar{F}}\,\bar{L}^{\chi,p}_{\bar{F}\bar{G}}\,\chi^p_{\bar{G}A,k}\right)\chi^{-1}_{Am} \\
&\quad -\nu^p_{la}\chi^e_{a\bar{A},k}\chi^{e\,-1}_{\bar{A}m} \qquad (3.7)
\end{aligned}
$$

The macro differential volume in the reference configuration dV_β at C_β maps to the intermediate ($d\bar{V}_\beta$) and current (dv_β) configurations as follows,

$$dv_\beta = JdV_\beta = J^e J^p dV_\beta = J^e d\bar{V}_\beta \tag{3.8}$$

where $J^e = \det(\boldsymbol{F}^e)$ and $J^p = \det(\boldsymbol{F}^p)$. likewise, the micro-element differential volumes mapping can be expressed as,

$$dv^{(\alpha)} = J^{(\alpha)} dV^{(\alpha)} = J^{e(\alpha)} J^{p(\alpha)} dV^{(\alpha)} = J^{e(\alpha)} d\bar{V}^{(\alpha)} \tag{3.9}$$

where $J^{e(\alpha)} = \det \boldsymbol{F}^{e(\alpha)}$ and $J^{p(\alpha)} = \det \boldsymbol{F}^{p(\alpha)}$. There is no need to decompose $\boldsymbol{F}^{(\alpha)}$ into $\boldsymbol{F}^{e(\alpha)}$ and $\boldsymbol{F}^{p(\alpha)}$ since it is not involved in the formulation of the constitutive equations (see discussion after equation (2.9)). But if such formulations were pursued, it would follow from (2.9). Likewise, the mass densities are mapped such that,

$$\rho_0 = \rho J = \rho J^e J^p = \bar{\rho} J^p \tag{3.10}$$

$$\rho_0^{(\alpha)} = \rho^{(\alpha)} J^{(\alpha)} = \rho^{(\alpha)} J^{e(\alpha)} J^{p(\alpha)} = \bar{\rho}^{(\alpha)} J^{p(\alpha)} \tag{3.11}$$

The above equations are obtained according to the conservation of mass and applying the integral averaging approach such that,

$$\rho dv_\beta \overset{\text{def}}{=} \int_{dv_\beta} \rho^{(\alpha)} dv^{(\alpha)} \tag{3.12}$$

$$\rho_0 dV_\beta \overset{\text{def}}{=} \int_{dV_\beta} \rho_0^{(\alpha)} dV^{(\alpha)} \tag{3.13}$$

$$\bar{\rho} d\bar{V}_\beta \overset{\text{def}}{=} \int_{d\bar{V}_\beta} \bar{\rho}^{(\alpha)} d\bar{V}^{(\alpha)} \tag{3.14}$$

Given these kinematics of finite strain micromorphic elastoplasticity, the Clausius-Duhem inequality can be derived to be able to construct the constitutive equations in the intermediate configuration.

3.2 Clausius-Duhem Inequality for Micromorphic Elastoplasticity

In this section, the Clausius-Duhem inequality will be mapped to the intermediate configuration where we formulate the constitutive equations. As it is mentioned earlier, micromorphic

elastoplasticity in the sense of Eringen, presents three levels of plasticity: macro, micro, and micro-gradient plasticity. These levels of plasticity are able to evolve separately, however, they are coupled via the constitutive equations and balance equations. By manipulating the Clausius-Duhem inequality, the evolution equations for various parts of the plastic velocity gradient and micro-gyration including $\bar{L}^{p}_{\bar{I}\bar{J}}$, $\bar{L}^{\chi,p}_{\bar{I}\bar{J}}$ and $\bar{L}^{\chi,p}_{\bar{I}\bar{J},\bar{L}}$ and their conjugate stresses will be obtained. In order to map the Clausius-Duhem inequality to the intermediate configuration, the micromorphic stresses in the current configuration are mapped to the intermediate configuration via the Piola transform such that,

$$\sigma_{kl} = \frac{1}{J^e} F^e_{k\bar{K}} \bar{S}_{\bar{K}\bar{L}} F^e_{l\bar{L}} \tag{3.15}$$

$$s_{kl} = \frac{1}{J^e} F^e_{k\bar{K}} \bar{\Sigma}_{\bar{K}\bar{L}} F^e_{l\bar{L}} \tag{3.16}$$

$$m_{klm} = \frac{1}{J^e} F^e_{k\bar{K}} F^e_{l\bar{L}} \bar{M}_{\bar{K}\bar{L}\bar{M}} \chi^e_{m\bar{M}} \tag{3.17}$$

The Clausius-Duhem inequality in the current configuration is as follows,

$$\int_{\mathcal{B}} \left[-\rho(\dot{\psi} + \eta\dot{\theta}) + \sigma_{kl}(v_{l,k} - \nu_{lk}) + s_{kl}\nu_{lk} + m_{klm}\nu_{lm,k} + \frac{1}{\theta} q_k \theta_{,k} \right] dv_\beta \geq 0 \tag{3.18}$$

The area-averaged unsymmetric Cauchy stress $\boldsymbol{\sigma}$, the volume-averaged symmetric micro-stress $\boldsymbol{s}$, and the area-averaged higher order couple stress $\boldsymbol{m}$ terms are obtained as,

$$
\begin{aligned}
\sigma_{ml} n_m da_\beta &\overset{\text{def}}{=} \int_{da_\beta} \sigma^{(\alpha)}_{ml} n^{(\alpha)}_m da^{(\alpha)} \\
&= \int_{d\bar{A}_\beta} \frac{1}{J^{e(\alpha)}} F^{e(\alpha)}_{m\bar{M}} \bar{S}^{(\alpha)}_{\bar{M}\bar{N}} F^{e(\alpha)}_{l\bar{N}} J^{e(\alpha)} F^{e(\alpha)^{-1}}_{\bar{A}m} \bar{N}^{(\alpha)}_{\bar{A}} d\bar{A}^{(\alpha)} \\
&= \int_{d\bar{A}_\beta} F^{e(\alpha)}_{l\bar{N}} \bar{S}^{(\alpha)}_{\bar{M}\bar{N}} \bar{N}^{(\alpha)}_{\bar{M}} d\bar{A}^{(\alpha)} \\
&= F^e_{l\bar{N}} \bar{S}_{\bar{M}\bar{N}} \bar{N}_{\bar{M}} d\bar{A}_\beta \\
&\qquad \text{where} \quad \bar{S}_{\bar{M}\bar{N}} \bar{N}_{\bar{M}} d\bar{A}_\beta \overset{\text{def}}{=} F^{e}_{\bar{N}a}{}^{-1} \int_{d\bar{A}_\beta} F^{e(\alpha)}_{a\bar{B}} \bar{S}^{(\alpha)}_{\bar{A}\bar{B}} \bar{N}^{(\alpha)}_{\bar{A}} d\bar{A}^{(\alpha)} \\
&\qquad \text{recall} \quad \bar{N}_{\bar{M}} d\bar{A}_\beta = \frac{1}{J^e} F^e_{m\bar{M}} n_m da_\beta \\
&= \underbrace{\frac{1}{J^e} F^e_{m\bar{M}} \bar{S}_{\bar{M}\bar{N}} F^e_{l\bar{N}}}_{=\sigma_{ml}} n_m da_\beta
\end{aligned} \tag{3.19}
$$

$$
\begin{aligned}
s_{kl} dv_\beta &\overset{\text{def}}{=} \int_{dv_\beta} \sigma^{(\alpha)}_{kl} dv^{(\alpha)} = \int_{d\bar{V}_\beta} \frac{1}{J^{e(\alpha)}} F^{e(\alpha)}_{k\bar{K}} \bar{S}^{(\alpha)}_{\bar{K}\bar{L}} F^{e(\alpha)}_{l\bar{L}} J^{e(\alpha)} d\bar{V}^{(\alpha)} \\
&= F^e_{k\bar{K}} F^e_{l\bar{L}} \bar{\Sigma}_{\bar{K}\bar{L}} d\bar{V}_\beta \\
&\qquad \text{where} \quad \bar{\Sigma}_{\bar{K}\bar{L}} d\bar{V}_\beta \overset{\text{def}}{=} F^{e}_{\bar{K}i}{}^{-1} F^{e}_{\bar{L}j}{}^{-1} \int_{d\bar{V}} F^{e(\alpha)}_{i\bar{I}} F^{e(\alpha)}_{j\bar{J}} \bar{S}^{(\alpha)}_{\bar{I}\bar{J}} d\bar{V}^{(\alpha)} \\
&= \underbrace{\frac{1}{J^e} F^e_{k\bar{K}} \bar{\Sigma}_{\bar{K}\bar{L}} F^e_{l\bar{L}}}_{=s_{kl}} dv_\beta
\end{aligned} \tag{3.20}
$$

$$
\begin{aligned}
m_{klm} n_k da_\beta &\overset{\text{def}}{=} \int_{da_\beta} \sigma^{(\alpha)}_{kl} \xi^{(\alpha)}_m n^{(\alpha)}_k da^{(\alpha)} \\
&= \int_{d\bar{A}_\beta} \frac{1}{J^{e(\alpha)}} F^{e(\alpha)}_{k\bar{K}} \bar{S}^{(\alpha)}_{\bar{K}\bar{L}} F^{e(\alpha)}_{l\bar{K}} \chi^e_{m\bar{M}} \bar{\Xi}^{(\alpha)}_{\bar{M}} J^{e(\alpha)} F^{e(\alpha)^{-1}}_{\bar{A}k} \bar{N}^{(\alpha)}_{\bar{A}} d\bar{A}^{(\alpha)} \\
&= \int_{d\bar{A}_\beta} F^{e(\alpha)}_{l\bar{L}} \chi^e_{m\bar{M}} \bar{S}^{(\alpha)}_{\bar{K}\bar{L}} \bar{\Xi}^{(\alpha)}_{\bar{M}} \bar{N}^{(\alpha)}_{\bar{K}} d\bar{A}^{(\alpha)} \\
&= F^e_{l\bar{L}} \chi^e_{m\bar{M}} \bar{M}_{\bar{K}\bar{L}\bar{M}} \bar{N}_{\bar{K}} d\bar{A}_\beta \\
&\qquad \text{where} \quad \bar{M}_{\bar{K}\bar{L}\bar{M}} \bar{N}_{\bar{K}} d\bar{A}_\beta \overset{\text{def}}{=} F^{e}_{\bar{L}a}{}^{-1} \int_{d\bar{A}} F^{e(\alpha)}_{a\bar{B}} \bar{S}^{(\alpha)}_{\bar{K}\bar{B}} \bar{\Xi}^{(\alpha)}_{\bar{M}} \bar{N}^{(\alpha)}_{\bar{K}} d\bar{A}^{(\alpha)} \\
&\qquad \text{recall} \quad \bar{N}_{\bar{K}} d\bar{A}_\beta = \frac{1}{J^e} F^e_{k\bar{K}} n_k da_\beta \\
&= \underbrace{\frac{1}{J^e} F^e_{k\bar{K}} F^e_{l\bar{L}} \chi^e_{m\bar{M}} \bar{M}_{\bar{K}\bar{L}\bar{M}}}_{=m_{klm}} n_k da_\beta
\end{aligned} \tag{3.21}
$$

where $\bar{S}^{(\alpha)}_{\bar{K}\bar{L}}$ is the symmetric second Piola-Kirchhoff stress in the micro-element intermediate configuration over $d\bar{V}_\beta$, $\bar{S}_{\bar{K}\bar{L}}$ is the unsymmetric macroscopic second Piola-Kirchhoff stress in the intermediate configuration $\bar{\mathcal{B}}$, $\bar{\Sigma}_{\bar{K}\bar{L}}$ is the symmetric second Piola-Kirchhoff micro-stress in the intermediate configuration $\bar{\mathcal{B}}$, $\bar{M}_{\bar{K}\bar{L}\bar{M}}$ is the higher order couple stress written in the intermediate configuration $\bar{\mathcal{B}}$, $\bar{N}_{\bar{K}}$ is the unit normal on $d\bar{A}$ in the intermediate configuration $\bar{\mathcal{B}}$, $\boldsymbol{F}^{e(\alpha)}$ is the elastic part of the micro-element deformation gradient which maps the micro-element differential line segment from the intermediate configuration $d\bar{V}_\beta$ to the current configuration dv_β. As mentioned earlier, the constitutive equations do not require $\boldsymbol{F}^{e(\alpha)}$ to be defined. The Clausius-Duhem inequality via mapping the couple stress from the current configuration to the intermediate configuration becomes,

$$\int_{\bar{\mathcal{B}}} \Big[-\bar{\rho}(\dot{\psi} + \bar{\eta}\dot{\theta}) + J^e \sigma_{kl}(v_{l,k} - \nu_{lk}) + J^e s_{kl}\nu_{lk} \\ + \nu_{lm,k}\left(F^e_{k\bar{K}} F^e_{l\bar{L}} \chi^e_{m\bar{M}} \bar{M}_{\bar{K}\bar{L}\bar{M}}\right) + \frac{1}{\theta}\bar{Q}_{\bar{K}}\theta_{,\bar{K}} \Big] d\bar{V}_\beta \geq 0 \tag{3.22}$$

The stress power terms in (3.22) are decomposed into the elastic and the plastic parts additively according to the decomposition of the velocity gradient, the micro-gyration tensors, and the spatial derivative of the micro-gyration tensor. The additive decomposition of the higher order couple stress power can be written as,

$$J^e \nu_{lm,k} m_{klm} = \nu_{lm,k}\left(F^e_{k\bar{K}} F^e_{l\bar{L}} \chi^e_{m\bar{M}} \bar{M}_{\bar{K}\bar{L}\bar{M}}\right) = \\ \left. \bar{M}_{\bar{K}\bar{L}\bar{M}} F^e{}_{l\bar{L}} \left(\dot{\chi}^e_{a\bar{M},\bar{K}} - \nu^e_{ln}\chi^e_{n\bar{M},\bar{K}}\right) \right\} \text{elastic} \\ \left. \begin{array}{r} + M_{\bar{K}\bar{L}\bar{M}} F^e_{l\bar{L}} \left(-\nu^p_{ln}\chi^e_{n\bar{M},\bar{K}}\right. \\ \left. + \left[\chi^e_{a\bar{C},\bar{K}}\dot{\chi}^p_{\bar{C}A} + \chi^e_{a\bar{D}}\dot{\chi}^p_{\bar{D}A,\bar{K}} - \chi^e{}_{a\bar{B}}\, \bar{L}^{\chi,p}_{\bar{B}\bar{E}}\, \chi^p_{\bar{E}A,\bar{K}}\right] \chi^{p-1}_{A\bar{M}}\right) \end{array} \right\} \text{plastic} \tag{3.23}$$

Note that the spatial derivative with respect to the intermediate configuration $\bar{\mathcal{B}}$ can be defined as,

$$(\bullet)_{,\bar{K}} \overset{\text{def}}{=} (\bullet)_{,k} F^e_{k\bar{K}} \tag{3.24}$$

The other stress power terms using (3.3,3.5) are written as,

$$J^e \sigma_{kl} v_{l,k} = \underbrace{F^e_{k\bar{L}} \dot{F}^e_{k\bar{K}} \bar{S}_{\bar{K}\bar{L}}}_{\text{elastic}} + \underbrace{\bar{C}^e_{\bar{L}\bar{B}} \bar{L}^p_{\bar{B}\bar{K}} \bar{S}_{\bar{K}\bar{L}}}_{\text{plastic}} \tag{3.25}$$

$$J^e \sigma_{kl} \nu_{lk} = \underbrace{\left(F^e_{l\bar{L}} \nu^e_{lk} F^e_{k\bar{K}}\right) \bar{S}_{\bar{K}\bar{L}}}_{\text{elastic}} + \underbrace{\bar{\Psi}^e_{\bar{L}\bar{E}} \bar{L}^{\chi,p}_{\bar{E}\bar{F}} \chi^{e\,-1}_{\bar{F}k} F^e_{k\bar{K}} \bar{S}_{\bar{K}\bar{L}}}_{\text{plastic}} \tag{3.26}$$

$$J^e s_{kl} \nu_{lk} = \underbrace{\left(F^e_{l\bar{L}} \nu^e_{lk} F^e_{k\bar{K}}\right) \bar{\Sigma}_{\bar{K}\bar{L}}}_{\text{elastic}} + \underbrace{\bar{\Psi}^e_{\bar{L}\bar{E}} \bar{L}^{\chi,p}_{\bar{E}\bar{F}} \chi^{e\,-1}_{\bar{F}k} F^e_{k\bar{K}} \bar{\Sigma}_{\bar{K}\bar{L}}}_{\text{plastic}} \tag{3.27}$$

Similar to the deformation measures of the finite strain micromorphic elasticity in the reference configuration given by Suhubi and Eringen [1964], the elastic deformation measures in the intermediate configuration can be expressed as,

$$\bar{C}^e_{\bar{K}\bar{L}} = F^e_{k\bar{K}} F^e_{k\bar{L}}, \qquad \bar{\boldsymbol{C}}^e = \bar{\boldsymbol{F}}^{eT} \cdot \bar{\boldsymbol{F}}^e, \tag{3.28}$$

$$\bar{\Psi}^e_{\bar{K}\bar{L}} = F^e_{k\bar{K}} \chi^e_{k\bar{L}}, \qquad \bar{\boldsymbol{\Psi}}^e = \bar{\boldsymbol{F}}^{eT} \cdot \bar{\boldsymbol{\chi}}^e, \tag{3.29}$$

$$\bar{\Gamma}^e_{\bar{K}\bar{L}\bar{M}} = F^e_{k\bar{K}} \chi^e_{k\bar{L},\bar{M}}, \qquad \bar{\boldsymbol{\Gamma}}^e = \bar{\boldsymbol{F}}^{eT} \cdot \left(\bar{\boldsymbol{\nabla}} \bar{\boldsymbol{\chi}}^e\right) \tag{3.30}$$

The Helmholtz free energy function per unit reference volume in the intermediate configuration originally proposed by Regueiro [2010] is assumed to take the following functional form as,

$$\bar{\rho}\psi(F^e_{k\bar{K}}, \chi^e_{k\bar{K}}, \chi^e_{k\bar{M},\bar{K}}, \bar{Z}_{\bar{K}}, \bar{Z}^{\chi}_{\bar{K}}, \bar{Z}^{\chi}_{\bar{K},\bar{L}}, \theta) \tag{3.31}$$

where $\bar{Z}_{\bar{K}}$ is a vector of the macro strain-like ISVs in $\bar{\mathcal{B}}$, $\bar{Z}^{\chi}_{\bar{K}}$ is a vector of the micro strain-like ISVs, and $\bar{Z}^{\chi}_{\bar{K},\bar{L}}$ is a spatial derivative of a vector of the micro strain-like ISVs. Note that all these vectors live in the intermediate configuration $\bar{\mathcal{B}}$. The material time derivative of the Helmholtz free energy can be expressed as,

$$\begin{aligned}\frac{D(\bar{\rho}\psi)}{Dt} &= \frac{\partial(\bar{\rho}\psi)}{\partial F^e_{k\bar{K}}}\dot{F}^e_{k\bar{K}} + \frac{\partial(\bar{\rho}\psi)}{\partial \chi^e_{k\bar{K}}}\dot{\chi}^e_{k\bar{K}} + \frac{\partial(\bar{\rho}\psi)}{\partial \chi^e_{k\bar{M},\bar{K}}}\frac{D(\chi^e_{k\bar{M},\bar{K}})}{Dt} \\ &+ \frac{\partial(\bar{\rho}\psi)}{\partial \bar{Z}_{\bar{K}}}\dot{\bar{Z}}_{\bar{K}} + \frac{\partial(\bar{\rho}\psi)}{\partial \bar{Z}^{\chi}_{\bar{K}}}\dot{\bar{Z}}^{\chi}{}_{\bar{K}} + \frac{\partial(\bar{\rho}\psi)}{\partial \bar{Z}^{\chi}_{\bar{K},\bar{L}}}\frac{D(\bar{Z}^{\chi}_{\bar{K},\bar{L}})}{Dt} + \frac{\partial(\bar{\rho}\psi)}{\partial\theta}\dot{\theta} \end{aligned} \tag{3.32}$$

where $\frac{D(\bar{\rho}\psi)}{Dt}$ can be written such that,

$$\begin{aligned}\dot{\bar{\rho}} &= D(\rho_0/J^p)/Dt = -\bar{\rho}\dot{J}^p/J^p \\ \frac{D(\bar{\rho}\psi)}{Dt} = \dot{\bar{\rho}}\psi + \bar{\rho}\dot{\psi} &= -(\bar{\rho}\psi)\frac{\dot{J}^p}{J^p} + \bar{\rho}\dot{\psi} \Longrightarrow \bar{\rho}\dot{\psi} = (\bar{\rho}\psi)\frac{\dot{J}^p}{J^p} + \frac{D(\bar{\rho}\psi)}{Dt}\end{aligned} \tag{3.33}$$

Inserting equations (3.33), (3.25), (3.26), and (3.27) into the Clasius-Duhem inequality (3.22) we have the following constitutive equations (following [Coleman and Noll, 1963] and [Coleman and Gurtin, 1967]),

$$\bar{S}_{\bar{K}\bar{L}} = \frac{\partial(\bar{\rho}\psi)}{\partial F^e_{k\bar{K}}}F^{e-1}_{\bar{L}k} \tag{3.34}$$

$$\begin{aligned}\bar{\Sigma}_{\bar{K}\bar{L}} &= \frac{\partial(\bar{\rho}\psi)}{\partial F^e_{k\bar{K}}}F^{e-1}_{\bar{L}k} + F^{e-1}_{\bar{K}c}\chi^e_{c\bar{A}}\frac{\partial(\bar{\rho}\psi)}{\partial \chi^e_{a\bar{A}}}F^{e-1}_{\bar{L}a} \\ &\quad + F^{e-1}_{\bar{K}d}\chi^e_{d\bar{M},\bar{E}}\frac{\partial(\bar{\rho}\psi)}{\partial \chi^e_{f\bar{M},\bar{E}}}F^{e-1}_{\bar{L}f}\end{aligned} \tag{3.35}$$

$$\bar{M}_{\bar{K}\bar{L}\bar{M}} = \frac{\partial(\bar{\rho}\psi)}{\partial \chi^e_{k\bar{M},\bar{K}}}F^{e-1}_{\bar{L}k} \tag{3.36}$$

$$\bar{\rho}\bar{\eta} = -\frac{\partial(\bar{\rho}\psi)}{\partial\theta} \tag{3.37}$$

The mapping of the micromorphic stresses to the current configuration is such that,

$$\sigma_{kl} = \frac{1}{J^e}F^e_{k\bar{K}}\bar{S}_{\bar{K}\bar{L}}F^e_{l\bar{L}} = \frac{1}{J^e}F^e_{k\bar{K}}\frac{\partial(\bar{\rho}\psi)}{\partial F^e_{l\bar{K}}} \tag{3.38}$$

$$\begin{aligned}s_{kl} &= \frac{1}{J^e}F^e_{k\bar{K}}\bar{\Sigma}_{\bar{K}\bar{L}}F^e_{l\bar{L}} \\ &= \frac{1}{J^e}\left(F^e_{k\bar{K}}\frac{\partial(\bar{\rho}\psi)}{\partial F^e_{l\bar{K}}} + \chi^e_{k\bar{A}}\frac{\partial(\bar{\rho}\psi)}{\partial \chi^e_{l\bar{A}}} + \chi^e_{k\bar{M},\bar{E}}\frac{\partial(\bar{\rho}\psi)}{\partial \chi^e_{l\bar{M},\bar{E}}}\right)\end{aligned} \tag{3.39}$$

$$m_{klm} = \frac{1}{J^e}F^e_{k\bar{K}}F^e_{l\bar{L}}\chi^e_{m\bar{M}}\bar{M}_{\bar{K}\bar{L}\bar{M}} = \frac{1}{J^e}\frac{\partial(\bar{\rho}\psi)}{\partial \chi^e_{l\bar{M},\bar{K}}}F^e_{k\bar{K}}\chi^e_{m\bar{M}} \tag{3.40}$$

The Helmholtz free energy function in terms of the micromorphic elastic deformation measure invariant equations (3.28-3.30) in the intermediate configuration the ISVs can be written as follows,

$$\bar{\rho}\psi(\bar{C}^{e}_{\bar{K}\bar{L}}, \Psi^{e}_{\bar{K}\bar{L}}, \bar{\Gamma}^{e}_{\bar{K}\bar{L}\bar{M}}, \bar{Z}_{\bar{K}}, \bar{Z}^{\chi}_{\bar{K}}, \bar{Z}^{\chi}_{\bar{K},\bar{L}}, \theta) \tag{3.41}$$

After some algebra, using the constitutive equations for the micromorphic stresses resulting from (3.34-3.36), we can derive the constitutive equations in terms of the elastic deformation measure invariants such that,

$$\begin{aligned}
\bar{S}_{\bar{K}\bar{L}} &= 2\frac{\partial(\bar{\rho}\psi)}{\partial \bar{C}^{e}_{\bar{K}\bar{L}}} + \frac{\partial(\bar{\rho}\psi)}{\partial \Psi^{e}_{\bar{K}\bar{B}}} \bar{C}^{e-1}_{\bar{L}\bar{A}}\, \Psi^{e}_{\bar{A}\bar{B}} \\
&\quad + \frac{\partial(\bar{\rho}\psi)}{\partial \bar{\Gamma}^{e}_{\bar{K}\bar{B}\bar{C}}} \bar{C}^{e-1}_{\bar{L}\bar{A}}\, \bar{\Gamma}^{e}_{\bar{A}\bar{B}\bar{C}} \qquad (3.42) \\
\bar{\Sigma}_{\bar{K}\bar{L}} &= 2\frac{\partial(\bar{\rho}\psi)}{\partial \bar{C}^{e}_{\bar{K}\bar{L}}} + 2\mathrm{sym}\left[\frac{\partial(\bar{\rho}\psi)}{\partial \Psi^{e}_{\bar{K}\bar{B}}} \bar{C}^{e-1}_{\bar{L}\bar{A}}\, \Psi^{e}_{\bar{A}\bar{B}}\right] \\
&\quad + 2\mathrm{sym}\left[\frac{\partial(\bar{\rho}\psi)}{\partial \bar{\Gamma}^{e}_{\bar{K}\bar{B}\bar{C}}} \bar{C}^{e-1}_{\bar{L}\bar{A}}\, \bar{\Gamma}^{e}_{\bar{A}\bar{B}\bar{C}}\right] \qquad (3.43) \\
\bar{M}_{\bar{K}\bar{L}\bar{M}} &= \frac{\partial(\bar{\rho}\psi)}{\partial \bar{\Gamma}^{e}_{\bar{L}\bar{M}\bar{K}}} \qquad (3.44)
\end{aligned}$$

where sym $[\bullet]$ denotes the symmetric part. The thermodynamically-conjugate stress-like ISVs are defined as,

$$\bar{Q}_{\bar{K}} \overset{\text{def}}{=} \frac{\partial(\bar{\rho}\psi)}{\partial \bar{Z}_{\bar{K}}}\,, \quad \bar{Q}^{\chi}_{\bar{K}} \overset{\text{def}}{=} \frac{\partial(\bar{\rho}\psi)}{\partial \bar{Z}^{\chi}_{\bar{K}}}\,, \quad \bar{Q}^{\nabla\chi}_{\bar{K}\bar{L}} \overset{\text{def}}{=} \frac{\partial(\bar{\rho}\psi)}{\partial \bar{Z}^{\chi}_{\bar{K},\bar{L}}} \tag{3.45}$$

The reduced dissipation inequality in the intermediate configuration is expressed as,

$$\begin{aligned}
&-(\bar{\rho}\psi)\tfrac{j^p}{J^p} + \tfrac{1}{\theta}\bar{Q}_{\bar{K}}\theta_{,\bar{K}} - \bar{Q}_{\bar{K}}\dot{\bar{Z}}_{\bar{K}} - \bar{Q}^{\chi}_{\bar{K}}\dot{\bar{Z}}^{\chi}{}_{\bar{K}} - \bar{Q}^{\nabla\chi}_{\bar{K}\bar{L}}\tfrac{D(\bar{Z}^{\chi}_{\bar{K},\bar{L}})}{Dt} \\
&+\bar{S}_{\bar{K}\bar{L}}\left(\bar{C}^{e}_{\bar{L}\bar{B}}\bar{L}^{p}_{\bar{B}\bar{K}}\right) + (\bar{\Sigma}_{\bar{K}\bar{L}} - \bar{S}_{\bar{K}\bar{L}})\left[\Psi^{e}_{\bar{L}\bar{E}}\bar{L}^{\chi,p}_{\bar{E}\bar{F}}\bar{C}^{\chi,e-1}_{\bar{F}\bar{N}}\Psi^{e}_{\bar{K}\bar{N}}\right] \qquad (3.46) \\
&+\bar{M}_{\bar{K}\bar{L}\bar{M}}\left\{\Psi^{e}_{\bar{L}\bar{D}}\bar{L}^{\chi,p}_{\bar{D}\bar{M},\bar{K}} - 2\Psi^{e}_{\bar{L}\bar{D}}\mathrm{skw}\left[\bar{L}^{\chi,p}_{\bar{D}\bar{C}}\Psi^{e-1}{}_{\bar{C}\bar{F}}\bar{\Gamma}^{e}_{\bar{F}\bar{M}\bar{K}}\right]\right\} \geq 0
\end{aligned}$$

where

$$\bar{C}^{\chi,e-1}_{\bar{K}\bar{N}} = \chi^{e-1}_{\bar{K}k}\chi^{e-1}_{\bar{N}k} \tag{3.47}$$

$$\Psi^{e-1}_{\bar{C}\bar{F}} = \chi^{e-1}_{\bar{C}i}F^{e-1}_{\bar{F}i} \tag{3.48}$$

skw $[\bullet]$ denotes the skew-symmetric part defined as,

$$2\text{skw}\,[\bullet] \overset{\text{def}}{=} \left[\bar{L}^{\chi,p}_{\bar{D}\bar{C}}\Psi^{e-1}_{\bar{C}\bar{F}}\bar{\Gamma}^{e}_{\bar{F}\bar{M}\bar{K}}\right] - \left[\bar{L}^{\chi,p}_{\bar{B}\bar{M}}\Psi^{e-1}_{\bar{D}\bar{G}}\bar{\Gamma}^{e}_{\bar{G}\bar{B}\bar{K}}\right] \tag{3.49}$$

and the spatial derivative of the micro-scale plastic velocity gradient can be expressed such that,

$$\bar{L}^{\chi,p}_{\bar{D}\bar{M},\bar{K}} = \left[\dot{\chi}^{p}_{\bar{D}B}\chi^{p-1}_{B\bar{M}}\right]_{,\bar{K}} = \left(\dot{\chi}^{p}_{\bar{D}B,\bar{K}} - \bar{L}^{\chi,p}_{\bar{D}\bar{B}}\,\chi^{p}_{\bar{B}B,\bar{K}}\right)\chi^{p-1}_{B\bar{M}} \tag{3.50}$$

3.2.1 Plastic Evolution Equations

Satisfying the reduced dissipation inequality (3.46) requires the plastic evolution equations to solve for $F^{p}_{\bar{K}K}$, $\chi^{p}_{\bar{K}K}$, and $\chi^{p}_{\bar{K}K,\bar{L}}$ such that,

$$\bar{C}^{e}_{\bar{L}\bar{B}}\bar{L}^{p}_{\bar{B}\bar{K}} - \Psi^{e}_{\bar{L}\bar{E}}\bar{L}^{\chi,p}_{\bar{E}\bar{F}}\bar{C}^{\chi,e-1}_{\bar{F}\bar{N}}\Psi^{e}_{\bar{K}\bar{N}} = \bar{H}_{\bar{L}\bar{K}}\left(\bar{\mathbf{S}},\bar{\mathbf{Q}}\right) \tag{3.51}$$

$$\text{solve for } F^{p}_{\bar{K}K} \text{ and } F^{e}_{k\bar{K}} = F_{kK}F^{p-1}_{K\bar{K}}$$

$$\Psi^{e}_{\bar{L}\bar{E}}\bar{L}^{\chi,p}_{\bar{E}\bar{F}}\bar{C}^{\chi,e-1}_{\bar{F}\bar{N}}\Psi^{e}_{\bar{K}\bar{N}} = \bar{H}^{\chi}_{\bar{L}\bar{K}}\left(\bar{\mathbf{\Sigma}},\bar{\mathbf{Q}}^{\chi}\right) \tag{3.52}$$

$$\text{solve for } \chi^{p}_{\bar{K}K} \text{ and } \chi^{e}_{k\bar{K}} = \chi_{kK}\chi^{p-1}_{K\bar{K}}$$

$$\Psi^{e}_{\bar{L}\bar{D}}\bar{L}^{\chi,p}_{\bar{D}\bar{M},\bar{K}} - 2\Psi^{e}_{\bar{L}\bar{D}}\text{skw}\left[\bar{L}^{\chi,p}_{\bar{D}\bar{C}}\Psi^{e-1}_{\bar{C}\bar{F}}\bar{\Gamma}^{e}_{\bar{F}\bar{M}\bar{K}}\right] = \bar{H}^{\nabla\chi}_{\bar{L}\bar{M}\bar{K}}\left(\bar{\mathbf{M}},\bar{\mathbf{Q}}^{\nabla\chi}\right) \tag{3.53}$$

$$\text{solve for } \chi^{p}_{\bar{K}K,\bar{L}} \text{ and } \chi^{e}_{k\bar{K},\bar{L}} = (\chi_{kK,\bar{L}} - \chi^{e}_{k\bar{A}}\chi^{p}_{\bar{A}K,\bar{L}})\chi^{p-1}_{K\bar{K}}$$

Note that the macro and micro-gradient plasticity levels are coupled to the micro-plasticity analysis through the plastic micro-gyration tensor $\bar{L}^{\chi,p}_{\bar{E}\bar{F}}$. This means that if plasticity occurs at the micro-scale regardless of whether yielding takes place in the macro or the micro-gradient plasticity levels,

the micro plasticity drives plasticity at the macro and the micro-gradient levels. Therefore, we have $F^p_{\bar{K}K}$ and $\chi^p_{\bar{K}K,\bar{L}}$ evolving when $\chi^p_{\bar{K}K}$ evolves. According to the reduced dissipation inequality, we proposed the evolution equation to solve for $\chi^p_{\bar{K}K,\bar{L}}$ (3.53) directly to lessen computational cost, although it can be calculated through the finite element interpolation of $\chi^P_{\bar{K}K}$. Note that the evolution equations for the macro and the micro plasticity presented in this section have been modified compared to that of Regueiro [2010]. The evolution equations proposed by Regueiro [2010] are such that,

$$\bar{C}^e_{\bar{L}\bar{B}}\bar{L}^p_{\bar{B}\bar{K}} = \bar{H}_{\bar{L}\bar{K}}\left(\bar{\mathbf{S}},\bar{\mathbf{Q}}\right) \tag{3.54}$$

$$\text{solve for } F^p_{\bar{K}K} \text{ and } F^e_{k\bar{K}} = F_{kK}F^{p-1}_{K\bar{K}}$$

$$\Psi^e_{\bar{L}\bar{E}}\bar{L}^{\chi,p}_{\bar{E}\bar{F}}\bar{C}^{\chi,e-1}_{\bar{F}\bar{N}}\Psi^e_{\bar{K}\bar{N}} = \bar{H}^{\chi}_{\bar{L}\bar{K}}\left(\bar{\mathbf{\Sigma}}-\bar{\boldsymbol{S}},\bar{\mathbf{Q}}^{\chi}\right) \tag{3.55}$$

$$\text{solve for } \chi^p_{\bar{K}K} \text{ and } \chi^e_{k\bar{K}} = \chi_{kK}\chi^{p-1}_{K\bar{K}}$$

$$\Psi^e_{\bar{L}\bar{D}}\bar{L}^{\chi,p}_{\bar{D}\bar{M},\bar{K}} - 2\Psi^e_{\bar{L}\bar{D}}\text{skw}\left[\bar{L}^{\chi,p}_{\bar{D}\bar{C}}\Psi^{e-1}_{\bar{C}\bar{F}}\bar{\Gamma}^e_{\bar{F}\bar{M}\bar{K}}\right] = \bar{H}^{\nabla\chi}_{\bar{L}\bar{M}\bar{K}}\left(\bar{\mathbf{M}},\bar{\mathbf{Q}}^{\nabla\chi}\right) \tag{3.56}$$

$$\text{solve for } \chi^p_{\bar{K}K,\bar{L}} \text{ and } \chi^e_{k\bar{K},\bar{L}} = (\chi_{kK,\bar{L}} - \chi^e_{k\bar{A}}\chi^p_{\bar{A}K,\bar{L}})\chi^{p-1}_{K\bar{K}}$$

According to these evolution equations, if plasticity occurs at micro scale, it only drives the micro-gradient plasticity level regardless of whether its yielding occurs or not. In the micromorphic elastoplasticity numerical simulations, it has been observed that defining the micro plastic evolution function $\bar{\boldsymbol{H}}^{\chi}$ in terms of the relative stress $\bar{\mathbf{\Sigma}} - \bar{\boldsymbol{S}}$ does not drive the plastic part of the micro-deformation tensor $\boldsymbol{\chi}^p$ to evolve consistently with the applied load and the plastic part of macro deformation gradient $\boldsymbol{F}^p$. In addition, through the simulations the sign of relative stress may change from positive to negative several times, which denotes that the direction of the micro plastic flow will change accordingly. This leads to severe numerical difficulties as well as its physical interpretation is under question. Also, note that if there is significant macro-scale plastic volume change through J^p, then the term $-(\bar{\rho}\psi)\dot{J}^p/J^p$ will contribute to the reduced dissipation inequality in (3.46). It

was shown in [Bennet et al., 2016] that the plastic evolution equations can be formulated in terms of a thermodynamically-conjugate Eshelby-Mandel stress by re-working (3.46). This is relevant for materials that experience finite plastic volume change or damage as well as texture effects. Such formulation will be considered later, not here.

3.3 Constitutive Equations

In this section, the constitutive equations for the micromorphic elastoplasticity will be derived. To this end, the quadratic form of the Helmholtz free energy function similar to micromorphic elasticity is used. The Helmholtz free energy function per unit volume is defined in the intermediate configuration $\bar{\mathcal{B}}$ and the energy terms of the internal state variables (ISVs) are involved such that,

$$\begin{aligned}\bar{\rho}\bar{\psi} \overset{\text{def}}{=}\ & \frac{1}{2}\bar{E}^e_{\bar{K}\bar{L}}\bar{A}_{\bar{K}\bar{L}\bar{M}\bar{N}}\bar{E}^e_{\bar{M}\bar{N}} + \frac{1}{2}\bar{\mathcal{E}}^e_{\bar{K}\bar{L}}\bar{B}_{\bar{K}\bar{L}\bar{M}\bar{N}}\bar{\mathcal{E}}^e_{\bar{M}\bar{N}} \\ & + \frac{1}{2}\bar{\Gamma}^e_{\bar{K}\bar{L}\bar{M}}\bar{C}_{\bar{K}\bar{L}\bar{M}\bar{N}\bar{P}\bar{Q}}\bar{\Gamma}^e_{\bar{N}\bar{P}\bar{Q}} + \bar{E}^e_{\bar{K}\bar{L}}\bar{D}_{\bar{K}\bar{L}\bar{M}\bar{N}}\bar{\mathcal{E}}^e_{\bar{M}\bar{N}} \\ & + \frac{1}{2}\bar{H}\bar{Z}^2 + \frac{1}{2}\bar{H}^\chi(\bar{Z}^\chi)^2 + \frac{1}{2}\bar{Z}^\chi_{,\bar{K}}\bar{H}^{\nabla\chi}_{\bar{K}\bar{L}}\bar{Z}^\chi_{,\bar{L}}\end{aligned} \tag{3.57}$$

Note that the ISVs related to the macro and micro scales are scalar quantities defining the strength of the material. $\bar{H}$ and $\bar{H}^\chi$ are scalar hardening/softening parameters at the macro and micro scales respectively. $\bar{H}^{\nabla\chi}_{\bar{K}\bar{L}}$ is a symmetric second order hardening/softening modulus tensor for the micro gradient plasticity level, which we will assume is an isotropic tensor as $\bar{H}^{\nabla\chi}_{\bar{K}\bar{L}} = (\bar{H}^{\nabla\chi})\delta_{\bar{K}\bar{L}}$. The elastic strains are defined similar to micromorphic elasticity as $2\bar{E}^e_{\bar{K}\bar{L}} = \bar{C}^e_{\bar{K}\bar{L}} - \delta_{\bar{K}\bar{L}}$, $\bar{\mathcal{E}}^e_{\bar{K}\bar{L}} = \bar{\Psi}^e_{\bar{K}\bar{L}} - \delta_{\bar{K}\bar{L}}$, and $\bar{\Gamma}^e_{\bar{K}\bar{L}\bar{M}} = F^e_{k\bar{K}}\chi^e_{k\bar{L},\bar{M}}$. The elastic moduli for isotropic linear elasticity can be expressed as,

$$\bar{A}_{\bar{K}\bar{L}\bar{M}\bar{N}} = \lambda\delta_{\bar{K}\bar{L}}\delta_{\bar{M}\bar{N}} + \mu\left(\delta_{\bar{K}\bar{M}}\delta_{\bar{L}\bar{N}} + \delta_{\bar{K}\bar{N}}\delta_{\bar{L}\bar{M}}\right) \tag{3.58}$$

$$\begin{aligned}\bar{B}_{\bar{K}\bar{L}\bar{M}\bar{N}} &= (\eta-\tau)\delta_{\bar{K}\bar{L}}\delta_{\bar{M}\bar{N}} + \kappa\delta_{\bar{K}\bar{M}}\delta_{\bar{L}\bar{N}} + \nu\delta_{\bar{K}\bar{N}}\delta_{\bar{L}\bar{M}} \\ &\quad -\sigma(\delta_{\bar{K}\bar{M}}\delta_{\bar{L}\bar{N}} + \delta_{\bar{K}\bar{N}}\delta_{\bar{L}\bar{M}})\end{aligned} \tag{3.59}$$

$$\begin{aligned}\bar{C}_{\bar{L}\bar{M}\bar{K}\bar{N}\bar{P}\bar{Q}} &= \tau_1\left(\delta_{\bar{L}\bar{M}}\delta_{\bar{K}\bar{N}}\delta_{\bar{P}\bar{Q}} + \delta_{\bar{L}\bar{Q}}\delta_{\bar{M}\bar{K}}\delta_{\bar{N}\bar{P}}\right) \\ &\quad +\tau_2\left(\delta_{\bar{L}\bar{M}}\delta_{\bar{K}\bar{P}}\delta_{\bar{N}\bar{Q}} + \delta_{\bar{L}\bar{K}}\delta_{\bar{M}\bar{Q}}\delta_{\bar{N}\bar{P}}\right) \\ &\quad +\tau_3\delta_{\bar{L}\bar{M}}\delta_{\bar{K}\bar{Q}}\delta_{\bar{N}\bar{P}} + \tau_4\delta_{\bar{L}\bar{N}}\delta_{\bar{M}\bar{K}}\delta_{\bar{P}\bar{Q}} \\ &\quad +\tau_5\left(\delta_{\bar{L}\bar{K}}\delta_{\bar{M}\bar{N}}\delta_{\bar{P}\bar{Q}} + \delta_{\bar{L}\bar{P}}\delta_{\bar{M}\bar{K}}\delta_{\bar{N}\bar{Q}}\right) \\ &\quad +\tau_6\delta_{\bar{L}\bar{K}}\delta_{\bar{M}\bar{P}}\delta_{\bar{N}\bar{Q}} + \tau_7\delta_{\bar{L}\bar{N}}\delta_{\bar{M}\bar{P}}\delta_{\bar{K}\bar{Q}} \\ &\quad +\tau_8\left(\delta_{\bar{L}\bar{P}}\delta_{\bar{M}\bar{Q}}\delta_{\bar{K}\bar{N}} + \delta_{\bar{L}\bar{Q}}\delta_{\bar{M}\bar{N}}\delta_{\bar{K}\bar{P}}\right) \\ &\quad +\tau_9\delta_{\bar{L}\bar{N}}\delta_{\bar{M}\bar{Q}}\delta_{\bar{K}\bar{P}} + \tau_{10}\delta_{\bar{L}\bar{P}}\delta_{\bar{M}\bar{N}}\delta_{\bar{K}\bar{Q}} \\ &\quad +\tau_{11}\delta_{\bar{L}\bar{Q}}\delta_{\bar{M}\bar{P}}\delta_{\bar{K}\bar{N}}\end{aligned} \tag{3.60}$$

$$\bar{D}_{\bar{K}\bar{L}\bar{M}\bar{N}} = \tau\delta_{\bar{K}\bar{L}}\delta_{\bar{M}\bar{N}} + \sigma(\delta_{\bar{K}\bar{M}}\delta_{\bar{L}\bar{N}} + \delta_{\bar{K}\bar{N}}\delta_{\bar{L}\bar{M}}) \tag{3.61}$$

where $\bar{A}_{\bar{K}\bar{L}\bar{M}\bar{N}}$ and $\bar{D}_{\bar{K}\bar{L}\bar{M}\bar{N}}$ have major and minor symmetry, while $\bar{B}_{\bar{K}\bar{L}\bar{M}\bar{N}}$ and $\bar{C}_{\bar{K}\bar{L}\bar{M}\bar{N}\bar{P}\bar{Q}}$ have only major symmetry. The micromorphic linear elastic isotropic continuum has 18 elastic parameters listed as λ, μ, η, τ, κ, ν, σ, $\tau_1 \ldots \tau_{11}$. Note that the elastic parameters related to the couple stress are defined according to the length scale. The units of $\tau_1 \ldots \tau_{11}$ are stress$\times$length^2 (e.g., Pa.m^2). After some algebra using (3.42-3.45), and (3.57), it can be shown that the stress constitutive relations are,

$$
\begin{aligned}
\bar{S}_{\bar{K}\bar{L}} &= \bar{A}_{\bar{K}\bar{L}\bar{M}\bar{N}}\bar{E}^{e}_{\bar{M}\bar{N}} + \bar{D}_{\bar{K}\bar{B}\bar{M}\bar{N}}\bar{\mathcal{E}}^{e}_{\bar{M}\bar{N}} \\
&\quad +(\bar{D}_{\bar{K}\bar{B}\bar{M}\bar{N}}\bar{E}^{e}_{\bar{M}\bar{N}} + \bar{B}_{\bar{K}\bar{B}\bar{M}\bar{N}}\bar{\mathcal{E}}^{e}_{\bar{M}\bar{N}})\left[\bar{C}^{e-1}_{\bar{L}\bar{A}}\bar{\mathcal{E}}^{e}_{\bar{A}\bar{B}} + \delta_{\bar{L}\bar{B}}\right] \\
&\quad +\bar{C}_{\bar{K}\bar{B}\bar{C}\bar{N}\bar{P}\bar{Q}}\bar{\Gamma}^{e}_{\bar{N}\bar{P}\bar{Q}}\bar{C}^{e-1}_{\bar{L}\bar{Q}}\bar{\Gamma}^{e}_{\bar{Q}\bar{B}\bar{C}} \qquad (3.62) \\
\bar{\Sigma}_{\bar{K}\bar{L}} &= \bar{A}_{\bar{K}\bar{L}\bar{M}\bar{N}}\bar{E}^{e}_{\bar{M}\bar{N}} + \bar{D}_{\bar{K}\bar{B}\bar{M}\bar{N}}\bar{\mathcal{E}}^{e}_{\bar{M}\bar{N}} \\
&\quad +2\text{sym}\left\{(\bar{D}_{\bar{K}\bar{L}\bar{M}\bar{N}}\bar{E}^{e}_{\bar{M}\bar{N}} + \bar{B}_{\bar{K}\bar{B}\bar{M}\bar{N}}\bar{\mathcal{E}}^{e}_{\bar{M}\bar{N}})\left[\bar{C}^{e-1}_{\bar{L}\bar{A}}\bar{\mathcal{E}}^{e}_{\bar{A}\bar{B}} + \delta_{\bar{L}\bar{B}}\right]\right. \\
&\quad \left.+\bar{C}_{\bar{K}\bar{B}\bar{C}\bar{N}\bar{P}\bar{Q}}\bar{\Gamma}^{e}_{\bar{N}\bar{P}\bar{Q}}\bar{C}^{e-1}_{\bar{L}\bar{Q}}\bar{\Gamma}^{e}_{\bar{Q}\bar{B}\bar{C}}\right\} \qquad (3.63) \\
\bar{M}_{\bar{K}\bar{L}\bar{M}} &= \bar{C}_{\bar{L}\bar{M}\bar{K}\bar{N}\bar{P}\bar{Q}}\bar{\Gamma}^{e}_{\bar{N}\bar{P}\bar{Q}} \qquad (3.64) \\
\bar{Q} &= \bar{H}\bar{Z} \qquad (3.65) \\
\bar{Q}^{\chi} &= \bar{H}^{\chi}\bar{Z}^{\chi} \qquad (3.66) \\
\bar{Q}^{\chi}_{\bar{L}} &= \bar{H}^{\nabla\chi}\bar{Z}^{\chi}_{,\bar{L}} \qquad (3.67)
\end{aligned}
$$

Assuming small elastic deformations and removing the quadratic terms in (3.62) and (3.63), the simplified stress constitutive equations for $\bar{S}_{\bar{K}\bar{L}}$, $\bar{\Sigma}_{\bar{K}\bar{L}}$, and $\bar{M}_{\bar{K}\bar{L}\bar{M}}$ can be written such as,

$$
\begin{aligned}
\bar{S}_{\bar{K}\bar{L}} &= (\lambda+\tau)(\bar{E}^{e}_{\bar{M}\bar{M}})\delta_{\bar{K}\bar{L}} + 2(\mu+\sigma)\bar{E}^{e}_{\bar{K}\bar{L}} \qquad (3.68) \\
&\quad +\eta(\bar{\mathcal{E}}^{e}_{\bar{M}\bar{M}})\delta_{\bar{K}\bar{L}} + \kappa\bar{\mathcal{E}}^{e}_{\bar{K}\bar{L}} + \nu\bar{\mathcal{E}}^{e}_{\bar{L}\bar{K}} \\
\bar{\Sigma}_{\bar{K}\bar{L}} &= (\lambda+\tau)(\bar{E}^{e}_{\bar{M}\bar{M}})\delta_{\bar{K}\bar{L}} + 2(\mu+\sigma)\bar{E}^{e}_{\bar{K}\bar{L}} \qquad (3.69) \\
&\quad +\eta(\bar{\mathcal{E}}^{e}_{\bar{M}\bar{M}})\delta_{\bar{K}\bar{L}} + 2\text{sym}\left[\kappa\bar{\mathcal{E}}^{e}_{\bar{K}\bar{L}} + \nu\bar{\mathcal{E}}^{e}_{\bar{L}\bar{K}}\right] \\
\bar{M}_{\bar{K}\bar{L}\bar{M}} &= \tau_1\left(\delta_{\bar{L}\bar{M}}\bar{\Gamma}_{\bar{K}\bar{P}\bar{P}} + \delta_{\bar{M}\bar{K}}\bar{\Gamma}_{\bar{P}\bar{P}\bar{L}}\right) + \tau_2\left(\delta_{\bar{L}\bar{M}}\bar{\Gamma}_{\bar{N}\bar{K}\bar{N}} + \delta_{LK}\bar{\Gamma}_{\bar{P}\bar{P}\bar{M}}\right) \qquad (3.70) \\
&+ \tau_3\delta_{\bar{L}\bar{M}}\bar{\Gamma}_{\bar{N}\bar{N}\bar{K}} + \tau_4\delta_{\bar{M}\bar{K}}\bar{\Gamma}_{\bar{L}\bar{P}\bar{P}} + \tau_5\left(\delta_{\bar{L}\bar{K}}\bar{\Gamma}_{\bar{M}\bar{P}\bar{P}} + \delta_{\bar{M}\bar{K}}\bar{\Gamma}_{\bar{N}\bar{L}\bar{N}}\right) \\
&+ \tau_6\delta_{\bar{L}\bar{K}}\bar{\Gamma}_{\bar{N}\bar{M}\bar{N}} + \tau_7\bar{\Gamma}_{\bar{L}\bar{M}\bar{K}} + \tau_8\left(\bar{\Gamma}_{\bar{K}\bar{L}\bar{M}} + \bar{\Gamma}_{\bar{M}\bar{K}\bar{L}}\right) \\
&+ \tau_9\bar{\Gamma}_{\bar{L}\bar{K}\bar{M}} + \tau_{10}\bar{\Gamma}_{\bar{M}\bar{L}\bar{K}} + \tau_{11}\bar{\Gamma}_{\bar{K}\bar{M}\bar{L}}
\end{aligned}
$$

3.4 Yield Functions and Evolution Equations

The micromorphic continuum introduces three levels of plasticity based on the three conjugate stress-plastic-power terms appearing in the reduced dissipation inequality (3.46) including the macro, micro, and micro-gradient plasticity levels. Therefore, the plastic deformations calculated from the evolution equations must satisfy the reduced dissipation inequality (3.46). This approach of formulating the micromorphic elastoplasticity allows yielding and plastic deformation at the macro, micro and micro-gradient levels separately. Note that $\chi^{p}_{\bar{K}K,\bar{L}}$ can be calculated from the finite element interpolation of $\chi^{p}_{\bar{K}K}$, however, in the simulations of this thesis the evolution equation (3.53) has been implemented directly for calculation $\chi^{p}_{\bar{K}K,\bar{L}}$. It is possible to define only one yield function to be a function of all three stresses ($\bar{\mathbf{S}}$, $\bar{\mathbf{\Sigma}}$, $\bar{\mathbf{M}}$). If this yield function detects yielding this means that yielding occurs at the all of the three scales at once (i.e., there is only one plastic multiplier). This approach will simplify the numerical implementation of the micromorphic elastoplasticity, and reduce the difficulty in finding appropriate plastic multipliers for each of the plasticity levels. However, this is not desirable and will not reflect the physics properly. Therefore, in this research, three distinct yield functions have been defined for each of the plasticity levels, and, thus $F^{p}_{\bar{I}I}$, $\chi^{p}_{\bar{I}I}$, and $\chi^{p}_{\bar{I}I,\bar{L}}$ are able to evolve separately through their separate evolution equations and separate plastic multipliers. In this thesis the micromorphic elastoplasticity will be developed based on the Drucker-Prager Pressure-Sensitive plasticity model.

Macro-scale plasticity

For macro-scale plasticity, the macroscopic yield function $\bar{F}_{(macro)}$ and the plastic potential function $\bar{G}_{(macro)}$ are written such that,

$$
\begin{aligned}
\bar{F}_{(macro)}(\bar{\mathbf{S}},\bar{c}) &\stackrel{\text{def}}{=} \|\text{dev}\bar{\mathbf{S}}\| - \left(A^{\phi}\bar{c} - B^{\phi}\bar{p}\right) \leq 0 \qquad (3.71)\\
&\quad \|\text{dev}\bar{\mathbf{S}}\| = \sqrt{(\text{dev}\bar{\mathbf{S}}) : (\text{dev}\bar{\mathbf{S}})}\\
&\quad (\text{dev}\bar{\mathbf{S}}) : (\text{dev}\bar{\mathbf{S}}) = (\text{dev}\bar{S}_{\bar{I}\bar{J}})(\text{dev}\bar{S}_{\bar{I}\bar{J}})\\
&\quad \text{dev}\bar{S}_{\bar{I}\bar{J}} \stackrel{\text{def}}{=} \bar{S}_{\bar{I}\bar{J}} - \left(\frac{1}{3}\bar{C}^{e}_{\bar{A}\bar{B}}\bar{S}_{\bar{A}\bar{B}}\right)\bar{C}^{e-1}_{\bar{I}\bar{J}}\\
&\quad \bar{p} \stackrel{\text{def}}{=} \frac{1}{3}\bar{C}^{e}_{\bar{A}\bar{B}}\bar{S}_{\bar{A}\bar{B}}\\
&\quad A^{\phi} = \beta^{\phi}\cos\phi\,, \quad B^{\phi} = \beta^{\phi}\sin\phi\,, \quad \beta^{\phi} = \frac{2\sqrt{6}}{3+\beta\sin\phi}\\
\bar{G}_{(macro)}(\bar{\mathbf{S}},\bar{c}) &\stackrel{\text{def}}{=} \|\text{dev}\bar{\mathbf{S}}\| - \left(A^{\psi}\bar{c} - B^{\psi}\bar{p}\right)\\
&\quad A^{\psi} = \beta^{\psi}\cos\psi\,, \quad B^{\psi} = \beta^{\psi}\sin\psi\,, \quad \beta^{\psi} = \frac{2\sqrt{6}}{3+\beta\sin\psi} \qquad (3.72)
\end{aligned}
$$

where $\bar{c}$ is the macro cohesion, ϕ the macro friction angle, ψ the macro dilation angle, and $-1 \leq \beta \leq 1$. Note that $\beta = 1$ makes the Drucker-Prager yield surface intersect the triaxial extension vertices of the Mohr-Coulomb yield surface, and $\beta = -1$ the triaxial compression vertices of the Mohr-Coulomb yield surface. The reduced dissipation inequality will be satisfied if the selected value for ϕ is larger than or equal to ψ, ($\phi \geq \psi$). This has been shown by Vermeer and de Borst [1984]. The evolution equations for the macro plasticity level is expressed such that,

$$
\begin{aligned}
\bar{C}^{e}_{\bar{L}\bar{B}}\bar{L}^{p}_{\bar{B}\bar{K}} - \bar{\Psi}^{e}_{\bar{L}\bar{E}}\bar{L}^{\chi,p}_{\bar{E}\bar{F}}\bar{C}^{\chi,e-1}_{\bar{F}\bar{N}}\bar{\Psi}^{e}_{\bar{K}\bar{N}} &\stackrel{\text{def}}{=} \dot{\bar{\gamma}}\frac{\partial\bar{G}_{(macro)}}{\partial\bar{S}_{\bar{K}\bar{L}}} \qquad (3.73)\\
&\quad \frac{\partial\bar{G}_{(macro)}}{\partial\bar{S}_{\bar{K}\bar{L}}} = \hat{\bar{N}}_{\bar{K}\bar{L}} + \frac{1}{3}B^{\psi}\bar{C}^{e}_{\bar{K}\bar{L}}\\
&\quad \hat{\bar{N}}_{\bar{K}\bar{L}} = \frac{\text{dev}\bar{S}_{\bar{K}\bar{L}}}{\|\text{dev}\bar{\mathbf{S}}\|}\\
\dot{\bar{Z}} &\stackrel{\text{def}}{=} -\dot{\bar{\gamma}}\frac{\partial\bar{G}_{(macro)}}{\partial\bar{c}} = A^{\psi}\dot{\bar{\gamma}} \qquad (3.74)\\
\bar{c} &= \bar{H}\bar{Z} \qquad (3.75)\\
\dot{\bar{c}} &= \bar{H}\dot{\bar{Z}} = \bar{H}A^{\psi}\dot{\bar{\gamma}} \qquad (3.76)\\
\bar{Q} &\stackrel{\text{def}}{=} \bar{c} \qquad (3.77)
\end{aligned}
$$

where $\dot{\bar{\gamma}}$ is the macro plastic multiplier in the intermediate configuration. The plastic part of the deformation gradient is solved by integrating the following equation, which is derived from (3.73) as,

$$\dot{\bar{F}}^{p}_{\bar{B}C} = \dot{\bar{\gamma}}\bar{C}^{e-1}_{\bar{B}\bar{L}}\frac{\partial \bar{G}_{(macro)}}{\partial \bar{S}_{\bar{K}\bar{L}}}\bar{F}^{p}_{\bar{K}C} + \bar{C}^{e-1}_{\bar{B}\bar{L}}\bar{\Psi}^{e}_{\bar{L}\bar{E}}\bar{L}^{\chi,p}_{\bar{E}\bar{F}}C^{\chi(e-1)}_{\bar{F}\bar{N}}\bar{\Psi}^{e}_{\bar{K}\bar{N}}\bar{F}^{p}_{\bar{K}C} \tag{3.78}$$

Micro-scale plasticity

For the micro-scale plasticity, the microscopic yield $\bar{F}^{\chi}_{(micro)}$ and the plastic potential $\bar{G}^{\chi}_{(micro)}$ functions are expressed as,

$$\begin{aligned}
\bar{F}^{\chi}_{(micro)}(\bar{\mathbf{\Sigma}}, \bar{c}^{\chi}) &\overset{\text{def}}{=} \|\text{dev}(\bar{\mathbf{\Sigma}})\| - \left(A^{\chi,\phi}\bar{c}^{\chi} - B^{\chi,\phi}\bar{p}^{\chi}\right) \leq 0 \qquad (3.79)\\
&\quad A^{\chi,\phi} = \beta^{\chi,\phi}\cos\phi^{\chi}\ ,\ B^{\chi,\phi} = \beta^{\chi,\phi}\sin\phi^{\chi}\ ,\ \beta^{\chi,\phi} = \frac{2\sqrt{6}}{3+\beta^{\chi}\sin\phi^{\chi}}\\
&\quad \text{dev}(\bar{\Sigma}_{\bar{I}\bar{J}}) \overset{\text{def}}{=} (\bar{\Sigma}_{\bar{I}\bar{J}}) - \bar{p}^{\chi}\bar{C}^{e-1}_{\bar{I}\bar{J}}\\
&\quad \bar{p}^{\chi} \overset{\text{def}}{=} \frac{1}{3}\bar{C}^{e}_{\bar{A}\bar{B}}(\bar{\Sigma}_{\bar{A}\bar{B}})\\
\bar{G}^{\chi}_{(micro)}(\bar{\mathbf{\Sigma}}, \bar{c}^{\chi}) &\overset{\text{def}}{=} \|\text{dev}(\bar{\mathbf{\Sigma}})\| - \left(A^{\chi,\psi}\bar{c}^{\chi} - B^{\chi,\psi}\bar{p}^{\chi}\right) \qquad (3.80)\\
&\quad A^{\chi,\phi} = \beta^{\chi,\psi}\cos\psi^{\chi}\ ,\ B^{\chi,\psi} = \beta^{\chi,\psi}\sin\psi^{\chi}\ ,\ \beta^{\chi,\psi} = \frac{2\sqrt{6}}{3+\beta^{\chi}\sin\psi^{\chi}}
\end{aligned}$$

where $\bar{c}^{\chi}$ is the micro cohesion, ϕ^{χ} the micro friction angle, ψ^{χ} the micro dilation angle, and $-1 \leq \beta^{\chi} \leq 1$, which are the material parameters to govern the plasticity at the micro-scale. It can be seen that all the material parameters for the micro plasticity level can be defined irrespective of the macro plasticity level parameters. This approach of formulating the micromorphic elastoplasticity provides us a chance of capturing the different phenomenological aspects of the macro and micro level plasticities. In this research, we employed the same functional forms for the macro and micro level yield and the plastic potential functions, but this is not a requirement. The evolution equations for the micro-scale plasticity can be written such that,

$$\bar{\Psi}^{e}_{\bar{L}\bar{E}}\bar{L}^{\chi,p}_{\bar{E}\bar{F}}\bar{C}^{\chi,e-1}_{\bar{F}\bar{N}}\bar{\Psi}^{e}_{\bar{K}\bar{N}} \overset{\text{def}}{=} \dot{\bar{\gamma}}^{\chi}\frac{\partial\bar{G}^{\chi}}{\partial(\bar{\Sigma}_{\bar{K}\bar{L}})} \tag{3.81}$$

$$\frac{\partial\bar{G}^{\chi}}{\partial(\bar{\Sigma}_{\bar{K}\bar{L}})} = \hat{\bar{N}}^{\chi}_{\bar{K}\bar{L}} + \frac{1}{3}B^{\chi,\psi}\bar{C}^{e}_{\bar{K}\bar{L}}$$

$$\hat{\bar{N}}^{\chi}_{\bar{K}\bar{L}} = \frac{\text{dev}(\bar{\Sigma}_{\bar{K}\bar{L}})}{\|\text{dev}(\bar{\boldsymbol{\Sigma}})\|}$$

$$\dot{\bar{Z}}^{\chi} \overset{\text{def}}{=} -\dot{\bar{\gamma}}^{\chi}\frac{\partial\bar{G}^{\chi}}{\partial\bar{c}^{\chi}} = A^{\chi,\psi}\dot{\bar{\gamma}}^{\chi} \tag{3.82}$$

$$\bar{c}^{\chi} = \bar{H}^{\chi}\bar{Z}^{\chi} \tag{3.83}$$

$$\dot{\bar{c}}^{\chi} = \bar{H}^{\chi}\dot{\bar{Z}}^{\chi} = \bar{H}^{\chi}A^{\chi,\psi}\dot{\bar{\gamma}}^{\chi} \tag{3.84}$$

$$\bar{Q}^{\chi} \overset{\text{def}}{=} \bar{c}^{\chi} \tag{3.85}$$

where $\dot{\bar{\gamma}}^{\chi}$ is the micro plastic multiplier in the intermediate configuration. The evolution of the plastic part of micro-deformation tensor is derived from (3.81) as,

$$\dot{\chi}^{p}_{\bar{B}N} = \dot{\bar{\gamma}}^{\chi}\bar{\Psi}^{e-1}_{\bar{B}\bar{P}}\frac{\partial\bar{G}^{\chi}_{(micro)}}{\partial\bar{\Sigma}_{\bar{O}\bar{P}}}\Psi^{e-1}_{\bar{T}\bar{O}}\bar{C}^{\chi,e}_{\bar{T}\bar{Q}}\chi^{p}_{\bar{Q}N} \tag{3.86}$$

Micro-scale gradient plasticity

For the micro-scale gradient plasticity, the micro-gradient yield $\bar{\boldsymbol{F}}^{\nabla\chi}$ and plastic potential $\bar{\boldsymbol{G}}^{\nabla\chi}$ functions are written such that,

$$\bar{F}^{\nabla\chi}_{\bar{K}(micro-grad)}(\bar{\mathbf{M}},\bar{\mathbf{c}}^{\nabla\chi}) \overset{\text{def}}{=} \|\text{dev}\bar{\mathbf{M}}\|_{\bar{K}} - \left(A^{\nabla\chi,\phi}\bar{c}^{\nabla\chi}_{\bar{K}} - B^{\nabla\chi,\phi}\bar{p}^{\nabla\chi}_{\bar{K}}\right) \leq 0 \tag{3.87}$$

$$A^{\nabla\chi,\phi} = \beta^{\nabla\chi,\phi}\cos\phi^{\nabla\chi}\ ,\ B^{\nabla\chi,\phi} = \beta^{\nabla\chi,\phi}\sin\phi^{\nabla\chi}\ ,\ \beta^{\nabla\chi,\phi} = \frac{2\sqrt{6}}{3+\beta^{\nabla\chi}\sin\phi^{\nabla\chi}}$$

$$\text{dev}\bar{M}_{\bar{I}\bar{J}\bar{K}} \overset{\text{def}}{=} \bar{M}_{\bar{I}\bar{J}\bar{K}} - \bar{C}^{e-1}_{\bar{I}\bar{J}}\bar{p}^{\nabla\chi}_{\bar{K}}$$

$$\|\text{dev}(\bar{\boldsymbol{M}})\|_{\bar{K}} = \sqrt{\text{dev}\bar{M}_{\bar{I}\bar{J}\textcircled{\bar{K}}}\text{dev}\bar{M}_{\bar{I}\bar{J}\textcircled{\bar{K}}}}$$

$$\bar{p}^{\nabla\chi}_{\bar{K}} \overset{\text{def}}{=} \frac{1}{3}\bar{C}^{e}_{\bar{A}\bar{B}}\bar{M}_{\bar{A}\bar{B}\bar{K}}$$

$$\bar{G}^{\nabla\chi}_{\bar{K}(micro-grad)}(\bar{\mathbf{M}},\bar{\mathbf{c}}^{\nabla\chi}) \overset{\text{def}}{=} \|\text{dev}\bar{\mathbf{M}}\|_{\bar{K}} - \left(A^{\nabla\chi,\psi}\bar{c}^{\nabla\chi}_{\bar{K}} - B^{\nabla\chi,\psi}\bar{p}^{\nabla\chi}_{\bar{K}}\right) \tag{3.88}$$

where $\bar{\mathbf{c}}^{\nabla\chi}$ is the micro gradient cohesion, $\phi^{\nabla\chi}$ the micro gradient friction angle, $\psi^{\nabla\chi}$ the micro gradient dilation angle, and $-1 \leq \beta^{\nabla\chi} \leq 1$. These are the material parameters which define

the behavior of the material at the micro-gradient plasticity level. Note that the symbol $\bar{\odot}$ is used to show that the index is not a dummy index, thus there is summation only over the other indices. This is used to present the spatial gradient direction for the micro-gradient plasticity. The micro-gradient plasticity is dependent on the spatial gradient direction. Therefore, for each of the Cartesian coordinate directions in space, the yield and the plastic potential functions must be defined. The evolution equations for the micro-gradient plasticity can be written such that,

$$\bar{\Psi}^{e}_{\bar{L}\bar{D}}\bar{L}^{\chi,p}_{\bar{D}\bar{M},\bar{K}} - 2\bar{\Psi}^{e}_{\bar{L}\bar{D}}\text{skw}\left[\bar{L}^{\chi,p}_{\bar{D}\bar{C}}\bar{\Psi}^{e-1}_{\bar{C}\bar{F}}\bar{\Gamma}^{e}_{\bar{F}\bar{M}\bar{K}}\right] \overset{\text{def}}{=} \dot{\bar{\gamma}}^{\nabla\chi}_{\bar{I}}\frac{\partial\bar{G}^{\nabla\chi}_{\bar{I}(micro-grad)}}{\partial\bar{M}_{\bar{K}\bar{L}\bar{M}}} \tag{3.89}$$

$$\frac{\partial\bar{G}^{\nabla\chi}_{\bar{I}(micro-grad)}}{\partial\bar{M}_{\bar{K}\bar{L}\bar{M}}} = \frac{\text{dev}\bar{M}_{\bar{K}\bar{L}\bar{M}}}{\|\text{dev}\bar{\mathbf{M}}\|_{\bar{I}}} + \frac{1}{3}B^{\nabla\chi,\psi}\bar{C}^{e}_{\bar{K}\bar{L}}\delta_{\bar{I}\bar{M}}$$

$$\dot{\bar{Z}}^{\chi}_{,\bar{A}} \overset{\text{def}}{=} -\dot{\bar{\gamma}}^{\nabla\chi}_{\bar{I}}\frac{\partial\bar{G}^{\nabla\chi}_{\bar{I}}}{\partial\bar{c}^{\nabla\chi}_{\bar{A}}} = A^{\nabla\chi,\psi}(\dot{\bar{\gamma}}^{\nabla\chi}_{\bar{I}})\delta_{\bar{I}\bar{A}} \tag{3.90}$$

$$\bar{c}^{\nabla\chi}_{\bar{L}} = \bar{H}^{\nabla\chi}\bar{Z}^{\chi}_{,\bar{L}} \tag{3.91}$$

where $\dot{\bar{\gamma}}^{\nabla\chi}_{\bar{I}}$ is the micro plastic gradient multiplier vector. The plastic part of micro-deformation gradient $\chi^{p}_{\bar{N}A,\bar{M}}$ is solved by integrating in time the following equation, which is derived from (3.89) as,

$$\begin{aligned}\dot{\chi}^{p}_{\bar{N}A,\bar{M}} &= \dot{\bar{\gamma}}^{\nabla\chi}_{\bar{I}}\bar{\Psi}^{e-1}_{\bar{N}\bar{L}}\frac{\partial\bar{G}^{\nabla\chi}_{I(micro-grad)}}{\partial\bar{M}_{\bar{M}\bar{L}\bar{P}}}\chi^{p}_{\bar{P}A} + 2\text{skw}\left[\bar{L}^{\chi,p}_{\bar{N}\bar{C}}\Psi^{e-1}_{\bar{C}\bar{F}}\Gamma^{e}_{\bar{F}\bar{P}\bar{M}}\right]\chi^{p}_{\bar{P}A} \\ &+ \bar{L}^{\chi,p}_{\bar{N}\bar{L}}\chi^{p}_{\bar{L}A,\bar{M}} - \chi^{p}_{\bar{N}A,\bar{L}}\bar{L}^{p}_{\bar{L}\bar{M}}\end{aligned} \tag{3.92}$$

Integrating in time these evolution equations (3.73), (3.81), and (3.89), we are able to solve for $F^{p}_{\bar{I}I}$, $\chi^{p}_{\bar{I}I}$, and $\chi^{p}_{\bar{I}I,\bar{L}}$. Using the multiplicative decomposition of the deformation gradient and the micro-deformation tensor, $F^{e}_{\bar{I}I}$, $\chi^{e}_{\bar{I}I}$, and $\chi^{e}_{\bar{I}I,\bar{L}}$ can be solved to calculate the micromorphic stresses $\bar{\mathbf{S}}$, $\bar{\mathbf{\Sigma}}$, and $\bar{\mathbf{M}}$ and update the evolution equations.

3.5 Numerical Time Integration

In this research the evolution equations (3.73), (3.81), and (3.89) are integrated over time used the scheme proposed by Moran et al. [1990] called "semi-implicit method". This approach is used

to avoid the complexity of a full implicit method for the micromorphic plastic evolution equations in solving for the macro-plastic multiplier $\dot{\bar{\gamma}}$, the micro-plastic multiplier $\dot{\bar{\gamma}}^{\chi}$, and the micro-gradient plastic multiplier $\dot{\bar{\gamma}}^{\nabla\chi}$. The employed semi-implicit method maintains the frame indifference of the integrated constitutive equations. Note that this integration method is conditionally stable and therefore, there is a limitation on time steps to obtain stable results. The semi-implicit numerical time integration scheme for the finite strain micromorphic elastoplasticity can be written such that Given: $\boldsymbol{F}_{n+1}$, $\boldsymbol{\chi}_{n+1}$, $\bar{\boldsymbol{C}}^{e}_{n}$,$\bar{\boldsymbol{C}}^{\chi,e}_{n}$, $\bar{\boldsymbol{\Psi}}^{e}_{n}$, $\boldsymbol{F}^{p}_{n}$, $\boldsymbol{\chi}^{p}_{n}$, $\bar{Z}_n$, $\bar{Z}^{\chi}_{n}$, $\bar{c}_n$, $\bar{c}^{\chi}_{n}$

- Calculate trial values of macroscopic and microscopic yield functions $\bar{F}_{macro}$ and $\bar{F}^{\chi}_{micro}$

$$
\begin{aligned}
\boldsymbol{F}^{e(tr)} &= \boldsymbol{F}_{n+1}\boldsymbol{F}_{n}^{p-1} \\
\bar{\boldsymbol{C}}^{e(tr)} &= \boldsymbol{F}^{e(tr)T}\boldsymbol{F}^{e(tr)} \\
\bar{\boldsymbol{E}}^{e(tr)} &= \left(\bar{\boldsymbol{C}}^{e(tr)} - \bar{\boldsymbol{I}}\right)/2 \\
\bar{\boldsymbol{\chi}}^{e(tr)} &= \boldsymbol{\chi}_{n+1}\boldsymbol{\chi}_{n}^{p-1} \\
\bar{\boldsymbol{\Psi}}^{e(tr)} &= \boldsymbol{F}^{e(tr)T}\boldsymbol{\chi}^{e(tr)} \\
\bar{\boldsymbol{\mathcal{E}}}^{e(tr)} &= \bar{\boldsymbol{\Psi}}^{e(tr)} - \bar{\boldsymbol{I}} \\
\bar{\boldsymbol{S}}^{e(tr)} &= (\lambda+\tau)\left(tr\bar{\boldsymbol{E}}^{e(tr)}\right)\boldsymbol{I} + 2(\mu+\sigma)\,\bar{\boldsymbol{E}}^{eT(tr)} + \eta\left(tr\bar{\boldsymbol{\mathcal{E}}}^{e(tr)}\right)\boldsymbol{I} + \kappa\bar{\boldsymbol{\mathcal{E}}}^{e(tr)} + \nu\bar{\boldsymbol{\mathcal{E}}}^{eT(tr)} \\
\bar{\boldsymbol{\Sigma}}^{e(tr)} &= (\lambda+2\tau)\left(tr\bar{\boldsymbol{E}}^{e(tr)}\right)\boldsymbol{I} + 2(\mu+2\sigma)\,\boldsymbol{E}^{eT(tr)} + (2\eta-\tau)\left(tr\bar{\boldsymbol{\mathcal{E}}}^{e(tr)}\right)\boldsymbol{I} \\
&\quad +2(\kappa+\nu-\sigma)\,\mathrm{sym}\left(\bar{\boldsymbol{\mathcal{E}}}^{e(tr)}\right) \\
\bar{F}^{\chi,tr}_{micro} &= \bar{F}^{\chi}_{micro}\left(\bar{\boldsymbol{\Sigma}}^{e(tr)}, \bar{\boldsymbol{C}}^{\chi,e(tr)}, \bar{c}^{\chi}_{n}\right) \\
\bar{F}^{tr}_{macro} &= \bar{F}_{macro}\left(\bar{\boldsymbol{S}}^{e(tr)}, \bar{\boldsymbol{C}}^{e(tr)}, \bar{c}_n\right)
\end{aligned}
\tag{3.93}
$$

- Plasticity may occur in both the macroscopic and microscopic scales, where the plastic part of the micro-deformation tensor $\boldsymbol{\chi}^{p}_{n+1}$ and deformation gradient $\boldsymbol{F}^{p}_{n+1}$ can be solved such that,

$$\bar{\Psi}^{e}_{\bar{L}\bar{E}(n)}\dot{\chi}^{p}_{\bar{E}I}\chi^{p-1}_{I\bar{F}(n)}\bar{C}^{\chi,e-1}_{\bar{F}\bar{N}(n)}\bar{\Psi}^{e}_{\bar{K}\bar{N}(n)} = \dot{\bar{\gamma}}^{\chi}\left(\frac{\partial\bar{G}^{\chi}_{(micro)}}{\partial(\bar{\Sigma}^{n}_{\bar{K}\bar{L}})}\right)_{n} \tag{3.94}$$

$$\chi^{p}_{\bar{B}N(n+1)} = \chi^{p}_{\bar{B}N(n)} + \Delta\bar{\gamma}^{\chi}_{n+1}\bar{\Psi}^{e-1}_{\bar{B}\bar{P}(n)}\left(\frac{\partial\bar{G}^{\chi}_{(micro)}}{\partial\bar{\Sigma}_{\bar{O}\bar{P}}}\right)_{n}\Psi^{e-1}_{\bar{T}\bar{O}(n)}\bar{C}^{\chi,e}_{\bar{T}\bar{Q}(n)}\chi^{p}_{\bar{Q}N(n)} \tag{3.95}$$

$$\Delta t\bar{L}^{\chi,p}_{\bar{E}\bar{F}(n+1)} = \left(\chi^{p}_{\bar{E}I(n+1)} - \chi^{p}_{\bar{E}I(n)}\right)\chi^{p-1}_{I\bar{F}(n)}$$

$$\bar{C}^{e}_{\bar{L}\bar{B}(n)}\dot{\bar{F}}^{p}_{\bar{B}I}\bar{F}^{p-1}_{I\bar{K}(n)} - \bar{\Psi}^{e}_{\bar{L}\bar{E}(n)}\bar{L}^{\chi,p}_{\bar{E}\bar{F}(n+1)}\bar{C}^{\chi,e-1}_{\bar{F}\bar{N}(n)}\bar{\Psi}^{e}_{\bar{K}\bar{N}(n)} = \dot{\bar{\gamma}}\left(\frac{\partial\bar{G}_{(macro)}}{\partial\bar{S}_{\bar{K}\bar{L}}}\right)_{n}$$

$$\begin{aligned}F^{p}_{\bar{B}C(n+1)} = {} & F^{p}_{\bar{B}C(n)} + \Delta\bar{\gamma}_{n+1}\bar{C}^{e-1}_{\bar{B}\bar{L}(n)}\left(\frac{\partial\bar{G}_{(macro)}}{\partial\bar{S}_{\bar{K}\bar{L}}}\right)_{n}F^{p}_{\bar{K}C(n)} \\ & + \bar{C}^{e-1}_{\bar{B}\bar{L}(n)}\bar{\Psi}^{e}_{\bar{L}\bar{E}(n)}\Delta t\bar{L}^{\chi,p}_{\bar{E}\bar{F}(n+1)}C^{\chi,e-1}_{\bar{F}\bar{N}(n)}\bar{\Psi}^{e}_{\bar{K}\bar{N}(n)}F^{p}_{\bar{K}C(n)}\end{aligned} \tag{3.96}$$

$$\Delta t\bar{L}^{p}_{\bar{E}\bar{F}(n+1)} = \left(F^{p}_{\bar{E}I(n+1)} - F^{p}_{\bar{E}I(n)}\right)F^{p-1}_{I\bar{F}(n)}$$

- Update elastic deformation

$$\begin{aligned}\boldsymbol{F}^{e}_{n+1} &= \boldsymbol{F}_{n+1}\boldsymbol{F}^{p-1}_{n+1} \\ \bar{\boldsymbol{C}}^{e}_{n+1} &= \boldsymbol{F}^{eT}_{n+1}\boldsymbol{F}^{e}_{n+1} \\ \bar{\boldsymbol{E}}^{e}_{n+1} &= \left(\bar{\boldsymbol{C}}^{e}_{n+1} - \boldsymbol{I}\right)/2 \\ \boldsymbol{\chi}^{e}_{n+1} &= \boldsymbol{\chi}_{n+1}\boldsymbol{\chi}^{p-1}_{n+1} \\ \bar{\boldsymbol{\Psi}}^{e}_{n+1} &= \boldsymbol{F}^{eT}_{n+1}\boldsymbol{\chi}^{e}_{n+1} \\ \bar{\boldsymbol{\mathcal{E}}}^{e}_{n+1} &= \bar{\boldsymbol{\Psi}}^{e}_{n+1} - \boldsymbol{I}\end{aligned} \tag{3.97}$$

- Update the second Piola Kirchhoff $\bar{\boldsymbol{S}}$ and the micro-stress $\bar{\boldsymbol{\Sigma}}$

$$\begin{aligned}\bar{\boldsymbol{S}}^{e} = {} & (\lambda+\tau)\left(tr\bar{\boldsymbol{E}}^{e}_{n+1}\right)\boldsymbol{I} + 2\left(\mu+\sigma\right)\bar{\boldsymbol{E}}^{eT}_{n+1} + \eta\left(tr\bar{\boldsymbol{\mathcal{E}}}^{e}_{n+1}\right)\boldsymbol{I} \\ & + \kappa\bar{\boldsymbol{\mathcal{E}}}^{e}_{n+1} + \nu\bar{\boldsymbol{\mathcal{E}}}^{eT}_{n+1}\end{aligned} \tag{3.98}$$

$$\begin{aligned}\bar{\boldsymbol{\Sigma}}^{e}_{n+1} = {} & (\lambda+2\tau)\left(tr\bar{\boldsymbol{E}}^{e}_{n+1}\right)\boldsymbol{I} + 2\left(\mu+2\sigma\right)\bar{\boldsymbol{E}}^{eT}_{n+1} + (2\eta-\tau)\left(tr\bar{\boldsymbol{\mathcal{E}}}^{e}_{n+1}\right)\boldsymbol{I} \\ & + 2\left(\kappa+\nu-\sigma\right)\mathrm{sym}\left(\bar{\boldsymbol{\mathcal{E}}}^{e}_{n+1}\right)\end{aligned}$$

- Internal state variables update

$$\bar{Z}_{n+1} = \bar{Z}_n + \Delta\bar{\gamma}_{n+1}$$

$$\bar{c}_{n+1} = \bar{H}\bar{Z}_{n+1} \tag{3.99}$$

$$\bar{Z}^{\chi}_{n+1} = \bar{Z}^{\chi}_n + \Delta\bar{\gamma}^{\chi}_{n+1}$$

$$\bar{c}^{\chi}_{n+1} = \bar{H}^{\chi}\bar{Z}^{\chi}_{n+1} \tag{3.100}$$

$$\tag{3.101}$$

Micro-gradient plasticity:

Given: $\boldsymbol{\nabla}_0\boldsymbol{\chi}_{n+1}$, $\boldsymbol{F}^e_{n+1}$, $\boldsymbol{\chi}^e_{n+1}$, $\bar{\boldsymbol{C}}^e_{n+1}$, $\bar{\boldsymbol{C}}^{\chi,e}_{n+1}$, $\bar{\boldsymbol{\Psi}}^e_{n+1}$, $\boldsymbol{F}^p_{n+1}$, $\boldsymbol{\chi}^p_{n+1}$, $\bar{\boldsymbol{\nabla}}\bar{Z}^{\nabla\chi}_n$, $\bar{Z}^{\chi}_n$, $\bar{c}_n$, $\bar{c}^{\chi}_n$

- Calculating trial values for micro-gradient plasticity

$$\begin{aligned}
\chi^{e(tr)}_{k\bar{L},\bar{M}} &= \chi_{kK,L(n+1)}F^{p-1}_{L\bar{M}(n)}\chi^{p-1}_{K\bar{L}(n)} - \chi^{e(tr)}_{k\bar{N}}\chi^{p}_{\bar{N}A,\bar{M}(n)}\chi^{p-1}_{A\bar{L}(n)} \\
\bar{\Gamma}^{e(tr)}_{\bar{K}\bar{L}\bar{M}} &= F^e_{k\bar{K}}\chi^{e(tr)}_{k\bar{L},\bar{M}} \\
\bar{M}^{e(tr)}_{\bar{Q}\bar{P}\bar{N}} &= \bar{C}_{\bar{Q}\bar{P}\bar{N}\bar{K}\bar{L}\bar{M}}\Gamma^{e(tr)}_{\bar{K}\bar{L}\bar{M}} \\
\bar{\boldsymbol{F}}^{\nabla\chi,(tr)}_{\bar{I}} &= \bar{\boldsymbol{F}}^{\nabla\chi}_{\bar{I}}\left(\bar{\boldsymbol{M}}^{(tr)}, \bar{c}^{\nabla\chi}_{\bar{I}(n)}\right)
\end{aligned} \tag{3.102}$$

- Numerical time integration of micro-gradient plastic evolution

$$\begin{aligned}
&\bar{\Psi}^e_{\bar{L}\bar{D}(n)}\left(\dot{\chi}^p_{\bar{D}B,\bar{K}} - \bar{L}^{\chi,p}_{\bar{D}\bar{B}(n+1)}\chi^p_{\bar{B}B,\bar{K}(n)}\right)\chi^{p-1}_{B\bar{M}(n)} - 2\bar{\Psi}^e_{\bar{L}\bar{D}(n)}\mathrm{skw}\left[\bar{L}^{\chi,p}_{\bar{D}\bar{C}(n+1)}\bar{\Psi}^{e-1}_{\bar{C}\bar{F}(n)}\bar{\Gamma}^e_{\bar{F}\bar{M}\bar{K}(n)}\right] \\
&\qquad = \dot{\bar{\gamma}}^{\nabla\chi}_{\bar{I}}\left(\frac{\partial\bar{G}^{\nabla\chi}_{\bar{I}(micro-grad)}}{\partial\bar{M}_{\bar{K}\bar{L}\bar{M}}}\right)_n \\
&\chi^p_{\bar{N}A,\bar{M}(n+1)} = \chi^p_{\bar{N}A,\bar{M}(n)} + \Delta\bar{\gamma}^{\nabla\chi}_{\bar{I}(n+1)}\bar{\Psi}^{e-1}_{\bar{N}\bar{L}(n)}\left(\frac{\partial\bar{G}^{\nabla\chi}_{I(micro-grad)}}{\partial\bar{M}_{\bar{M}\bar{L}\bar{P}}}\right)_n\chi^p_{\bar{P}A(n)} \\
&\qquad +2\mathrm{skw}\left[\Delta t\bar{L}^{\chi,p}_{\bar{N}\bar{C}(n+1)}\Psi^{e-1}_{\bar{C}\bar{F}(n)}\Gamma^e_{\bar{F}\bar{P}\bar{M}(n)}\right]\chi^p_{\bar{P}A(n)} \\
&\qquad +\Delta t\bar{L}^{\chi,p}_{\bar{N}\bar{L}(n+1)}\chi^p_{\bar{L}A,\bar{M}(n)} - \chi^p_{\bar{N}A,\bar{L}(n)}\Delta t\bar{L}^p_{\bar{L}\bar{M}(n+1)}
\end{aligned} \tag{3.103}$$

$$\chi^e_{k\bar{M},\bar{L}(n+1)} = \chi_{kK,L(n+1)}F^{p-1}_{L\bar{M}(n)}\chi^{p-1}_{K\bar{L}(n)} - \chi^e_{k\bar{N}(n+1)}\chi^p_{\bar{N}A,\bar{M}(n+1)}\chi^{p-1}_{A\bar{L}(n+1)} \tag{3.104}$$

- Updating couple stress

$$\Gamma^{e}_{\bar{K}\bar{L}\bar{M}(n+1)} = F^{e}_{k\bar{K}(n+1)}\chi^{e}_{k\bar{L},\bar{M}(n+1)} \tag{3.105}$$

$$\bar{M}_{\bar{Q}\bar{P}\bar{N}(n+1)} = \bar{C}_{\bar{Q}\bar{P}\bar{N}\bar{K}\bar{L}\bar{M}}\Gamma^{e}_{\bar{K}\bar{L}\bar{M}(n+1)} \tag{3.106}$$

- Updating internal state variables of micro-gradient plasticity

$$\begin{aligned}\bar{Z}^{\nabla\chi}_{\bar{I}(n+1)} &= \bar{Z}^{\nabla\chi}_{\bar{I}(n)} + \Delta\bar{\gamma}^{\nabla\chi}_{\bar{I}(n+1)} \\ \bar{c}^{\nabla\chi}_{\bar{I}(n+1)} &= \bar{H}^{\nabla\chi}\bar{Z}^{\nabla\chi}_{\bar{I}(n+1)}\end{aligned} \tag{3.107}$$

3.5.1 Finite Element Formulation for Micromorphic Elastoplasticity in the Intermediate Configuration

For the finite element formulation, the coupled strong form (S) of the micromorphic balance of momenta in the current configuration are presented such that,

$$(S)\begin{cases} \text{Find } u_k(\boldsymbol{x},t) : \hat{\mathcal{B}} \times [0, t_{\text{final}}] \mapsto \mathbb{R}^3, \quad \text{and} \quad \phi_{kK}(\boldsymbol{x},t) : \hat{\mathcal{B}} \times [0, t_{\text{final}}] \mapsto \mathbb{R}^9, \text{such that} \\ \sigma_{lk,l} + \rho(f_k - \ddot{u}_k) = 0 \in \mathcal{B} \\ u_k(t) = g^u_k(t) \text{ on } \Gamma^u_g \\ \sigma_{lk}n_l(t) = t^\sigma_k(t) \text{ on } \Gamma_t \\ u_k(\boldsymbol{x},0) = u_{k0}(\boldsymbol{x}) \in \mathcal{B} \\ \sigma_{mk} - s_{mk} + m_{lkm,l} + \rho(\ell_{km} - \omega_{km}) = 0 \in \mathcal{B} \\ \phi_{kl}(t) = g^\phi_{kl}(t) \text{ on } \Gamma^\phi_g \\ m_{klm}n_k(t) = \mathcal{M}_{lm}(t) \text{ on } \Gamma_{\mathcal{M}} \\ \phi_{kl}(\boldsymbol{x},0) = \phi_{kl0}(\boldsymbol{x}) \in \mathcal{B} \end{cases} \tag{3.108}$$

where $\hat{\mathcal{B}} = \mathcal{B} \cup \Gamma$, and $\Gamma = \Gamma_g \cup \Gamma_t = \Gamma_G \cup \Gamma_{\mathcal{M}}$. The finite element formulation will be presented in the intermediate configuration for a Total Lagrangian implementation of the micromorphic elastoplasticity. Through the weighted residual method and integration by parts, the balance of linear

momentum in the current configuration can be expressed as,

$$\int_{\mathcal{B}} w_k \left[\sigma_{lk,l} + \rho\left(f_k - \ddot{u}_k\right)\right] dv_\beta = \int_{\partial\mathcal{B}} w_k \sigma_{lk} n_l da - \int_{\mathcal{B}} \left[w_{k,l}\sigma_{lk} + w_k \rho\left(f_k - \ddot{u}_k\right)\right] dv_\beta = 0 \tag{3.109}$$

Applying the Piola transforms and mapping $\bar{P}_{l\bar{L}} = J^e \sigma_{lk} F^{e-1}_{\bar{L}k}$ and $\sigma_{lk} = \dfrac{1}{J^e} F^e_{l\bar{L}} \bar{S}_{\bar{L}\bar{K}} F^e_{k\bar{K}}$, and Nanson's formula to relate area change $n_l da_\beta = J^e F^{e-1}_{\bar{K}l} \bar{N}_{\bar{K}} d\bar{A}_\beta$, the variational form of the balance of linear momentum can be written as,

$$\int_{\partial\bar{\mathcal{B}}} w_k (\bar{P}_{k\bar{K}} \bar{N}_{\bar{K}}) d\bar{A}_\beta - \int_{\bar{\mathcal{B}}} \left[w_{k,l} (F^e_{l\bar{L}} \bar{S}_{\bar{L}\bar{K}} F^e_{k\bar{K}}) + w_k \bar{\rho}\left(f_k - \ddot{u}_k\right)\right] d\bar{V}_\beta = 0 \tag{3.110}$$

Similarly, the variational form of the balance of first moment of momentum in the current configuration is such that,

$$\int_{\mathcal{B}} \eta_{ml} \left[\sigma_{ml} - s_{ml} + m_{lkm,l} + \rho\left(\lambda_{lm} - \omega_{lm}\right)\right] dv_\beta = 0 \tag{3.111}$$

Using the mapping (3.19)-(3.21) to the intermediate configuration, the variational form of the balance of first moment of momentum in the intermediate configuration is such that,

$$\begin{aligned} &\int_{\bar{\mathcal{B}}} \eta_{ml} \left[F^e_{m\bar{M}} \bar{S}_{\bar{M}\bar{L}} F^e_{l\bar{L}} - F^e_{m\bar{M}} \bar{\Sigma}_{\bar{M}\bar{L}} F^e_{l\bar{L}} + \bar{\rho}\left(\lambda_{lm} - \omega_{lm}\right)\right] d\bar{V}_\beta \\ &- \int_{\bar{\mathcal{B}}} \eta_{ml,k} F^e_{k\bar{K}} F_{l\bar{L}} \bar{M}_{\bar{K}\bar{L}\bar{M}} \chi^e_{m\bar{M}} d\bar{V}_\beta + \int_{\bar{\Gamma}_{\hat{\bar{\mathcal{M}}}}} \eta_{ml} \hat{\bar{\mathcal{M}}}_{lm} d\bar{A}_\beta = 0 \end{aligned} \tag{3.112}$$

where the couple traction term $\hat{\bar{\mathcal{M}}}_{lm} = m_{klm} J^e F^{e-1}_{\bar{K}k} \bar{N}_{\bar{K}} = \hat{\bar{M}}_{lm\bar{K}} \bar{N}_{\bar{K}}$. The coupled weak form for micromorphic elastoplastic-dynamics in $\bar{\mathcal{B}}$ can be stated as

$$
(W)\begin{cases}
\text{Find } u_k(\boldsymbol{X},t)\in\mathscr{S}^u \text{ and } \Phi_{kK}(\boldsymbol{X},t)\in\mathscr{S}^\Phi \text{ such that}\\
\quad \int_{\bar{\mathcal{B}}}\left[w_{k,l}(F^e_{l\bar{L}}\bar{S}_{\bar{L}\bar{K}}F^e_{k\bar{K}})+w_k\bar{\rho}f_k\right]d\bar{V}_\beta-\int_{\bar{\Gamma}_T}w_k(\bar{T}^P_{\bar{K}})d\bar{A}_\beta-\int_{\bar{\mathcal{B}}}w_k\bar{\rho}\ddot{u}_k d\bar{V}_\beta=0\\
\quad \int_{\bar{\mathcal{B}}}\eta_{ml}\left[F^e_{m\bar{M}}(\bar{S}_{\bar{M}\bar{L}}-\bar{\Sigma}_{\bar{M}\bar{L}})F^e_{l\bar{L}}+\bar{\rho}\lambda_{lm}\right]d\bar{V}_\beta\\
\quad -\int_{\bar{\mathcal{B}}}(\eta_{ml,k})\left[F^e_{k\bar{K}}F^e_{l\bar{L}}\bar{M}_{\bar{K}\bar{L}\bar{M}}\chi^e_{m\bar{M}}\right]d\bar{V}_\beta+\int_{\bar{\Gamma}_{\hat{\mathcal{M}}}}\eta_{ml}\hat{\bar{\mathcal{M}}}_{lm}d\bar{A}_\beta-\int_{\bar{\mathcal{B}}}(\eta_{ml,k})\bar{\rho}\omega_{lm}d\bar{V}_\beta=0\\
\text{holds } \forall w_k(\boldsymbol{X})\in\mathscr{V}^u \text{ and } \eta_{ml}(\boldsymbol{X})\in\mathscr{V}^\Phi\\
\mathscr{S}^u=\{u_k:\mathcal{B}_0\times[0,t_{\text{final}}]\mapsto\mathbb{R}^3, u_k\in H^1, u_k(\boldsymbol{X},t)=g^u_k(t)\,\text{on}\,\Gamma^u_g, u_k(\boldsymbol{X},0)=u_{k0}(\boldsymbol{X})\}\\
\mathscr{S}^\Phi=\{\Phi_{kK}:\mathcal{B}_0\times[0,t_{\text{final}}]\mapsto\mathbb{R}^9, \Phi_{kK}\in H^1, \Phi_{kK}(\boldsymbol{X},t)=G^\Phi_{kK}(t)\,\text{on}\,\Gamma^\Phi_G, \Phi_{kK}(\boldsymbol{X},0)=\Phi_{k0}(\boldsymbol{X})\}\\
\mathscr{V}^u=\{w_k:\mathcal{B}_0\mapsto\mathbb{R}^3, w_k\in H^1, w_k=0\,\text{on}\,\Gamma^u_g\}\\
\mathscr{V}^\Phi=\{\eta_{ml}:\mathcal{B}_0\mapsto\mathbb{R}^9, \eta_{ml}\in H^1, \eta_{ml}=0\,\text{on}\,\Gamma^\Phi_G\}
\end{cases}
\tag{3.113}
$$

Ignoring the boundary traction ($\bar{T}^P_{\bar{K}}$), the body force ($\bar{\rho}f_k$), and the body force couple ($\bar{\rho}\lambda_{lm}$), and boundary traction couple terms ($\hat{\bar{\mathcal{M}}}$), we arrive at the following equations,

$$
\mathcal{G} = \int_{\bar{\mathcal{B}}}w_{k,l}(F^e_{l\bar{L}}\bar{S}_{\bar{L}\bar{K}}F^e_{k\bar{K}})d\bar{V}_\beta+\int_{\bar{\mathcal{B}}}w_k\bar{\rho}\ddot{u}_k d\bar{V}_\beta=0 \tag{3.114}
$$

$$
\begin{aligned}
\mathcal{H} &= \int_{\bar{\mathcal{B}}}\eta_{ml}F^e_{m\bar{M}}\left(\bar{\Sigma}_{\bar{M}\bar{L}}-\bar{S}_{\bar{M}\bar{L}}\right)F^e_{l\bar{L}}d\bar{V}_\beta+\int_{\bar{\mathcal{B}}}\eta_{ml,k}F^e_{k\bar{K}}F^e_{l\bar{L}}\bar{M}_{\bar{K}\bar{L}\bar{M}}\chi^e_{m\bar{M}}d\bar{V}_\beta\\
&+ \int_{\bar{\mathcal{B}}}\eta_{ml}\bar{\rho}\omega_{lm}d\bar{V}_\beta=0
\end{aligned}
\tag{3.115}
$$

The linearization can be written as,

$$
\mathcal{L}\mathcal{G}=\mathcal{G}+\delta\mathcal{G}=0\ ,\ \mathcal{L}\mathcal{H}=\mathcal{H}+\delta\mathcal{H}=0 \tag{3.116}
$$

where $\delta(\bullet)$ is the incremental operator with respect to the linearization procedure. Note that the superscript $(n+1)$ is dropped from the formulations but is implied. The variational formulation of the elastic and plastic part of the micromorphic deformations are derived such that,

$$\delta\chi^{p}_{\bar{B}N} = \delta(\Delta\bar{\gamma})^{\chi}\bar{\Psi}^{e-1(n)}_{\bar{B}\bar{P}}\left(\frac{\partial\bar{G}^{\chi}_{(micro)}}{\partial\bar{\Sigma}_{\bar{O}\bar{P}}}\right)^{(n)}\Psi^{e-1(n)}_{\bar{T}\bar{O}}\bar{C}^{\chi,e(n)}_{\bar{T}\bar{Q}}\chi^{p(n)}_{\bar{Q}N} \tag{3.117}$$

$$\delta\chi^{p-1}_{N\bar{B}} = -\chi^{p-1}_{N\bar{P}}\left[\delta\chi^{p}_{\bar{P}J}\right]\chi^{p-1}_{J\bar{P}} \tag{3.118}$$

$$\delta\left[\Delta\bar{L}^{\chi,p}_{\bar{E}\bar{F}}\right] = \chi^{p(n)}_{\bar{E}A}\chi^{p-1}_{A\bar{B}}\left[\delta\chi^{p}_{\bar{B}N}\right]\chi^{p-1}_{N\bar{F}} \tag{3.119}$$

$$\begin{aligned}\delta F^{p}_{\bar{B}C} &= \delta(\Delta\bar{\gamma})\bar{C}^{e-1(n)}_{\bar{B}\bar{L}}\left(\frac{\partial\bar{G}_{(macro)}}{\partial\bar{S}_{\bar{K}\bar{L}}}\right)^{(n)}F^{p(n)}_{\bar{K}C}\\ &+ \bar{C}^{e-1(n)}_{\bar{B}\bar{L}}\bar{\Psi}^{e(n)}_{\bar{L}\bar{E}}\delta\left[\bar{L}^{\chi,p}_{\bar{E}\bar{F}}\right]C^{\chi,e-1(n)}_{\bar{F}\bar{N}}\bar{\Psi}^{e(n)}_{\bar{K}\bar{N}}F^{p(n)}_{\bar{K}C}\end{aligned} \tag{3.120}$$

$$\delta F^{p-1}_{N\bar{B}} = -F^{p-1}_{N\bar{P}}\delta F^{p}_{\bar{P}J}F^{p-1}_{J\bar{P}} \tag{3.121}$$

$$\delta\left[\Delta\bar{L}^{p}_{\bar{E}\bar{F}}\right] = F^{p(n)}_{\bar{E}A}F^{p-1}_{A\bar{B}}\delta F^{p}_{\bar{B}N}F^{p-1}_{N\bar{F}} \tag{3.122}$$

$$\begin{aligned}\delta\chi^{p}_{\bar{N}A,\bar{M}} &= \left(\delta\Delta\bar{\gamma}^{\nabla\chi}_{\bar{I}}\right)\bar{\Psi}^{e-1(n)}_{\bar{N}\bar{L}}\left(\frac{\partial\bar{G}^{\nabla\chi}_{I(micro-grad)}}{\partial\bar{M}_{\bar{M}\bar{L}\bar{P}}}\right)^{(n)}\chi^{p(n)}_{\bar{P}A}\\ &+ 2\mathrm{skw}\left[\left(\delta\Delta\bar{L}^{\chi,p}_{\bar{N}\bar{C}}\right)\Psi^{e-1(n)}_{\bar{C}\bar{F}}\Gamma^{e(n)}_{\bar{F}\bar{P}\bar{M}}\right]\chi^{p(n)}_{\bar{P}A}\\ &+ \left[\delta\Delta\bar{L}^{\chi,p}_{\bar{N}\bar{L}}\right]\chi^{p(n)}_{\bar{L}A,\bar{M}} - \chi^{p(n)}_{\bar{N}A,\bar{L}}\left[\delta\Delta\bar{L}^{p}_{\bar{L}\bar{M}}\right]\end{aligned} \tag{3.123}$$

$$\delta F^{e}_{i\bar{I}} = \left(\delta u_i\right)_{,I}F^{p-1}_{I\bar{I}} - F^{e}_{i\bar{P}}\left(\delta F^{p}_{\bar{P}J}\right)F^{p-1}_{J\bar{I}} \tag{3.124}$$

$$\delta\chi^{e}_{i\bar{I}} = \left(\delta\Phi_{i\bar{I}}\right)\chi^{p-1}_{I\bar{I}} - \chi^{e}_{i\bar{P}}\left(\delta\chi^{p}_{\bar{P}J}\right)\chi^{p-1}_{J\bar{I}} \tag{3.125}$$

$$\delta\chi_{lK} = \delta\Phi_{lK} \tag{3.126}$$

$$\delta\left(w_{k,l}\right) = -w_{k,a}(\delta F_{aA})F^{-1}_{Al} \tag{3.127}$$

$$\begin{aligned}\delta\chi^{e}_{k\bar{L},\bar{M}} &= \left(\delta\Phi_{kB,L}F^{p-1}_{L\bar{M}} - \chi^{e}_{k\bar{R}}\chi^{p}_{\bar{R}B,L}F^{p-1}_{L\bar{M}}\right)\chi^{p-1}_{B\bar{L}} &(3.128)\\ &+ \left(\chi_{kB,L}\delta F^{p-1}_{L\bar{M}} - \chi^{e}_{k\bar{R}}\chi^{p}_{\bar{R}B,L}F^{p-1}_{L\bar{M}}\right)\chi^{p-1}_{B\bar{L}} &(3.129)\\ &+ \left(\chi_{kB,L}F^{p-1}_{L\bar{M}} - \delta\chi^{e}_{k\bar{R}}\chi^{p}_{\bar{R}B,L}F^{p-1}_{L\bar{M}}\right)\chi^{p-1}_{B\bar{L}} &(3.130)\\ &+ \left(\chi_{kB,L}F^{p-1}_{L\bar{M}} - \chi^{e}_{k\bar{R}}\delta\chi^{p}_{\bar{R}B,L}F^{p-1}_{L\bar{M}}\right)\chi^{p-1}_{B\bar{L}} &(3.131)\\ &+ \left(\chi_{kB,L}F^{p-1}_{L\bar{M}} - \chi^{e}_{k\bar{R}}\chi^{p}_{\bar{R}B,L}\delta F^{p-1}_{L\bar{M}}\right)\chi^{p-1}_{B\bar{L}} &(3.132)\\ &+ \left(\chi_{kB,L}F^{p-1}_{L\bar{M}} - \chi^{e}_{k\bar{R}}\chi^{p}_{\bar{R}B,L}F^{p-1}_{L\bar{M}}\right)\delta\chi^{p-1}_{B\bar{L}} &(3.133)\end{aligned}$$

The linearization of the micromorphic strains and stresses are written such that,

$$\delta\bar{E}^e_{\bar{L}\bar{K}} = \frac{1}{2}\left[(\delta F^e_{i\bar{L}})F^e_{i\bar{K}} + F^e_{i\bar{L}}(\delta F^e_{i\bar{K}})\right] \tag{3.134}$$

$$\delta\bar{\mathcal{E}}^e_{\bar{L}\bar{K}} = \left[(\delta F^e_{i\bar{L}})\chi^e_{i\bar{K}} + F^e_{i\bar{L}}(\delta\chi^e_{i\bar{K}})\right] \tag{3.135}$$

$$\delta\bar{\Gamma}^e_{\bar{K}\bar{L}\bar{M}} = \delta F^e_{k\bar{K}}\chi^e_{k\bar{L},\bar{M}} + F^e_{k\bar{K}}\delta\chi^e_{k\bar{L},\bar{M}} \tag{3.136}$$

$$\begin{aligned}\delta\bar{S}_{\bar{K}\bar{L}} &= (\lambda+\tau)\,(\delta\bar{E}^e_{\bar{M}\bar{M}})\delta_{\bar{K}\bar{L}} + 2\,(\mu+\sigma)\,(\delta\bar{E}^e_{\bar{K}\bar{L}}) \\ &+ \eta(\delta\bar{\mathcal{E}}^e_{\bar{M}\bar{M}})\delta_{\bar{K}\bar{L}} + \kappa(\delta\bar{\mathcal{E}}^e_{\bar{K}\bar{L}}) + \nu(\delta\bar{\mathcal{E}}^e_{\bar{L}\bar{K}})\end{aligned} \tag{3.137}$$

$$\begin{aligned}\delta\bar{\Sigma}_{\bar{K}\bar{L}} &= (\lambda+2\tau)\,(\delta\bar{E}^e_{\bar{M}\bar{M}})\delta_{\bar{K}\bar{L}} + 2\,(\mu+2\sigma)\,(\delta\bar{E}^e_{\bar{L}\bar{K}}) \\ &+ (2\eta-\tau)(\delta\bar{\mathcal{E}}^e_{\bar{M}\bar{M}})\delta_{\bar{K}\bar{L}} + 2(\kappa+\nu-\sigma)\mathrm{sym}(\delta\bar{\mathcal{E}}^e_{\bar{K}\bar{L}})\end{aligned} \tag{3.138}$$

$$\delta\bar{M}_{\bar{K}\bar{L}\bar{M}} = \bar{C}_{\bar{K}\bar{L}\bar{M}\bar{N}\bar{P}\bar{Q}}\delta\bar{\Gamma}^e_{\bar{N}\bar{P}\bar{Q}} \tag{3.139}$$

Using the linearized formulations of the micromorphic deformation and stresses tensors, the linearized formulation of the balance of linear momentum can be expressed as follows,

$$\begin{aligned}\delta\mathcal{G} &= \int_{\bar{\mathcal{B}}}\delta\left(w_{k,l}\right)\left(F^e_{l\bar{L}}\bar{S}_{\bar{L}\bar{K}}F^e_{k\bar{K}}\right)d\bar{V}_\beta + \int_{\bar{\mathcal{B}}} w_{k,l}\left(\delta F^e_{l\bar{L}}\right)\bar{S}_{\bar{L}\bar{K}}F^e_{k\bar{K}}d\bar{V}_\beta \\ &+ \int_{\bar{\mathcal{B}}} w_{k,l}F^e_{l\bar{L}}\left(\delta\bar{S}_{\bar{L}\bar{K}}\right)F^e_{k\bar{K}}d\bar{V}_\beta + \int_{\bar{\mathcal{B}}} w_{k,l}F^e_{l\bar{L}}\bar{S}_{\bar{L}\bar{K}}\left(\delta F^e_{k\bar{K}}\right)d\bar{V}_\beta \\ &+ \int_{\bar{\mathcal{B}}} w_k\bar{\rho}\left(\delta\ddot{u}_k\right)d\bar{V}_\beta\end{aligned} \tag{3.140}$$

and for the balance of first moment of momentum we have,

$$\begin{aligned}\delta\mathcal{H} &= \int_{\bar{\mathcal{B}}}\eta_{ml}\left(\delta F^e_{m\bar{M}}\right)\left(\bar{\Sigma}_{\bar{M}\bar{L}} - \bar{S}_{\bar{M}\bar{L}}\right)F^e_{l\bar{L}}d\bar{V}_\beta + \int_{\bar{\mathcal{B}}}\eta_{ml}F^e_{m\bar{M}}\delta\left(\bar{\Sigma}_{\bar{M}\bar{L}} - \bar{S}_{\bar{M}\bar{L}}\right)F^e_{l\bar{L}}d\bar{V}_\beta \\ &+ \int_{\bar{\mathcal{B}}}\eta_{ml}F^e_{m\bar{M}}\left(\bar{\Sigma}_{\bar{M}\bar{L}} - \bar{S}_{\bar{M}\bar{L}}\right)\left(\delta F^e_{l\bar{L}}\right)d\bar{V}_\beta + \int_{\bar{\mathcal{B}}}\delta(\eta_{ml,k})F^e_{k\bar{K}}F^e_{l\bar{L}}M_{\bar{K}\bar{L}\bar{M}}\chi^e_{m\bar{M}}d\bar{V}_\beta \\ &+ \int_{\bar{\mathcal{B}}}\eta_{ml,k}\left(\delta F^e_{k\bar{K}}\right)F^e_{l\bar{L}}\bar{M}_{\bar{K}\bar{L}\bar{M}}\chi^e_{m\bar{M}}d\bar{V}_\beta + \int_{\bar{\mathcal{B}}}\eta_{ml,k}F^e_{k\bar{K}}\left(\delta F^e_{l\bar{L}}\right)\bar{M}_{\bar{K}\bar{L}\bar{M}}\chi^e_{m\bar{M}}d\bar{V}_\beta \\ &+ \int_{\bar{\mathcal{B}}}\eta_{ml,k}F^e_{k\bar{K}}F^e_{l\bar{L}}\delta\left(\bar{M}_{\bar{K}\bar{L}\bar{M}}\right)\chi^e_{m\bar{M}}d\bar{V}_\beta + \int_{\bar{\mathcal{B}}}\eta_{ml,k}F^e_{k\bar{K}}F^e_{l\bar{L}}\bar{M}_{\bar{K}\bar{L}\bar{M}}\left(\delta\chi^e_{m\bar{M}}\right)d\bar{V}_\beta \\ &+ \int_{\bar{\mathcal{B}}}\eta_{ml}\left(\delta\ddot{\chi}_{lK}\right)\chi^e_{m\bar{L}}\bar{\rho}\bar{I}_{\bar{K}\bar{L}(\beta)}d\bar{V}_\beta + \int_{\bar{\mathcal{B}}}\eta_{ml}\ddot{\chi}_{lK}\left(\delta\chi^e_{m\bar{L}}\right)\bar{\rho}\bar{I}_{\bar{K}\bar{L}(\beta)}d\bar{V}_\beta \\ &+ \int_{\bar{\mathcal{B}}}\eta_{ml}\ddot{\chi}_{lK}\chi^e_{m\bar{L}}\delta\left(\bar{\rho}\bar{I}_{\bar{K}\bar{L}(\beta)}\right)d\bar{V}_\beta\end{aligned} \tag{3.141}$$

The micro-inertia term $\bar{I}_{\bar{K}\bar{L}(\beta)}$ in the intermediate configuration is defined as follows,

$$\bar{\rho}\bar{I}_{\bar{K}\bar{L}(\beta)}d\bar{V}_\beta \overset{\text{def}}{=} \int_{d\bar{V}_\beta} \bar{\rho}^{(\alpha)}\bar{\Xi}^{(\alpha)}_{\bar{K}}\bar{\Xi}^{(\alpha)}_{\bar{L}}d\bar{V}^{(\alpha)} \tag{3.142}$$

where the plastically deformed relative position vector in the intermediate configuration is written as follows,

$$\bar{\Xi}^{(\alpha)}_{\bar{K}} = \chi^p_{\bar{K}K}\Xi^{(\alpha)}_K \tag{3.143}$$

Moment of micro-inertia in the reference configuration $\boldsymbol{I}_\beta$ is related to moment of micro-inertia in the intermediate configuration $\bar{\boldsymbol{I}}_\beta$ as follows,

$$\begin{aligned}
\bar{\rho}_\beta\bar{I}_{\bar{K}\bar{L}(\beta)}d\bar{V}_\beta &\overset{\text{def}}{=} \int_{d\bar{V}_\beta} \bar{\rho}^{(\alpha)}\bar{\Xi}^{(\alpha)}_{\bar{K}}\bar{\Xi}^{(\alpha)}_{\bar{L}}d\bar{V}^{(\alpha)} &(3.144)\\
&= \chi^p_{\bar{K}K}\chi^p_{\bar{L}L}\int_{d\bar{V}_\beta} \bar{\rho}^{(\alpha)}\Xi^{(\alpha)}_K\Xi^{(\alpha)}_L d\bar{V}^{(\alpha)}\\
&= \chi^p_{\bar{K}K}\chi^p_{\bar{L}L}\rho_{0(\beta)}\Xi^{(\alpha)}_K\Xi^{(\alpha)}_L dV_\beta = \chi^p_{\bar{K}K}\chi^p_{\bar{L}L}\rho_{0(\beta)}I_{KL(\beta)}dV_\beta\\
&\implies I_{KL(\beta)} = \chi^{p-1}_{K\bar{K}}\chi^{p-1}_{L\bar{L}}\bar{I}_{\bar{K}\bar{L}(\beta)} &(3.145)
\end{aligned}$$

The coupled finite element formulation can be written upon using the linearization of the balance of linear and first moment of momenta equations. Note that the terms involving $\delta\boldsymbol{u}$ and $\delta\boldsymbol{\Phi}$ are the "stiffness" matrix components. The terms involving $\delta\ddot{\boldsymbol{u}}$ and $\delta\ddot{\boldsymbol{\Phi}}$ are the "mass" matrix components. The system of coupled finite element equations can be expressed such that,

$$\begin{bmatrix} \boldsymbol{M}_{dd} & \boldsymbol{M}_{d\phi} \\ \boldsymbol{M}_{\phi d} & \boldsymbol{M}_{\phi\phi} \end{bmatrix} \cdot \begin{Bmatrix} \delta\ddot{\boldsymbol{u}} \\ \delta\ddot{\boldsymbol{\Phi}} \end{Bmatrix} + \begin{bmatrix} \boldsymbol{K}_{dd} & \boldsymbol{K}_{d\phi} \\ \boldsymbol{K}_{\phi d} & \boldsymbol{K}_{\phi\phi} \end{bmatrix} \cdot \begin{Bmatrix} \delta\boldsymbol{u} \\ \delta\boldsymbol{\Phi} \end{Bmatrix} = \begin{Bmatrix} -\boldsymbol{R}_d \\ -\boldsymbol{R}_\phi \end{Bmatrix} \tag{3.146}$$

where $\boldsymbol{R}_d$ and $\boldsymbol{R}_\phi$ are the residual vectors at the current iteration of the Newton-Raphson algorithm [Isbuga, 2012]. $\boldsymbol{K}_{dd}$, $\boldsymbol{K}_{d\phi}$ are the stiffness matrix components related to the balance of linear momentum involving $\delta\boldsymbol{u}$ and $\delta\boldsymbol{\Phi}$ respectively. $\boldsymbol{K}_{\phi d}$, $\boldsymbol{K}_{\phi\phi}$ are the stiffness matrix terms related to the balance of first moment of momentum involving $\delta\boldsymbol{u}$ and $\delta\boldsymbol{\Phi}$. Similarly we have $\boldsymbol{M}_{dd}$, $\boldsymbol{M}_{d\phi}$,

and $\boldsymbol{M}_{\phi d}$, $\boldsymbol{M}_{\phi\phi}$ which are the components of mass matrix related to the balance of linear and the balance of first moment of momenta respectively. The coupled finite element formulation for the quasi-static micromorphic elastoplasticity can derived as follows,

$$\begin{bmatrix} \boldsymbol{K}_{dd} & \boldsymbol{K}_{d\phi} \\ \boldsymbol{K}_{\phi d} & \boldsymbol{K}_{\phi\phi} \end{bmatrix} \cdot \begin{Bmatrix} \delta \boldsymbol{u} \\ \delta \boldsymbol{\Phi} \end{Bmatrix} = \begin{Bmatrix} -\boldsymbol{R}_d \\ -\boldsymbol{R}_\phi \end{Bmatrix} \tag{3.147}$$

Chapter 4

Applying Micromorphic Filter on 3D Beam Finite Element Analysis with Idealized Periodic Micro-Structure

This chapter is devoted to applying a micromorphic filter on a 3D beam finite element analysis (FEA) with idealized periodic micro-structure by Bishop and Lim [2016]. The goal of this study is to present the physical motivation of a micromorphic continuum in a framework of multiscale material modeling. This brief study presents a tool called "micromorphic filter" to perform the bridging of underlying direct numerical simulation (DNS) of the material at grain scale to continuum finite element scale. This is beneficial in terms of better understanding the effect of material's micro-structure on macroscopic behavior and perhaps improving macroscopic quantities including stiffness and strength of materials via fabricating heterogeneous particulate physics at micro-scale (see Gheibi and Gassman [2016], Khabiri et al. [2016], Sasanakul et al. [2017]). The micromorphic filter works as a direct link between overlapping micromorphic continuum and DNS regions. This is done through discretizing the DNS region into a number of averaging domains (called macro-elements (dv_β in continuum framework)). The number of averaging domains defines the picture of micromorphic continuum from the underlying micro-structure of the material. The micromorphic continuum theory of Eringen was proposed to incorporate micro-structures of materials in a continuum framework. Therefore, micro-deformation tensor is proposed to govern "micro-element"

deformations, besides the deformation gradient capturing macroscopic deformations. In this chapter the approach of applying micromorphic filter will be briefly reviewed and some initial results will be presented.

4.1 Applying Micromorphic Filter and Stress Calculations from 3D DNS

To start, we should first recall the kinematics and balance equations of the micromorphic continuum derived in Chapter 2. The idea of micromorphic filter is based on enforcing a direct link between the DNS region and the micromorphic continuum. This is done through discretizing the DNS region into a number of averaging domains Ω_β^{avg} (macro-element β with differential dv_β) in such a way that each averaging domain is composed of a number of micro-element volumes $v^{(\alpha)}$ in the current configuration (similar to $dv^{(\alpha)}$ in the continuum description). Through the discretization, the micromorphic continuum parameters including the micromorphic stresses, micro-deformation tensor $\boldsymbol{\chi}$, and the micromorphic strain tensors can be calculated. This chapter deals with the calculation of micromorphic stresses. Figure 4.1 illustrates the schematic of discretized DNS region into a number of the averaging domains Ω_β^{avg} with 8 micro-element volumes within each averaging domain $v^{(\alpha)}, \alpha = 1, ..., 8$ for the symmetric micro-element Cauchy stress $\boldsymbol{\sigma}^{(\alpha)}$ calculations. For the analysis in this chapter, we take $\boldsymbol{\sigma}^{(\alpha)}$ from DNS by Bishop and Lim [2016] which is the average stress of each unit cell. (see Fig.4.2)

In the micromorphic continuum, it is assumed that a macro-scale continuum material point is comprised of micro-elements. Therefore, we define averaging domain Ω_β^{avg} which contains 8 smaller discrete micro-element domains (α) with $v^{(\alpha)}$ (micro-elements). The relative position vector $\boldsymbol{\xi}^{(\alpha)}$ extends from c_β (centroid of micromorphic filter averaging domain Ω_β^{avg}) to $c^{(\alpha)}$ (centroid of micro-element (α)) in the current configuration. Note that discrete averaging domain Ω_β^{avg} corresponds to dv_β macroscopic differential volume in the micromorphic continuum framework. Similarly, $v^{(\alpha)}$ corresponds to $dv^{(\alpha)}$ micro-element volume (see Fig.2.1). Therefore, we can approximate the integrals in a continuum framework by discrete definitions, such that,

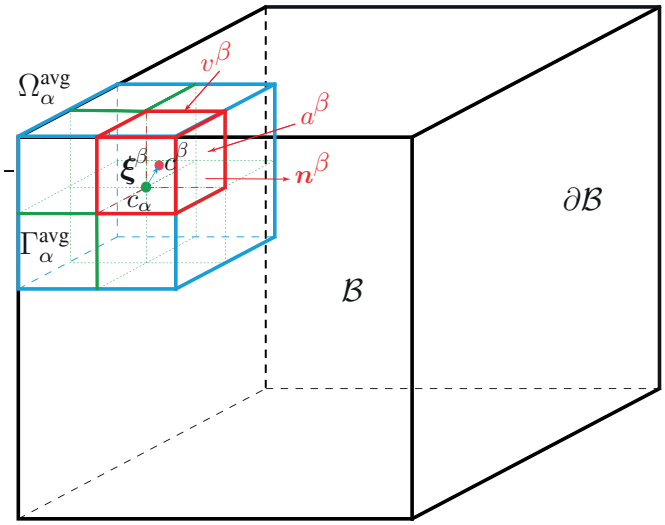

Figure 4.1. Illustration of micromorphic stress averaging domain Ω_β^{avg} and micro-element domains $\alpha = 1, ..., 8$ with centroid of $c^{(\alpha)}$, volume $v^{(\alpha)}$, surface area $a^{(\alpha)}$, unit normal vector $\boldsymbol{n}^{(\alpha)}$

$$\int_{\mathcal{B}} (\bullet)\, dv_\beta = \sum_{\beta=1}^{n_{avg}} \left[\int_{\Omega_\beta^{avg}} (\bullet)^{(\alpha)}\, dv^{(\alpha)} \right] \approx \sum_{\beta=1}^{n_{avg}} (\bullet)_\beta\, W^{avg} \Omega_\beta^{avg} \tag{4.1}$$

$$\int_{\Omega_\beta^{avg}} (\bullet)^{(\alpha)}\, dv^{(\alpha)} \approx \sum_{\alpha=1}^{n_{micro}} (\bullet)^{(\alpha)}\, W^{(\alpha)} v^{(\alpha)} \tag{4.2}$$

where W^{avg} and $W^{(\alpha)}$ are the weights of integration which we assume $W^{avg} = W^{(\alpha)} = 1$ for consistency of volume calculations assuming $\Omega_\beta^{avg} = \sum_{\alpha=1}^{n_{micro}} v^{(\alpha)}$. From Fig.4.1, there are $n_{micro} = 8$ micro-elements to generate the average. Note that n_{micro} could be increased to $27, 64, ...$, but, 8 is the minimum. Based on the previous discussion, the symmetric micro-stress s_{kl} and unsymmetric couple stress m_{klm} are written as

$$s_{kl} \overset{\text{def}}{=} \frac{1}{dv_\beta} \int_{dv_\beta} \sigma_{kl}^{(\alpha)} dv^{(\alpha)} \tag{4.3}$$

$$m_{klm} \overset{\text{def}}{=} \frac{1}{dv_\beta} \int_{dv_\beta} \sigma_{kl}^{(\alpha)} \xi_m^{(\alpha)} dv^{(\alpha)} \tag{4.4}$$

Using (4.2), (4.3), and (4.4), symmetric micro-stress and unsymmetric couple stress at point c_β in the averaging domain Ω_β^{avg} can be derived such that

$$(s_{kl})_\beta = \frac{1}{\Omega_\beta^{avg}} \sum_{\alpha=1}^{n_{micro}} \sigma_{kl}^{(\alpha)} v^{(\alpha)} \tag{4.5}$$

$$(m_{klm})_\beta = \frac{1}{\Omega_\beta^{avg}} \sum_{\alpha=1}^{n_{micro}} \sigma_{kl}^{(\alpha)} \xi_m^{(\alpha)} v^{(\alpha)} \tag{4.6}$$

Through (4.5) and (4.6), we can obtain micro-stress and couple stress in discretized averaging domain Ω_β^{avg}. Now, we look into the balance of first moment of momentum (2.67) to calculate the unsymmetric Cauchy stress $\boldsymbol{\sigma}_\beta$ at point c_β. The balance of first moment of momentum integrated over the body $\mathcal{B}$ in the current configuration is such that

$$\int_{\mathcal{B}} \left[\sigma_{mk} - s_{mk} + m_{lkm,l} + \rho(\ell_{km} - \omega_{km})\right] dv_\beta = 0 \tag{4.7}$$

In this chapter, we are assuming that the body force couple ℓ_{km} (no body force terms like gravity) and micro-spin inertia ω_{km} are zero, since we are dealing with quasi-static analysis. The balance of first moment of momentum in the discretized averaging domain is such that,

$$\sum_{\beta=1}^{n_{avg}} \left[(\sigma_{mk})_\beta - (s_{mk})_\beta + (m_{lkm,l})_\beta + \rho\left((\ell_{km})_\beta - (\omega_{km})_\beta\right)\right] \Omega_\beta^{avg} = 0 \tag{4.8}$$

Assuming the balance equation is satisfied "pointwise" at each β averaging domain, such that,

$$(\sigma_{mk})_\beta = (s_{mk})_\beta - (m_{lkm,l})_\beta - \rho\left((\ell_{km})_\beta - (\omega_{km})_\beta\right) \tag{4.9}$$

The remaining terms of (4.8) can be written in the discretized averaging domain such that

$$\int_{\mathcal{B}} \sigma_{mk} dv_\beta \approx \sum_{\beta=1}^{n_{avg}} \left[(\sigma_{mk})_\beta \Omega_\beta^{avg}\right] \tag{4.10}$$

$$\int_{\mathcal{B}} s_{mk} dv_\beta \approx \sum_{\beta=1}^{n_{avg}} \left[(s_{mk})_\beta \Omega_\beta^{avg}\right] = \sum_{\beta=1}^{n_{avg}} \left[\sum_{\alpha=1}^{n_{micro}} \sigma_{kl}^{(\alpha)} v^{(\alpha)}\right] \tag{4.11}$$

$$\int_{\mathcal{B}} m_{lkm,l} dv_\beta = \int_{\partial\mathcal{B}} m_{lkm} n_l da \approx \sum_{\beta=1}^{n_{avg}} \left[\sum_{\alpha=1}^{n_{micro}} \sigma_{lk}^{(\alpha)} \xi_m^{(\alpha)} n_l^{(\alpha)} a^{(\alpha)}\right] \tag{4.12}$$

In the next section the numerical results on micromorphic filter and stress calculations are presented for three dimensional beam FE models with 128 ($4 \times 4 \times 8$) and 1024 ($8 \times 8 \times 16$) periodic unit cells.

4.2 Numerical Example

This section is devoted to presenting the numerical results of the micromorphic filter and the stress calculations on three dimensional beam models with idealized periodic micro-structures. Figure 4.2 depicts the schematic of beam models with two idealized periodic micro-structures [Bishop and Lim, 2016] on which we applied micromorphic filter. In this chapter the micromorphic filter is applied on either 16 averaging domains $n_{avg} = 2 \times 2 \times 4$ (2 averaging domains in x direction, 2 averaging domains in y direction, 4 averaging domains in z direction) or 64 averaging domains $n_{avg} = 4 \times 4 \times 8$. According to the number of averaging domains on which the micromorphic filter is applied ($2 \times 2 \times 4$ or $4 \times 4 \times 8$) in Fig.4.2, the results of the micromorphic stresses are plotted along the centroids of the darkened block at the top left edge of the beam models. Figure 4.3 illustrates the contour plot of σ_{33}^{cell} (averaged σ_{33} stress of each unit cell) for the beam models. For the case in which the averaging domain Ω_{β}^{avg} is selected such that the micro-element volume $v^{(\alpha)}$ is equal to the unit cell volume, σ_{33}^{cell} is equal to $\sigma_{33}^{(\alpha)}$ (micro-element Cauchy stress in top and bottom models). Note that based on the number of unit cells in the beam model, we can choose the number of micromorphic averaging domains n_{avg} to calculate the micromorphic stresses. For the model with ($4 \times 4 \times 8$) unit cells (4 unit cells in x direction, 4 unit cells in y direction, 8 unit cells in z direction) we calculated the stresses through ($n_{avg} = 2 \times 2 \times 4 = 16$) averaging domains each with $n_{micro} = 8$. For the case with ($8 \times 8 \times 16$) unit cells, we calculated the micromorphic stresses through ($n_{avg} = 2 \times 2 \times 4 = 16$) and ($n_{avg} = 4 \times 4 \times 8 = 128$) averaging domains. Note that in the case ($n_{avg} = 2 \times 2 \times 4 = 16$) each micro-element $v^{(\alpha)}$ contains 8 unit cells, however, in the other case ($n_{avg} = 4 \times 4 \times 8 = 128$) each micro-element $v^{(\alpha)}$ corresponds to one unit cell. In each case n_{micro} is equal to 8. Figures 4.4, 4.5, 4.6, and 4.7 show the micro-element Cauchy stress component $\sigma_{33}^{(\alpha)}$, the calculated macro-element micromorphic Cauchy stress component $(\sigma_{33})_{\beta}$, the

micro-stress component $(s_{33})_\beta$, and the couple stress components $(m_{331})_\beta$, $(m_{332})_\beta$, and $(m_{333})_\beta$ out of the discretized averaging domain Ω_β^{avg} along the length of the beams with $(4 \times 4 \times 8)$ and $(8 \times 8 \times 16)$ unit cells.

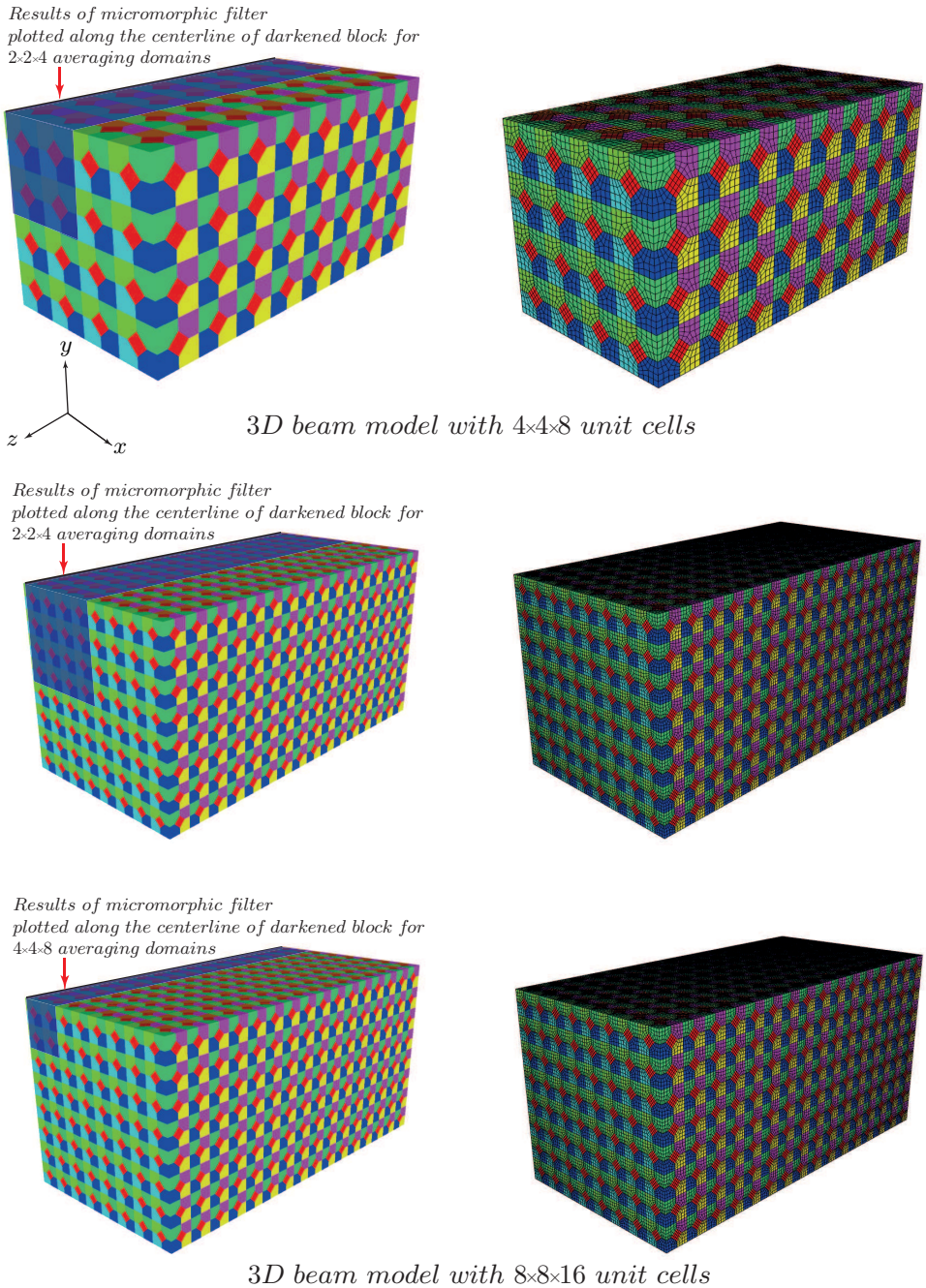

Figure 4.2. schematic of beam models with periodic micro-structure

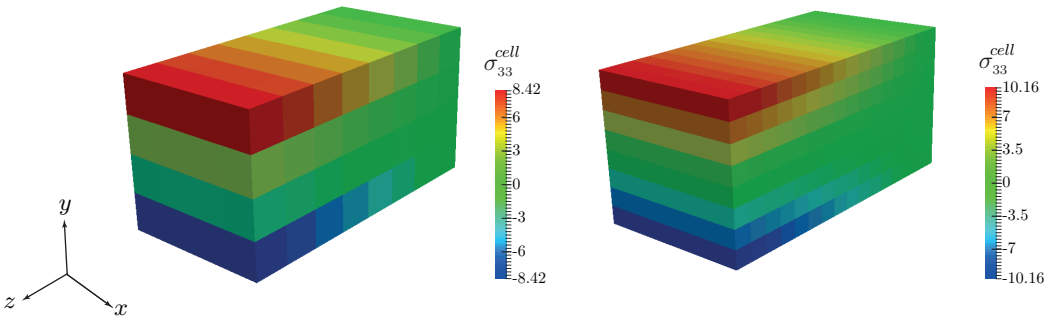

Figure 4.3. Contour plot of σ_{33}^{cell} averaged stress in unit cells [Bishop and Lim, 2016].

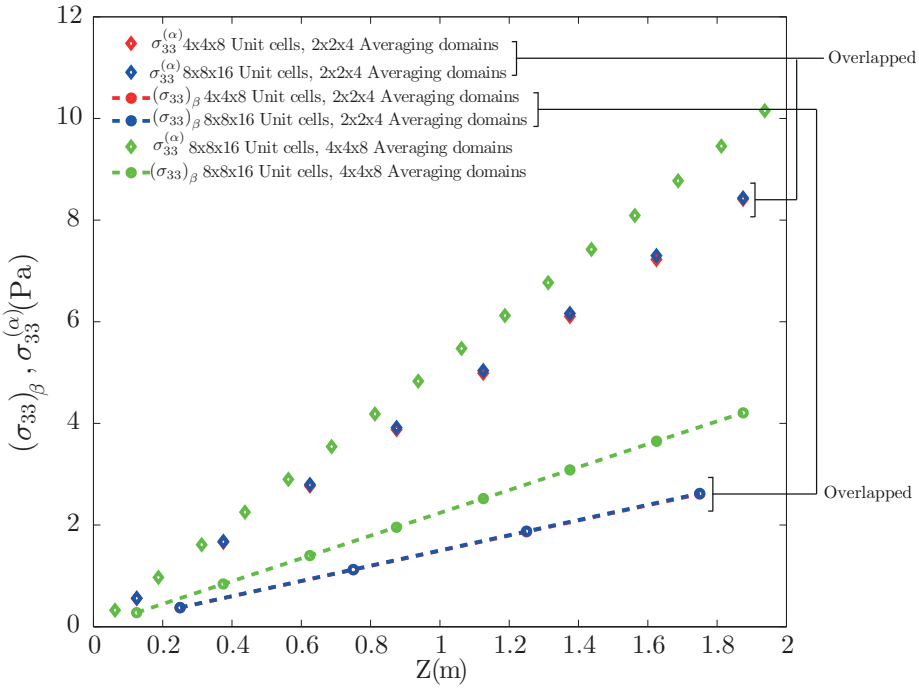

Figure 4.4. Unsymmetric Cauchy stress component $(\sigma_{33})_\beta$ vs Symmetric micro-element Cauchy stress component $\sigma_{33}^{(\alpha)}$

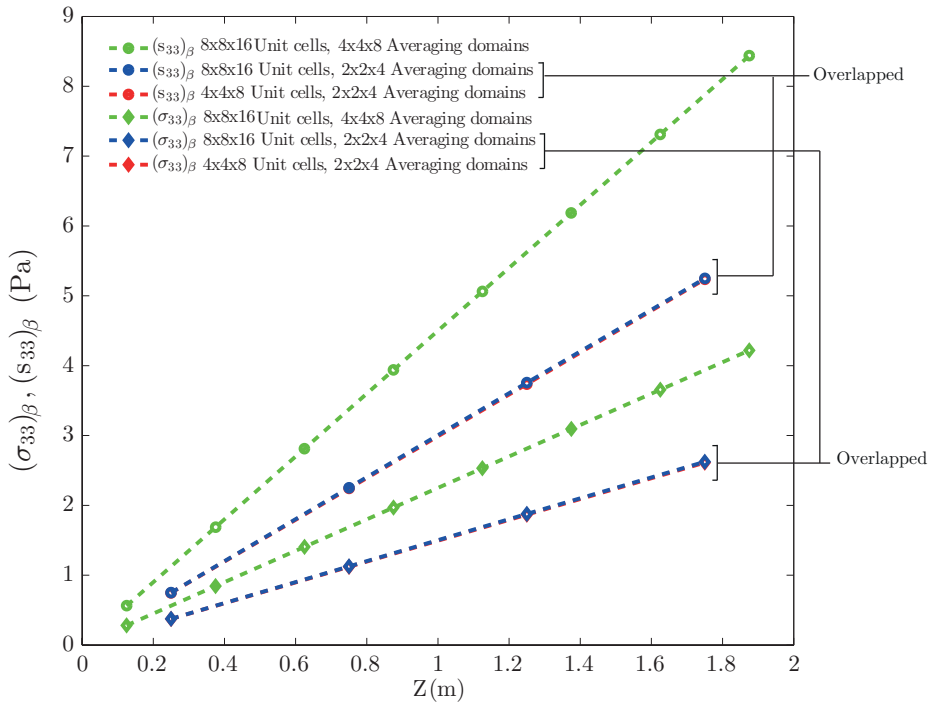

Figure 4.5. Micromorphic stresses, unsymmetric Cauchy stress component $(\sigma_{33})_\beta$, symmetric micro-stress component $(s_{33})_\beta$

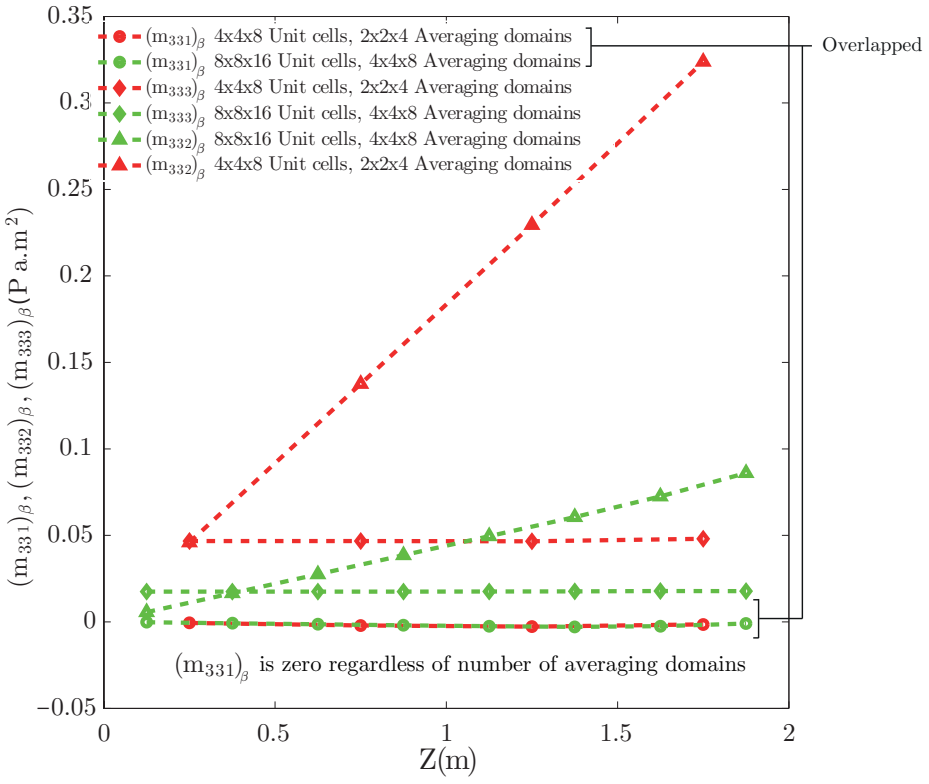

Figure 4.6. Couple stress components $(m_{331})_\beta$, $(m_{332})_\beta$, and $(m_{333})_\beta$

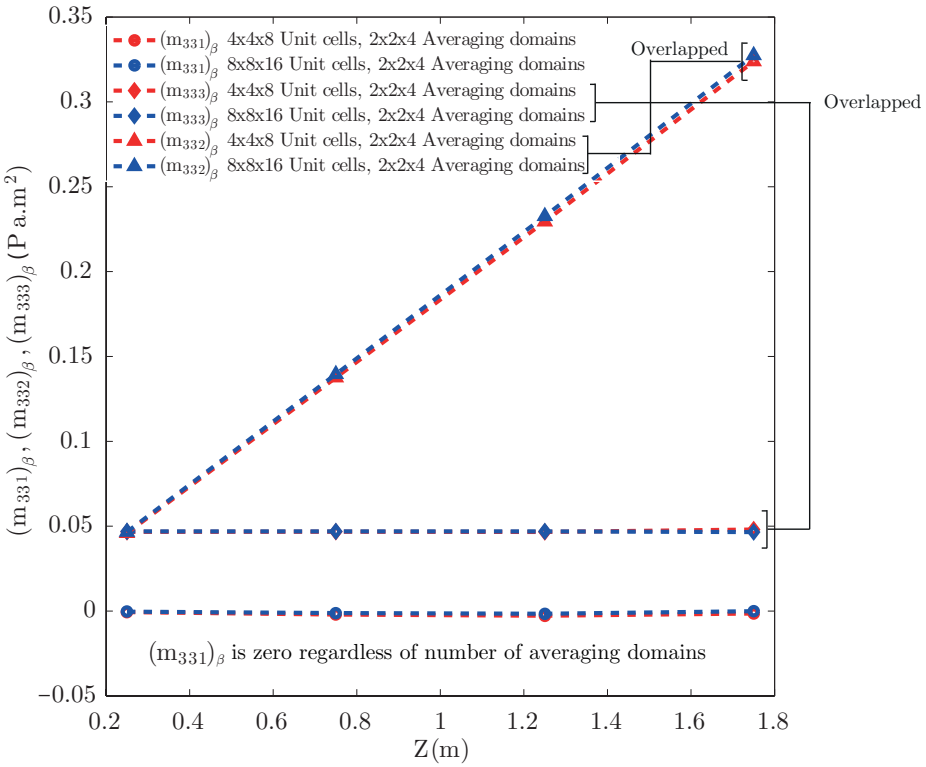

Figure 4.7. Couple stress components $(m_{331})_\beta$, $(m_{332})_\beta$, and $(m_{333})_\beta$ for cases with $(4\times4\times8)$ and $(8\times8\times16)$ unit cells and $(2 \times 2 \times 4)$ averaging domains

In Fig.4.4, the micro-element Cauchy stress component $\sigma_{33}^{(\alpha)}$ of the case with $(8\times8\times16)$ unit cells and $(2\times2\times4)$ averaging domains (blue solid diamonds in Fig.4.4) is equal to the case with $(4\times4\times8)$ unit cells and $(2\times2\times4)$ averaging domains (red solid diamonds in Fig.4.4). Therefore, the obtained unsymmetric Cauchy stress component $(\sigma_{33})_\beta$ (blue and red dashed lines) for these two cases are equal. This figure also shows the micro-element Cauchy stress component $\sigma_{33}^{(\alpha)}$ of the case with $(8\times8\times16)$ unit cells and (4×4) averaging domains (green solid diamonds). It can be seen that for this case with more averaging domains, the model captures higher $\sigma_{33}^{(\alpha)}$ which leads to the higher $(\sigma_{33})_\beta$ in comparison with the case with $(2\times2\times4)$ averaging domains. Note that with the lower number of averaging domains, the micro-element stress is calculated via averaging over a larger domain (more unit cells). Therefore, the obtained accuracy in calculating micro-element stress and macro-element stress tensors will be lowered. Figure 4.5 illustrates the unsymmetric Cauchy stress component $(\sigma_{33})_\beta$ in comparison with the symmetric micro-stress component $(s_{33})_\beta$. Similarly, the symmetric micro-stress component $(s_{33})_\beta$ obtained from the case with $(8\times8\times16)$ unit cells and $(2\times2\times4)$ averaging domains is overlapped with that of the case with $(4\times4\times8)$ unit cells and $(2\times2\times4)$ averaging domains. In the case with $(8\times8\times16)$ unit cells, there is a discrepancy between the calculated stresses out of the model with $(4\times4\times8)$ averaging domains and those of the model with $(2\times2\times4)$ averaging domains. This shows that the size of averaging domains is playing a crucial role in calculating the micromorphic stresses. Increasing the size of averaging domains in calculating the micromorphic stresses is equal to having a larger relative position vector $\boldsymbol{\xi}^{(\alpha)}$ and a coarser micro-structure (a coarser interpretation of the micro-structure). Therefore, in the case with $(8\times8\times16)$ unit cells and $(2\times2\times4)$ averaging domains, the picture of micromorphic continuum from the underlying micro-structure is equal to the case with $(4\times4\times8)$ unit cells and $(2\times2\times4)$ averaging domains for this particular example. Figure 4.6 illustrates the couple stress components $(m_{331})_\beta$, $(m_{332})_\beta$, and $(m_{333})_\beta$ for the both models with $(4\times4\times8)$ and $(8\times8\times16)$ unit cells. It can be seen that the couple stress component $(m_{331})_\beta$ is zero for all the models which is related to the uniform distribution of the average unit cell Cauchy stress σ_{33}^{cell} (Fig.4.3) along the x axis. Note that the model with $(4\times4\times8)$ unit cells and $(2\times2\times4)$ averaging domains has larger

$(m_{332})_\beta$ and $(m_{333})_\beta$ in magnitude in comparison with the model with $(8 \times 8 \times 16)$ unit cells and $(4 \times 4 \times 8)$ averaging domains. The model with the assumed coarser micro-structure for $(2 \times 2 \times 4)$ averaging domains has longer relative position vector $\boldsymbol{\xi}^{(\alpha)}$ and therefore, with regard to (4.4) the couple stress components have higher magnitudes. Figure 4.7 illustrates the calculated components of couple stress $(m_{331})_\beta$, $(m_{332})_\beta$, and $(m_{333})_\beta$ from the model with $(8 \times 8 \times 16)$ unit cells and $(2 \times 2 \times 4)$ averaging domains overlapped with those of the model with $(4 \times 4 \times 8)$ unit cells and $(2 \times 2 \times 4)$ averaging domains, respectively. It is shown that the couple stress component $(m_{331})_\beta$ is zero which mean that there is no gradient in the micro-element Cauchy stress component $\sigma_{33}^{(\alpha)}$ along direction 1. The couple stress component $(m_{333})_\beta$ is constant which means that the gradient of micro-element Cauchy stress component $\sigma_{33}^{(\alpha)}$ is constant along direction 3 (see contour plots of σ_{33}^{cell} Fig.4.3).

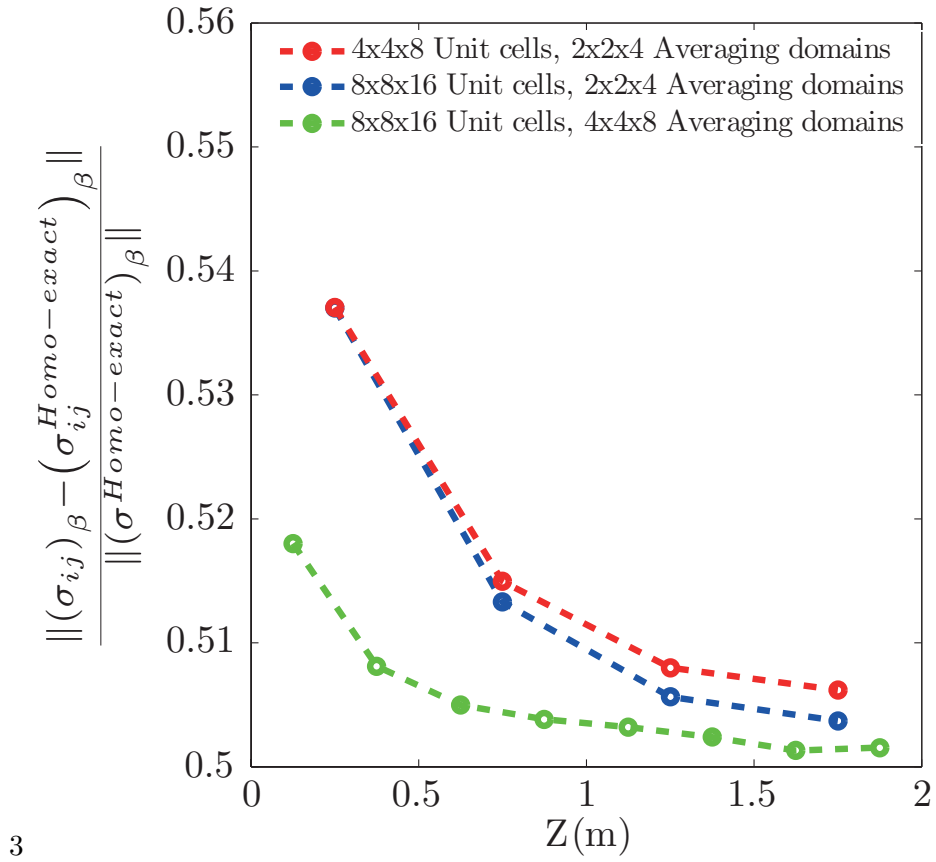

Figure 4.8. Difference between the norm of Cauchy stress of the beam with periodic micro-structure and that of the homogenized beam.

Figure 4.8 illustrates the difference of the micromorphic Cauchy stress obtained from the micromorphic filter for beam with FE analysis idealized periodic micro-structures, and the exact solution of the homogenous linear elastic isotropic beam model at small strain with no micro-structure [Bishop and Lim, 2016]. From this figure it can be noticed that the difference of the micromorphic Cauchy stress with that of the classical elasticity is smaller for the beam model with $(8 \times 8 \times 16)$ unit cells and $(4 \times 4 \times 8)$ averaging domains in comparison with the other models. This denotes that with the smaller relative position vector $\boldsymbol{\xi}^{(\alpha)}$ (finer interpretation of the micro-structure), the heterogeneity effect of the micro-elements will be reduced (smaller couple stress), and the obtained micromorphic Cauchy stress is closer to the exact homogenized solution. But the relative difference is still high ($\approx 50\%$), which is likely a result of ignoring cancellation of tractions across averaging domains when going from equations (4.7) to (4.8) to (4.9). A weighted residual approach to (4.7) with weighting function would be worthwhile considering because the traction forces would fall out explicitly.

Chapter 5

Finite Element Analysis of Finite Strain Micromorphic Elasticity, Elastoplasticity, and Dynamics

In previous chapters, we presented the balance equations, thermodynamics, constitutive relations and the extension of micromorphic elasticity to elastoplasticity, all at finite strain. Note that more details on micromorphic elasticity and its extension to elastoplasticity can be found in Eringen and Suhubi [1964], Isbuga [2012], Regueiro [2011], Regueiro [2010] and Regueiro [2009]. This chapter is devoted to presenting numerical examples to investigate the modeling of materials with a periodic micro-structure from the perspective of micromorphic continuum. Non-periodic micro-structured materials will be considered as future work. As mentioned earlier, the micromorphic continuum of this thesis ($\boldsymbol{\Xi}^{(\alpha)}$ is not function of position vector $\boldsymbol{X}_\beta$) is consistent with a material with idealized periodic micro-structure. Three dimensional finite element analysis of micromorphic elasticity, elastoplasticity, and dynamics are performed to investigate the effect of deformable micro-elements on macroscopic mechanical behavior at finite strain. Note that the selected material parameters in this research do not belong to any specific material, but satisfy positive definiteness of strain energy and the reduced dissipation inequality (Smith [1968]). For the purpose of presenting micromorphic continuum response, we start with a column in uniaxial strain in compression to better illustrate the micromorphic stresses, strains, and micro-element deformations. This is an example of a 1D micromorphic continuum and, therefore, from the nine additional micromorphic dofs we only have one component of micro-displacement tensor Φ_{33} in-

cluded to represent the compression of the micro-elements including the axial displacement u_3. We could also allow dofs Φ_{11}, Φ_{22}, but this will be considered in future work. In the numerical results, first we provide discussion of the finite elements which are available in Tahoe with the capability of dealing with two-field problems. Note that a micromorphic continuum is a two-field problem in terms of dealing with the deformation of the micro and macro-elements (i.e., $\boldsymbol{\Phi}$ and $\boldsymbol{u}$, respectively). The performance of these two element types are compared to deduce which element is the most appropriate one for the micromorphic simulations in terms of accuracy and computational cost. The elastoplasticity analysis in micro-structured materials from the view point of micromorphic continuum will be presented through numerical simulations. It will be shown that there are three levels of micromorphic elastoplasticity evolving throughout the continuum body, and the effect of micro-element elastoplastic deformation on the macroscopic mechanical behavior will be discussed. The dynamic analysis of a micromorphic continuum will also be presented to investigate the effect of the micro-element deformation under dynamic loading on the continuum scale mechanical response.

5.1 Elements Used in Finite Element Simulations

In this section, we discuss the element types used to solve the coupled equations (2.158). There are two 3D element types in Tahoe which are able to perform a two-field finite element simulation. One uses a mixed 27-node triquadratic hexahedral interpolation for $\boldsymbol{u}^h$, and 8-node trilinear hexahedral interpolation for $\boldsymbol{\Phi}^h$ (Q27P8). The schematic of this element is depicted in Fig.5.1 (a). The other one uses the same 8-noded hexahedral trilinear interpolation for both fields, $\boldsymbol{u}^h$ and $\boldsymbol{\Phi}^h$, shown in Fig.5.1 (b).

Note that mixed methods for approximating two-field problems is shown to be convergent by increasing the number of elements for small strain problems [Hughes, 1987], but for finite strain problems there is no such a proof. Isbuga [2012] illustrated several simulations to show the convergence trend in various models by increasing the number of elements. This is done to check the applicability of the mixed method approximation for the micromorphic continuum simulations.

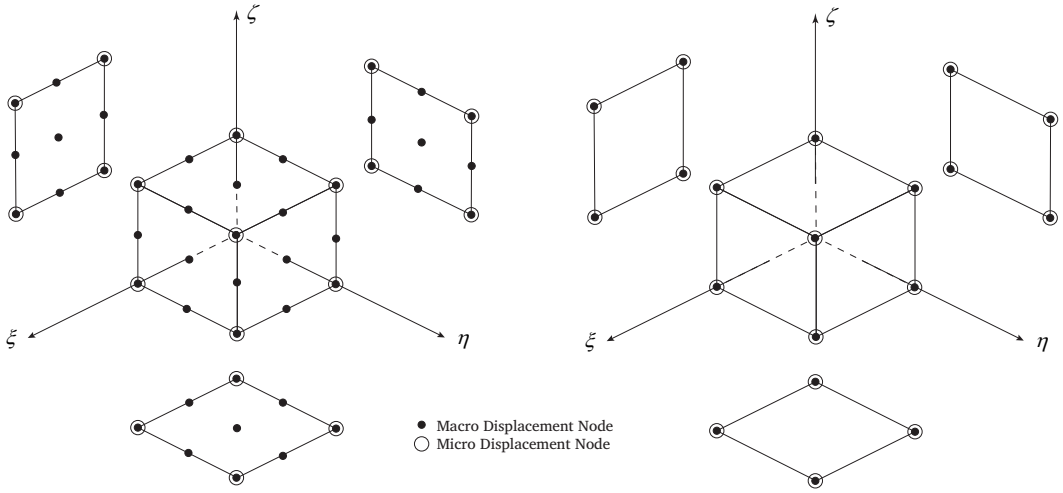

(a) Schematic of Q27P8 element

(b) Schematic of Q8P8 element

Figure 5.1. Schematic of Q27P8 and Q8P8 elements in Tahoe.

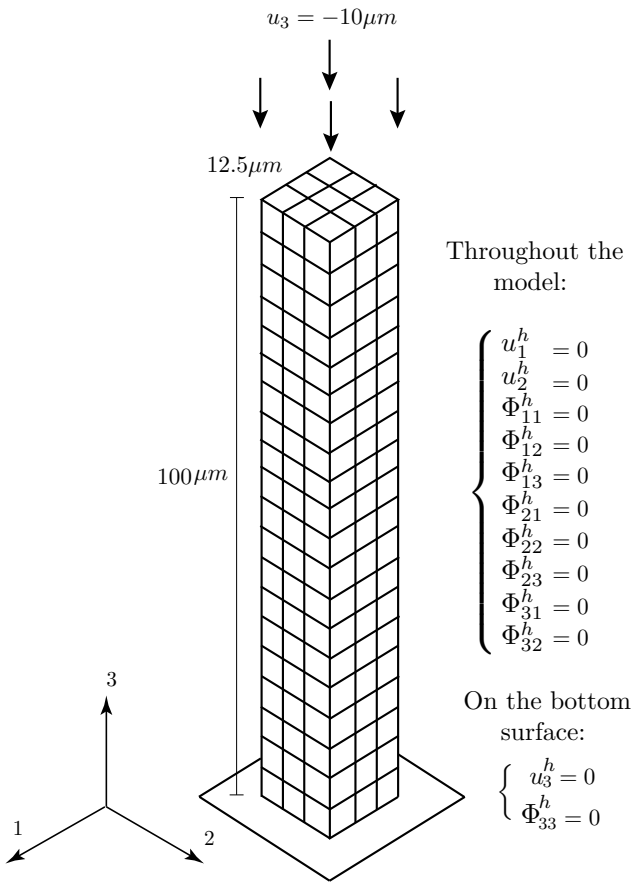

Figure 5.2. Schematic of a column under compressive load. BCs are selected to represent a one dimensional uniaxial strain in compression at both macro and micro scales (only u_3^h and Φ_{33}^h dofs).

Furthermore, a comparison is made to illustrate the performance of these two elements for micromorphic continuum. The comparison is done via the uniaxial strain example which represents a 1D micromorphic continuum. The schematic of the geometry, mesh configuration, and BCs are presented in Fig.5.2. All of the micromorphic dofs are assumed to be zero, except the micro-displacement component Φ^h_{33} illustrating the micro-stretch deformation of the micro-elements in the Z direction. The micro-displacement tensor component Φ^h_{33} is zero on the bottom surface of the column. Similar comparison between Q27P8 and Q8P8 elements is done for the beam bending example.

Figure 5.3 compares the results of micromorphic dof Φ^h_{33}, second Piola Kirchhoff component S^h_{33}, symmetric micro stress component Σ^h_{33}, and couple stress component M^h_{333} at top of the column obtained from the Q27P8 and Q8p8 elements. It can be seen that the numerical results obtained from Q27P8 and Q8P8 finite element models are consistent with each other. Figure 5.4 illustrates the profile of micromorphic dof Φ^h_{33}, the nodal values of second Piola Kirchhoff component S^h_{33}, symmetric micro stress component Σ^h_{33}, and couple stress component M^h_{333} through the length of the column. Similarly, these results are in a good agreement with each other. This simple example of column compression in a micromorphic continuum shows that the Q8P8 element is able to successfully perform approximations of macro displacement $\boldsymbol{u}^h$ and micro displacement $\boldsymbol{\Phi}^h$ fields. Therefore, to reduce the computational costs of simulations by the micromorphic finite element code, the Q8P8 element will be used to create meshes for the numerical examples of this research. Note that the Q27P8 element may be used for more complicated simulations of the micromorphic elastoplasticity and dynamics in the future if required. In the next section, we will discuss micromorphic elasticity and elastoplasticity in comparison with classical continuum elasticity and elastoplasticity through finite strain analysis of a column under compressive load.

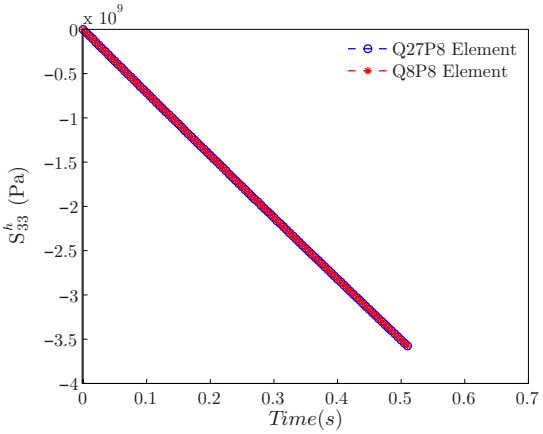

(a) Second Piola Kirchhoff S^h_{33} at top of column.

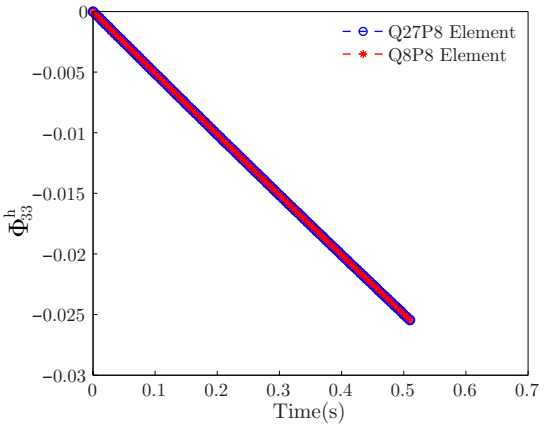

(b) Φ^h_{33} at top of column.

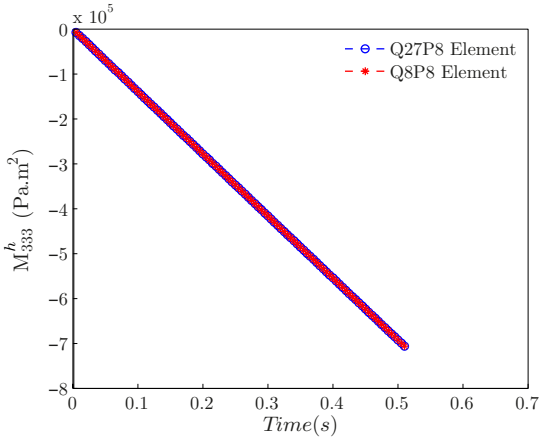

(c) Couple stress component M^h_{333} at top of column.

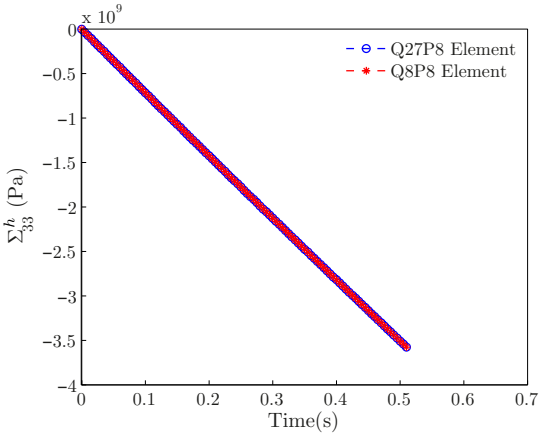

(d) Symmetric micro stress Σ^h_{33} at top of column.

Figure 5.3. Comparison of Q27P8 and Q8P8 elements.

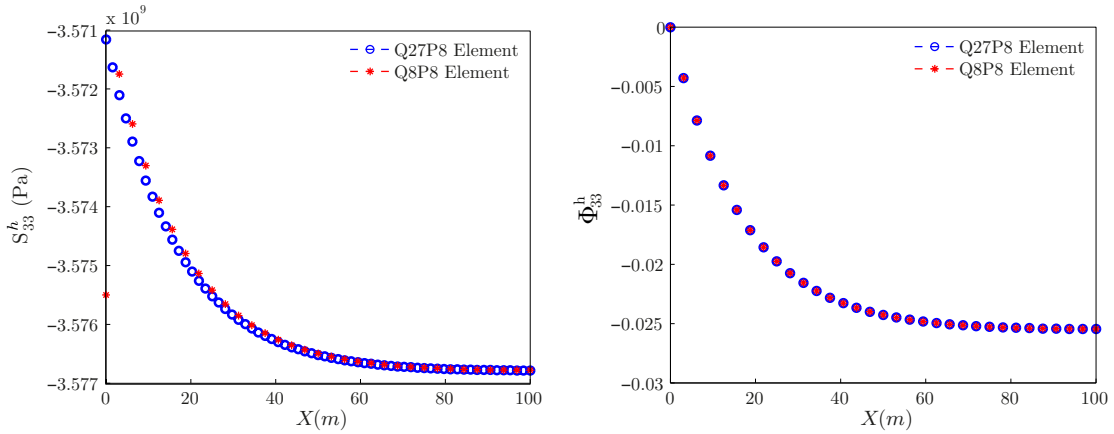

(a) S^h_{33} along length of column.

(b) Φ^h_{33} along length of column.

(c) M^h_{333} along length of column.

(d) Σ^h_{33} along length of column.

Figure 5.4. Comparison of Q27P8 and Q8P8 elements: results of Φ^h_{33} and micromorphic stresses at top of column.

5.2 Finite Strain Micromorphic Elastoplasticity Analysis of a Uniaxial Strain Column under Compressive Load

This section presents the finite strain micromorphic elastoplasticity analysis of a column under compressive load in uniaxial strain. Note that the column is selected as a simple model to better illustrate micromorphic elastoplasticity. This model has axial macro-element dof u_3^h and micro-element dof Φ_{33}^h. As discussed in the micromorphic elastoplasticity formulation section, plasticity occurs at three levels: macroscopic, microscopic, and micro-gradient scales. In this example, it is presented how these plasticity scales occur in a micromorphic continuum column under uniaxial strain. The schematic of the geometry, mesh, BCs and loading condition are explained in Fig.5.5. The selected material parameters for the elastoplastic micromorphic continuum are presented in Table 5.1. In this table the terminology "Micro/Macro Perfect Plasticity" represents micromorphic elastoplasticity model in which perfect plasticity occurs at microscopic and macroscopic scales, and there is no micro-gradient plasticity level ($\boldsymbol{\nabla}\boldsymbol{\chi}^p = \mathbf{0}$). In the model "Micro/Macro Softening Plasticity", softening plasticity will only take place at microscopic and macroscopic scales and no micro-gradient plasticity level ($\boldsymbol{\nabla}\boldsymbol{\chi}^p = \mathbf{0}$). The terminologies "Micro/Macro/Micro-grad Perfect Plasticity" and "Micro/Macro/Micro-grad Softening Plasticity" refer to the models in which the perfect and softening plasticity will happen at all three micromorphic plasticity scales. The terminologies "Micro Perfect Plasticity" and "Micro Softening Plasticity" indicate the perfect and softening plasticity only occur at the microscopic scale. This analysis is done to illustrate the effect of elastoplasticity in the micro-elements of a micromorphic continuum on the macroscopic behavior of the material in comparison with classical elastoplasticity. The BCs on micromorphic column are presented in Table 5.2.

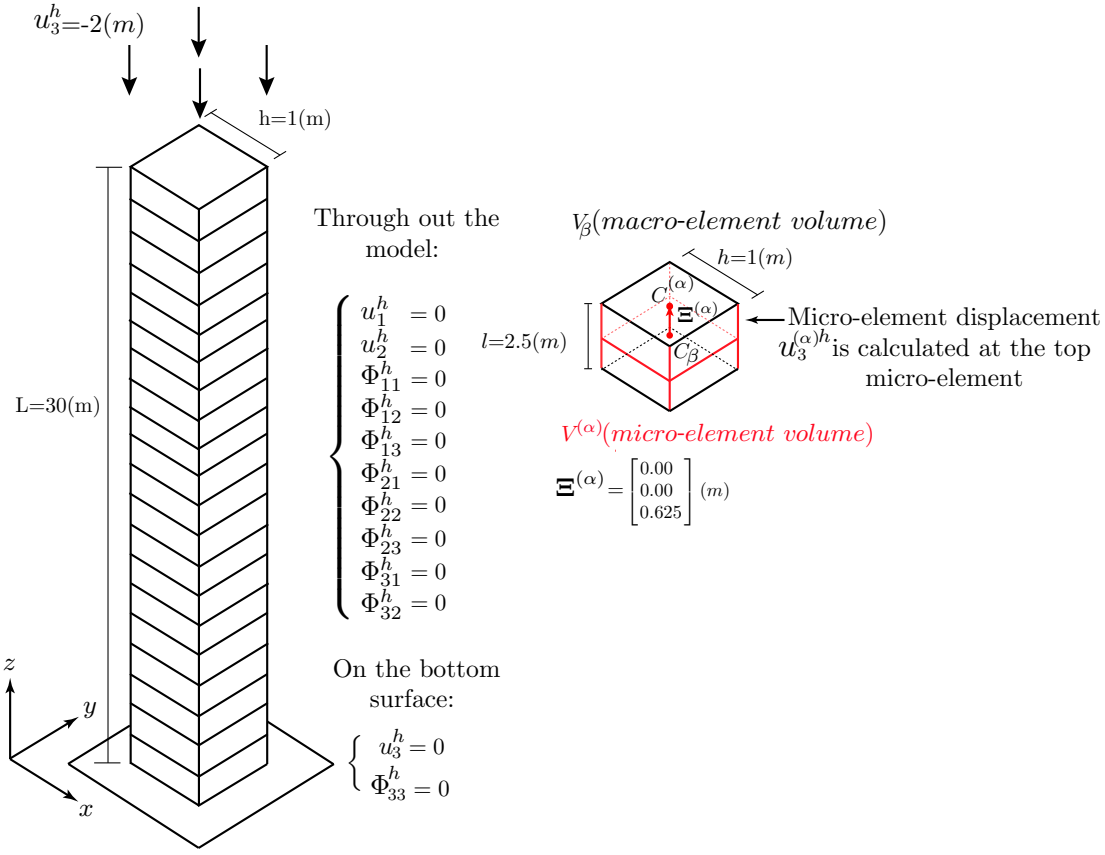

Figure 5.5. Schematic of a column under compressive uniaxial strain load.

Table 5.1. The selected material parameters for the micromorphic continuum.

Micromorphic Elasticity (linear, isotropic)					
$\lambda(Pa)$	$\mu(Pa)$	$\eta(Pa)$	$\kappa(Pa)$	$\nu(Pa)$	$\sigma(Pa)$
29.48e9	25.48e9	1e9	-1.5e9	-1.4e9	-3e9
$\tau(Pa)$	$\tau_1(Pa.m^2)$	$\tau_2(Pa.m^2)$	$\tau_3(Pa.m^2)$	$\tau_4(Pa.m^2)$	$\tau_5(Pa.m^2)$
0.4e9	0.0	0.0	0.0	0.0	0.0
$\tau_6(Pa.m^2)$	$\tau_7(Pa.m^2)$	$\tau_8(Pa.m^2)$	$\tau_9(Pa.m^2)$	$\tau_{10}(Pa.m^2)$	$\tau_{11}(Pa.m^2)$
0.0	10e11	0.0	0.0	0.0	0.0
Drucker-Prager					
ϕ	ψ	ϕ^χ	ψ^χ	$\phi^{\nabla\chi}$	$\psi^{\nabla\chi}$
0.2	0.0	0.2	0.0	0.2	0.0
Micro/Macro Perfect Plasticity					
	$H(Pa)$	$\bar{c}(Pa)$	$H^\chi(Pa)$	$\bar{c}^\chi(Pa)$	
	0.0	5e6	0.0	4e6	
Micro/Macro/Micro-gradient Perfect Plasticity					
$\bar{H}(Pa)$	$\bar{c}(Pa)$	$\bar{H}^\chi(Pa)$	$\bar{c}^\chi(Pa)$	$\bar{H}_3^{\nabla\chi}(Pa)$	$\bar{c}_3^{\nabla\chi}(Pa)$
0.0	5e6	0.0	4e6	0.0	5e7
Micro/Macro Softening Plasticity					
	$H(Pa)$	$\bar{c}(Pa)$	$H^\chi(Pa)$	$\bar{c}^\chi(Pa)$	
	-1e8	5e6	-1e8	4e6	
Micro/Macro/Micro-gradient Softening Plasticity					
$\bar{H}(Pa)$	$\bar{c}(Pa)$	$\bar{H}^\chi(Pa)$	$\bar{c}^\chi(Pa)$	$\bar{H}_3^{\nabla\chi}(Pa)$	$\bar{c}_3^{\nabla\chi}(Pa)$
-1e8	5e6	-1e8	4e6	-1e8	5e7
Micro Perfect Plasticity			Micro Softening Plasticity		
	$\bar{c}^\chi(Pa)$	$H^\chi(Pa)$	$\bar{c}^\chi(Pa)$	$H^\chi(Pa)$	
	4e6	0.0	4e6	-1e8	
Classical Continuum		Perfect Plasticity		Softening Plasticity	
$\lambda(Pa)$	$\mu(Pa)$	$\bar{c}(Pa)$	$\bar{H}(Pa)$	$\bar{c}(Pa)$	$\bar{H}(Pa)$
28.9e8	22.48e8	5e6	0	5e6	-1e8

Table 5.2. Selected BCs for column under uniaxial strain in compression loading.

Micromorphic Continuum	Throughout the column	On surface Γ
BC on Φ_{33}^h	$\Phi_{11}^h, \Phi_{22}^h, \Phi_{12}^h, \Phi_{21}^h, \Phi_{13}^h, \Phi_{31}^h, \Phi_{23}^h, \Phi_{32}^h = 0$	$\Phi_{33}^h = 0$
	$u_1^h, u_2^h = 0$	$u_3^h = 0$
Classical Continuum	Throughout the column	On surface Γ
	$\Phi_{11}^h, \Phi_{22}^h, \Phi_{12}^h, \Phi_{21}^h, \Phi_{13}^h, \Phi_{31}^h, \Phi_{23}^h, \Phi_{32}^h, \Phi_{33}^h = 0$	
	$u_1^h, u_2^h = 0$	$u_3^h = 0$

The contour plots of macroscopic, microscopic, and micro-gradient plastic multipliers for the Micro/Macro/Micro-gradient softening plasticity (micromorphic softening plasticity at all three scales) are presented in Fig.5.6. This figure shows the trend of elastoplasticity in a micromorphic continuum. It can be seen that in Fig.5.6(a), the elastoplasticity starts at microscopic scale all along the micromorphic column, and the macroscopic and the micro-gradient scales deform elastically. In Fig.5.6(b) a transition between the macroscopic and the microscopic plasticity scales take place close to the lower boundary. There is no plasticity in the micro-gradient scale. Figure 5.6(c) illustrates the micromorphic column where all three plasticity scales occur simultaneously. There is a transition between macroscopic and microscopic plasticity at the middle of the column, and micro-gradient plasticity occurs close to the bottom boundary. Figure 5.6(d) shows the micromorphic column in which the plasticity occurs at the macroscopic and the micro-gradient scales. Therefore, the plasticity at the microscopic scale is driven by the micro-gradient plasticity scale rather than the microscopic scale itself. Figure 5.7 illustrates the contour plots of $\bar{\gamma}$, $\bar{\gamma}^{\chi}$, and $\bar{\gamma}_3^{\nabla\chi}$ along the length of the column for the same time steps as Figs.5.6 (a)-(d). This figure shows the accumulated plastic deformation in the macro, micro, and micro-gradient plasticity levels. Figure 5.8 illustrates the schematic of elastoplastic deformations in the micromorphic column under tension in which micro-elements are expanding plastically through $\boldsymbol{\chi}^p$. This figure also shows positive $\boldsymbol{\nabla}\boldsymbol{\chi}^p$ where the micro-elements plastic expansion of adjacent macro-elements are increasing. This figure presents the picture of micromorphic continuum from the elastoplastic deformation at micro-scale through $\boldsymbol{\chi}^p$ and $\boldsymbol{\nabla}\boldsymbol{\chi}^p$. Similar to classical elastoplasticity models, the macro-element elastoplastic deformation is defined through the plastic part of the deformation gradient $\boldsymbol{F}^p$. The micromorphic continuum provides two separate plastic deformations for the micro-elements via the plastic part of micro-deformation tensor $\boldsymbol{\chi}^p$ and the gradient of the micro-deformation tensor $\boldsymbol{\nabla}\boldsymbol{\chi}^p$. These two levels of plasticity represent plastic deformation of the underlying sub-bodies. The plastic part of the micro-deformation tensor $\boldsymbol{\chi}^p$ defines the plastic deformation of the micro-elements in the micromorphic continuum. As discussed earlier through constitutive equations (3.95), (3.96), and (3.103), the plastic part of the micro-deformation tensor $\boldsymbol{\chi}^p$ drives plasticity at the macro and

micro-gradient scales irrespective of the yielding at these two scales. The gradient of the micro-deformation tensor $\boldsymbol{\nabla}\boldsymbol{\chi}^p$ shows the gradient of the plastic deformation of the micro-elements along the spatial direction. Note that $\Delta\bar{\gamma}^{\chi} = 0$ and therefore, $\dot{\boldsymbol{\chi}}^p = \mathbf{0}$, however we have $\boldsymbol{\nabla}\boldsymbol{\chi}^p$ evolving via the micro-gradient plasticity scale which drives $\boldsymbol{\nabla}\boldsymbol{\chi}^p$ independently. In terms of the micromorphic evolution equations, the developed formulation for micromorphic elastoplasticity cannot recognize the conflict of $\dot{\boldsymbol{\chi}}^p = \mathbf{0}$, while $\boldsymbol{\nabla}\boldsymbol{\chi}^p$ is evolving through micro-gradient plasticity level.

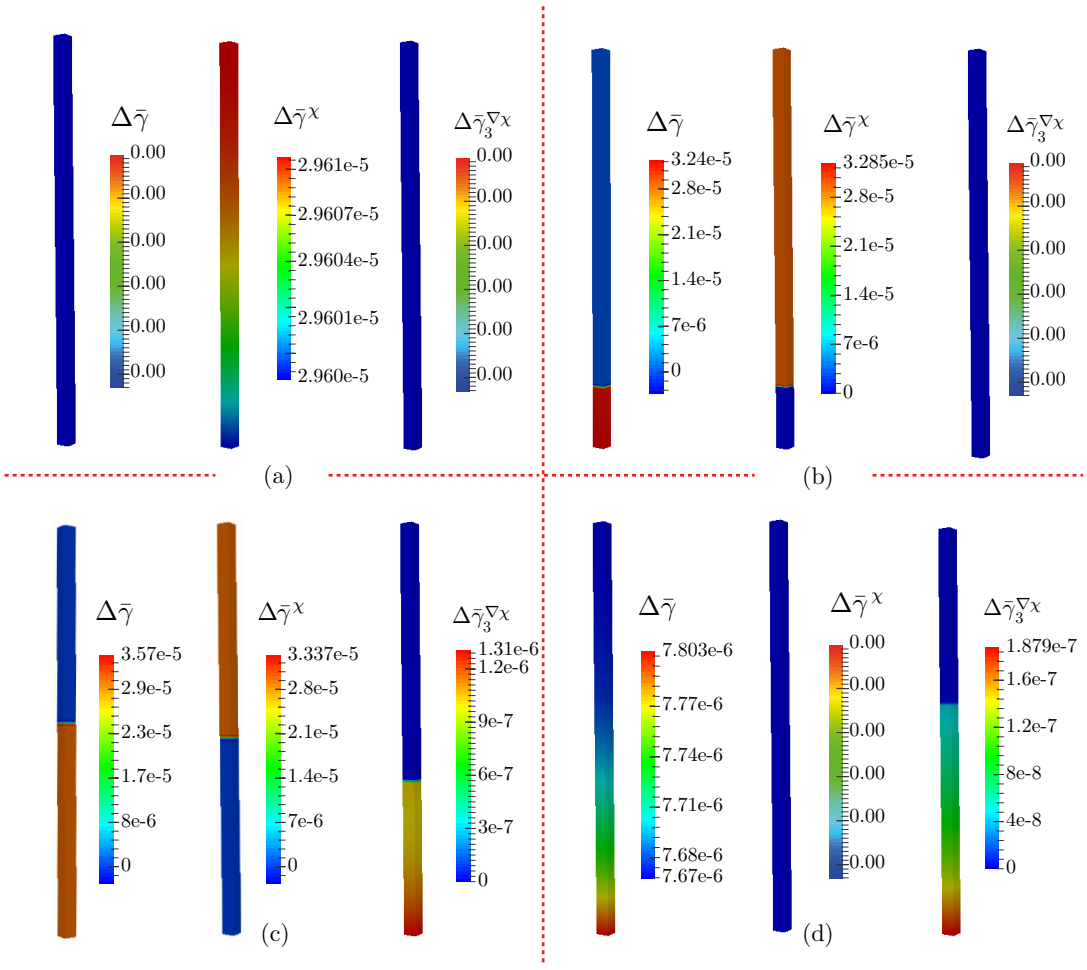

Figure 5.6. Contour plots of $\Delta\bar{\gamma}$, $\Delta\bar{\gamma}^{\chi}$, and $\Delta\bar{\gamma}_3^{\nabla\chi}$ for case Micro/Macro/Micro-gradient softening Plasticity.

Figure 5.9 illustrates the cohesion versus plastic multiplier for the micromorphic elastoplasticity models such as micro perfect plasticity, micro softening plasticity, micro/macro perfect plasticity, and micro/macro softening plasticity. These figures present the softening and perfect plastic-

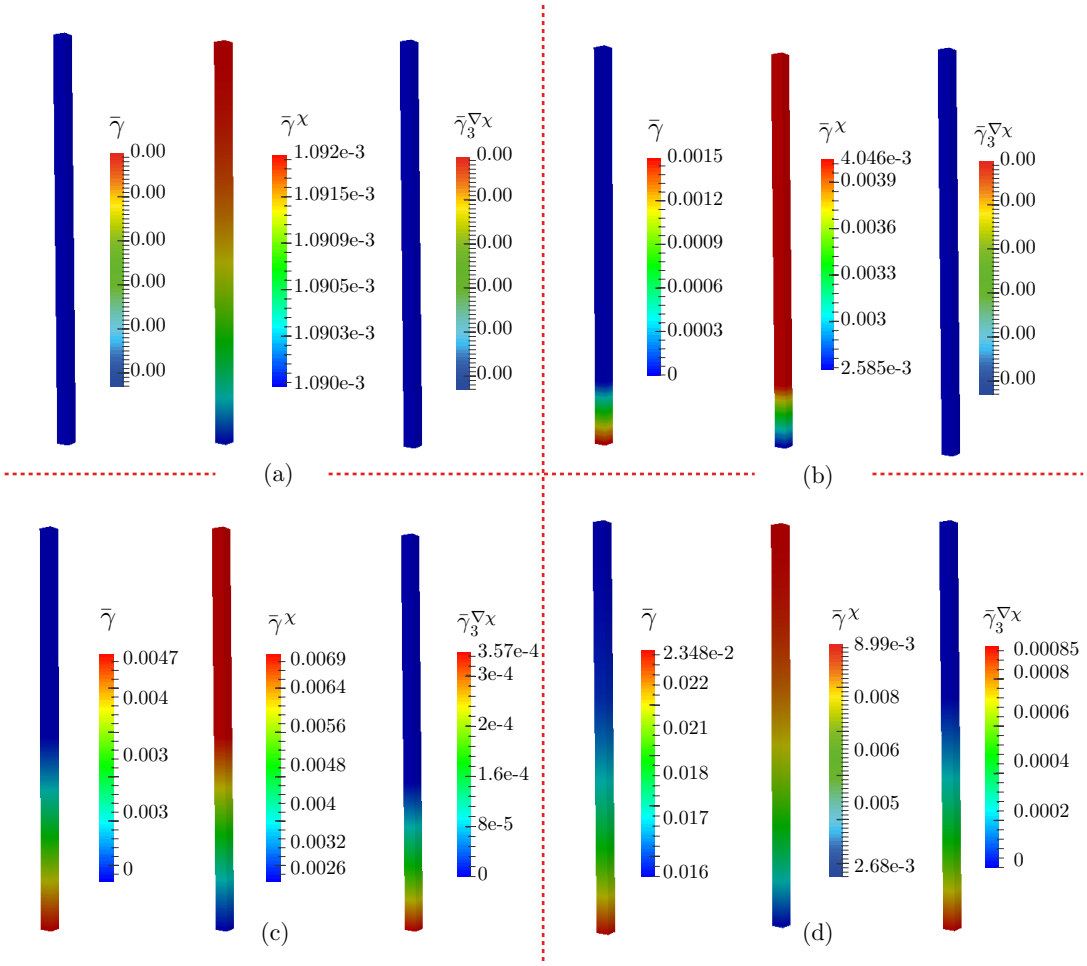

Figure 5.7. Contour plots of $\bar{\gamma}$, $\bar{\gamma}^{\chi}$, and $\bar{\gamma}_3^{\nabla\chi}$ for case Micro/Macro/Micro-gradient softening Plasticity.

ity behavior of micromorphic column. From these figures, it can be noticed that micro softening/perfect plasticity, the plastic multiplier $\bar{\gamma}^{\chi}$ reaches a larger value in comparison with the cases micro/macro/(perfect/softening plasticity). This denotes differences in the micromorphic elastoplasticity models. In the case in which both of macroscopic and microscopic plasticity levels are evolving the microscopic plasticity will be replaced with the macroscopic plasticity level. Whereas, the case with only micro plasticity, it is the only source of elastoplastic deformation. Figure 5.10 presents the Cauchy stress σ_{33}^{h} versus Eulerian strain e_{33}^{h} plot of the micromorphic elastic and elastoplastic column in comparison with the classical elastic and elastoplastic column. This figure shows that the classical softening plasticity deforms more for the fixed amount of loading in com-

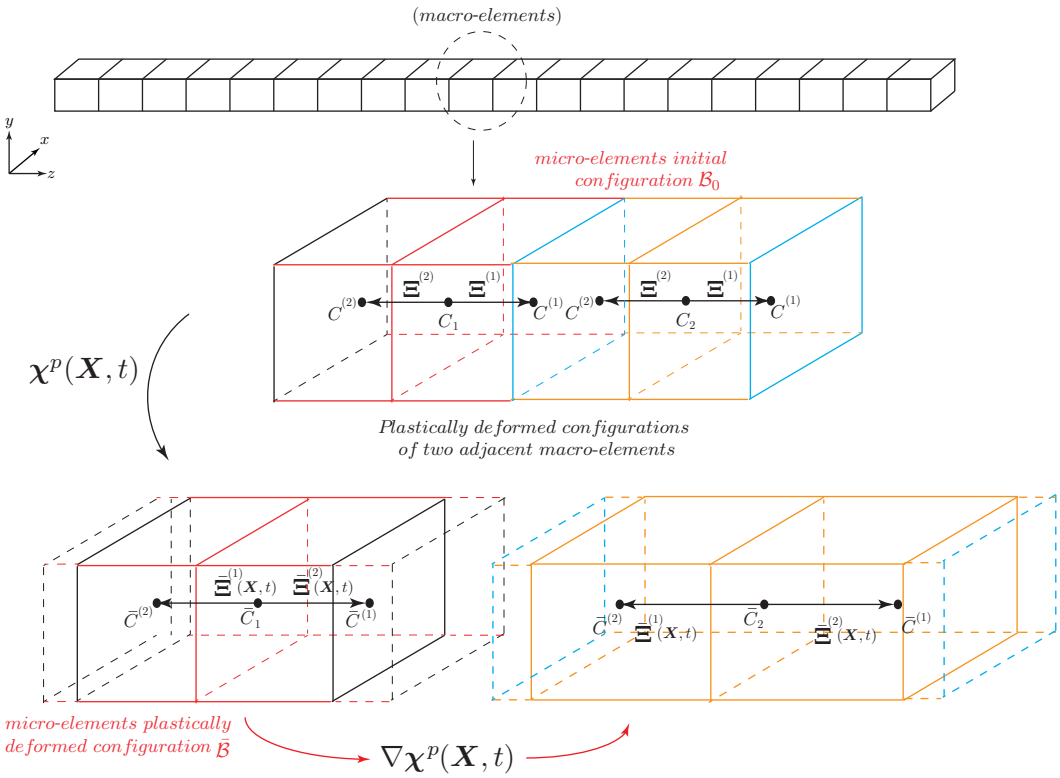

Figure 5.8. Description of plastic deformation of the micro-elements.

parison with the micromorphic softening plastic model. Figure 5.11 demonstrates the stress-strain $(\sigma^h_{33} - e^h_{33})$ curve of classical and micromorphic elastoplastic columns for both softening and the perfect plasticity models. It can be seen that plasticity at the micro-gradient level does not have a noticeable effect on the macroscopic Cauchy stress component σ^h_{33}.

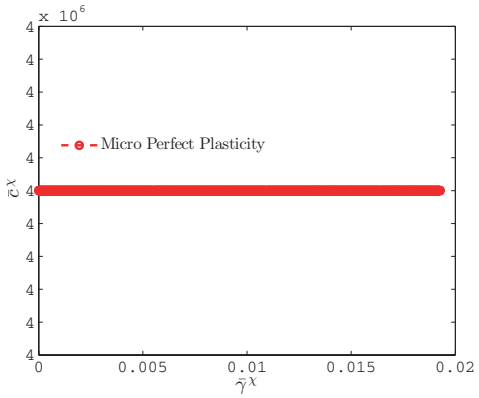

(a) $\bar{c}^\chi$-$\bar{\gamma}^\chi$ for micro perfect plasticity

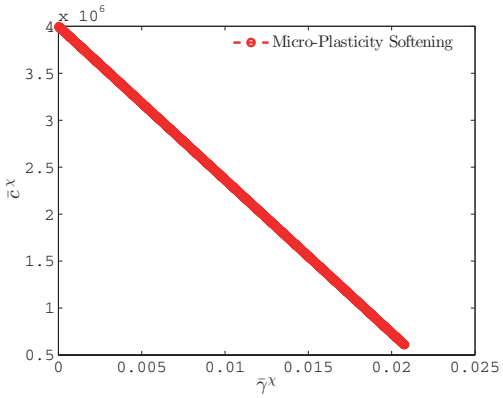

(b) $\bar{c}^\chi$-$\bar{\gamma}^\chi$ for micro softening plasticity

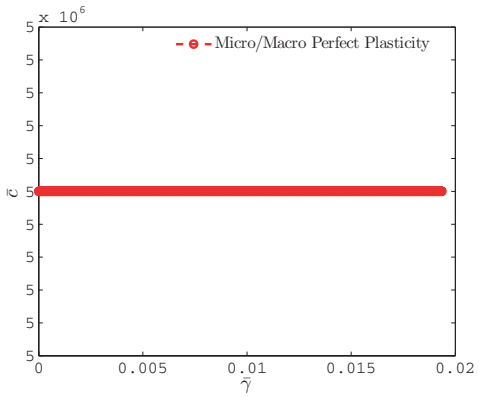

(c) $\bar{c}$-$\bar{\gamma}$ for micro/macro perfect plasticity

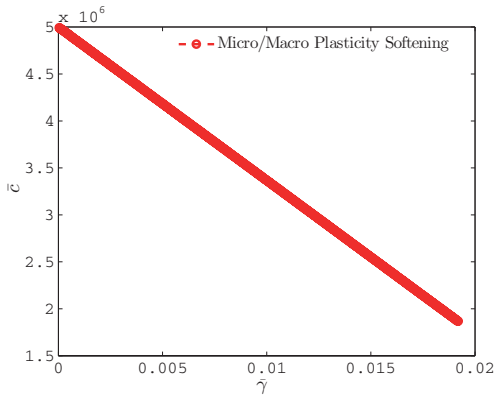

(d) $\bar{c}$-$\bar{\gamma}$ for micro/macro softening plasticity

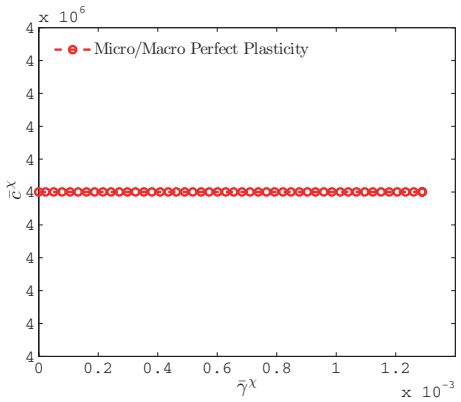

(e) $\bar{c}^\chi$-$\bar{\gamma}^\chi$ for micro/macro perfect plasticity

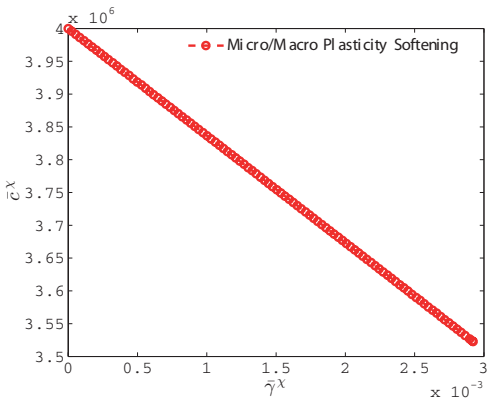

(f) $\bar{c}^\chi$-$\bar{\gamma}^\chi$ for micro/macro softening plasticity

Figure 5.9. Cohesion versus plastic multiplier for micromorphic elastoplasticity

Figure 5.12 depicts the micro-displacement component Φ^h_{33} along the length of the column. The case micro/macro/micro-grad softening plasticity (black line) shows the effect of the micro-gradient plasticity (larger gradient of Φ^h_{33} along the length as a result of the micro-gradient softening plasticity) in comparison with the case micro/macro softening plasticity without the micro-gradient softening (green line). Note that micro-gradient plasticity takes place near the bottom boundary of the column in which there is a gradient in the profile of Φ^h_{33} and in turn χ^h_{33}. Therefore, in the case micro/macro/micro-gradient perfect plasticity (blue line), larger gradient of Φ^h_{33} at the bottom boundary, is observed as a result of micro-gradient perfect plasticity in comparison with the case micro/macro softening plasticity (green line). The effect of micro-gradient perfect plasticity diminishes at the locations far from the bottom boundary, and the case micro/macro softening plasticity gets larger values for Φ^h_{33} due to micro-scale softening plasticity. Figure 5.13 presents the couple stress component $\bar{M}^h_{333}$ along the length of the micromorphic column. The cases with micro-gradient plasticity (black and blue lines) have lower magnitude of couple stress component $\bar{M}^h_{333}$ in comparison with cases with no micro-gradient plasticity (red and green lines). This happens mainly due to the larger elastoplasticity as a result of the micro-gradient plasticity and smaller portion of elastic deformation of the body. Therefore, according to the constitutive equation of the couple stress component $\bar{M}^h_{333}$ (3.104) and (3.106), the larger gradient of the plastic part of the micro-deformation tensor $\boldsymbol{\nabla\chi}^p$ leads to the smaller elastic part of the micro-deformation tensor $\nabla\boldsymbol{\chi}^e$ and, therefore, smaller $\bar{M}^h_{333}$. The comparison of couple stress component $\bar{M}^h_{333}$ from the softening plasticity analysis (for both elastoplasticity analyses with/without the micro-gradient plasticity, green and black lines) has larger magnitude than those of the prefect plasticity analyses (blue and red lines). According to Fig.5.12, the softening plasticity analysis has larger total gradient of the micro-deformation tensor $\boldsymbol{\nabla\chi}$ (larger gradient of Φ^h_{33}). This can be considered as the source of difference in the profile of $\bar{M}^h_{333}$ from softening and perfect plasticity analyses. Figure 5.14 demonstrates the effect of micro-gradient plasticity on the micro-stress component $\bar{\Sigma}^h_{33}$. The profile of the micro-stress component $\bar{\Sigma}^h_{33}$ has a gradient close to the bottom boundary of column ($u^h_3 = 0$, $\Phi^h_{33} = 0$) which is related to the gradient of the micro-displacement tensor Φ^h_{33} at that

location. Similar reasoning as those provided for the couple stress component $\bar{M}^h_{333}$ can be used to explain the effect of micromorphic elastoplasticity analyses on the profile of micro-stress component $\bar{\Sigma}^h_{33}$. Figure 5.15(b) depicts the macroscopic Cauchy stress component σ^h_{33} obtained from the micromorphic and classical elasticity and elastoplasticity analyses. Figure 5.15(a) compares the micromorphic elastoplastic models and the classical elastoplasticity via the Cauchy stress component σ^h_{33} along the length. This figure shows that in softening plasticity, the Cauchy stress component σ^h_{33} is smaller in magnitude than that of perfect plasticity model. This is because of the larger plastic deformation of the column with softening plasticity models than that of the column with perfect plasticity. This conclusion is valid for both the micromorphic and classical columns.

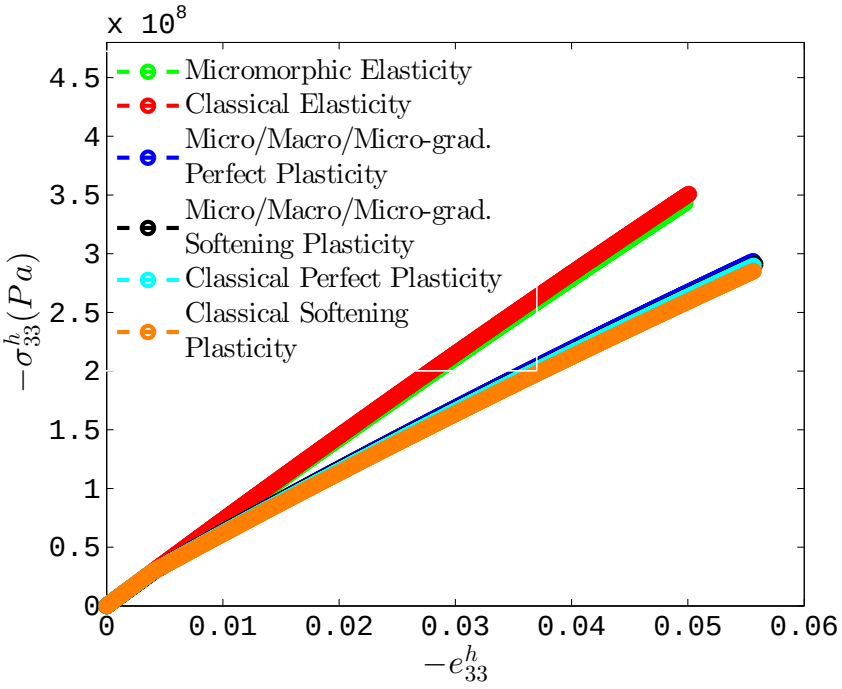

Figure 5.10. Stress-strain plot of micromorphic column versus classical column

Figure 5.16 plots stress paths for the micromorphic elastoplasticity model micro/macro perfect plasticity to better illustrate the plasticity trend in a micromorphic continuum. Figure 5.16(a) shows the second Piola Kirchhoff $\bar{\boldsymbol{S}}^h$ stress path and macroscopic yield function to demonstrate the macroscopic plasticity level in the micromorphic column. The model is perfect macroscopic plasticity, therefore, the macroscopic yield function remains unchanged. Figure 5.16(b) shows

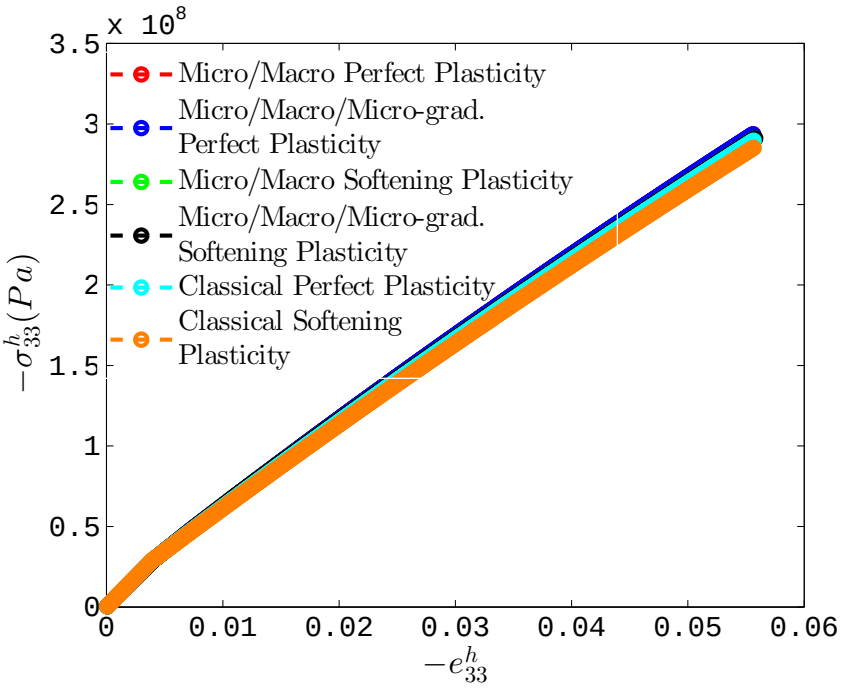

Figure 5.11. Stress-strain plots of micromorphic elastoplastic column versus classical elastoplastic column

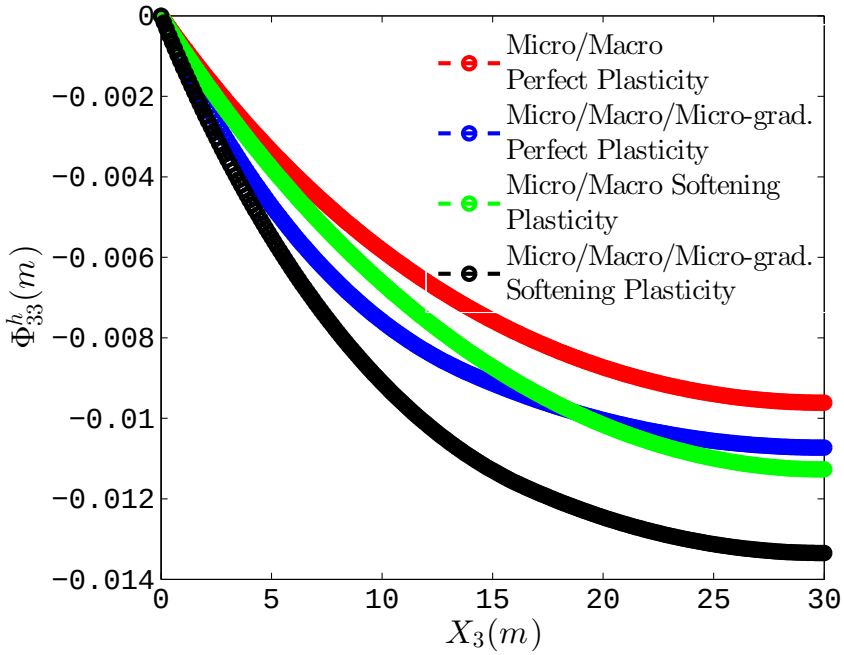

Figure 5.12. Micro-displacement tensor Φ_{33}^h along length of column

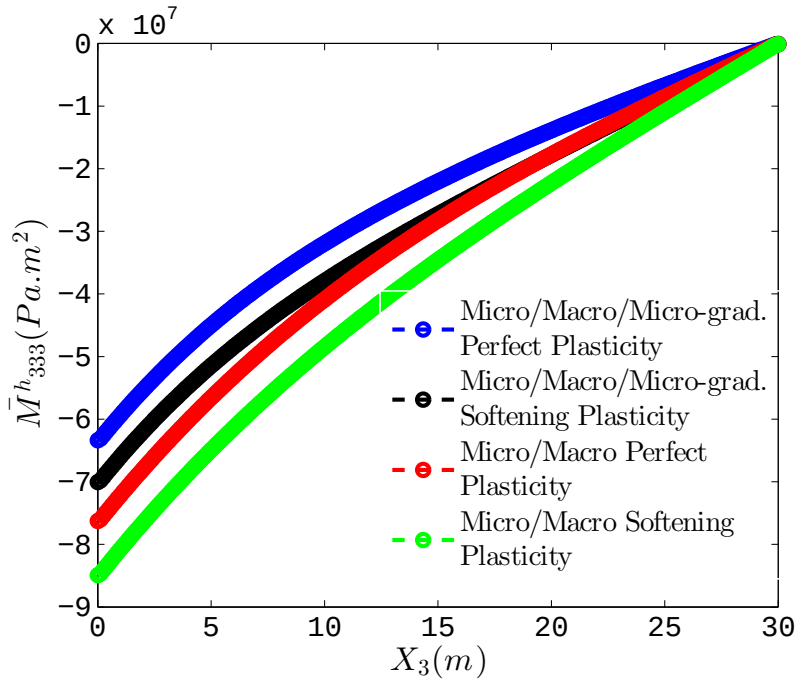

Figure 5.13. Couple stress component $\bar{M}^h_{333}$ along length of column

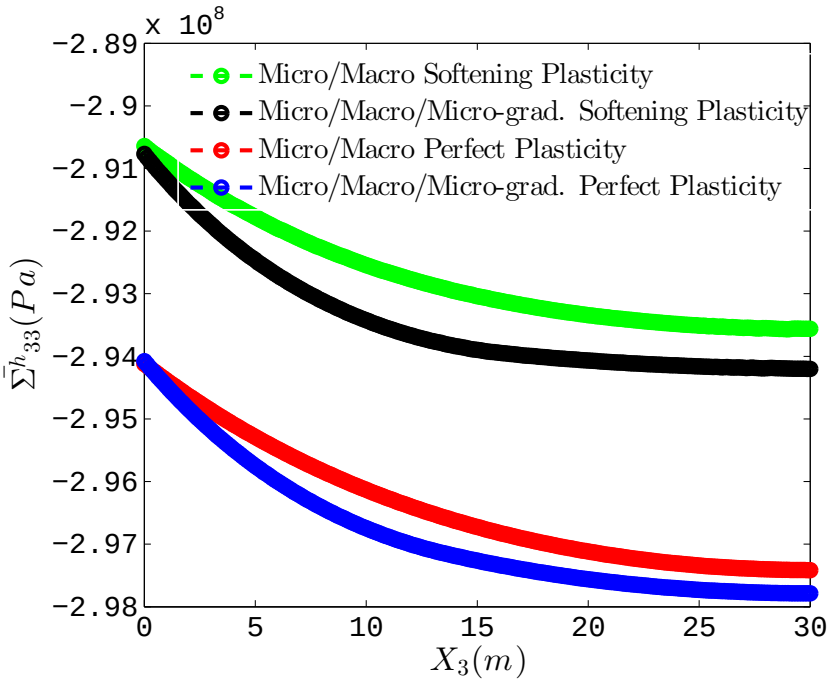

Figure 5.14. Micro-stress component $\bar{\Sigma}^h_{33}$ along length of column

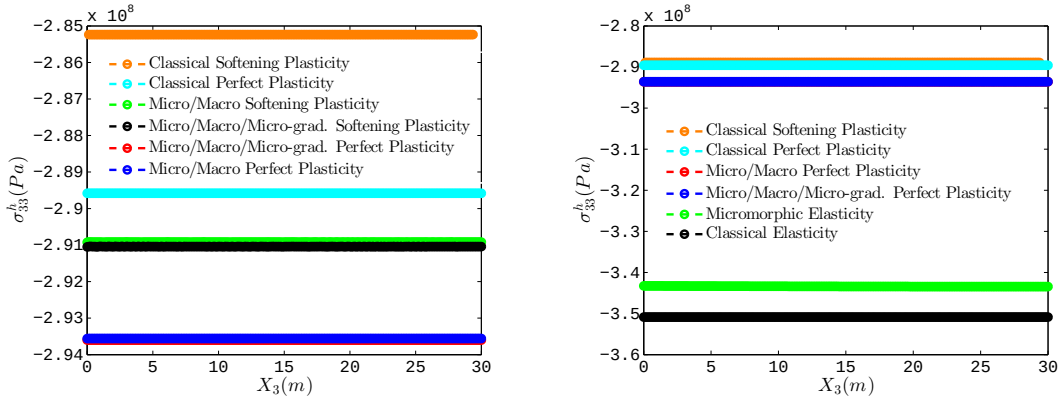

(a) Micromorphic and classical elastoplastic σ^h_{33} through length of column

(b) Comparison of σ^h_{33} obtained from elasticity and elastoplasticity analyses

Figure 5.15. Micromorphic and classical elastoplastic σ^h_{33} versus micromorphic and classical elastic σ^h_{33}

the initial steps of loading to compare the stress path of the classical perfectly plastic model and micro/macro perfectly plastic. It can be seen that in the classical perfectly plastic model, plasticity occurs earlier than that of the micro/macro perfectly plastic model. Figure 5.16(c) presents the stress path of coupled stress $\bar{\boldsymbol{M}}^h$ in elastic region and, therefore, there is no micro-gradient plasticity level in this model. Figures 5.16(d) and 5.16(e) show the stress path of micro-stress $\bar{\boldsymbol{\Sigma}}^h$ and the microscopic yield function. These plots demonstrate the microscopic plasticity level in a micromorphic column. As explained earlier, the micro-stress path will fall beneath the microscopic yield function and, therefore, there is no microscopic plasticity afterward. It can be seen that at some time steps in the model both macroscopic and microscopic plasticity occur simultaneously.

Figure 5.17 depicts stress paths for the case micro/macro/micro-grad perfect plasticity model. In this model, Fig.5.17(c) presents the micro-gradient plasticity level and couple stress $\bar{\boldsymbol{M}}^h$ stress path versus the micro-gradient yield function. Figure 5.17(e) compares the micromorphic model with only microscopic perfectly plastic micro-stress path (other levels of micromorphic plasticity will not be involved) and that of the micro/macro/micro-grad perfectly plasticity model. This figure shows that for the further time steps the microscopic plasticity in the micro/macro/micro-grad perfect plasticity model will be diminished from the model. However, this is not the case of the

micromorphic elastoplastic model with only microscopic perfect plasticity.

Figure 5.18 presents the stress path and yield functions for micromorphic case micro/macro softening plasticity. Figure 5.18(a) shows the second Piola Kirchhoff stress path and the macroscopic yield function. Figure 5.18(b) compares the second Piola Kirchhoff stress path of the micromorphic case micro/macro softening plasticity with that of classical softening plasticity. In this simulation, the micro-gradient plasticity is not involved, and the couple stress path remains in the elastic region Fig.5.18(c). Figure 5.18(d) presents the micro-stress path for micromorphic micro-plasticity level, which shows that micro-plasticity does not continue to evolve to the end of loading. Therefore, softening plasticity in the microscopic level is not noticeable in comparison with softening at macroscopic level. Figure 5.18(e) presents the micro-stress path transition from elastic to plastic loading.

Figure 5.19 presents the micromorphic elastoplasticity stress paths for case micro/macro/micro-grad softening plasticity. In this case, the micro-gradient plasticity level is also involved. Figures 5.19(a) and 5.19(b) depict micromorphic macroscopic plasticity softening through plotting the second Piola Kirchhoff stress path. Figure 5.19(c) represents the couple stress path to show the micromorphic micro-gradient plasticity level. The softening at the micro-gradient level is not considerable which can be related to the selected material parameters of elastoplastic micromorphic continuum. Figure 5.19(d) shows the micro-stress path. Similar to what is observed in the previous case, microscopic plasticity does not continue to evolve to the end of the loading, and it will be replaced with micromorphic macroscopic plasticity. Figure 5.19(e) demonstrates transition from the elastic material behavior to elastoplastic yielding via plotting the initial steps of loading.

5.2.1 Discussion on Micromorphic Elastoplastic Material Parameters

This section is presented to discuss the reasoning behind selection of micromorphic elastoplastic material parameters for the previous example (micromorphic column under uniaxial strain in compression), and also difficulties that are involved in elastoplastic analysis of a micromorphic continuum. As observed in Fig.5.6, for the case Micro/Macro/Micro-gradient Perfect Plasticity, the

selection of micromorphic elastoplastic material parameters are such that plasticity starts through yielding at the micro-scale with $\Delta\bar{\gamma}^{\chi}$ evolving. According to the evolution equations of micromorphic continuum (3.78), (3.86), (3.92), yielding at micro-scale plasticity level ($\boldsymbol{\chi}^p$ evolving) is able to drive plasticity at other scales (macro and micro-gradient) through the coupling term of $\boldsymbol{\chi}^p$ in their evolution equations ((3.78), (3.92)). Therefore, we have inherent macro and micro-gradient plasticity evolution regardless of yielding at these scales. The cases Micro Perfect/Softening Plasticity (only $\boldsymbol{\chi}^p$ evolving) are presented for the motive of presenting the effect of inherent macro and micro-gradient plasticity levels on the elastoplastic behavior of a micromorphic column in uniaxial strain comparison within the cases that the yielding occurs at the macro and micro-gradient levels. Also, this is one of the reasons for selecting the micromorphic elastoplasticity material parameters such that the micro-scale plasticity level occurs first. Then, we have the other levels of plasticity already occurring when their yieldings occur. Note that this is the only selection of micromorphic elastoplastic material parameters for which all their micromorphic plasticity levels occurred simultaneously during loading of the column. It has been observed that for selected elastic micromorphic material parameters, if macro-scale plasticity occurs first, then micro-scale plasticity will not occur throughout the simulation. The micro-gradient level plasticity may happen regardless of micro-scale plasticity level. In terms of physical interpretation, this simulation is questionable when there is no $\boldsymbol{\chi}^p$ evolving via the micro-scale plasticity level, how we can justify $\bar{\boldsymbol{\nabla}}\boldsymbol{\chi}^p$ which is the spatial gradient of $\boldsymbol{\chi}^p$. Another issue associated with this micromorphic elastoplastic simulation is that for softening plasticity analysis, after a certain amount of loading, the micro-displacement tensor component Φ^h_{33} shows expansion of micro-elements (Φ^h_{33} becomes positive, inconsistent with the macro-element displacement u^h_3) under compressive loading. As discussed earlier in the selection of micromorphic elastic material parameters, the inconsistency in the deformations of macro and micro-elements in terms of physical interpretation is not acceptable.

The difficulties involved with numerical implementation of micromorphic elastoplasticity are mainly related to searching for the macro and micro plastic multipliers $\Delta\bar{\gamma}$, $\Delta\bar{\gamma}^{\chi}$ simultaneously for the cases in which macro and micro-scale plasticity levels yieldings occur at once. The algorithm

designed for such cases in Tahoe starts solving for positive (Kuhn-Tucker condition) macro and micro-plastic multipliers ($\Delta\bar{\gamma}$, $\Delta\bar{\gamma}^{\chi}$). If the obtained plastic multipliers are not positive, then the algorithm tries to find either a positive macro-plastic multiplier $\Delta\bar{\gamma}$ or a positive micro-plastic multiplier $\Delta\bar{\gamma}^{\chi}$. If either a positive macro or micro-plastic multiplier is found then the yield function of the other scale (macro or micro yield function) must be negative (deform elastically) to accept the solution for micromorphic elastoplasticity step.

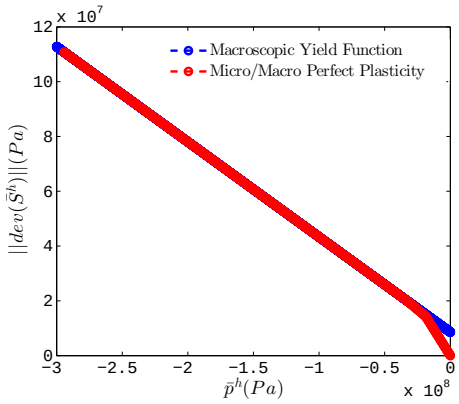

(a) $\bar{S}^h_{33}$ stress path and yield function for the micro/macro perfect plasticity

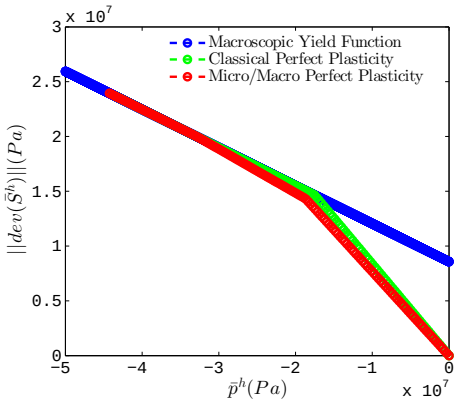

(b) The initial steps of $\bar{S}^h_{33}$ stress path of the micro/macro perfect plasticity

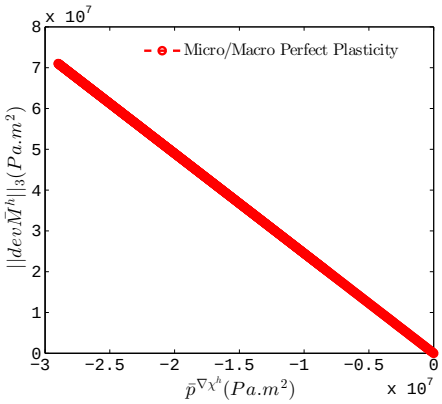

(c) $\bar{M}^h_{333}$ stress path and yield function for the micro/macro perfect plasticity

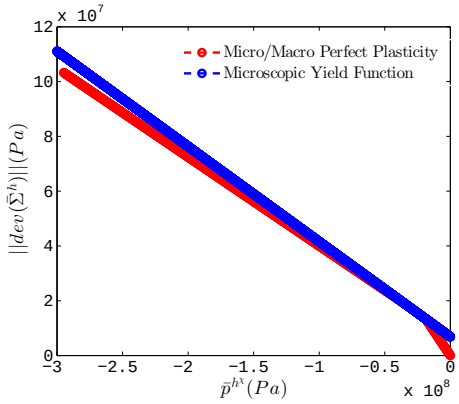

(d) $\bar{\Sigma}^h_{33}$ stress path and yield function for the micro/macro perfect plasticity

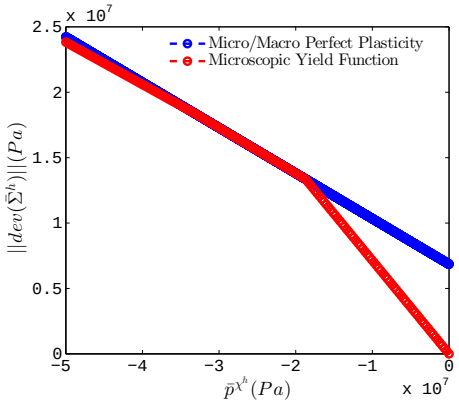

(e) The initial steps of $\bar{\Sigma}^h_{33}$ stress path of micro/macro perfect plasticity

Figure 5.16. Stress path for the micromorphic elastoplasticity case micro/macro perfect plasticity

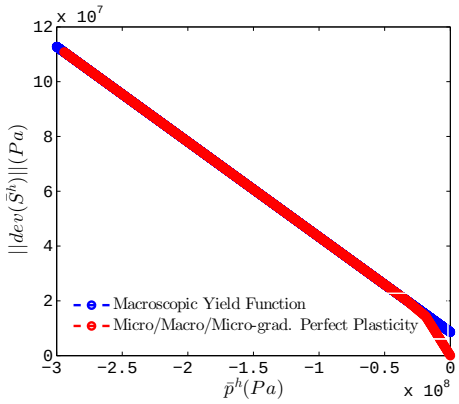

(a) $\bar{\boldsymbol{S}}^h$ stress path and yield function for micro/macro/micro-grad perfect plasticity

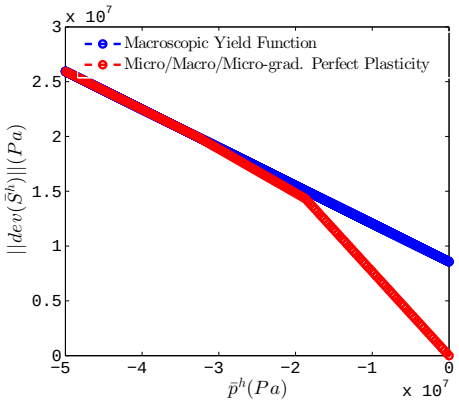

(b) Initial steps of $\bar{\boldsymbol{S}}^h$ stress path of micro/macro/micro-grad perfect plasticity

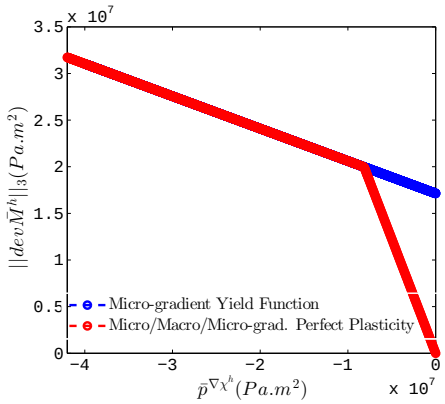

(c) $\bar{\boldsymbol{M}}^h$ stress path and yield function for micro/macro/micro-grad perfect plasticity

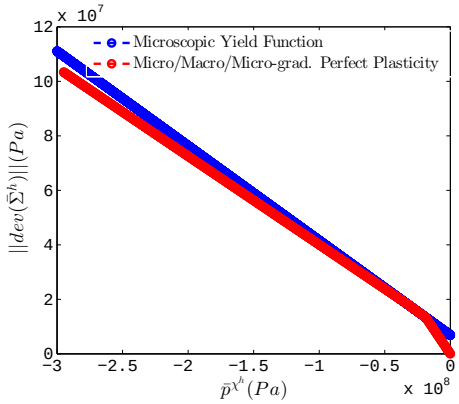

(d) $\bar{\boldsymbol{\Sigma}}^h$ stress path and yield function for micro/macro/micro-grad perfect plasticity

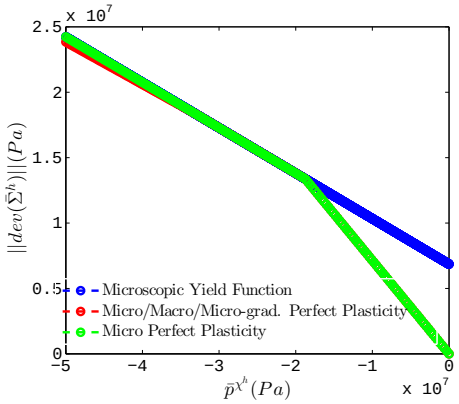

(e) Initial steps of $\bar{\boldsymbol{\Sigma}}^h$ stress path of micro/macro/micro-grad perfect plasticity

Figure 5.17. Stress path for micromorphic elastoplasticity case micro/macro/micro-grad perfect plasticity.

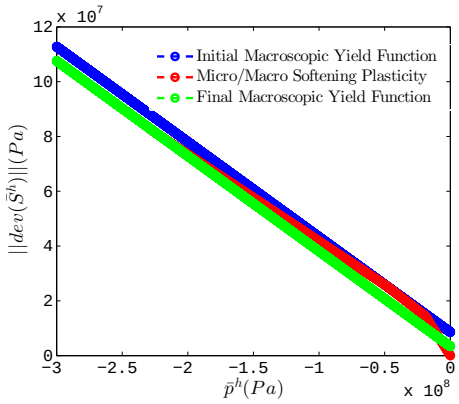

(a) $\bar{\boldsymbol{S}}^h$ stress path and yield function for micro/macro softening plasticity

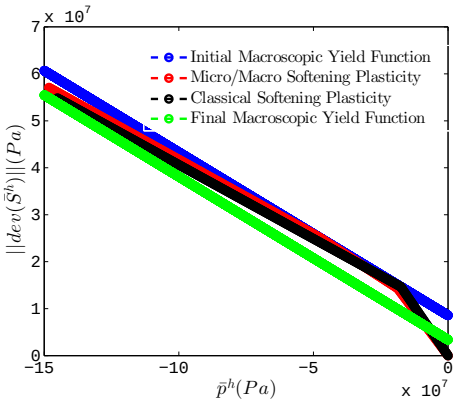

(b) Initial steps of $\bar{\boldsymbol{S}}^h$ stress path of micro/macro softening plasticity

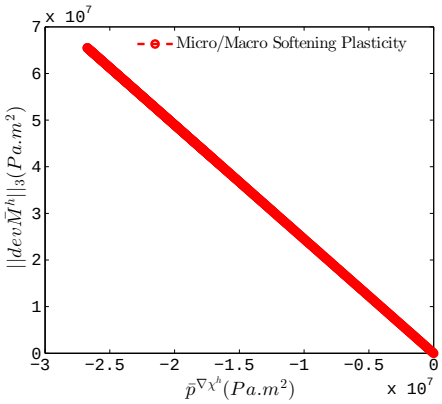

(c) $\bar{\boldsymbol{M}}^h$ stress path and yield function for micro/macro softening plasticity

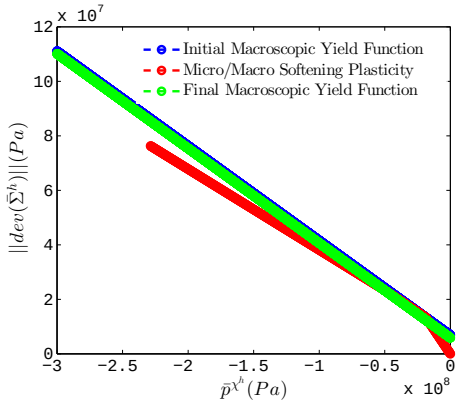

(d) $\bar{\boldsymbol{\Sigma}}^h$ stress path and yield function for micro/macro softening plasticity

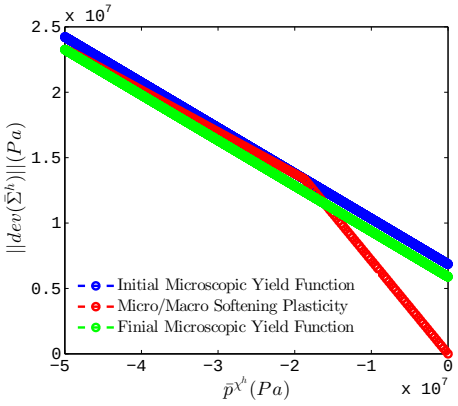

(e) Initial steps of $\bar{\boldsymbol{\Sigma}}^h$ stress path of micro/macro softening plasticity

Figure 5.18. Stress path for micromorphic elastoplasticity case micro/macro softening plasticity

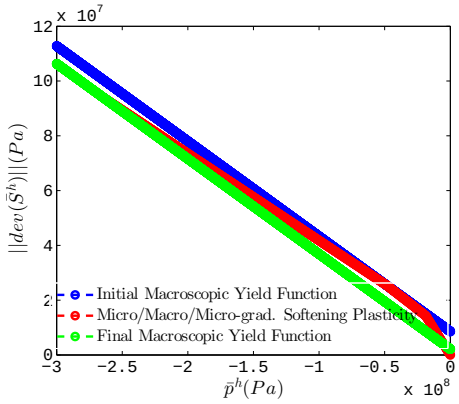

(a) $\bar{\boldsymbol{S}}^h$ stress path and yield function for micro/macro/micro-grad softening plasticity

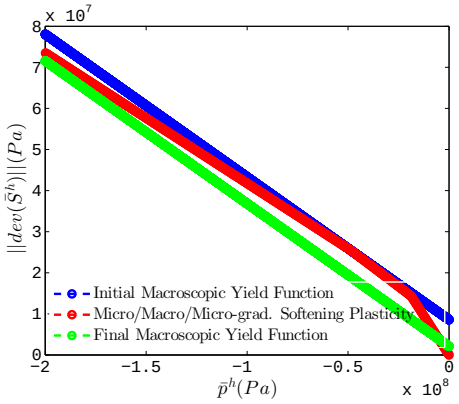

(b) Initial steps of $\bar{\boldsymbol{S}}^h$ stress path of micro/macro/micro-grad softening plasticity

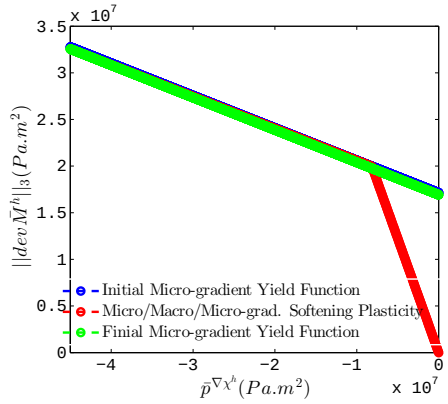

(c) $\bar{\boldsymbol{M}}^h$ stress path and yield function for micro/macro/micro-grad softening plasticity

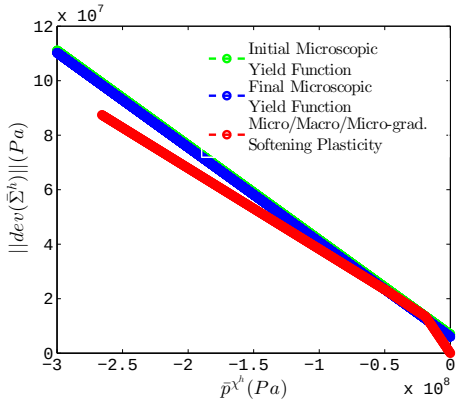

(d) $\bar{\boldsymbol{\Sigma}}^h$ stress path and yield function for micro/macro/micro-grad softening plasticity

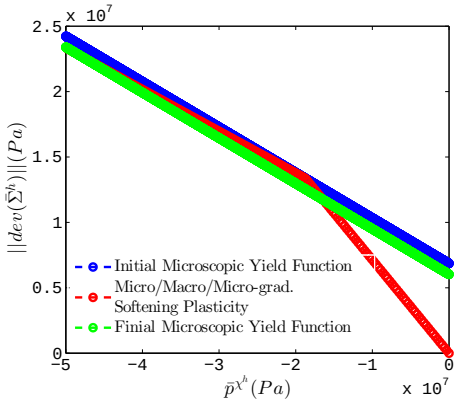

(e) Initial steps of $\bar{\boldsymbol{\Sigma}}^h$ stress path of micro/macro/micro-grad softening plasticity

Figure 5.19. Stress path for micromorphic elastoplasticity case micro/macro/micro-grad softening plasticity.

5.3 Mesh Dependence and Micromorphic Regularization of Strain Softening Plasticity

The finite element analysis of strain localization in classical softening elastoplasticity analysis might be mesh dependent. This is a fundamental issue in classical softening elastoplasticity analysis which has been addressed in the literature by Wu and Wang [2010], Borja and Regueiro [2001]. Mathematically speaking, it has been recognized that in a finite element analysis of strain localization as a result of softening elastoplasticity the governing equations may become ill-posed under certain circumstances (will not remain elliptic) [De Borst et al., 1993]. The ill-posedness of governing equations is the source of mesh dependent finite element analysis of softening elastoplasticity. Note that mesh dependency will not take place in the softening elastoplasticity where the plastic deformation is uniform (no localization). Micromorphic elastoplasticity will be investigated in this section as an applicable method which is able to regularize the mesh dependent behavior of strain localization in softening elastoplasticity analysis. Figure 5.20 illustrates the model in which strain localization is simulated by the micromorphic and classical elastoplasticity models.

Note that the imperfection in the FE mesh in applied through a weak element in the middle of the column for all the mesh configurations is used to study mesh dependency. A weak element denotes an element with lower cohesion $\bar{c}$ and micro-cohesion $\bar{c}^{\chi}$. Note that with a finer mesh, the imperfection in the model will be smaller in terms of weak element length versus the column length. The elastic material parameters are similar to those of Table 5.1. The parameters associated with elastoplastic analysis are presented in Table 5.3. The BCs are presented in Table 5.4.

Figure 5.21 plots the Cauchy stress component σ^h_{33} versus the displacement component u^h_3 for different meshes. As noted earlier, the size of imperfection zone is equal to the thickness of the element in the middle of the column. As the mesh is refined the size of imperfection becomes smaller. From Fig.5.21(a), it can be seen that for the finer mesh, the plastic strain localized in the imperfection zone is larger, and the resulting load drop is considerable. This figure shows that in this model, softening elastoplasticity behavior of classical continuum is totally dependent

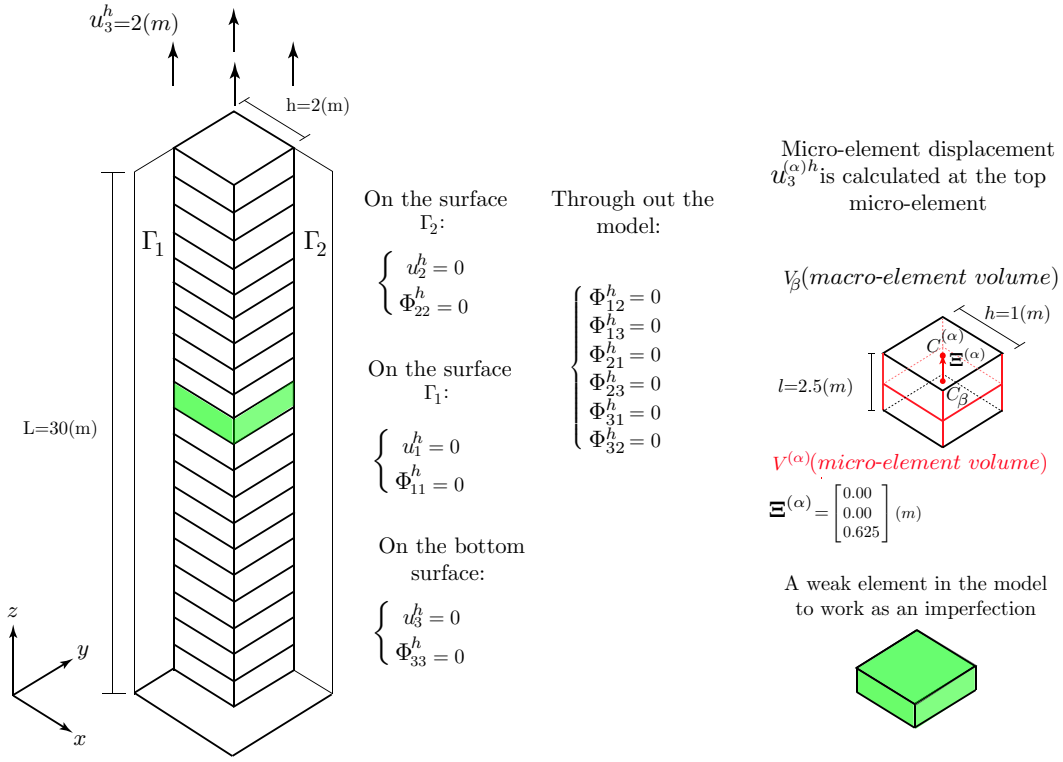

Figure 5.20. Schematic of the model for mesh dependency analysis

on the mesh size and the size of imperfection region. Figure 5.21(b) shows that micromorphic elastoplasticity can be considered as a remedy to the mesh dependent deficiency of the classical elastoplasticity. The results from the micromorphic elastoplasticity analysis converged for the finer meshes.

Table 5.3. The selected material parameters for micromorphic continuum

Micromorphic Elastoplasticity				
$H(Pa)$	$\bar{c}(Pa)$	$H^{\chi}(Pa)$	$\bar{c}^{\chi}(Pa)$	
-9e7	5e6	-9e7	4e6	
Micromorphic weak element				
$H(Pa)$	$\bar{c}(Pa)$	$H^{\chi}(Pa)$	$\bar{c}^{\chi}(Pa)$	
-9e7	4.1e6	-9e7	3.1e6	
Classical Continuum	Softening properties		Weak element properties	
	$H(Pa)$	$\bar{c}(Pa)$	$H(Pa)$	$\bar{c}(Pa)$
	-9e7	5e6	-9e7	4.1e6

Table 5.4. Selected BCs for column under tensional load

Micromorphic Continuum			
Throughout the column	On surface Γ_1	On surface Γ_2	On bottom Surface
$\Phi^h_{12}, \Phi^h_{21}, \Phi^h_{13}, \Phi^h_{31}, \Phi^h_{23}, \Phi^h_{32} = 0$	$\Phi^h_{11} = 0$	$\Phi^h_{22} = 0$	$\Phi^h_{33} = 0$
	$u^h_1 = 0$	$u^h_2 = 0$	$u^h_3 = 0$
Classical Continuum			
Throughout the column	On surface Γ_1	On surface Γ_2	On bottom Surface
	$u^h_1 = 0$	$u^h_2 = 0$	$u^h_3 = 0$

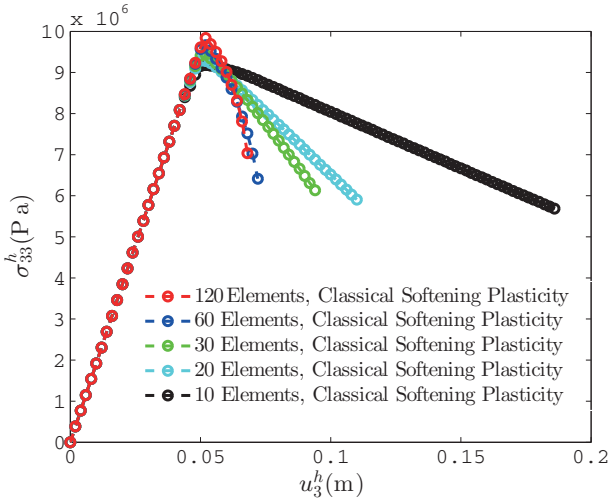

(a) Cauchy stress component σ^h_{33} versus displacement component u^h_3 for classical elastoplasticity

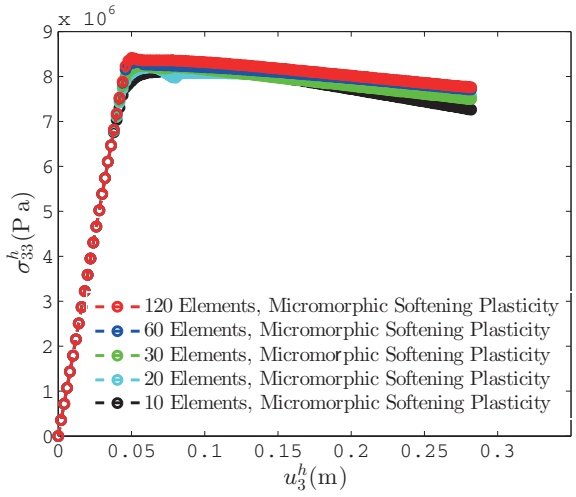

(b) Cauchy stress component σ^h_{33} versus displacement component u^h_3 for micromorphic elastoplasticity

Figure 5.21. Mesh dependent classical softening elastoplasticity versus mesh independent micromorphic softening elastoplasticity

The next few sections focus on comparing micromorphic to micropolar and classical elasticity.

5.4 Beam Bending

5.4.1 Comparison of Q27P8 and Q8P8 Elements

Before evaluating the similarities and differences between micromorphic and micropolar elasticity theories, the performance of these two elements are compared to deduce which element is the most appropriate for micromorphic simulations considering convergence as well as cost. The comparison is done via simulating a cantilevered beam under a concentrated load applied at the end of the beam. The schematic of the beam is shown in Fig.5.22. From this figure it can be seen that there are three sets of boundary conditions (BCs) on the micro-displacement tensor $\mathbf{\Phi}^h$ to investigate their effects on the macroscopic behavior of the beam. Table 5.5 summarizes the cases with various sets of BCs on the micromorphic dofs, as well as setting certain dofs=0 within the beam.

Table 5.5. Selected BCs for micromorphic dofs.

	On surface Γ	Throughout the beam
Case A	$\Phi^h_{11}, \Phi^h_{22}, \Phi^h_{33}, \Phi^h_{13}, \Phi^h_{31} = 0$	$\Phi^h_{21}, \Phi^h_{21}, \Phi^h_{23}, \Phi^h_{32} = 0$
Case B	$\Phi^h_{11}, \Phi^h_{22}, \Phi^h_{33} = 0$	$\Phi^h_{21}, \Phi^h_{21}, \Phi^h_{23}, \Phi^h_{32}, \Phi^h_{13}, \Phi^h_{31} = 0$
Case C	$\Phi^h_{13}, \Phi^h_{31} = 0$	$\Phi^h_{11}, \Phi^h_{22}, \Phi^h_{33}, \Phi^h_{21}, \Phi^h_{21}, \Phi^h_{23}, \Phi^h_{32} = 0$

Note that the FE results are plotted along the bold line at the top left of the beam shown in Fig.5.22. The performance of the Q8P8 and Q27P8 elements has been investigated via selecting the BCs and dofs Case A for which the micro-stretch, as well as micro-rotation dofs, are included in the simulation of micromorphic beam bending. The selected material parameters for the beam model are presented in Table 5.6.

Figure 5.23 illustrates the performance of the Q8P8 and Q27P8 elements for the normalized deflection $3EIu^h_3/(FL^3)$ and rotation $\Phi_2^{\mathrm{rot},h}$ of the cantilevered beam (recall for the micromorphic FE model, $\Phi_2^{\mathrm{rot},h} = (\Phi^h_{13} - \Phi^h_{31})/2$). It can be concluded that the results of the Q8P8 and Q27P8 elements are relatively close to each other. Note that Isbuga and Regueiro [2011] used the Q27P8 element in creating meshes for their three-dimensional micromorphic finite element models. In this

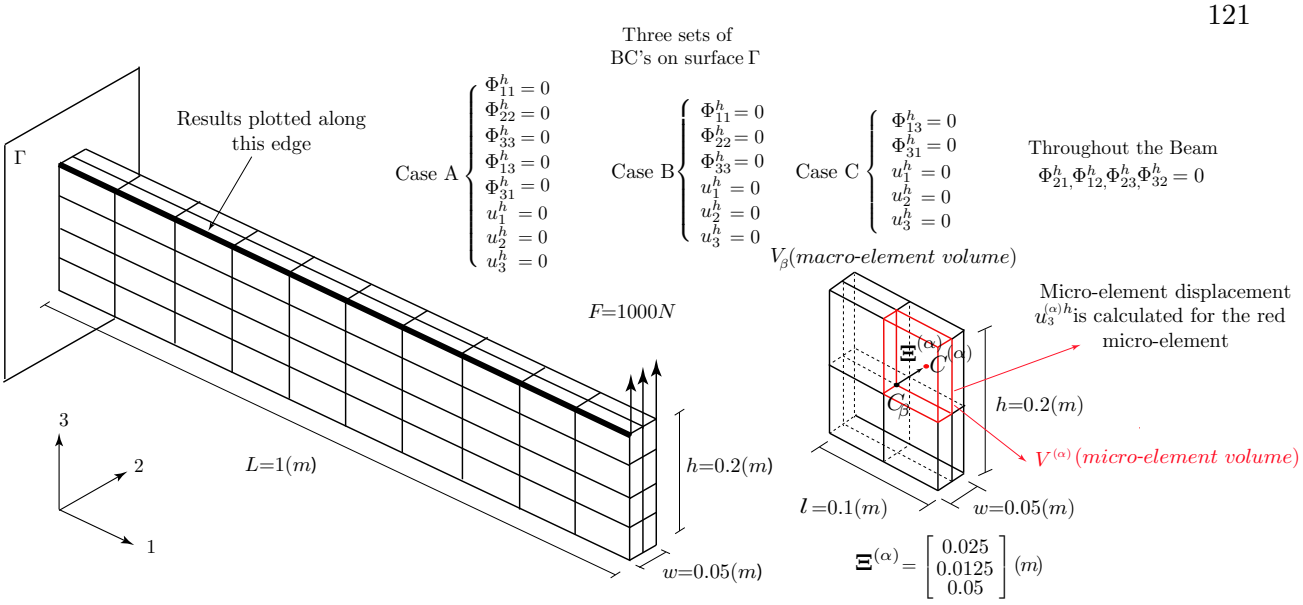

Figure 5.22. Schematic of cantilevered beam under concentrated load. V_β denotes the averaging domain for a macro-element continuum point with centroid C_β. The red cube denotes the micro-element volume $V^{(\alpha)}$ with centroid $C^{(\alpha)}$ and relative position vector $\boldsymbol{\Xi}^{(\alpha)}$.

section, relying on the good accuracy obtained from the Q8P8 element in comparison with the Q27P8 element, the rest of the simulations are conducted with the Q8P8 element to reduce the computational cost of 3D micromorphic FEA. The obtained convergence profile by the Newton-Raphson algorithm at the first and last time steps is presented in Table 5.7. Figure 5.24 illustrates a mesh refinement study on the micromorphic cantilevered beam using Q8P8 element. By demonstration, the results are convergent with respect to mesh refinement.

5.4.1.1 Effects of $\boldsymbol{\Phi}^h$ BCs and dofs

Regarding the micromorphic elastic material parameters, it should be mentioned that the constitutive equations for the micromorphic stresses may be calibrated through lower length-scale direct numerical simulation (DNS) micro-structural simulations [Regueiro et al., 2014] as shown in chapter 4. Since we are not yet able to calibrate material parameters in that manner, they are instead selected within the range of Smith [1968]'s constraints not to violate positiveness of the strain energy function. Besides those constraints, we should be aware of the values of $\boldsymbol{u}^h$, $\boldsymbol{u}^{(\alpha),h}$ and $\boldsymbol{\Phi}^h$ reflecting

Table 5.6. Selected material parameters for micromorphic beam bending example.

Micromorphic Continuum					
$\lambda(Pa)$	$\mu(Pa)$	$\eta(Pa)$	$\kappa(Pa)$	$\nu(Pa)$	$\sigma(Pa)$
8e9	11e9	2e9	-1.0e9	-1.39e9	-2.11e9
$\tau(Pa)$	$\tau_1(Pa.m^2)$	$\tau_2(Pa.m^2)$	$\tau_3(Pa.m^2)$	$\tau_4(Pa.m^2)$	$\tau_5(Pa.m^2)$
1.538e9	0.0	0.0	0.0	0.0	0.0
$\tau_6(Pa.m^2)$	$\tau_7(Pa.m^2)$	$\tau_8(Pa.m^2)$	$\tau_9(Pa.m^2)$	$\tau_{10}(Pa.m^2)$	$\tau_{11}(Pa.m^2)$
0.0	0.769e6	0.0	0.0	0.0	0.0
Micropolar Continuum					
$\lambda(Pa)$	$\bar{\mu}(Pa)$	$\bar{\eta}(Pa)$	$\bar{\alpha}(Pa.m^2)$	$\beta(Pa.m^2)$	$\bar{\gamma}(Pa.m^2)$
11.53e9	7.5e9	3.84e9	0.0	0.0	1.53e6

the deformations of micro-structured solids. The macro and micro scale deformations should be consistent with each other (i.e., both in tension, both in compression, etc.). From the physical perspective, this means that the resulting macroscopic displacement vector $\boldsymbol{u}^h$ and micro-displacement tensor $\boldsymbol{\Phi}^h$ need to be consistent with each other (i.e., if a micromorphic continuum solid is under quasi-static compression in the X_3 direction, u_3^h and Φ_{33}^h should both be negative to reflect compression in both of the macro and micro-elements). From Table 5.6, it can be observed that the selected material parameters, κ, ν, and σ have negative values. The reason for this selection is that it has been observed that if all of the micromorphic material parameters are selected to be positive, we are not able to obtain consistent macro and micro-element deformations through $\boldsymbol{u}^h$ and $\boldsymbol{\Phi}^h$. The inconsistent deformations in the micromorphic continuum means that the micro-element deformation represents tension while the macro-elements and the whole macroscopic structure are under compression. In this paper, therefore, the material parameters are selected such that the positiveness of strain energy function will be satisfied as well as the deformations of the micromorphic solid in the macro and micro-elements are representing the physics of the problem. In the following, the effects of BCs on $\boldsymbol{\Phi}^h$ will be investigated, and the numerical results will be compared with an analytical solution of a micropolar cantilevered beam model by Ramezani et al. [2009] (a similar problem was analyzed using a 1D micropolar FE model in Regueiro and Duan [2015]). Figure 5.25(a) illustrates the normalized deflection of a micromorphic cantilevered beam for three sets of micromorphic BCs,

Table 5.7. Global convergence profile obtained by Newton-Raphson at the first and final time steps.

Step	Iteration Number	residual error
1 of 20	1^{st}	7.811564×10^{-04}
	2^{nd}	1.584514×10^{-09}
20 of 20	1^{st}	2.217045×10^{-02}
	2^{nd}	5.267324×10^{-08}

and is compared with the micropolar theory, classical FE model, and the classical beam models. From the figure, it can be observed that an appropriate selection of BCs on $\mathbf{\Phi}^h$ is crucial. One of the challenges associated with using micromorphic continua is an appropriate selection of BCs for the additional dofs $\mathbf{\Phi}^h$. Selecting inappropriate BCs may either lead to insensible results or numerical instabilities in the nonlinear finite element model. The normalized deflection from Case B, which only involves the micro-stretch dofs ($\Phi^h_{11}, \Phi^h_{22}, \Phi^h_{33}$), exhibits considerably stiff macroscopic behavior. By involving the micro-shear dofs Φ^h_{31} and Φ^h_{13} in Cases A and C, with and without the micro-stretch components, respectively, the normalized deflections then fall in the same range as the classical (Timoshenko and Goodier [1969]) and the micropolar (Ramezani et al. [2009]) theories. Note that the largest deflection is obtained from the micromorphic model Case A involving all the micro-stretch and micro-shear components of $\mathbf{\Phi}^h$ enabled. From the perspective of comparing to the micropolar theory, it can be noticed that the deflection from the micromorphic Case C (only the micro-shear dofs Φ^h_{13}, Φ^h_{31}) are in good agreement with the micropolar theory, as is to be expected since these are the only additional dofs available to the micropolar theory. Figure 5.25(b) illustrates the micro-rotation $\Phi^{\mathrm{rot},h}_2$ from the micromorphic theory as it compares to the micropolar theory for two sets of micromorphic BCs: Case A (micro-stretch with micro-shear components), and Case C (micro-shear without micro-stretch components). It is observed that the micro-rotation from Case C is in good agreement with the micropolar theory. Figure 5.26 illustrates the macroscopic axial displacement u^h_1 and the micro-stretch component Φ^h_{11} plotted along the bold solid line in Fig.5.22. It can be observed that the micro-stretch component Φ^h_{11} has a sharp gradient near the boundary. Note that the macroscopic and microscopic deformations are consistent: the macroscopic displacement of the beam, u^h_1, illustrates compression, and the corresponding micro-stretch component Φ^h_{11}

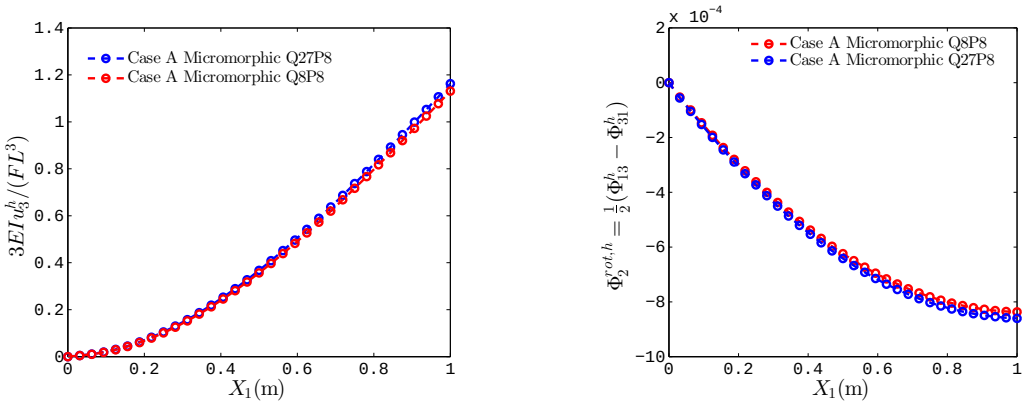

(a) Normalized beam deflection. (b) $\Phi_2^{\text{rot},h}$ along beam length.

Figure 5.23. Comparison of performance of Q8P8 and Q27P8 elements in Tahoe.

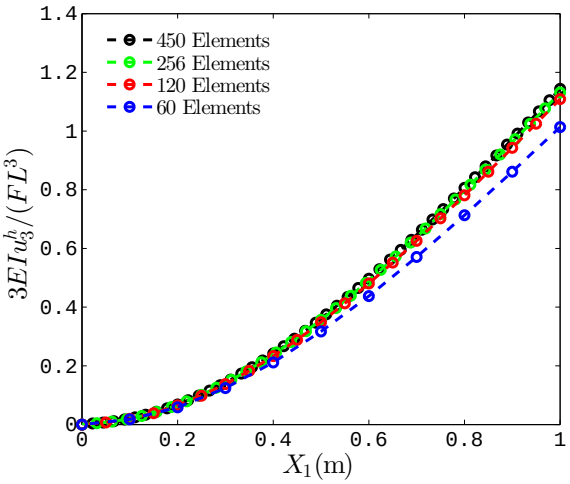

Figure 5.24. Mesh refinement study on cantilevered beam using Q8P8 element.

is also in compression. Figure 5.27 shows the contour plots of u_3^h and Φ_{11}^h for the micromorphic cantilevered beam.

Figure 5.28 illustrates the macroscopic displacement u_3^h and the micro-element displacement $u_3^{(\alpha),h}$ for small and finite strain FE analyses. As mentioned earlier, $u_3^{(\alpha),h}$ represents the micro-element displacement by accounting for the relative position vector $\boldsymbol{\Xi}^{(\alpha)}$ and the micro-displacement tensor $\boldsymbol{\Phi}^h$. It can be seen that in case B, in which the only dofs are the micro-stretch terms, the macro-element displacement u_3^h and the micro-element displacement $u_3^{(\alpha),h}$ are close representing very stiff material micro-structure. Note that in the other cases $u_3^{(\alpha),h}$ is larger than u_3^h, but only slightly.

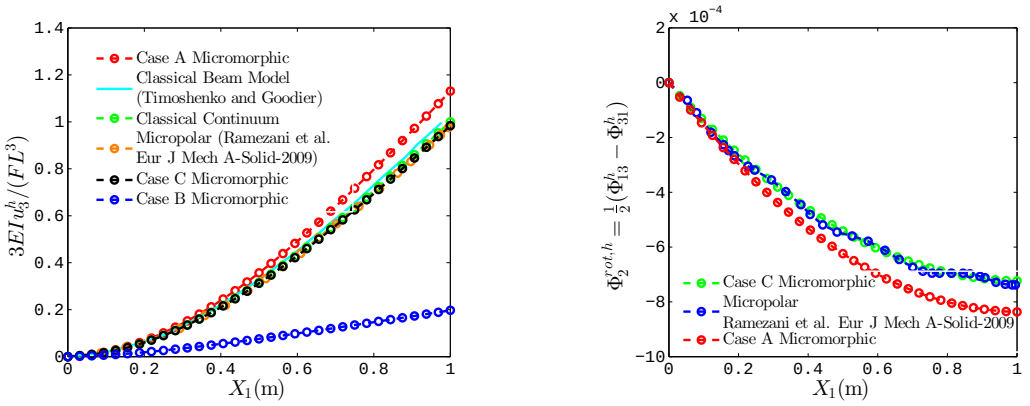

(a) Normalized vertical deflection of cantilevered beam.

(b) Micro-rotation $\Phi_2^{\mathrm{rot},h}$ obtained from micromorphic and micropolar continua.

Figure 5.25. Normalized deflection and micro-rotation along the length.

Since the selected relative position vector $\boldsymbol{\Xi}^{(\alpha)}$ is relatively large compared to the geometry of the model (see Fig.5.22), the difference between the micro-element displacement $u_3^{(\alpha),h}$ and the macro-element displacement u_3^h becomes noticeable.

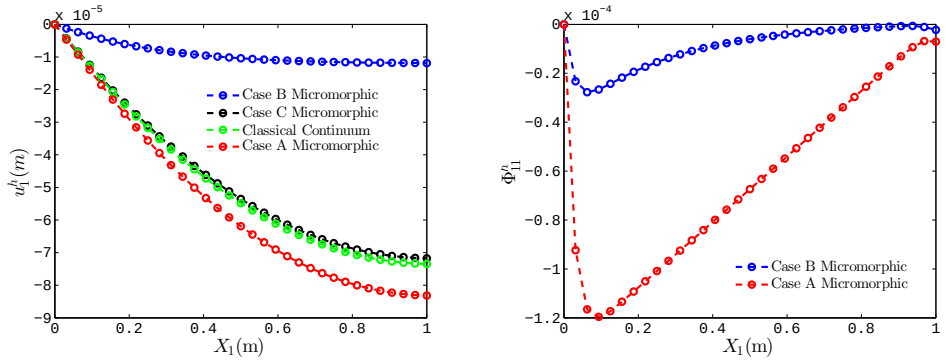

(a) Axial displacement u_1^h along the length. (b) Φ_{11}^h along the length.

Figure 5.26. Macroscopic displacements and micro-stretch components plotted along the length of the beam along the bold line in Fig.5.22.

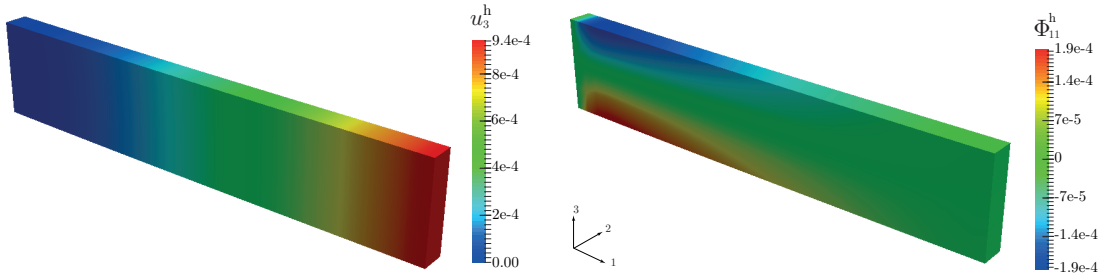

(a) Vertical deflection u_3^h. (b) Micro-stretch Φ_{11}^h.

Figure 5.27. Contour plots and deformed shape of cantilevered beam.

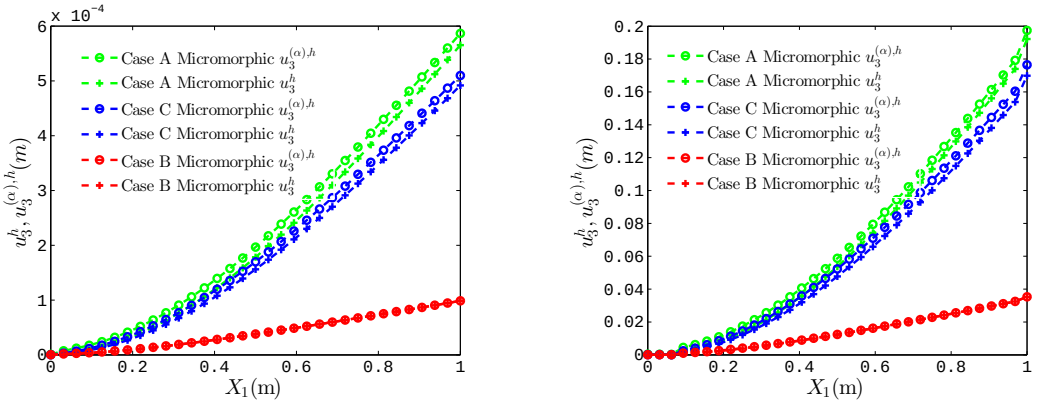

(a) Vertical deflection u_3^h and $u_3^{(\alpha),h}$ for small strain analysis. (b) Vertical deflection u_3^h and $u_3^{(\alpha),h}$ for finite strain analysis.

Figure 5.28. Comparison of macroscopic displacement u_3^h and micro-element displacement $u_3^{(\alpha),h}$.

5.4.2 Plate with a Circular Hole under Uniform Loading

The second example is a 1m square plate with a hole (radius $a = 0.05m$), at the center under a uniform loading $t^{\sigma} = 2 \times 10^4 (Pa)$ at the left and right edges (Fig.5.29). This example is conducted to compare the micromorphic continuum theory against the classical and the micropolar continuum theories on calculating stress concentration and stress distribution around a circular hole.

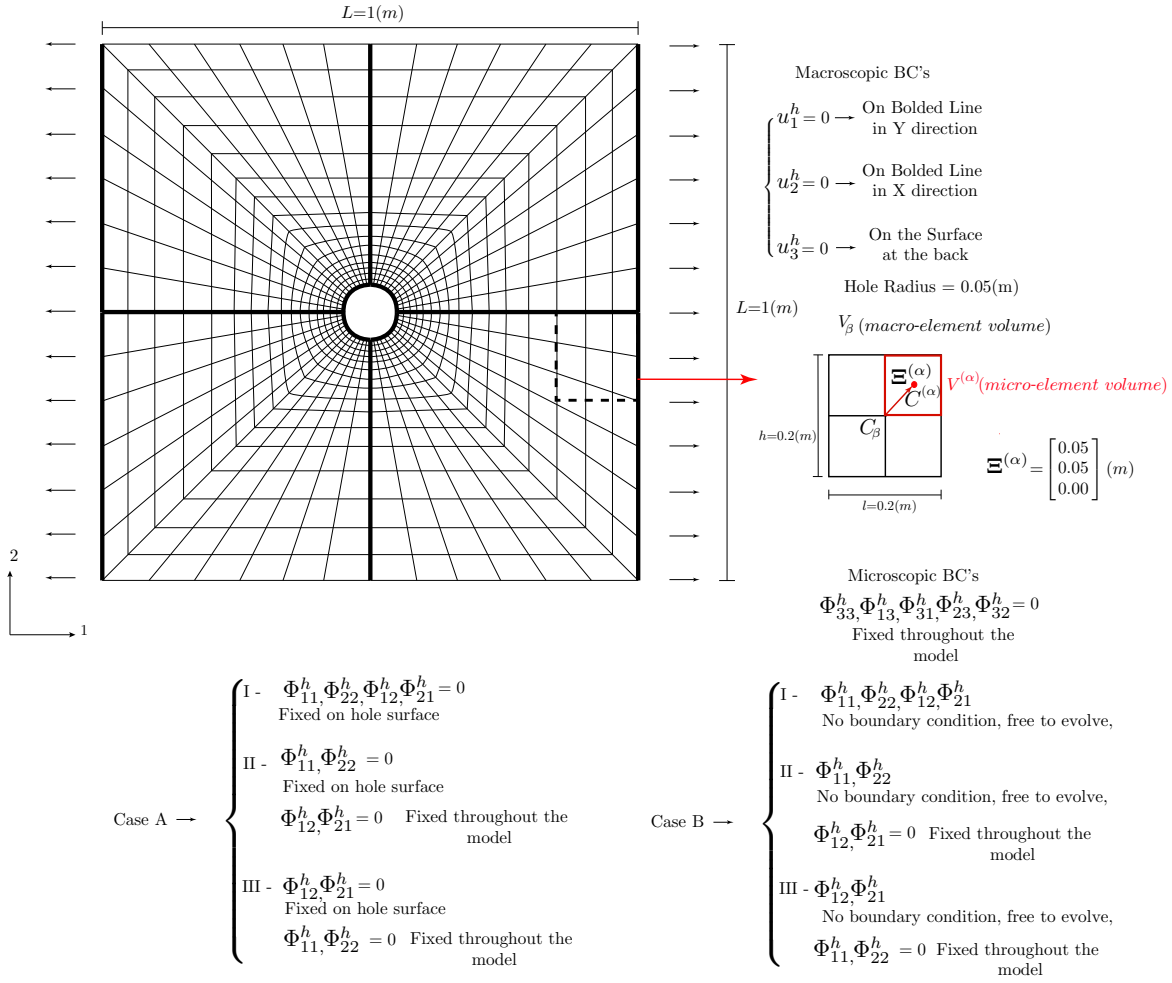

Figure 5.29. Schematic of FE mesh and BCs for plate with circular hole at center.

According to Fig.5.29 and Table 5.8, six sets of BCs on the micromorphic dofs have been considered. The BCs have been divided into two main categories: Case A and Case B. In Case A, BCs on $\mathbf{\Phi}^h$ have been applied to the hole surface, and in Case B there are no BCs applied on $\mathbf{\Phi}^h$. In each of

Table 5.8. Selected BCs and micromorphic dofs for plate with hole.

Case A	On the hole	Throughout the plate
I	$\Phi^h_{11}, \Phi^h_{22}, \Phi^h_{12}, \Phi^h_{21} = 0$	$\Phi^h_{13}, \Phi^h_{31}, \Phi^h_{23}, \Phi^h_{32}, \Phi^h_{33} = 0$
II	$\Phi^h_{11}, \Phi^h_{22} = 0$	$\Phi^h_{12}, \Phi_{21}, \Phi^h_{13}, \Phi^h_{31}, \Phi^h_{23}, \Phi^h_{32}, \Phi^h_{33} = 0$
III	$\Phi^h_{12}, \Phi^h_{21} = 0$	$\Phi^h_{11}, \Phi_{22}, \Phi^h_{13}, \Phi^h_{31}, \Phi^h_{23}, \Phi^h_{32}, \Phi^h_{33} = 0$
Case B	Free dofs	
I	$\Phi^h_{11}, \Phi^h_{22}, \Phi^h_{12}, \Phi^h_{21}$	$\Phi^h_{13}, \Phi^h_{31}, \Phi^h_{23}, \Phi^h_{32}, \Phi^h_{33} = 0$
II	Φ^h_{11}, Φ^h_{22}	$\Phi^h_{12}, \Phi_{21}, \Phi^h_{13}, \Phi^h_{31}, \Phi^h_{23}, \Phi^h_{32}, \Phi^h_{33} = 0$
III	Φ^h_{12}, Φ^h_{21}	$\Phi^h_{11}, \Phi_{22}, \Phi^h_{13}, \Phi^h_{31}, \Phi^h_{23}, \Phi^h_{32}, \Phi^h_{33} = 0$

the Cases A and B, the effects of BCs on the micro-shear, micro-stretch, and their combination on the macroscopic response have been studied. The selected material parameters for micromorphic and micropolar elasticity are presented in Table 5.9.

Figure 5.30 illustrates the stress concentration with respect to radial distance r from the center of the circular hole (with radius $a = 0.05m$) estimated by the micromorphic, micropolar, and the classical elasticity theories. Note in the figure that the results of the micromorphic continuum for Case B (there is no BC applied on $\mathbf{\Phi}^h$) are compared with the micropolar and classical elasticity theories. The micromorphic continuum theory with only micro-shear dofs Φ^h_{12} and Φ^h_{21} (Case B-III) simulates the closest result to the micropolar theory in Bauer et al. [2010]. Note that this is similar to the beam example in Section 5.4 wherein the results of a micromorphic beam with only the micro-shear dofs are closest to those of the micropolar theory. The cases with only micro-stretch dofs (Case B-II), and the combination of micro-stretch and micro-shear dofs (Case B-I), estimate slightly lower stress around the hole. Figure 5.31 shows the effect of micromorphic BCs on the macroscopic response. It can be seen that for Case A (BCs on $\mathbf{\Phi}^h$ around the hole) where the micro-stretch dofs (Φ^h_{11},Φ^h_{22}, Case A-II), and the combination of micro-stretch and micro-shear (Φ^h_{11}, Φ^h_{22}, Φ^h_{12}, Φ^h_{21}, Case A-I), have been fixed around the hole, a considerable stress concentration has been observed. This can be interpreted that the micro-elements of the micromorphic continuum are constrained when applying BCs on the micro-stretch dofs (Φ^h_{11}, Φ^h_{22}) around the hole which results in a higher stress concentration. Note that for Case A with micro-shear dofs only fixed around the hole surface (Case A-III), the resulting stress concentration is closer to that of Case B (I,III),

Table 5.9. Selected material parameters for plate with circular hole.

Micromorphic Continuum					
$\lambda(MPa)$	$\mu(MPa)$	$\eta(MPa)$	$\kappa(MPa)$	$\nu(MPa)$	$\sigma(MPa)$
1e5	2.2e5	3.0e4	-1.0e4	-8.0e4	-7.0e4
$\tau(MPa)$	$\tau_1(Pa.m^2)$	$\tau_2(Pa.m^2)$	$\tau_3(Pa.m^2)$	$\tau_4(Pa.m^2)$	$\tau_5(Pa.m^2)$
2.75e4	0.0	0.0	0.0	0.0	0.0
$\tau_6(Pa.m^2)$	$\tau_7(Pa.m^2)$	$\tau_8(Pa.m^2)$	$\tau_9(Pa.m^2)$	$\tau_{10}(Pa.m^2)$	$\tau_{11}(Pa.m^2)$
0.0	525	0.0	0.0	0.0	0.0
Micropolar Continuum					
$\lambda(MPa)$	$\bar{\mu}(MPa)$	$\bar{\eta}(MPa)$	$\bar{\alpha}(Pa.m^2)$	$\beta(Pa.m^2)$	$\bar{\gamma}(Pa.m^2)$
15.75e4	7e4	7e4	0.0	0.0	1050

wherein there are no BCs applied on micro-shear. This shows that the effects of shear deformations of the micro-elements are negligible on stress concentration due to the extensional-like deformation of this example, while the micro-stretch dofs (Φ^h_{11}, Φ^h_{22}) play the main role and reflect the effect of micro-elements stretched in tension for generating stress concentration around the hole.

Figure 5.32 illustrates the stress concentration plotted circumferentially around the hole (with respect to θ) obtained from the micromorphic continuum theory in comparison with the micropolar and classical continuum theories. In the micromorphic continuum, Case B-III with only micro-shear dofs predicts the closest result to the micropolar theory results presented in Bauer et al. [2010] as seen in Fig.5.32(a). Figure 5.32(b) shows the effect of micromorphic BCs on the stress distribution around the hole. For Case A-I with micro-stretch and micro-shear components, and Case A-II with micro-stretch components fixed on the hole surface, larger stress values are observed around the hole. As mentioned earlier, this is the direct result of the constrained micro-elements of a micromorphic solid through fixing the micromorphic dofs on the hole surface. Figure 5.33(a) compares the stress concentration modeled by the micromorphic continuum at finite strain for Case B (I-III) with classical elasticity. It can be noticed that the stress concentration captured by Case B-I (no BCs on $\Phi^h_{11}, \Phi^h_{22}, \Phi^h_{12}, \Phi^h_{21}$) is slightly larger than those of Case B-II and III. However, this is not the case for the small strain analysis in Fig.5.30(b). Figure 5.33(b) illustrates that for Case A (I-III) with micromorphic BCs around the hole, at finite strain the obtained trend for the stress concentration

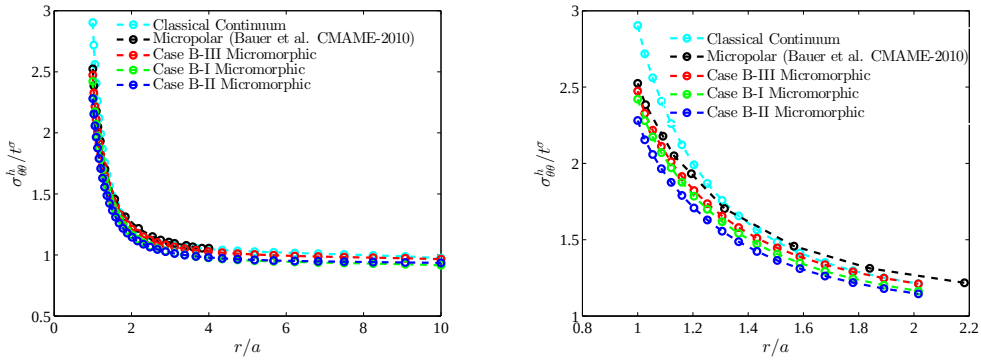

(a) Plot in 0-10 r/a range. (b) Plot in 0-2 r/a range.

Figure 5.30. Stress distribution obtained from micromorphic, micropolar, and classical elasticity.

is similar to the small strain analysis. Figure 5.34 illustrates the distribution of $\sigma^h_{r\theta}$ and $\sigma^h_{\theta r}$ along the diagonal of the plate. This figure compares the results of the micromorphic continuum for Case B with the micropolar and classical theories, and the effects of BCs between Cases A and B. Note that the macroscopic Cauchy stress is not symmetric for the micromorphic and micropolar theories, and thus $\sigma^h_{r\theta}$ and $\sigma^h_{\theta r}$ are not equal (this is also observed in Bauer et al. [2010]). Figure 5.34(d) shows that at $r = a$, $\sigma^h_{\theta r}$ starts near zero. For Cases A-I and A-II with BCs on the micro-stretch and micro-shear components, the effect of rigid micro-elements can be observed. Further from the hole surface, $\sigma^h_{\theta r}$ reaches its maximum value. The effect of rigid micro-elements around the hole surface on $\sigma^h_{\theta r}$ diminishes further from the hole surface. A similar trend for $\sigma^h_{r\theta}$ can be observed in Fig.5.34(b). Figure 5.35 shows the contour plots of Φ^h_{11}, Φ^h_{22}, Φ^h_{21}, and Φ^h_{12} throughout the model. Note that Φ^h_{21} and Φ^h_{12} do not evolve symmetrically. Therefore, it can be concluded that once the shear components of $\mathbf{\Phi}^h$ begin to evolve, symmetric BCs on $\mathbf{\Phi}^h$ are not applicable (which we do not assume for this plate example). Note that this could be the case for micro-stretch terms as well.

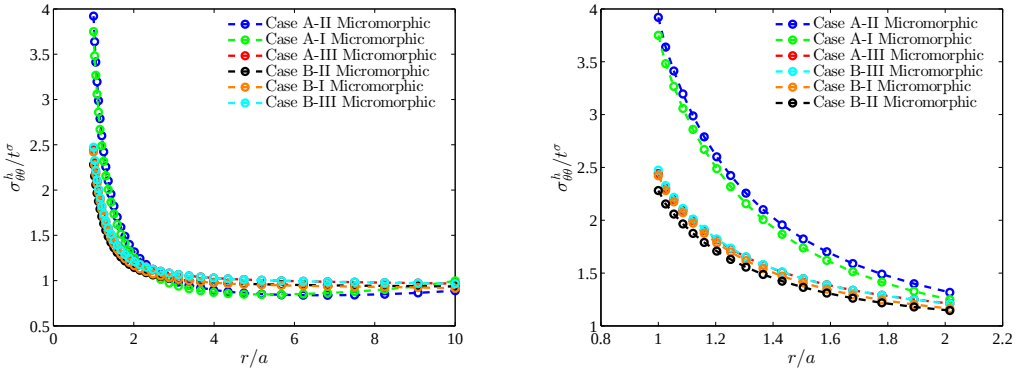

(a) Plot in $0 - 10r/a$ range. (b) Plot in $0 - 2r/a$ range.

Figure 5.31. The effect of BCs on the calculated stress distribution from the micromorphic continuum.

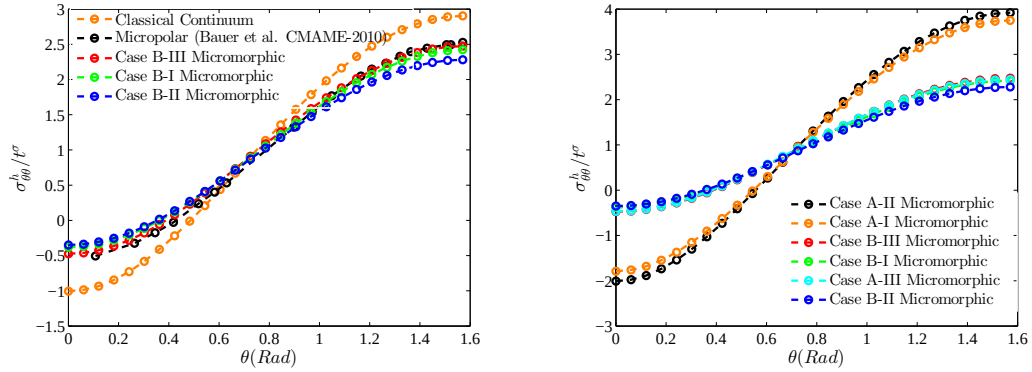

(a) Distribution of $\sigma^h_{\theta\theta}$ around hole (b) Effect of $\mathbf{\Phi}^h$ BCs on stress distribution

Figure 5.32. Effect of $\mathbf{\Phi}^h$ BCs on distribution of $\sigma_{\theta\theta}$ around circular hole.

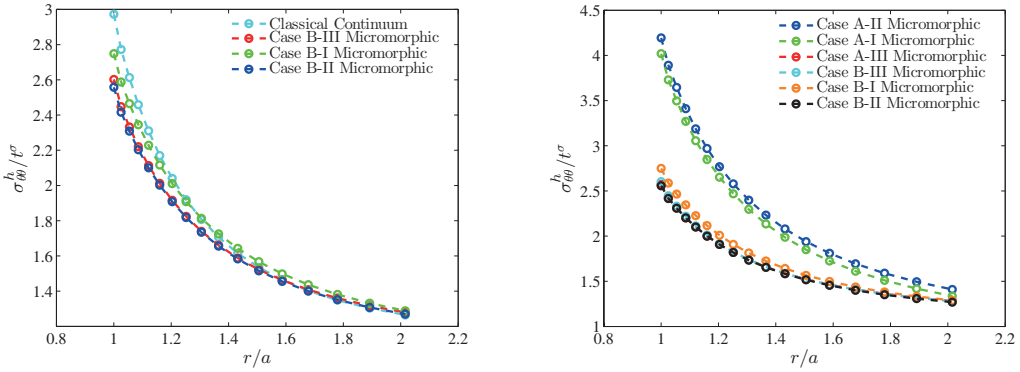

(a) Comparison of $\sigma^h_{\theta\theta}$ from micromorphic continuum with that of classical elasticity at finite strain. (b) Effect of micromorphic BCs on $\sigma^h_{\theta\theta}$ at finite strain.

Figure 5.33. Stress concentration at finite strain from micromorphic continuum.

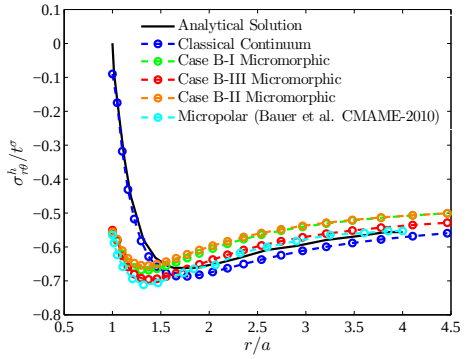

(a) Distribution of $\sigma^h_{r\theta}$ on plate diagonal.

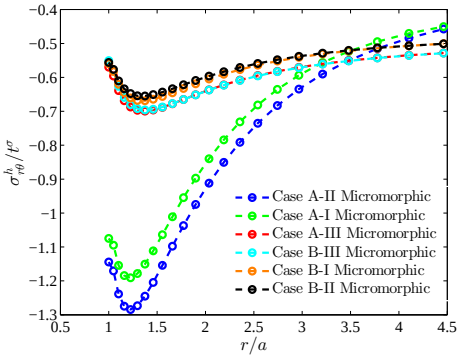

(b) Effect of $\mathbf{\Phi}^h$ on $\sigma^h_{r\theta}$ along plate diagonal.

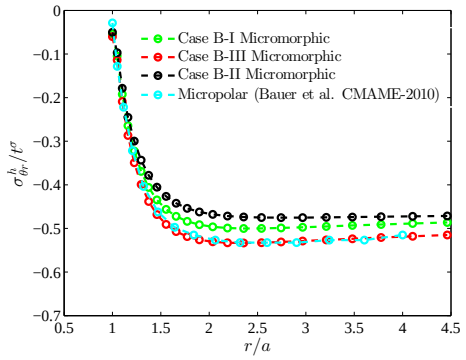

(c) Distribution of $\sigma^h_{\theta r}$ on plate diagonal.

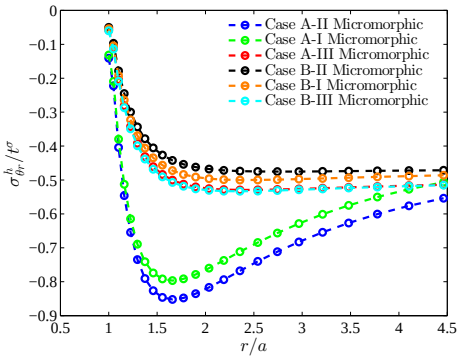

(d) Effect of $\mathbf{\Phi}^h$ BCs on $\sigma^h_{\theta r}$ along plate diagonal.

Figure 5.34. Effect of $\mathbf{\Phi}^h$ BCs on distribution of $\sigma^h_{r\theta}$ and $\sigma^h_{\theta r}$ along plate diagonal.

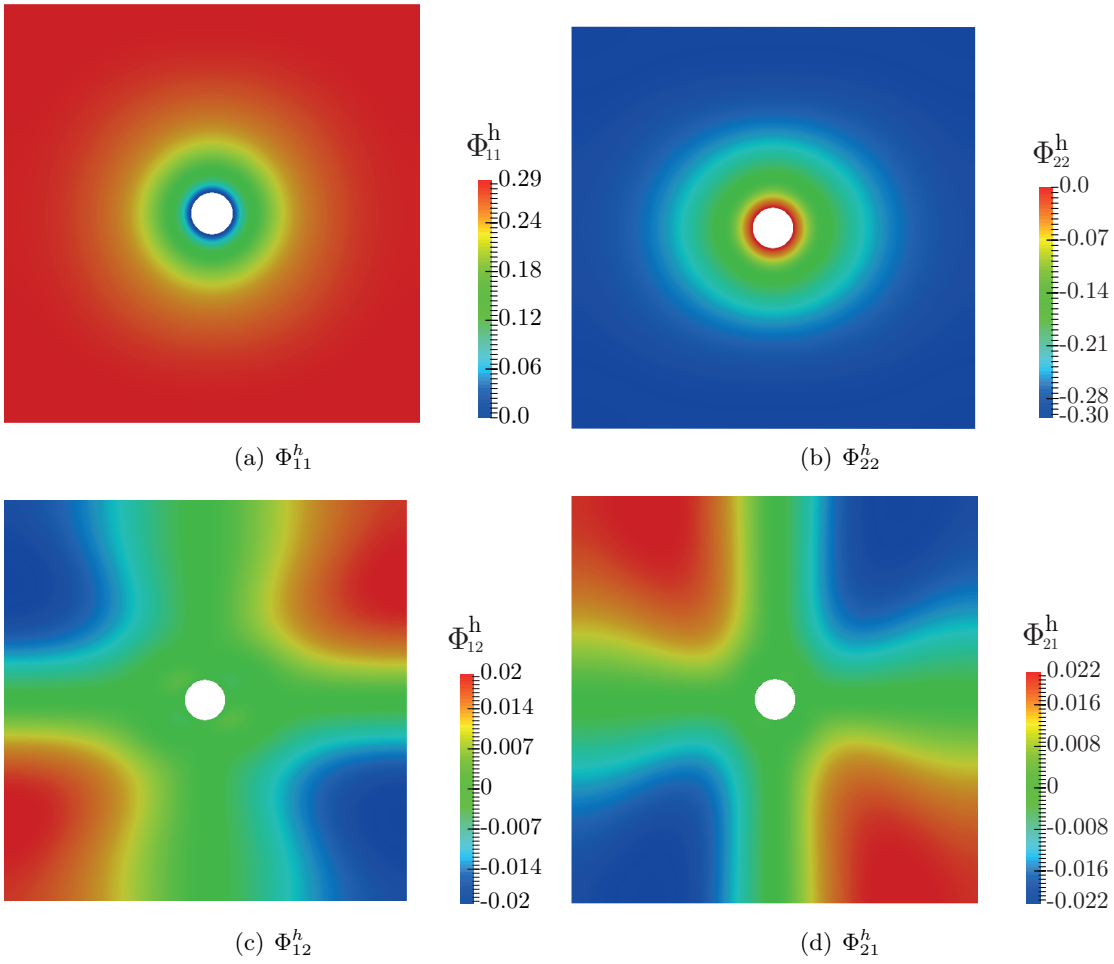

(a) Φ^h_{11} (b) Φ^h_{22}

(c) Φ^h_{12} (d) Φ^h_{21}

Figure 5.35. Contour plots of Φ^h_{11}, Φ^h_{22}, Φ^h_{21}, and Φ^h_{12}

5.4.3 Plate Bending

The third example is devoted to presenting bending analysis in a micromorphic plate. The selected material parameters, mesh configuration, and considered BCs on $\boldsymbol{\Phi}^h$ are illustrated in Table 5.10, Figure 5.36, and Table 5.11, respectively.

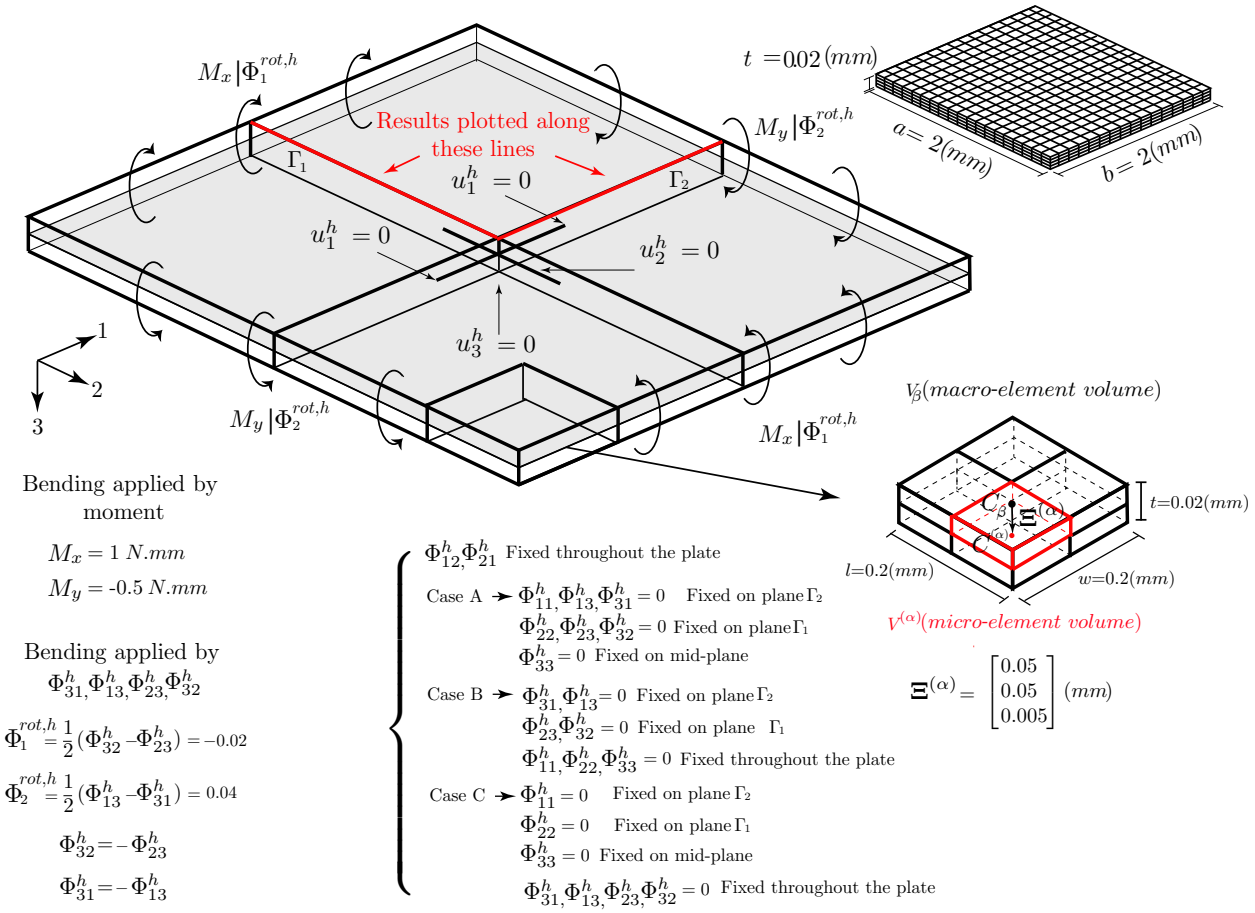

Figure 5.36. Schematic of mesh configuration and selected micromorphic BCs on $\boldsymbol{\Phi}^h$ for plate bending analysis.

Note that four sets of material parameters for the couple stress have been selected to illustrate their effect on the macroscopic response. In Figure 5.36, it can be seen that the moment has been applied in two ways: (i) force on the plate edges to mimic a bending moment, and (ii) rotation through the micromorphic dofs $\Phi_1^{\text{rot},h}$ is the micro-rotation about axis 1, and $\Phi_2^{\text{rot},h}$ is the micro-rotation about axis 2). Note that applying moment through the micro-rotation from the modeling perspective can

be described as applying moment on the individual micro-elements of the micromorphic continuum rather than the macro-elements. From the physical point of view, it can be interpreted as applying moment on the material micro-structure. Figure 5.37(a) shows the lateral plate deflection which is plotted along the bold red lines in Fig.5.36 obtained from the micromorphic continuum theory in comparison with the classical and micropolar theories. The results for the micromorphic continuum are obtained by using Set I of material parameters listed in Table 5.10. Note that for Case A, in which the micro-stretch and micro-shear dofs are active, and for Case B, in which only the micro-shear dofs are active, the resulting deflections are overlapping. However, for Case C, in which only the micro-stretch dofs are active and the micro-shear dofs are zero, the lateral deflection of the plate is noticeably smaller (i.e, more stiff) than that of Cases A and B. Apparently, this means that fixing the micro-shear dofs removes shear deformation of the micro-elements of a micromorphic plate which makes the plate considerably more stiff in bending than for Cases A and B that include micro-shear deformation. Lateral deflection of the plate from the micromorphic continuum Cases A and B compared to the micropolar theory shows that the micromorphic plate deforms more than the micropolar one. This demonstrates the significance of micro-shear (micropolar does not consider micro-shear in micro-elements) as well as micro-rotation which are both captured by the micromorphic theory, in contrast to the micropolar theory that only accounts for the micro-rotation of micro-elements. The interesting point in this figure is that the lateral deflection of the model for which the bending moment is mimicked via applying rotations $\Phi_1^{\mathrm{rot},h}$ and $\Phi_2^{\mathrm{rot},h}$, is close to that of the other models for which bending moment is applied by forces ("Bending by moment"). This is observed for small strain analysis, and is not the case for finite strain problems (large strain deflection of the micromorphic plate will be presented later in Fig.5.40). Figure 5.37(b) illustrates the effect of couple stress material parameters on the macroscopic lateral deflection of the plate. For the purpose of adjusting the micromorphic couple stress material parameters with those of micropolar elasticity, with regard to (2.132), there are several choices for selections of couple stress material parameters.

Table 5.10. Selected material parameters for plate bending.

Micromorphic Continuum					
$\lambda(MPa)$	$\mu(MPa)$	$\eta(MPa)$	$\kappa(MPa)$	$\nu(MPa)$	$\sigma(MPa)$
1e5	2.2e5	3.0e4	-1.0e4	-8.0e4	-7.0e4
$\tau(MPa)$	$\tau_1(Pa.m^2)$	$\tau_2(Pa.m^2)$	$\tau_3(Pa.m^2)$	$\tau_4(Pa.m^2)$	$\tau_5(Pa.m^2)$
Set I					
2.75e4	0.0	0.0	0.0	625	0.0
Set II					
2.75e4	0.0	0.0	0.0	675	100
Set III					
2.75e4	0.0	0.0	0.0	1250	0
Set IV					
2.75e4	0.0	0.0	0.0	0.0	0.0
$\tau_6(Pa.m^2)$	$\tau_7(Pa.m^2)$	$\tau_8(Pa.m^2)$	$\tau_9(Pa.m^2)$	$\tau_{10}(Pa.m^2)$	$\tau_{11}(Pa.m^2)$
Set I					
675	675	0.0	0.0	0.0	0.0
Set II					
675	625	0.0	0.0	0.0	0.0
Set III					
0.0	625	0.0	0.0	0.0	0.0
Set IV					
1250	1250	0.0	0.0	625	0.0
Micropolar Continuum					
$\lambda(MPa)$	$\bar{\mu}(MPa)$	$\bar{\eta}(MPa)$	$\bar{\alpha}(Pa.m^2)$	$\beta(Pa.m^2)$	$\bar{\gamma}(Pa.m^2)$
15.75e4	7e4	7e4	0.0	-1250	2500

Table 5.11. Selected BCs for micromorphic dofs of plate under bending.

	On plane Γ_1	On plane Γ_2	On mid-plane	Throughout the plate
Case A	$\Phi^h_{22}, \Phi^h_{23}, \Phi^h_{32} = 0$	$\Phi^h_{11}, \Phi^h_{31}, \Phi^h_{13} = 0$	$\Phi^h_{33} = 0$	$\Phi^h_{12}, \Phi^h_{21} = 0$
Case B	$\Phi^h_{23}, \Phi^h_{32} = 0$	$\Phi^h_{31}, \Phi^h_{13} = 0$	$\Phi^h_{11}, \Phi^h_{22}, \Phi^h_{33} = 0$	$\Phi^h_{12}, \Phi^h_{21} = 0$
Case C	$\Phi^h_{22} = 0$	$\Phi^h_{11} = 0$	$\Phi^h_{33} = 0$	$\Phi^h_{12}, \Phi^h_{21}, \Phi^h_{23}, \Phi^h_{32}, \Phi^h_{31}, \Phi^h_{13} = 0$

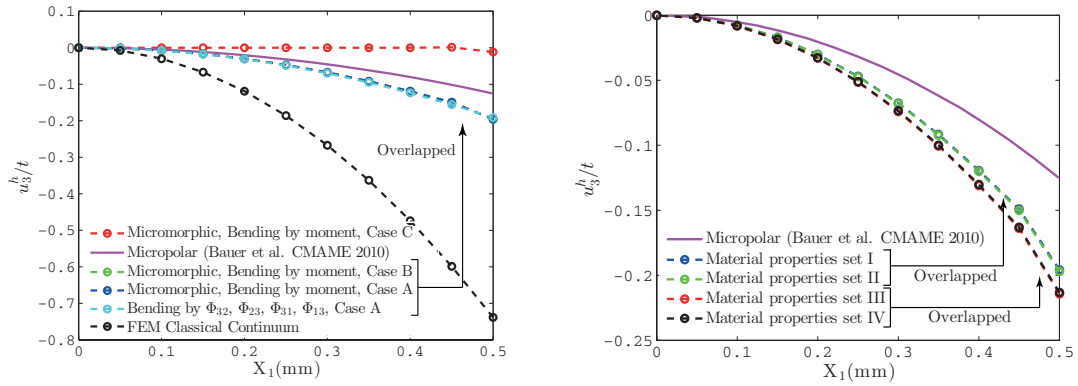

(a) Normalized lateral plate deflection as a result of bending along the red line in X_1 direction.

(b) Effect of material parameters on lateral deflection of plate along the red line in X_1 direction.

Figure 5.37. Lateral deflection of plate

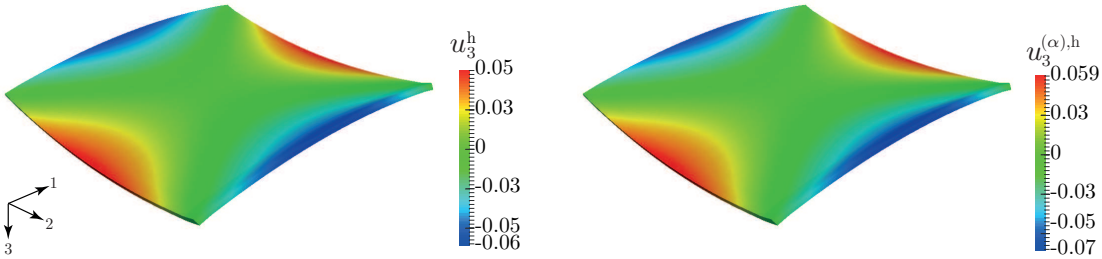

Figure 5.38. Deformed shape of plate in bending.

It can be seen that for material sets III and IV, the lateral deflection is slightly larger than that of the material sets I and II. The couple stress material parameters τ_i are somewhat related to the relative position vector $\boldsymbol{\Xi}^{(\alpha)}$ which is related to the length scale of the problem. Therefore, τ_i is closely related to the size of the micro-elements inside a micromorphic continuum. Note that defining the relation between the τ_i to $\boldsymbol{\Xi}^{(\alpha)}$ is beyond the scope of this chapter. Changing the τ_i's may lead to changes in $\boldsymbol{\Xi}^{(\alpha)}$ that affects the size and number of micro-elements within a macro-element. Therefore, different micro-element sizes will influence the macroscopic mechanical behavior. But, here we follow the assumption that through changing τ_i's the micro-element sizes will remain unchanged to avoid the complication of the relation of $\boldsymbol{\Xi}^{(\alpha)}$ and τ_i's. Figure 5.38 depicts the contour plot of macroscopic displacement u_3^h and micro-element displacement $u_3^{(\alpha),h}$

of the micromorphic plate for which it is observed that $u_3^{(\alpha),h}$ is slightly larger than u_3^h because of the contribution of relative position vector $\boldsymbol{\Xi}^{(\alpha)}$ (see Fig.5.36) multiplying by evolving $\boldsymbol{\Phi}^h$ in (2.15). Figure 5.39 illustrates the M_{12}^h, M_{21}^h (2.130), and $\Phi_2^{\mathrm{rot},h}$ (2.136) values obtained from the micromorphic plate (Case A with four sets of material parameters for τ_i) and those of the micropolar plate. Note that the micromorphic couple stress is related to the micropolar couple stress through (2.130) for small strain analysis. Physically speaking, the couple stress can be interpreted as the moment of the micro-element stress $\boldsymbol{\sigma}^{(\alpha)}$ inside a macro-element. Therefore, the couple stress for the idealized periodic micro-structure ($\boldsymbol{\Xi}^{(\alpha)}$ is assumed to be spatially uniform at each $\boldsymbol{X}_\beta$ in $\mathcal{B}_0$) defines the gradient of micro-element stress $\boldsymbol{\sigma}^{(\alpha)}$ in a micromorphic continuum. Figures 5.39(a),(b) illustrate the effect of τ_i's on the micromorphic couple stress in comparison with the micropolar couple stress. We do not expect the micromorphic couple stress to overlap the micropolar couple stress, because it has been observed earlier, the significance of micro-shear dofs in the macroscopic response of a micromorphic plate under bending. Note that there is a jump in the plot of resulting micropolar couple stress M_{21}^h near the edge of the plate in Fig.5.39(b), which pertains to the localized stress as a result of applying force to mimic the bending moment. Figure 5.39(c) shows that the resulting micro-rotation $\Phi_2^{rot,h}$ from micromorphic elasticity is higher than that for micropolar theory. Apparently, this reflects the significance of micro-shear dofs included in the micromorphic continuum for bending analysis which results in larger micro-rotation. Note that micro-rotation curves captured by Case A and Case B are overlapping in Fig.5.39(c), which means that the micro-stretch terms do not have a considerable effect on micro-rotation for this plate bending example. Figure 5.40 illustrates the macroscopic lateral deflection of the plate under finite strain bending analysis. It can be seen that for Case A at finite strain in which bending is applied through $\Phi_1^{\mathrm{rot},h}$ and $\Phi_2^{\mathrm{rot},h}$, the lateral deflection starts deviating from that of Case B for which bending moment is applied directly (compared to Fig.5.37(a) for small deflections wherein the curves for Cases A and B overlap).

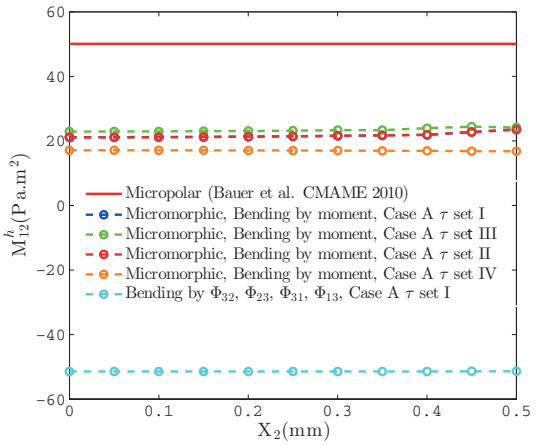

(a) M^h_{12}

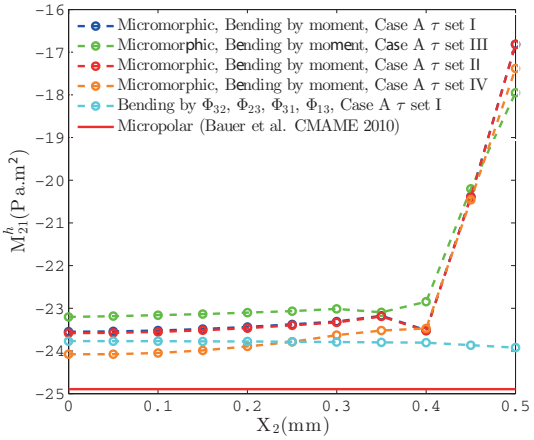

(b) M^h_{21}

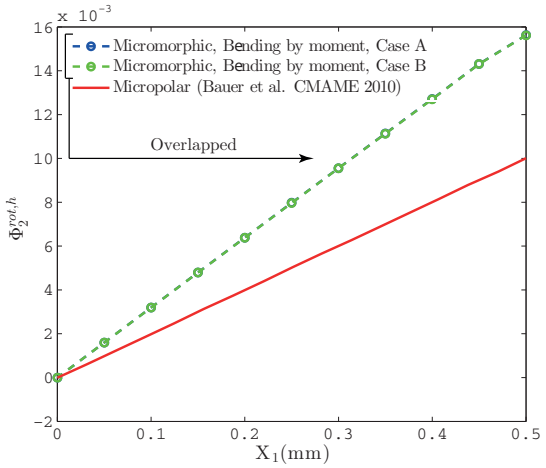

(c) $\Phi_2^{\mathrm{rot},h}$

Figure 5.39. Comparison of M^h_{12}, M^h_{21}, and $\Phi_2^{\mathrm{rot},h}$ from micromorphic and micropolar theories.

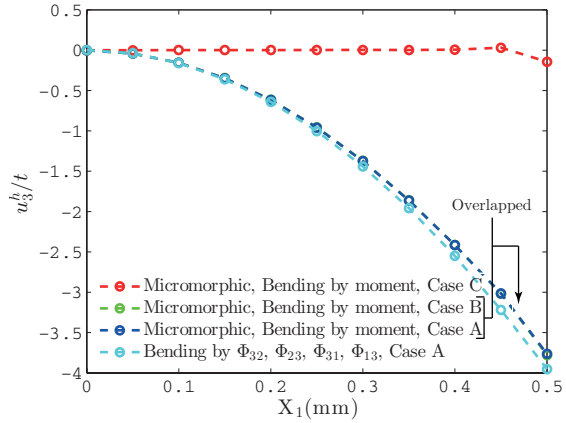

Figure 5.40. Lateral deflection of plate under bending at finite strain.

5.4.4 Twisting of T-shaped Rod

The fourth example involves large twisting of a T-shaped rod to illustrate the capability of the developed code in Tahoe to perform a large deformation 3D micromorphic FE analysis. Note that there are no quantitative data presented by Bauer et al. [2010] on micropolar FEA of a T-shaped rod to compare with the micromorphic model presented here. The selected material parameters for the micromorphic T-shaped rod are listed in Table 5.12.

Table 5.12. Selected material parameters for the micromorphic T-shaped rod.

Micromorphic Continuum					
$\lambda(MPa)$	$\mu(MPa)$	$\eta(MPa)$	$\kappa(MPa)$	$\nu(MPa)$	$\sigma(MPa)$
29.31e3	25.48e3	1e3	-1.5e3	-1.4e3	-3e3
$\tau(MPa)$	$\tau_1(Pa.m^2)$	$\tau_2(Pa.m^2)$	$\tau_3(Pa.m^2)$	$\tau_4(Pa.m^2)$	$\tau_5(Pa.m^2)$
4e2	0.0	0.0	0.0	0.0	0.0
$\tau_6(Pa.m^2)$	$\tau_7(Pa.m^2)$	$\tau_8(Pa.m^2)$	$\tau_9(Pa.m^2)$	$\tau_{10}(Pa.m^2)$	$\tau_{11}(Pa.m^2)$
0.0	10e5	0.0	0.0	0.0	0.0

Table 5.13 summarizes the BCs on the micromorphic dofs $\boldsymbol{\Phi}^h$. The geometry, schematic of FE mesh, and applied BCs are illustrated in Figure 5.41. Note that the twist is applied on the T-shaped rod in two ways: (i) the macroscopic displacement $\boldsymbol{u}^h$, and (ii) the micro-rotation $\Phi_3^{\mathrm{rot},h}$.

Table 5.13. Selected BCs for micromorphic dofs of T-shaped rod.

	Throughout the model	Throughout the T	No boundary condition
	Set I, Fixed Micro-stretch		
Case A	$\Phi^h_{11}, \Phi^h_{22}, \Phi^h_{33}, \Phi^h_{31}, \Phi^h_{13}, \Phi^h_{23}, \Phi^h_{32} = 0$		Φ^h_{12}, Φ^h_{21}
	Set I, With Micro-stretch		
Case B	$\Phi^h_{31}, \Phi^h_{13}, \Phi^h_{23}, \Phi^h_{32} = 0$	$\Phi^h_{11}, \Phi^h_{22}, \Phi^h_{33} = 0$	Φ^h_{12}, Φ^h_{21}
	Set II, Fixed Micro-stretch		
Case C	$\Phi^h_{11}, \Phi^h_{22}, \Phi^h_{33}, \Phi^h_{31}, \Phi^h_{13}, \Phi^h_{23}, \Phi^h_{32} = 0$	$\Phi^h_{12}, \Phi^h_{21} = 0$	
	Set II, With Micro-stretch		
Case D	$\Phi^h_{31}, \Phi^h_{13}, \Phi^h_{23}, \Phi^h_{32} = 0$	$\Phi^h_{11}, \Phi^h_{22}, \Phi^h_{33}, \Phi^h_{12}, \Phi^h_{21} = 0$	

Figure 5.42 shows the effects of micromorphic BCs as well as the manner by which twist is applied (by (i) displacement $\boldsymbol{u}^h$, or by (ii) micro-rotation $\Phi_3^{\mathrm{rot},h}$) on the macroscopic displacement result u_3^h. It is seen that the profile of u_3^h in Fig.5.42(a) obtained from the micromorphic T-shaped rod is not similar to that of classical elasticity which is a straight line. Micro-stretch terms do not

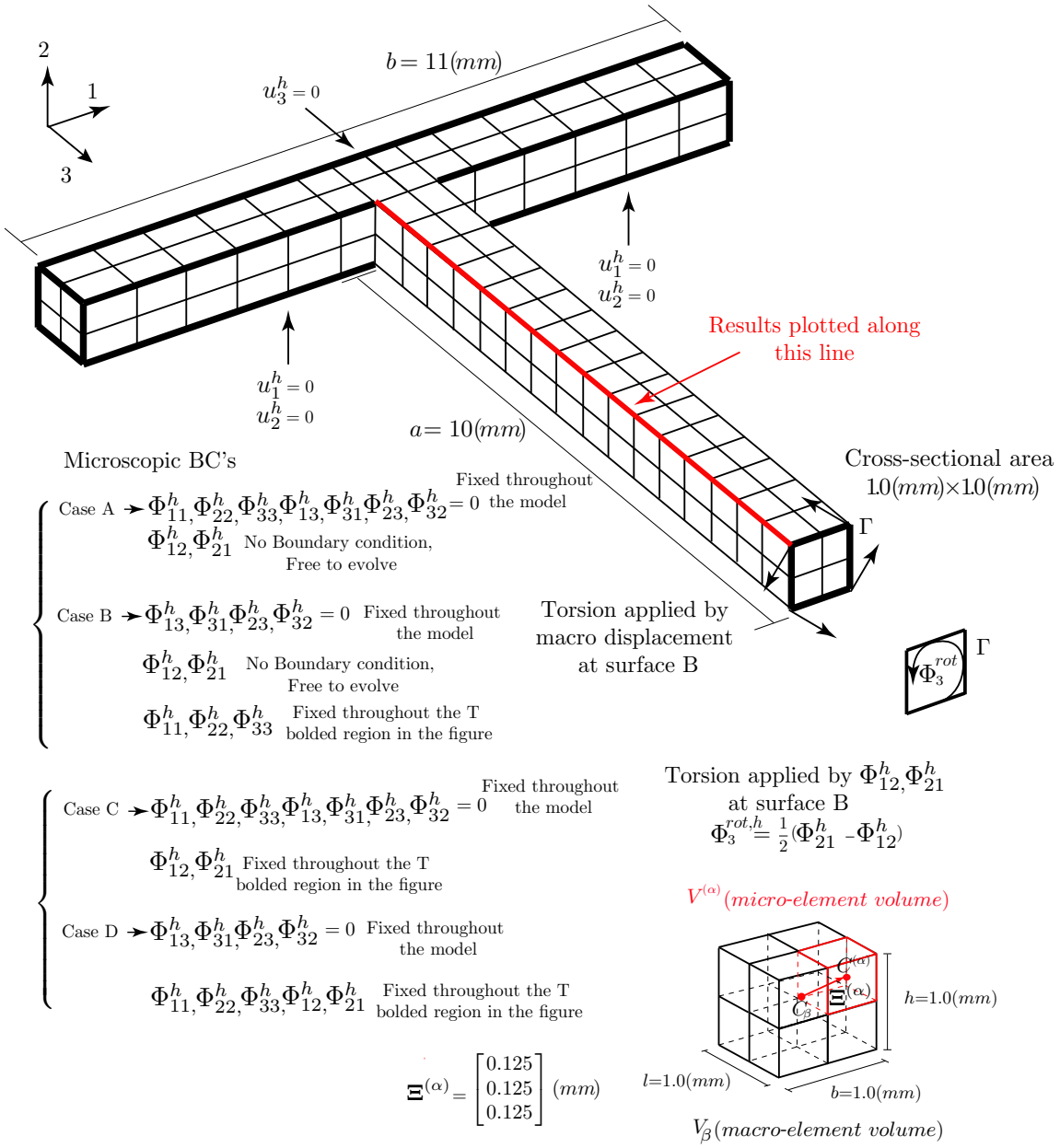

Figure 5.41. Geometry, schematic of FE mesh, and applied BCs on micromorphic T-shaped rod.

have a significant effect on the profile of u_3^h. Note that in the micromorphic T-shaped rod model in which the twist is applied by micro-rotation $\Phi_3^{rot,h}$, the resulting u_3^h does not follow the same trend as the case in which twist is applied by displacement $\boldsymbol{u}^h$. In the model in which twist is applied through macro-displacement, at the very end of the rod, u_3^h is positive which shows axial stretch in the rod. However, for the model in which twist is applied through micro-rotation, u_3^h

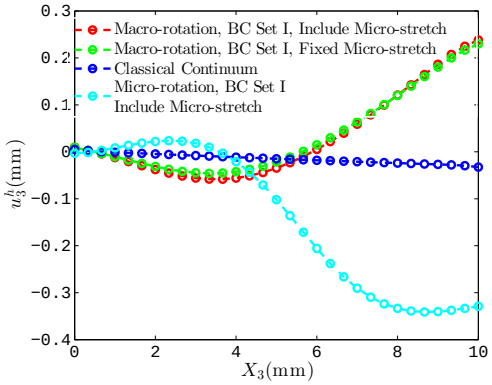

(a) u_3^h obtained from classical elasticity theory compared to micromorphic elasticity.

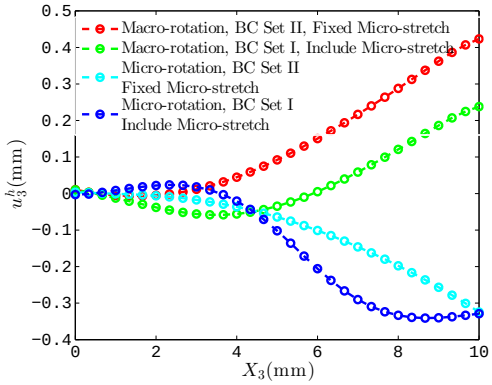

(b) effect of micromorphic BCs on u_3^h.

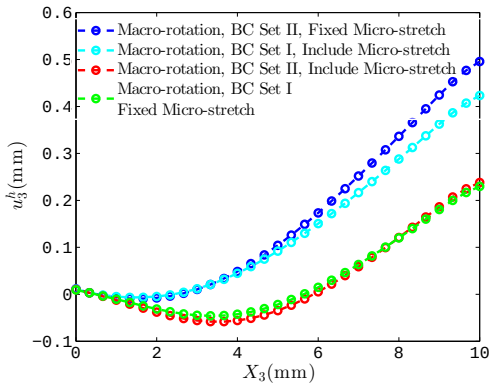

(c) Comparison of applying rotation by macroscopic displacement and micro-rotation.

Figure 5.42. u_3^h from micromorphic elasticity FE solution plotted along the red bold line in Fig.5.41.

is negative at the end of the rod where it is under compression. In the profile of u_3^h along the length of the rod, where u_3^h is negative (in compression), this is the location where considerable twisting occurs (see Figs.5.46(d),(e)). For the model for which load is applied through micro-rotation, considerable amount of twisting occurs in the middle of rod. On the other hand, for the model in which load is applied through macro-displacement, significant twisting occurs near the T position (Figs.5.46(a),(b)). Therefore, two different deformed shapes of the T-shaped rod have been observed as a result of two different BCs. From the mathematical perspective, we have two sets of nonlinear partial differential equations (balance of linear and first moment of momenta) (2.158) for the micromorphic solid, in which two different sets of BCs lead to different results.

Therefore, we do not expect to observe similar deformed shapes of the micromorphic T-shaped rod with different BCs. Figure 5.42(a) also compares the axial displacement u_3^h obtained from classical continuum theory and that of micromorphic theory. The classical continuum predicts a nearly linear distribution for u_3^h, however, the simulations using the micromorphic continuum do not follow a similar trend for u_3^h. The linear distribution of u_3^h along the length of the T-shaped rod implies that the twist is distributed uniformly along the length as well (see Fig.5.46(c)). The profile of u_3^h obtained from the micromorphic continuum model shows both tension and compression along the length of the rod. This denotes that the twist in the micromorphic T-shaped rod is not uniform. This example illustrates that the results of a micromorphic continuum at finite strain are deviating from the classical continuum result. Figures 5.42(b) and 5.42(c) illustrate the effect of micromorphic BCs as well as the ways of applying twist on the rod (by displacement and by micro-rotation) on u_3^h. Note that the distribution of u_3^h throughout the length of the rod is affected by the manner of twist on the rod. This occurs as a result of applying two different BCs on (2.158). Figure 5.42(b) shows that for the cases in which twist is applied through displacement, the twisted rod is under stretch and u_3^h is positive. However, if the twist is applied via micro-rotation, the rod will be under compression and u_3^h is negative. Figure 5.42(c) illustrates the effect of including micro-stretch on u_3^h. It can be noticed that including micro-stretch term leads to larger u_3^h. Note that for the case with BC set I with micro-stretch, the value of u_3^h is slightly larger than that of the case in which micro-stretch is fixed all through the T-shaped rod.

Figure 5.43 illustrates Φ_{33}^h (micro-stretch in axial direction) along the length of the rod on the red solid line in Fig.5.41. Figure 5.43(a) compares the micro-displacement component Φ_{33}^h obtained for the micromorphic T-shaped rod in which the twist is applied through macro-element displacement u_3^h and micro-rotation $\Phi_3^{rot,h}$. It can be seen that in both cases, there is a gradient in the profile of Φ_{33}^h near the T, and it levels out further away from the T. Note that Φ_{33}^h is in compression when the twist is applied by micro-rotation (u_3^h is also in compression). However, it is in tension for the case in which the twist is applied by displacement (u_3^h is also in tension). Figure 5.43(b) illustrates the effect of BCs sets I and II on the profile of Φ_{33}^h. It can be seen that for

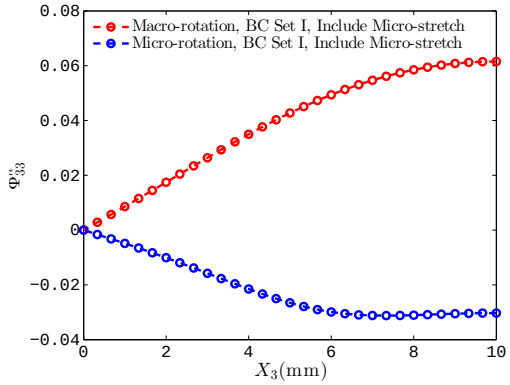

(a) effect of applying twist by macroscopic displacement $\boldsymbol{u}^h$, and micro-rotation on $\Phi_3^{\mathrm{rot},h}$.

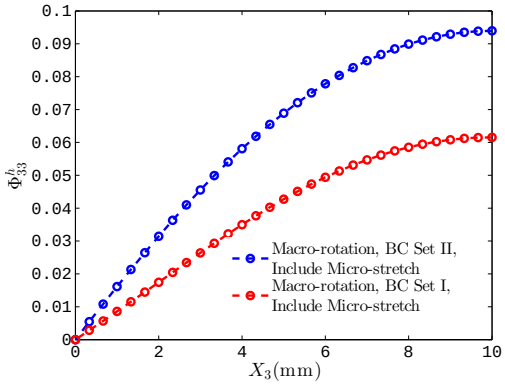

(b) effect of micromorphic BCs on $\Phi_3^{\mathrm{rot},h}$.

Figure 5.43. Micro-stretch Φ^h_{33} along the red bolded line Fig.5.41.

BC set II Φ^h_{33} is larger than that of BC set I (u^h_3 in Fig.5.42(c) for BC set II is also larger than set I). Figure 5.44 depicts the profile of the Second Piola-Kirchhoff stress S^h_{33} along the length of the T-shaped rod (red solid line Fig.5.41). The results from classical continuum FEA show that the profile of S^h_{33} is nearly uniform. However, in the micromorphic T-shaped rod this is not the case. The peak in the profile of S^h_{33} along the length indicates a considerable twisting at that location. Figure 5.45 illustrates the micro-rotation of macro-elements and micro-elements of the micromorphic T-shaped rod as a result of applying twist via displacement and micro-rotation. By investigating $\boldsymbol{\chi}$, it is found that for the case for which micro-rotation is applied on the model, the local rotation of the micro-elements is higher than that of the case for which twist is applied through displacement. Therefore, the differences in the micro-element deformations lead to the different deformed configuration of the T-shaped model at finite strain. Apparently, considering the effect of deformable micro-elements in the micromorphic continuum is the source of pronounced differences with classical elasticity. It is noteworthy to mention that when we look more closely into the micro-element displacement $\boldsymbol{u}^{(\alpha),h}$ (Fig.5.45), overlaps in the adjacent deformed micro-elements are noticeable. In terms of a micromorphic continuum the compatibility of strain tensors are ensured in order to obtain single-valued continuous macroscopic displacement $\boldsymbol{u}$ and micro-displacement tensor $\boldsymbol{\Phi}$ fields [Eringen, 1968]. However, through (2.15) and the choice of $\boldsymbol{\Xi}^{(\alpha)}$ in

Fig.5.41, we do not expect the secondary quantity of micro-displacement $\boldsymbol{u}^{(\alpha),h}$ to be a single-valued continuous field. Figure 5.46 shows the final deformed configurations of the T-shaped rod model using classical and micromorphic theories. The figure shows the deformed meshes of the cases in which twist is applied via displacement or micro-rotation, as well as comparing to the classical continuum result. The deformed meshes show that differences in micro-element deformation lead to different deformed shapes of the micromorphic T-shaped rods.

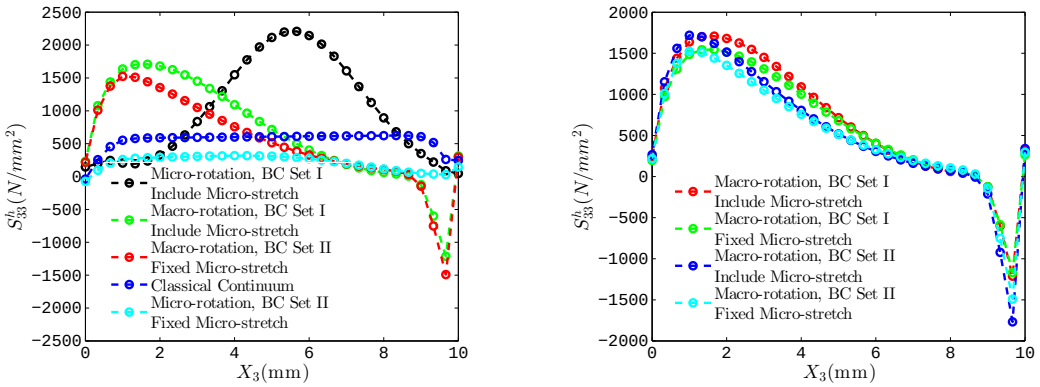

(a) S^h_{33} obtained from classical and micromorphic elasticity theories.

(b) effect of micromorphic BCs on S^h_{33}.

Figure 5.44. Second Piola-Kirchhoff stress S^h_{33} along the red bold line in Fig.5.41.

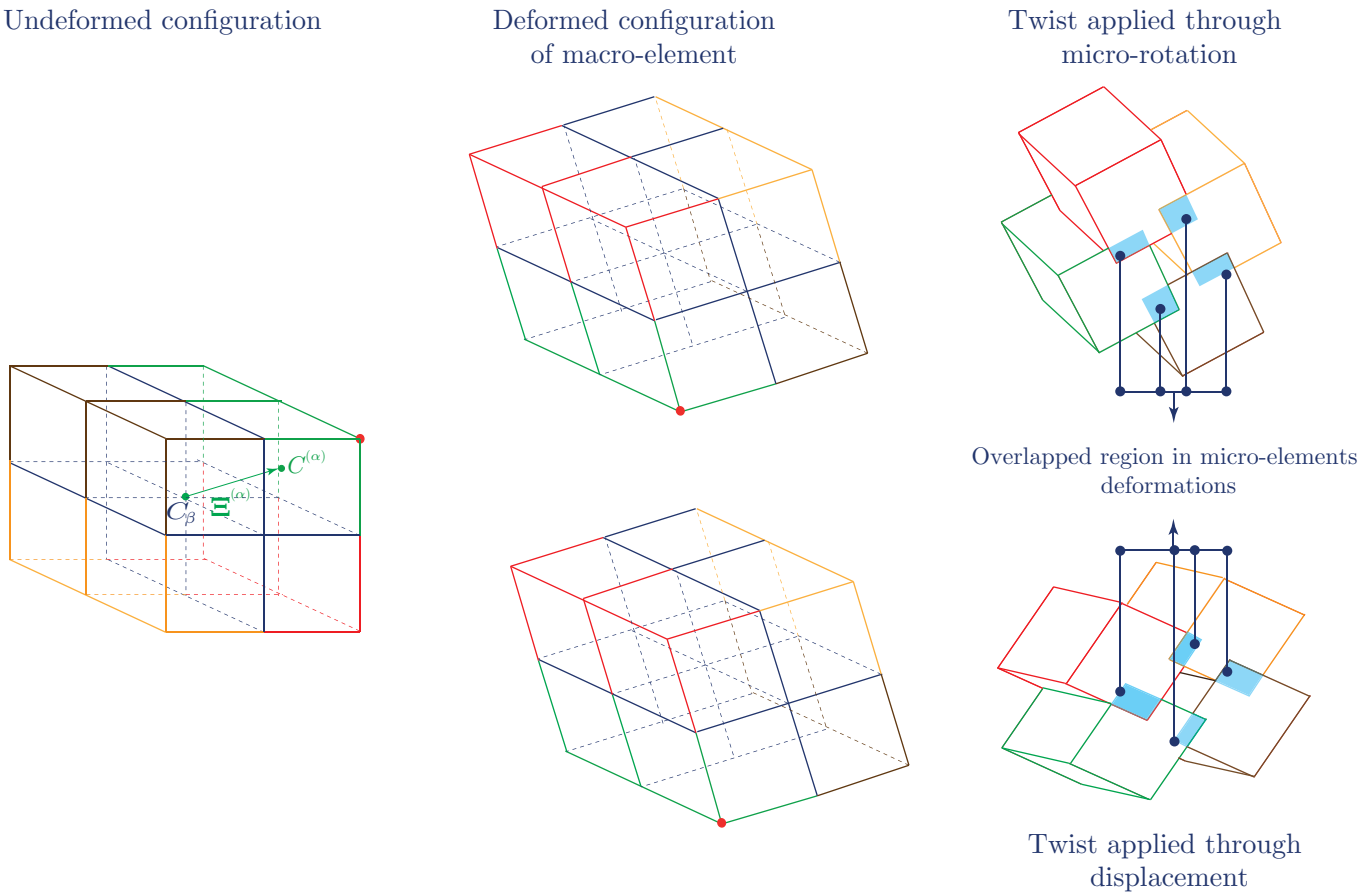

Figure 5.45. Schematic of macro-element and micro-element rotation with twist applied via displacement and micro-rotation.

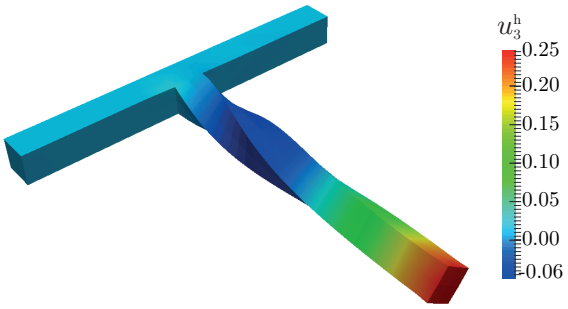

(a) twist applied by macroscopic displacement (micro-shear and micro-stretch dofs).

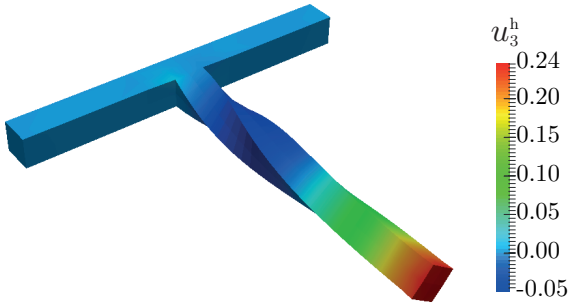

(b) twist applied by macroscopic displacement (micro-shear dofs).

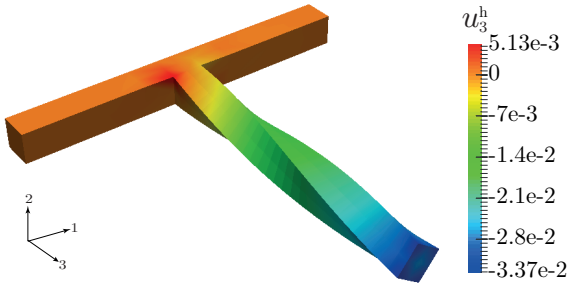

(c) deformed T-shape mesh for classical elasticity.

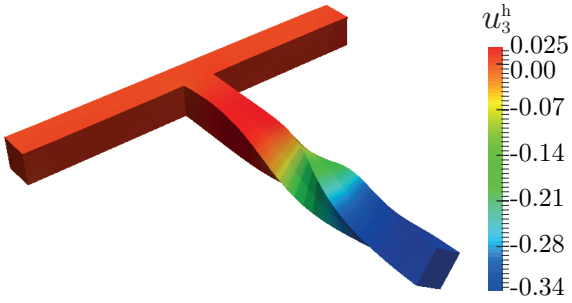

(d) twist applied by micro-rotation (micro-shear and micro-stretch dofs).

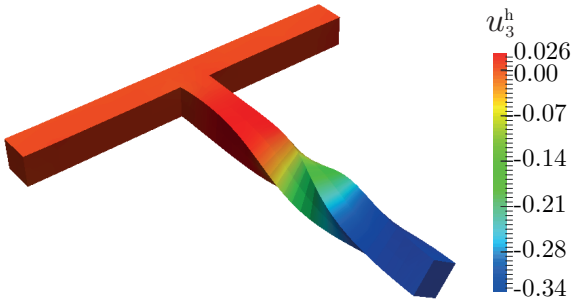

(e) twist applied by micro-rotation (micro-shear dofs).

Figure 5.46. Deformed meshes for T-shaped model. 1× displacement magnitude.

5.5 Micromorphic Elasticity: Dynamics

5.5.1 Uniaxial Strain Column

To start, we investigate the dynamic behavior of a micromorphic continuum through a uniaxial strain column example. The advantage of starting with this model is that it is a one-dimensional simulation of micromorphic continuum with the macro-element displacement component u_3^h and the micro-displacement tensor component Φ_{33}^h dofs. The schematic of mesh configuration, geometry, and BCs are illustrated in Fig.5.47. Note that the relative position vector $\boldsymbol{\Xi}^{(\alpha)} = [0 \quad 0 \quad 0.625]$ in Fig.5.47 belongs to the micro-element located in the positive portion of the macro-element. In this analysis, we are assuming that the material is made of an idealized periodic micro-structure through the Z direction. Each of the macro-volumes dV_β is made up of two micro-elements $dV^{(\alpha)}$ which are deformed in the Z direction through Φ_{33}^h dof. The selected material parameters and the BCs for the micromorphic column is presented in Table 5.14 and 5.15, respectively. Figure 5.48(a) shows the dispersion diagram of a one-dimensional longitudinal wave in the micromorphic and classical column. The dispersion diagram relates the wave number (wave length) of a wave to its frequency in a continuum. The numerical dispersion diagrams are obtained from the finite element solution and are compared with the small strain analytical solution of the classical continuum for the one dimensional wave. Regarding the dispersion analysis, there are a number of studies available in the literature that discuss the analytical and numerical approaches (Khajehtourian and Hussein [2014], Hussein et al. [2014], Hussein and Khajehtourian [2015]). It has been found that the finite element method is not the best numerical tool for conducting dispersion analysis. The dispersion diagrams of micromorphic versus classical continuum illustrate that for the selected material parameters in the small strain regimen differences in the wave velocity and the wave length of micromorphic and classical continua are negligible. It is to be noted that the obtained dispersion diagrams from the finite element method show a dispersive wave propagation (dispersion diagram is not linear unlike the analytical solution) in both of classical and micromorphic continua. This issue can be related to the finite element analysis that adds artificial dispersive properties in the wave propagation

simulation. On top of that our finite element model is developed based on finite strain analysis and to capture small strain analysis, loads with small amplitudes are used. Therefore, the geometric non-linearity is another source of dispersion of the wave propagation. Figure 5.48(b) illustrates the results of Cauchy stress σ_{33}^h from the three-dimensional finite element analysis for micromorphic and classical continua versus the analytical solution of classical continuum. As mentioned, in the finite element model, load with small amplitude is used to reduce the effect of non-linear geometric terms. The time integration parameter is $\alpha = -0.05$, (2.159), such that to remove some high frequency oscillations without adding a considerable amount of algorithmic damping in comparison with the trapezoidal time integration method which has zero algorithmic damping.

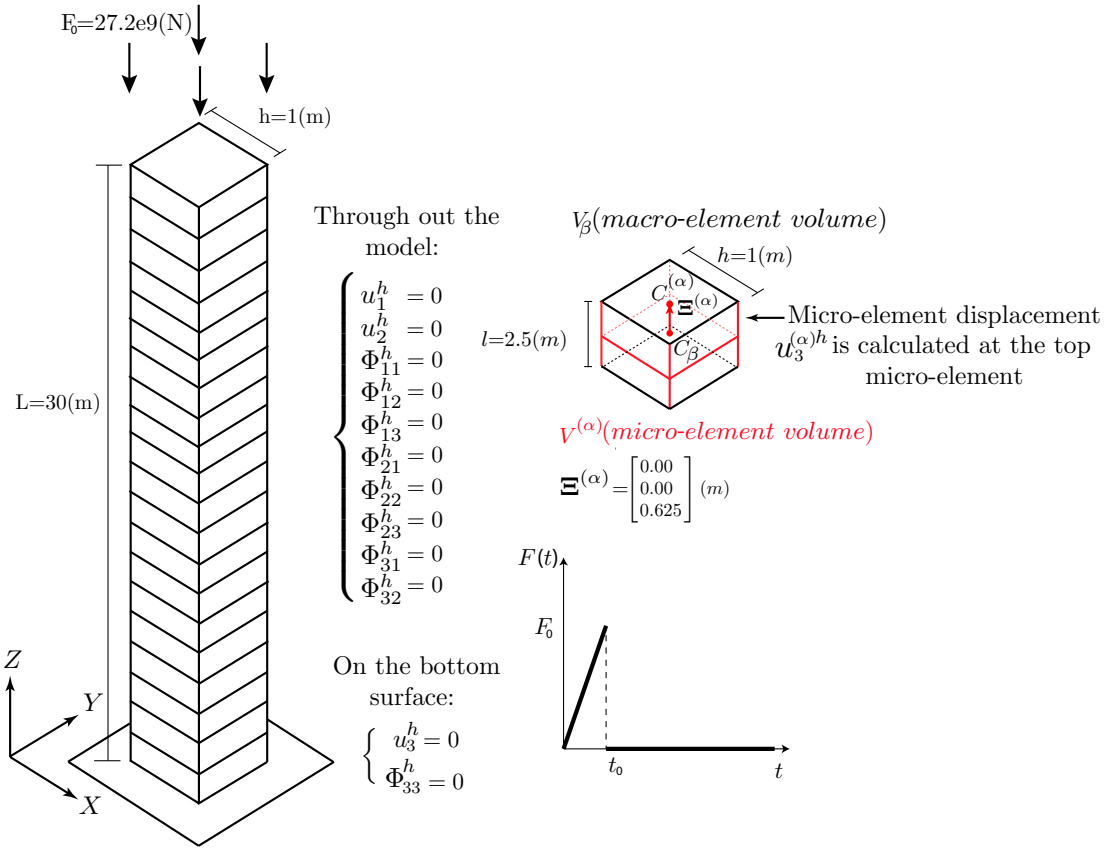

Figure 5.47. Uniaxial strain column under compression.

Table 5.14. Micromorphic elastic material parameters.

Micromorphic Continuum					
$\lambda(Pa)$	$\mu(Pa)$	$\eta(Pa)$	$\kappa(Pa)$	$\nu(Pa)$	$\sigma(Pa)$
29.31e8	25.48e8	1e8	-1.5e8	-1.4e8	-3e8
$\tau(Pa)$	$\tau_1(Pa.m^2)$	$\tau_2(Pa.m^2)$	$\tau_3(Pa.m^2)$	$\tau_4(Pa.m^2)$	$\tau_5(Pa.m^2)$
4e7	0.0	0.0	0.0	0.0	0.0
$\tau_6(Pa.m^2)$	$\tau_7(Pa.m^2)$	$\tau_8(Pa.m^2)$	$\tau_9(Pa.m^2)$	$\tau_{10}(Pa.m^2)$	$\tau_{11}(Pa.m^2)$
0.0	1e11	0.0	0.0	0.0	0.0
		$\rho_0(Kg/m^3)$	$t_0(s)$		
		2700	0.00026		
Classical Continuum					
	$\lambda(Pa)$	$\mu(Pa)$	$\rho_0(Kg/m^3)$	$t_0(s)$	
	28.9e8	22.48e8	2700	0.00026	

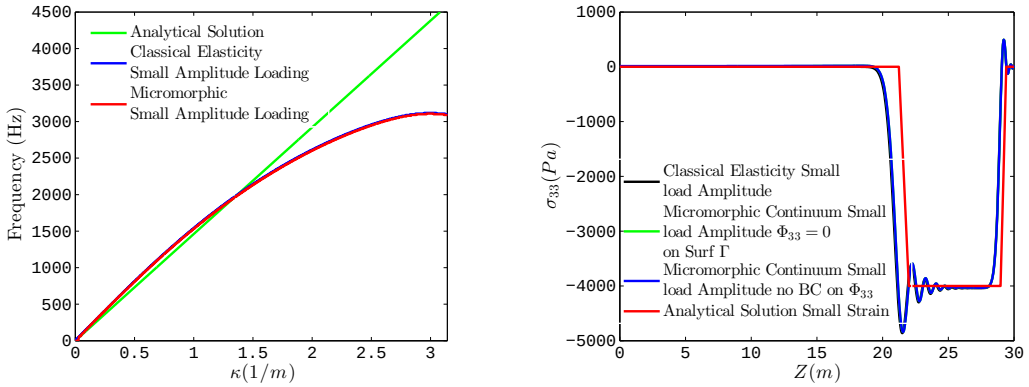

(a) Dispersion Analysis (frequency-wave number) of micromorphic continuum vs classical elasticity.

(b) Analytical solution versus finite element analysis.

Figure 5.48. Dispersion analysis and wave profile.

Table 5.15. Selected boundary conditions for the column under compressive loading.

Micromorphic Continuum	Throughout the column	On surface Γ
BC on Φ^h_{33}	$\Phi^h_{11},\Phi^h_{22},\Phi^h_{12},\Phi^h_{21},\Phi^h_{13},\Phi^h_{31},\Phi^h_{23},\Phi^h_{32}=0$	$\Phi^h_{33}=0$
	$u^h_1,u^h_2=0$	$u^h_3=0$
No BC on Φ^h_{33}	$\Phi^h_{11},\Phi^h_{22},\Phi^h_{12},\Phi^h_{21},\Phi^h_{13},\Phi^h_{31},\Phi^h_{23},\Phi^h_{32}=0$	
	$u^h_1,u^h_2=0$	$u^h_3=0$
Classical Continuum	Throughout the column	On surface Γ
	$u^h_1,u^h_2=0$	$u^h_3=0$

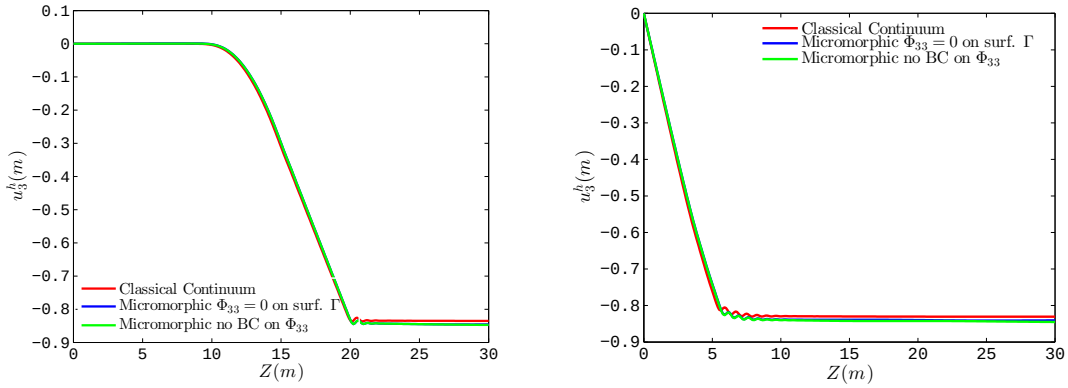

(a) Displacement u_3^h at t=0.01(s).

(b) Displacement u_3^h at t=0.02(s).

(c) Displacement u_3^h at t=0.025(s).

(d) Displacement u_3^h at t=0.035(s).

Figure 5.49. Comparison of displacements from classical and micromorphic continua through the length of the column.

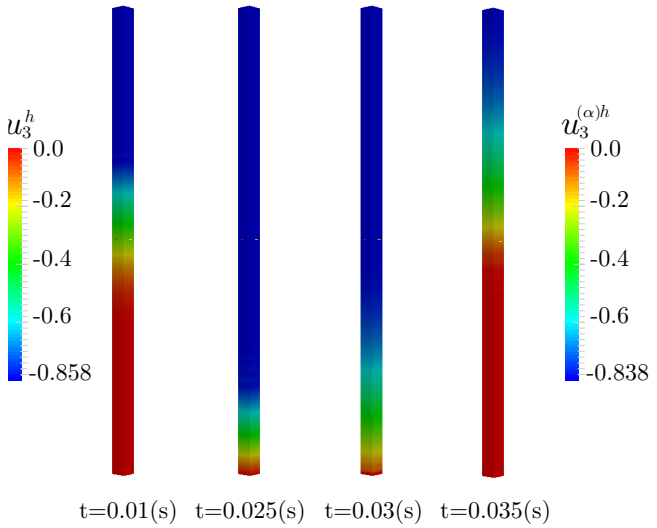

Figure 5.50. Contour plots of macro-element displacement u_3^h and micro-element displacement $u_3^{(\alpha)h}$.

Since our loading is an impulse, the obtained results of stress show numerical oscillations at the two sharp ends of the load profile. The rest of this section is devoted to demonstrating the dynamic behavior of micromorphic continuum in comparison with classical continuum. The results of macro-element displacement u_3^h are plotted along the length of the column in Fig.5.49. At $t = 0.01(s)$ the wave is in the middle of the column heading downward (Fig.5.49(a)), at $t = 0.02(s)$ the wave is about to hit the bottom surface (Fig.5.49(b)), at $t = 0.025(s)$ the wave is reflecting off the bottom surface heading back up the column (Fig.5.49(c)), and at $t = 0.025(s)$ the wave is in the middle of the column heading upward (Fig.5.49(d)).

From Fig.5.49, it can be seen that the difference between the macro-element displacement u_3^h from classical and micromorphic continua is not significant especially for the times when the wave is heading downward before hitting the bottom surface. The difference in the wave profile (wave speed and wave displacement amplitude) of the micromorphic and classical continua become evident when the wave is reflected off the bottom surface. It can be noticed that the effect of BC on Φ_{33}^h does not affect u_3^h from micromorphic continuum noticeably. Figure 5.50 illustrates contour plots of the macro and the micro-element displacements u_3^h, $u_3^{(\alpha)h}$. From the contour plots, it can be observed that the difference of micro-element displacement (maximum value of $u_3^{(\alpha)h} = -0.838(m)$) and the macro-element displacement (maximum value of $u_3^h = -0.858(m)$) is not large. According to the

selected length of the relative position vector $\|\boldsymbol{\Xi}^{(\alpha)}\| = 0.625(m)$ which is about 2% of the total length of the column, we did not expect considerable differences in the obtained displacements. Note that as the size of relative position vector becomes smaller, micromorphic continuum behavior will be closer to classical continuum (smaller macro and micro-elements sizes reduce the inhomogeneity of the micro-structured material). Figure 5.51 illustrates the micro-displacement component Φ^h_{33} along the length of the column. Through Φ^h_{33} we should be able to look more closely into the changes in the length of relative position vector component $\Xi^{(\alpha)}_3$, and, also, the micro-element deformations. As mentioned earlier, the macro-element deformation is illustrated through the displacement vector $\boldsymbol{u}$. But, the micro-element displacement vector $\boldsymbol{u}^{(\alpha)}$ is calculated through (2.15) which is related to the macro-element displacement $\boldsymbol{u}$, the micro-displacement tensor $\boldsymbol{\Phi}$, and the relative position vector $\boldsymbol{\Xi}^{(\alpha)}$, (2.15). Therefore, if $\boldsymbol{\Phi} = \mathbf{0}$, the macro-element displacement and the micro-element displacement are equal (no micro-element deformation). Figure 5.51 is presented to study the micro-element deformation and to understand the picture of micromorphic continuum from the micro-structural deformation via plotting Φ^h_{33} through the length of the column. Note that in this paper the term "Small load amplitude" corresponds to capturing the small strain results through the finite strain model by applying a small amplitude load. The term "Large load amplitude" denotes applying load with a large amplitude to trigger the non-linear geometric effects. Figure 5.51(a) illustrates Φ^h_{33} when the wave is at its very initial steps heading downward. It can be seen that the effect of BC on Φ^h_{33} is not evident. According to the plots, the larger load amplitude (the blue and cyan lines in comparison with the red and green lines) leads to the larger amplitude of Φ^h_{33} along the length and, therefore, larger micro-element deformation. Figure 5.51(b) shows the profile of Φ^h_{33} when the wave is in the middle of the column heading downward (Fig.5.49(a)). The picture that micromorphic continuum captures from the micro-structural deformation for the selected elastic material parameters is that due to non-zero Φ^h_{33} throughout the column, the micro-elements are deforming all through the column; however, the wave (macro-element displacement $\boldsymbol{u}$) is in the middle of the column. The wave in the middle of the column denotes that the macro-elements are deforming up to the middle of the column, and the rest of the column is macroscopically

undeformed while microscopically, micro-elements are deforming throughout the column via the micro-displacement tensor $\boldsymbol{\Phi}$. For the micromorphic column in which Φ^h_{33} is free to evolve, Φ^h_{33} plots (green and cyan lines) show compression all through the column. However, for the cases with BCs on Φ^h_{33}, compression of micro-elements in the middle of the column (location where the wave is passing) makes the micro-elements at the top of the column to be under extension through positive Φ^h_{33} (Fig.5.52). Note that the micro-element displacements $u_3^{(\alpha)h}$ at the top of the column are negative which indicates the contribution of macro-element displacement $\boldsymbol{u}^h$ to the micro-element displacement $\boldsymbol{u}^{(\alpha),h}$ (micro-elements are located within the macro-element, Fig.2.1). However, the micro-elements themselves are under extension through positive Φ^h_{33}. Figure 5.51(c) shows that as the wave is traveling downward, the micro-elements at the top of the column are under larger extension as larger values of Φ^h_{33} are observed. Figure 5.51(d) illustrates the longitudinal compressive wave traveling upward through the column. For the case with a large load amplitude and no BC on Φ^h_{33} (cyan line), the micro-elements at top of the column are under larger extension (larger Φ^h_{33}) in comparison with the other cases. This is related to the large load amplitude that compresses the micro-elements close to the bottom end of the column that leads to larger extension of the micro-elements at top of the column via positive value of Φ^h_{33}. Figure 5.51(e) depicts Φ^h_{33} profile along the length of the column when the wave is traveling back up the column. It can be seen that for the case that the micromorphic BC is applied on Φ^h_{33} and the load amplitude is large (blue line) we can observe the finite strain deformation effects such that the profile of Φ^h_{33} is oscillatory. The next few figures are devoted to presenting the couple stress component M^h_{333}. In the finite element calculation, the couple stress component M^h_{333} has been calculated through constitutive equation, however, for the purpose of getting insight into the couple stress physical concept, we can use its basic definition (4.4), which interprets the couple stress in the current configuration $\mathcal{B}$ as the volume average of the micro-element stress $\boldsymbol{\sigma}^{(\alpha)}$ multiplied by the relative position vector $\boldsymbol{\xi}^{(\alpha)}$ over the macro-element domain. Therefore, the couple stress is a micro-scale moment-like stress, in which it reflects the spatial gradient of the multiplication of micro-element stress $\boldsymbol{\sigma}^{(\alpha)}$ and the relative position vector $\boldsymbol{\xi}^{(\alpha)}$ in Fig.5.53. The spatial gradient of the relative

position vector is related to the micro-displacement tensor $\boldsymbol{\Phi}$ through $\boldsymbol{\chi}(\boldsymbol{X}_\beta, t) = \mathbf{1} + \boldsymbol{\Phi}(\boldsymbol{X}_\beta, t)$ and (2.3). Note that the negative or positiveness of the couple stress does not necessarily imply that the structure is either under compression or tension. Figure 5.54 depicts the couple stress component M^h_{333} through the length of the column for the times $t = 0.002(s), 0.01(s), 0.02(s), 0.025(s)$, and $0.035(s)$. Figure 5.54(a) illustrates M^h_{333} along the length of the column at time $t = 0.002(s)$. It can be seen that at time $t = 0.002(s)$ the BC on Φ^h_{33} does not affect the profile of couple stress (similar to what is observed in Fig.5.51(a)).

From Figs.5.54, it can be seen that when there is no BC on Φ^h_{33}, its gradient around the boundary is zero and the resulting couple stress M^h_{333} will be zero as well. Therefore, for the cases with no BC on Φ^h_{33}, the couple stress M^h_{333} is zero at the two ends of the column. Figure 5.54(e) illustrates M^h_{333} at time $t = 0.035(s)$. This figure reflects the effect of finite strain analysis on the profile of M^h_{333} along the length of the column similar to what is observed in the plot of the micro-displacement tensor component Φ^h_{33} in Fig.5.51(e). Figure 5.55 compares motion u^h_3 at the top of the column obtained from the finite strain micromorphic continuum with and without BC on Φ^h_{33} and that of the classical continuum. The obtained displacements are close to each other which can reflect the effect of small inhomogeneity due to small value of selected relative position vector (small sizes of macro and micro-elements). Figure 5.56 depicts the finite strain analysis versus the small amplitude model (small strain analysis) to highlight the non-linear geometry effect on the displacement at top of the column. For the purpose of comparison, the obtained results of the small amplitude load analysis are scaled with the ratio of large amplitude load to small amplitude load. It can be seen that beside the larger macro-element displacement u^h_3 obtained from the finite strain analysis in comparison with the small load amplitude models (for both classical and micromorphic continua), the scaled wave from the small load amplitude model has a larger velocity than that of the wave from finite strain analysis.

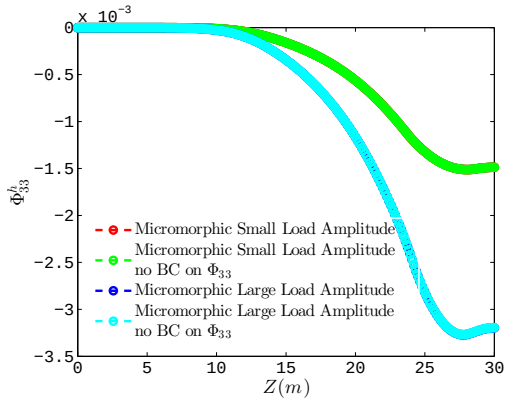

(a) Micro-displacement tensor component Φ^h_{33} at t=0.002(s).

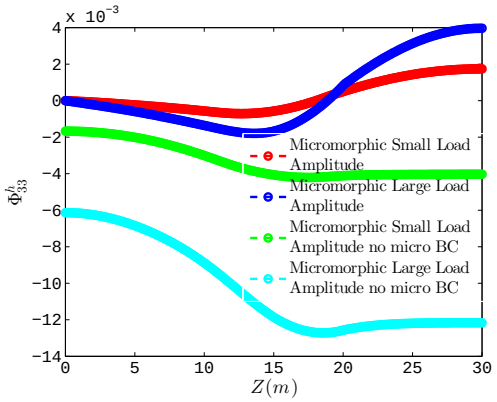

(b) Micro-displacement tensor component Φ^h_{33} at t=0.01(s).

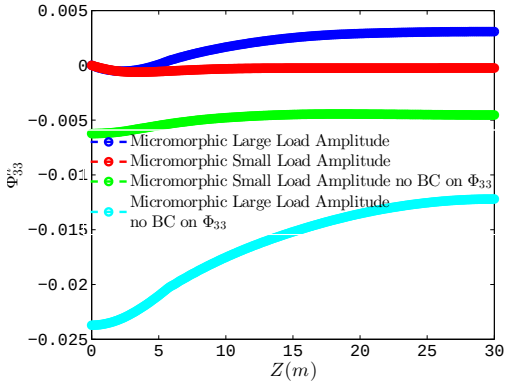

(c) Micro-displacement tensor component Φ^h_{33} at t=0.02(s).

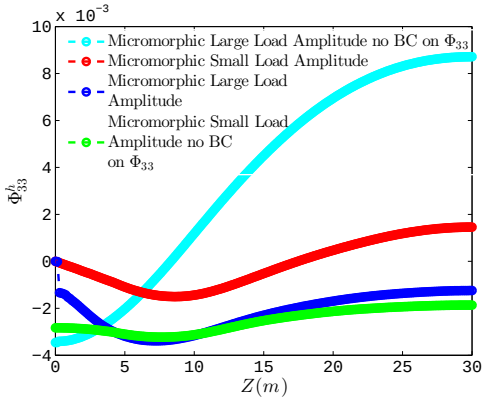

(d) Micro-displacement tensor component Φ^h_{33} at t=0.025(s).

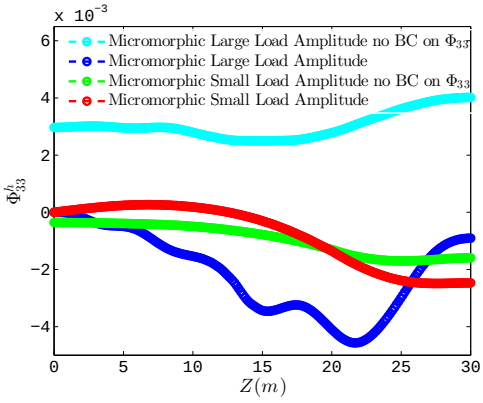

(e) Micro-displacement tensor component Φ^h_{33} at t=0.035(s).

Figure 5.51. Micro-displacement tensor component Φ^h_{33} through the length of the column.

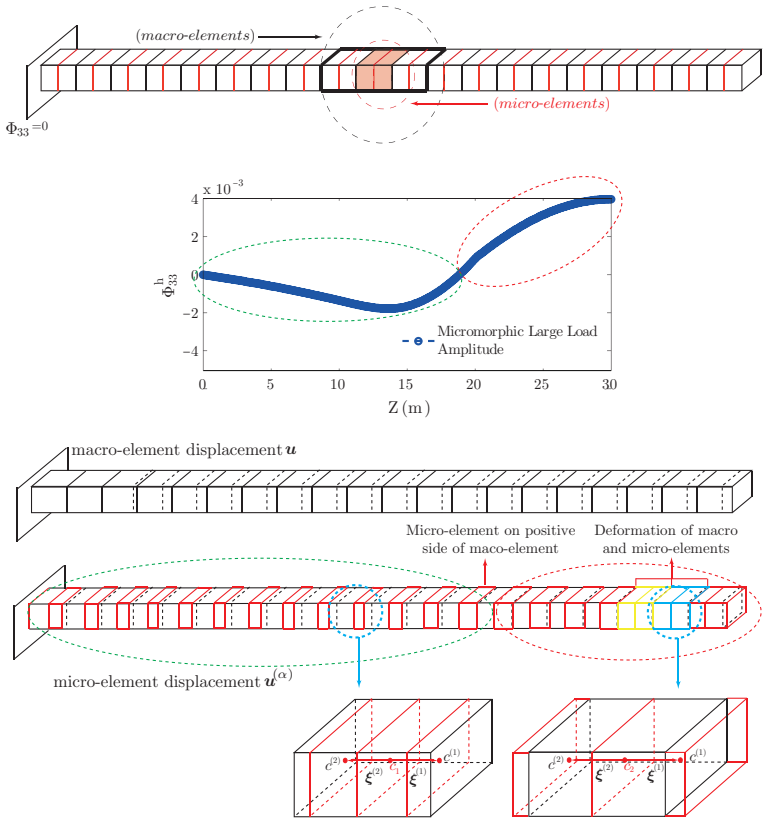

Figure 5.52. Schematic of Φ^h_{33} throughout the column.

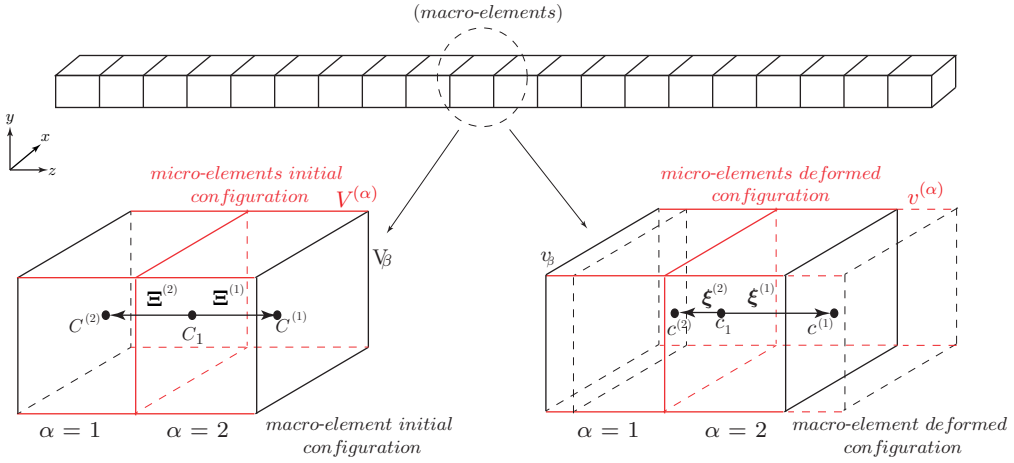

$$(m_{klm})_\beta = \frac{1}{v_\beta}\sum_{\alpha=1}^{2}\sigma^{(\alpha)}_{kl}\xi^{(\alpha)}_m v^{(\alpha)}$$

Figure 5.53. Couple stress interpretation.

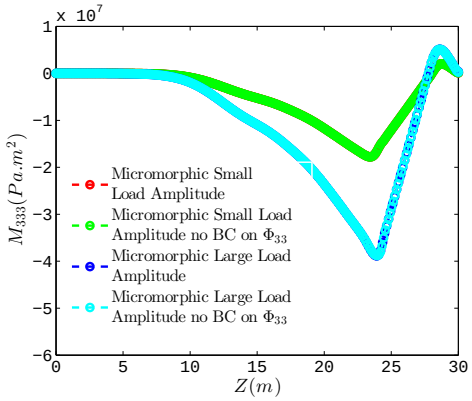

(a) Coupled stress component M^h_{333} at t=0.002(s).

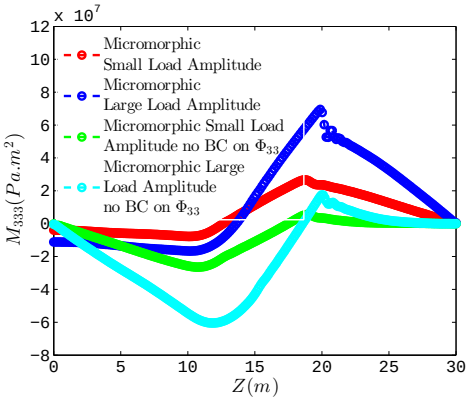

(b) Coupled stress component M^h_{333} at t=0.01(s).

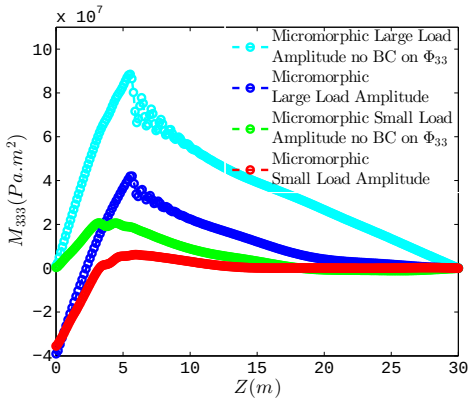

(c) Coupled stress component M^h_{333} at t=0.02(s).

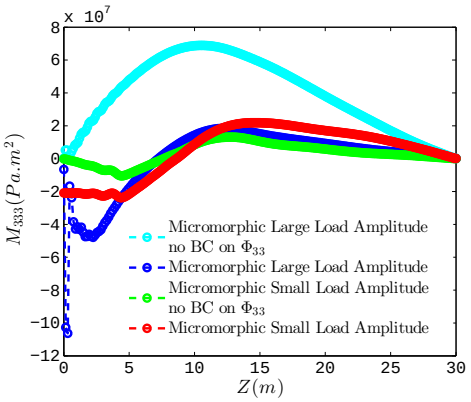

(d) Coupled stress component M^h_{333} at t=0.025(s).

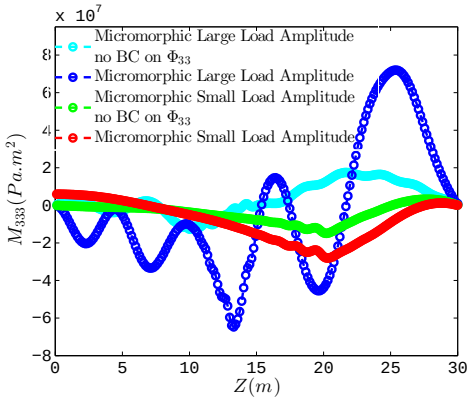

(e) Coupled stress component M^h_{333} at t=0.035(s).

Figure 5.54. Couple stress component M^h_{333} through the length of column

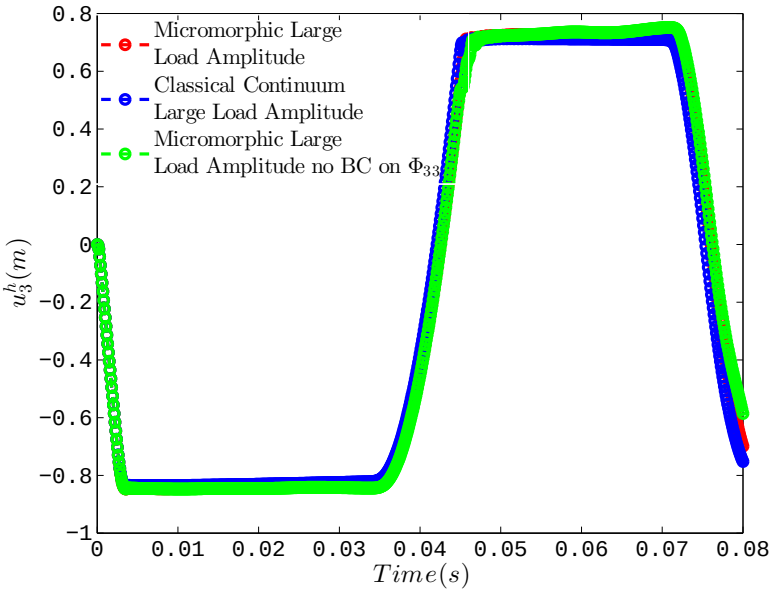

Figure 5.55. Track of displacement u_3^h at top of the column over time

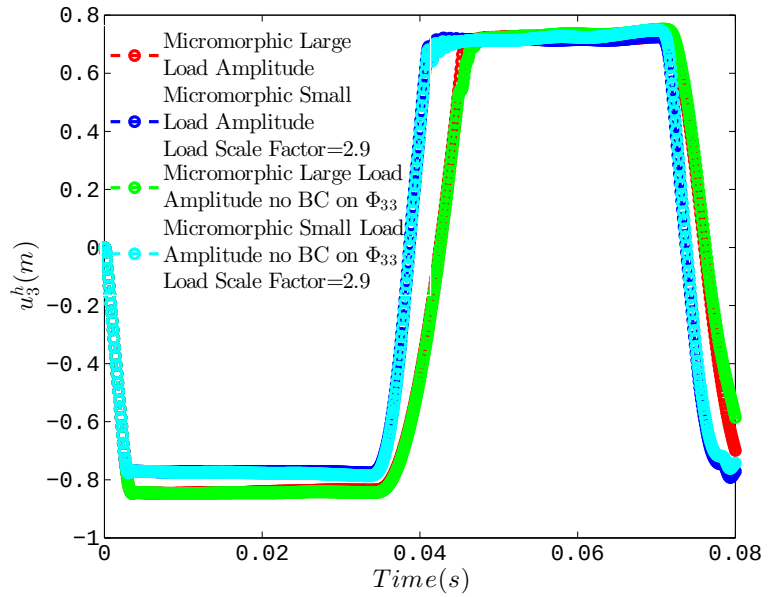

Figure 5.56. finite strain analysis versus small strain analysis on dynamic motion u_3^h at top of the column over time

5.5.2 Beam Bending Dynamics at Finite Strain

The second example is for beam bending dynamics at finite strain in which a lateral load is applied in the middle of the beam, and the two ends of the beam are fixed (Fig.5.57). The beam bending model is made up of two blocks of materials to investigate the effect of transition from micromorphic continuum/classical continuum to classical continuum/micromorphic continuum for beam bending dynamics. The first block is located in the middle of the beam, and the second block is made of two volumes located at the two sides of the beam (Fig.5.57). Note that each block can be either micromorphic continuum or classical continuum. Therefore, there are four models to investigate for beam bending dynamics.

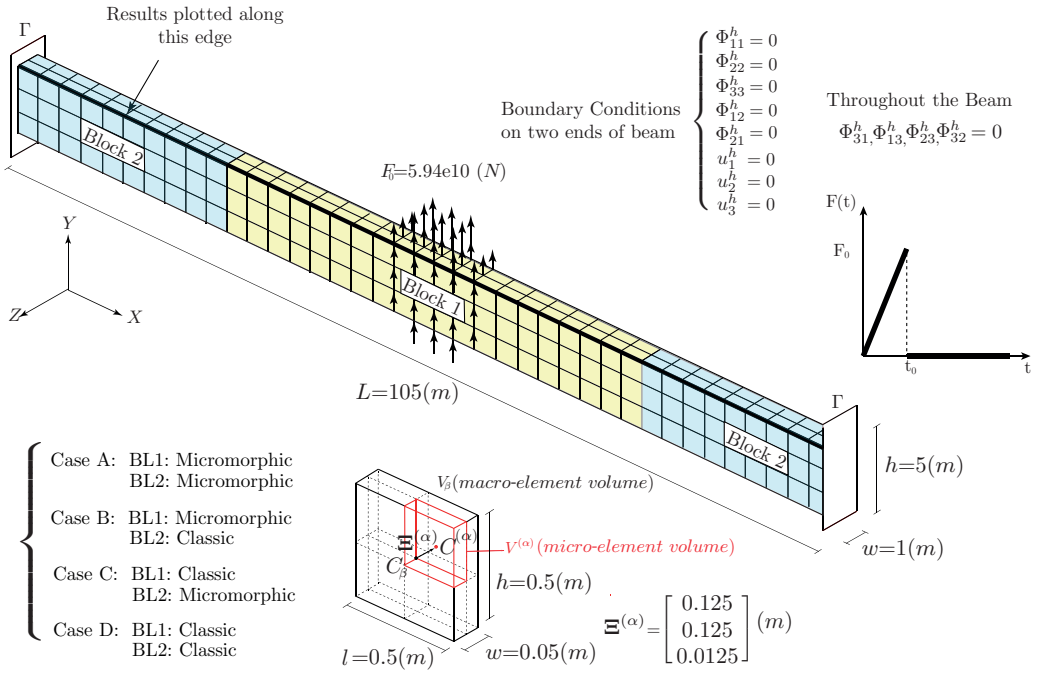

Figure 5.57. Schematic of finite element mesh and BC for beam bending dynamics.

The selected material parameters are similar to the previous example and are presented in Table 5.14. The selected relative position vector for the micro-element in the positive part of the macro-element is $\boldsymbol{\Xi}^{(\alpha)} = [0.125 \quad 0.125 \quad 0.0125]\,(m)$. Table 5.16 illustrates the BCs applied on the micromorphic and classical continuum blocks of the beam models.

Table 5.16. Selected boundary conditions for beam bending dynamics.

Micromorphic Continuum	Throughout the beam	On surface Γ (both sides)
	$\Phi^h_{21}, \Phi^h_{12}, \Phi^h_{23}, \Phi^h_{32} = 0$	$\Phi^h_{11}, \Phi^h_{22}, \Phi^h_{33}, \Phi^h_{13}, \Phi^h_{31} = 0$
		$u^h_1, u^h_2, u^h_3 = 0$
Classical Continuum		On surface Γ (both sides)
		$u^h_1, u^h_2, u^h_3 = 0$

Figure 5.58 depicts the macro-element displacement component along the length of the beam models at times $t = 0.005(s), t = 0.025(s), t = 0.06(s), t = 0.12(s), t = 0.18(s)$, and $t = 0.22(s)$. These figures are presented to illustrate the effect of micromorphic and classical continuum interface on the beam bending displacement. Note that the legends "Micromorphic-Micromorphic" and "Classic-Classic" denote that both the first and second blocks are micromorphic and classical continuum, respectively. The legends "Micromorphic-Classic" and "Classic-Micromorphic" denote the first block is micromorphic continuum/classical continuum, and the second block is classical continuum/micromorphic continuum. In the figures, a comparison is made between these four beam models. Note that the dashed blue lines in the figures indicate the interfaces of micromorphic and classical continuum. Figure 5.58(a) illustrates the beam macro-element displacement at the initial stage of loading. It can be seen that the beam with micromorphic continuum block in the middle deforms more than the beam with classical continuum blocks in the middle. Figures 5.58(b) and 5.58(c) show the bending wave in the beam when it is about to hit the interface of micromorphic and classical continuum. From Fig.5.58(c), it can be seen that the interface does not have a significant effect on the wave when it transfers from the micromorphic continuum block to the classical continuum block and vice versa. Figures 5.58(d), 5.58(e), and 5.58(f) show that when the wave is reflected from the two sides of the beam we can notice the effect of the interface on the macro-element displacement profile along the length. The effect of the interface is more highlighted as the wave travels back and forth through the beam. This is related to the differences of the wave velocities in micromorphic and classical continua. Figure 5.59 demonstrates the deformed configuration, the macro-element displacement component u^h_2, and the micro-element displacement component $u^{(\alpha)h}_2$ of the micromorphic-micromorphic beam under bending.

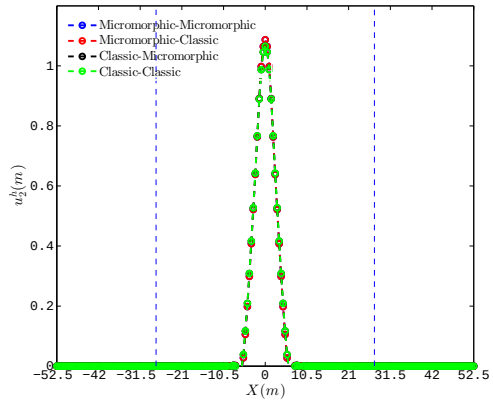

(a) Macro-element displacement component u_2^h at $t = 0.005(s)$.

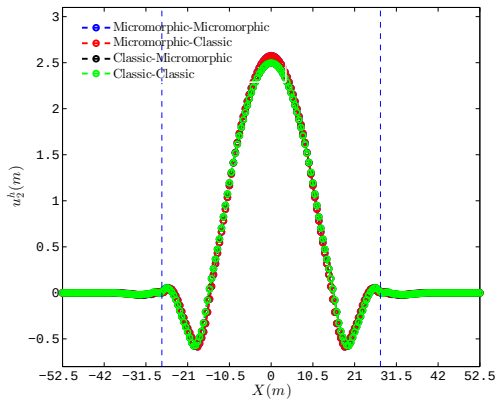

(b) Macro-element displacement component u_2^h at $t = 0.025(s)$.

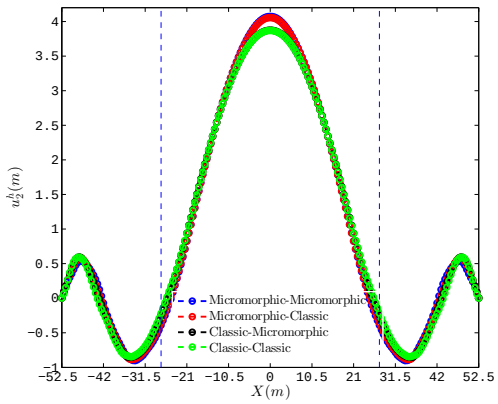

(c) Macro-element displacement component u_2^h at $t = 0.06(s)$.

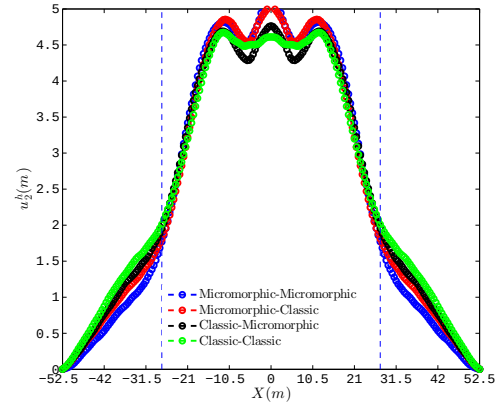

(d) Macro-element displacement component u_2^h at $t = 0.12(s)$.

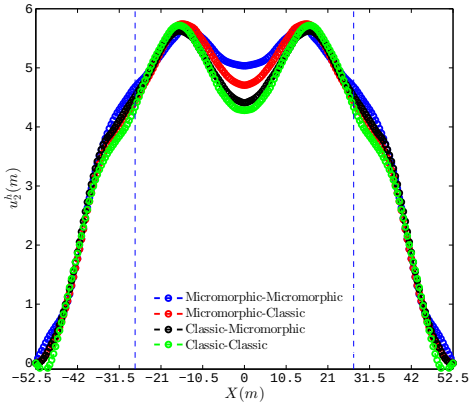

(e) Macro-element displacement component u_2^h at $t = 0.18(s)$.

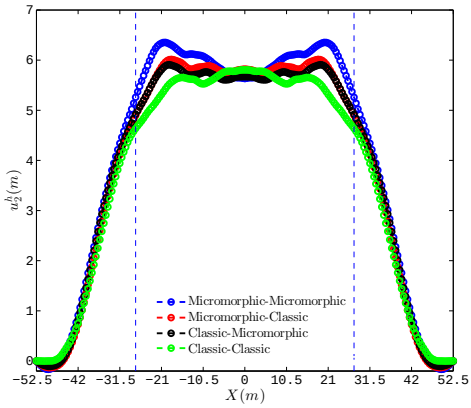

(f) Macro-element displacement component u_2^h at $t = 0.22(s)$.

Figure 5.58. Macro-element displacement component u_2^h along the length of the beam

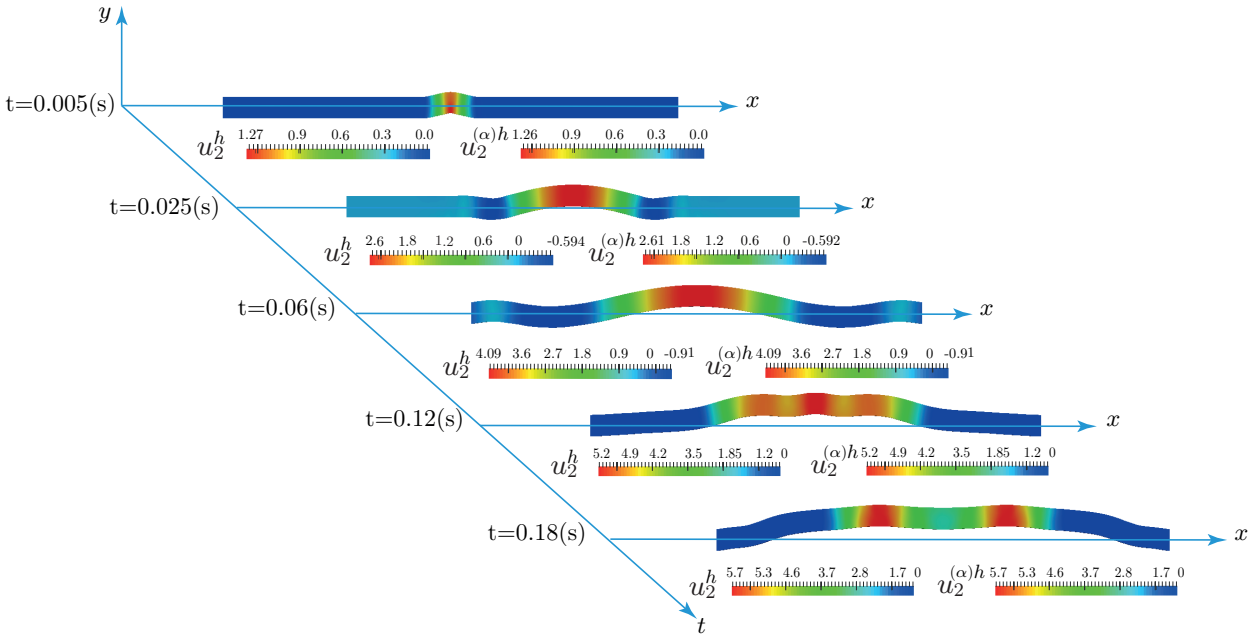

Figure 5.59. Contour plots of macro-element displacement u_2^h and micro-element displacement $u_2^{(\alpha)h}$ for the micromorphic-micromorphic beam models

The contour plots show that the difference between the micro-element displacement $u_2^{(\alpha)h}$ and the macro-element displacement u_2^h is not significant, and as the displacements become larger their difference becomes negligible. This indicates that the micro-element deformation through the micro-displacement tensor $\mathbf{\Phi}$ is not significant which may be related to the selected elastic material parameters for micromorphic continuum and, also, the size of the relative position vector. Figures 5.60(a) and 5.60(b) illustrate the macro-element displacement u_2^h in the middle and at the interface of micromorphic and classical continuum blocks over time. From the perspective of displacement magnitude, it is noticed that the micromorphic-micromorphic beam is the most flexible one, and the classic-classic beam model is the stiffest. Note that when the wave is passing the interface toward the middle of the beam (interface macro-element displacement u_2^h is decreasing in Fig.5.60(a)) the deviation between the macro-element displacement u_2^h of the four beam models become noticeable (the second time wave is passing the interface).

Figures 5.61 depicts the second Piola Kirchhoff stress components S_{11}^h and S_{22}^h along the length of the beam for the times $t = 0.005(s)$ and $t = 0.025(s)$. These figures demonstrate two stress

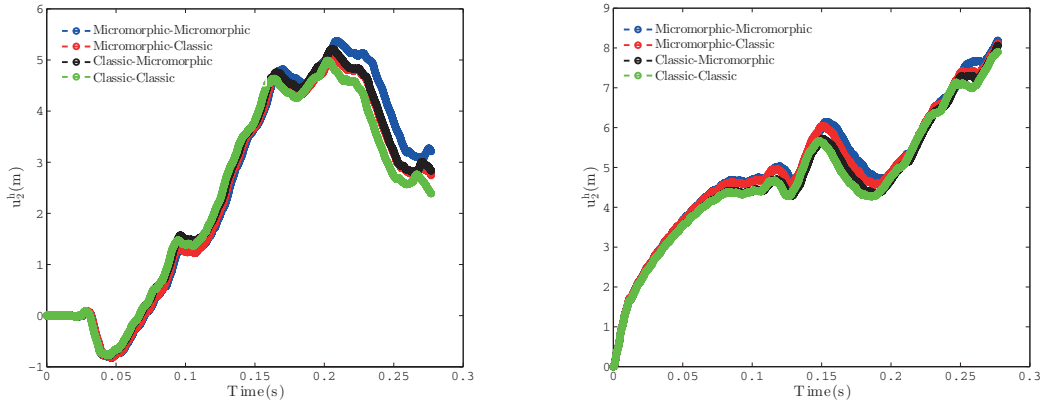

(a) History of macro-element displacement component u_2^h at the interface of micromorphic and classical elasticity.

(b) History of macro-element displacement component u_2^h in the middle of the beam.

Figure 5.60. Macro-element displacement component u_2^h at the micromorphic and classical elasticity interface and in the middle of the beam over time.

waves S_{11}^h and S_{22}^h are traveling in two opposite directions toward the beam ends. For all the four beam models the results of the second Piola Kirchhoff stress component S_{11}^h are overlapped (axial wave); however, this is not the case for the second Piola Kirchhoff stress component S_{22}^h (transverse wave). Note that the profile of second Piola Kirchhoff stress component S_{22}^h at time $t = 0.025(s)$ has numerical oscillations. Similar to what is observed in Fig.5.48(b), these numerical oscillations are related to the sharp profile of impulse load in which the developed implicit finite element model with the employed time integration scheme is not able to remove them completely from the stress results. The results can become improved by developing a micromorphic explicit dynamic finite element analysis with smaller time steps and more accuracy which is beyond the scope of this chapter. Figure 5.62 shows the micro-displacement component Φ_{22}^h along the length of the beam for the times $t = 0.005(s)$, $t = 0.025(s)$, and $t = 0.06(s)$. Figure 5.62(a) illustrates Φ_{22}^h at the initial stage of loading. The plot of micro-displacement component Φ_{22}^h shows that for the micromorphic-micromorphic beam (blue circles) and the micromorphic-classic beam model (red circles), the micro-elements throughout these two beam models are under extension in the direction of loading. Also, the results of these two models are overlapped around the peak of Φ_{22}^h plots in

the middle of the beam. Note that for the classic-micromorphic beam model the bending wave has not yet arrived at the micromorphic blocks (green circle) and the micro-displacement component Φ^h_{22} profile is zero all throughout the beam. Figure 5.62(b) shows Φ^h_{22} at the time when the wave is about to hit the interface of micromorphic and classical continuum (Fig.5.58(b)). The plots of Φ^h_{22} show that at time $t = 0.025(s)$, the micro-element extensional wave spreads throughout the micromorphic blocks (for both the micromorphic-micromorphic and the micromorphic-classic models) of the beam models. We can see the two peaks in the plot of Φ^h_{22} that shows the micro-element extensional waves are traveling toward the two sides of the beam. From the micro-element deformation perspective, the classic-micromorphic beam model behaves differently, and the micro-elements in its micromorphic blocks show compression. This is related to the negative macro-element displacement u^h_2 when the wave is about to hit the interface (Fig.5.58(b)). In Figure 5.62(c), the micro-element extensional wave is about to leave the middle part of the beam and, therefore, the amplitude of Φ^h_{22} is decreasing. Note that for the micromorphic-classic beam the reduction in the amplitude of Φ^h_{22} is more noticeable due to the transition from the micromorphic continuum to the classical continuum blocks. For the classic-micromorphic beam, we can see that Φ^h_{22} is turning to positive value which is related to the positive macro-element displacement arrived at the two sides of the beam. Figure 5.63 demonstrates the couple stress component M^h_{222} along the length of the beam for times $t = 0.005(s)$, $t = 0.025(s)$, and $t = 0.06(s)$. As mentioned earlier, negative or positive couple stress components do not necessarily imply that the structure is under tension or compression. Therefore, if the couple stress component is negative, it can be concluded that either the gradient of the relative position vector (which is related to $\mathbf{\Phi}$) or the gradient to the micro-element stress is negative. In Fig.5.62(a), the spatial gradient of the micro-displacement component Φ^h_{22} is positive for the first half of the beam, and it is negative for the other half of the beam. There is a trough in the plot of M^h_{222} in Fig.5.63(a), which reflects the effect of the negative spatial gradient of the micro-element stress in the Y direction. Figures 5.63(b) and 5.63(c) show that for times $t = 0.025(s)$ and $t = 0.06(s)$ the profiles of couple stress component M^h_{222} for the middle block of the micromorphic-micromorphic and micromorphic-classic models are overlapped,

unlike the micro-displacement component Φ^h_{22} in Figs.5.62(b) and 5.62(c). This can be related to similar spatial gradient of the micro-element stresses of these two models that compensate for their differences with regard to the spatial gradient of the micro-displacement tensor component Φ^h_{22}. Figure 5.64 demonstrates the contour plot of the couple stress components M^h_{111} and M^h_{222} along the length of the micromorphic-micromorphic beam. The contour plots of the couple stress component M^h_{111} show that it has a smooth distribution along the length of the beam. This is related to the smooth gradient of the micro-element stress along the X axis. However, the couple stress component M^h_{222} represents the gradient of stress along the Y axis which is the thickness of the beam. Therefore, in the region in which an abrupt change in deformation occurred, we can expect the significant gradient of micro-element stress along the Y direction and this is the reason for localized distribution of M^h_{222} along the thickness of the beam.

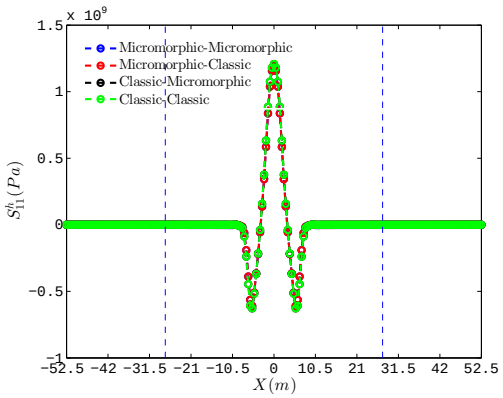

(a) Second Piola Kirchhoff S_{11}^h stress along length of beam at $t = 0.005(s)$.

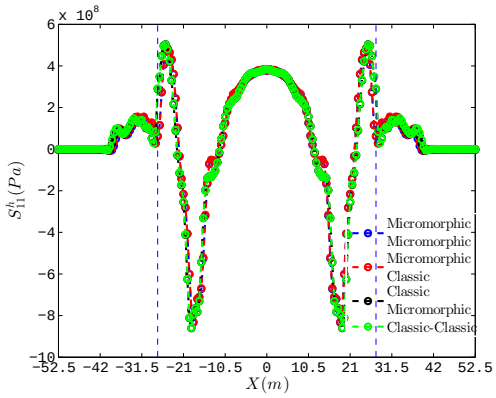

(b) Second Piola Kirchhoff S_{11}^h stress along length of beam at $t = 0.025(s)$.

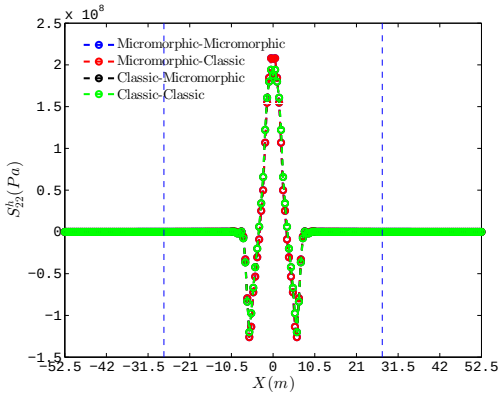

(c) Second Piola Kirchhoff S_{22}^h stress along length of beam at $t = 0.005(s)$.

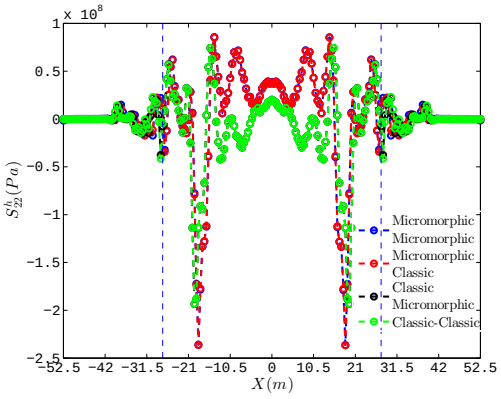

(d) Second Piola Kirchhoff S_{22}^h stress along length of beam at $t = 0.025(s)$.

Figure 5.61. Second Piola Kirchhoff stress components S_{11}^h and S_{22}^h along length of beam.

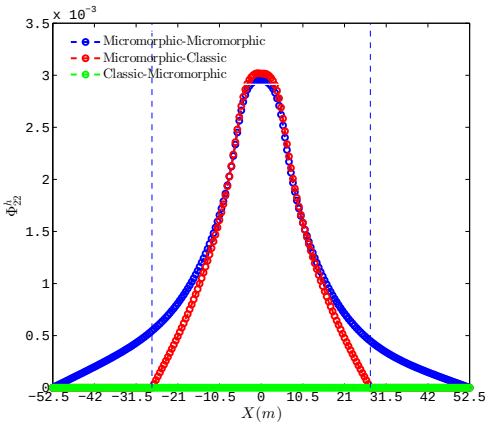

(a) Micro-displacement component Φ^h_{22} at $t = 0.005(s)$.

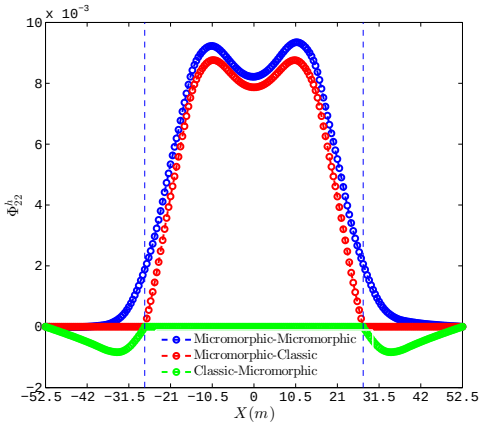

(b) Micro-displacement component Φ^h_{22} at $t = 0.025s$.

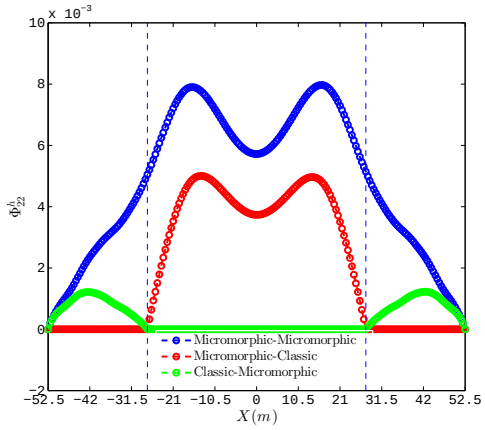

(c) Micro-displacement component Φ^h_{22} at $t = 0.06s$.

Figure 5.62. Micro-displacement component Φ^h_{22} along length of beam.

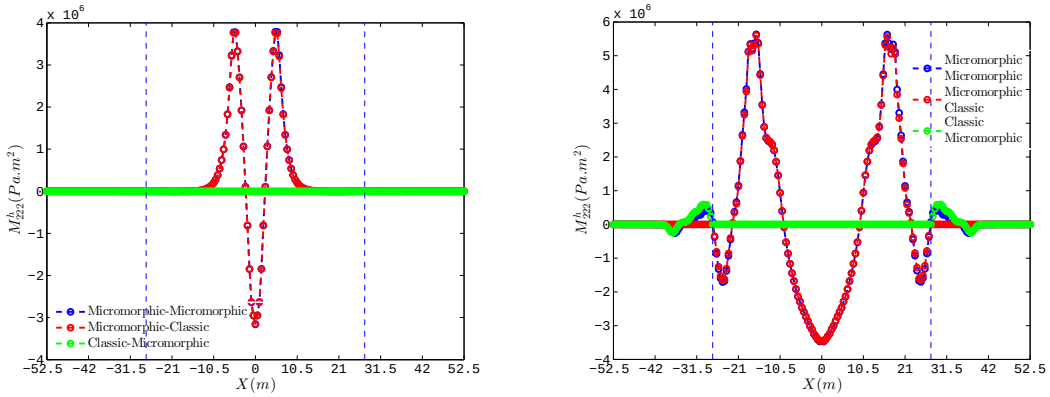

(a) Couple stress component M^h_{222} at $t = 0.005(s)$. (b) Couple stress component M^h_{222} at $t = 0.025(s)$.

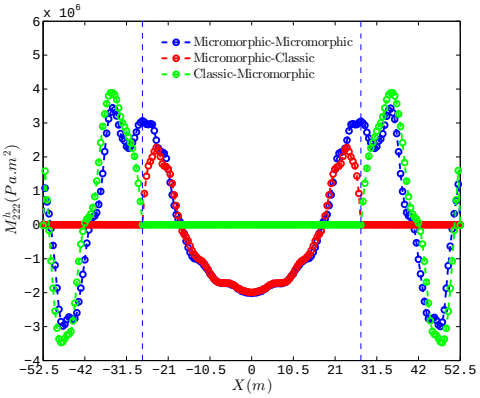

(c) Couple stress component M^h_{222} at $t = 0.06(s)$.

Figure 5.63. Couple stress component M^h_{222} along length of beam.

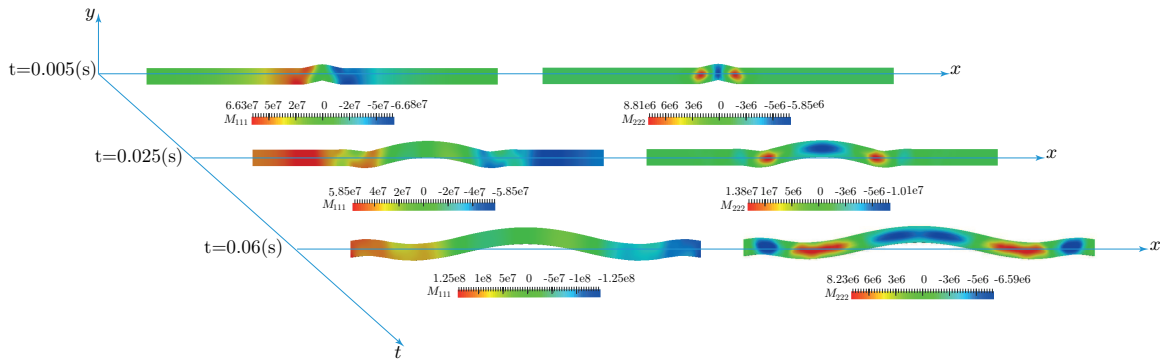

Figure 5.64. Contour plots couple stress components M^h_{111} and M^h_{222}.

5.5.3 Plate Dynamics Under In-plane Loading

In this section, numerical results on the dynamic analysis of a plate under in-plane loading will be presented. Figure 5.65 illustrates the geometry, mesh schematic, and BCs of the plate. The plate is made of two blocks in which either micromorphic or classical continuum can be associated with these blocks. Therefore, similar to the beam bending example, there are four cases such as "micromorphic-micromorphic", "micromorphic-classic", "classic-micromorphic", and "classic-classic" to study the dynamic behavior of the plate.

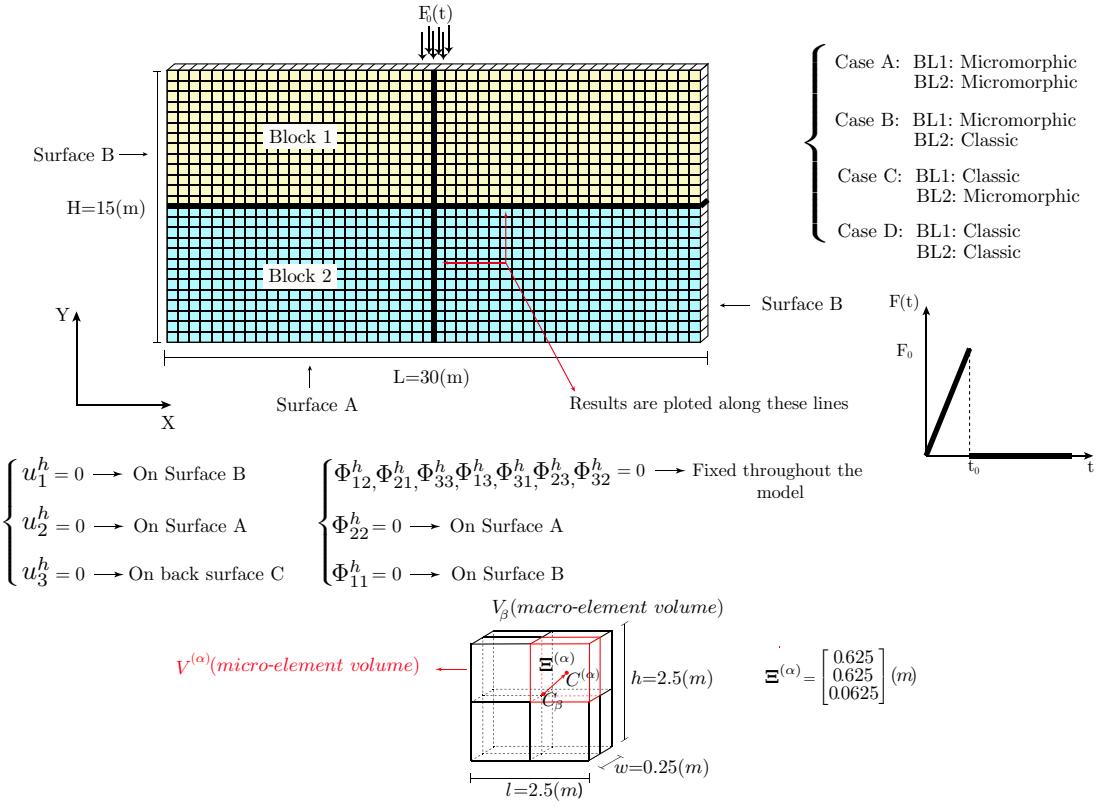

Figure 5.65. Configuration of plate under in-plane loading

The selected material parameters for the plate is similar to those of the previous examples and is presented in Table 5.14. The BCs on the micromorphic dofs $\boldsymbol{\Phi}^h$ and the macro-element displacement $\boldsymbol{u}^h$ (displacement in classical continuum) are illustrated in Table 5.17.

Table 5.17. selected boundary conditions for plate under in-plane loading

Micromorphic Continuum	Throughout the plate	
	$\Phi^h_{12}, \Phi^h_{21}, \Phi^h_{33}, \Phi^h_{13}, \Phi^h_{31}, \Phi^h_{23}, \Phi^h_{32} = 0$	
On surface A	On surface B	On surface C
$\Phi^h_{22} = 0$	$\Phi^h_{11} = 0$	
$u^h_2 = 0$	$u^h_1 = 0$	$u^h_3 = 0$
Classical Continuum	Throughout the plate	
On surface A	On surface B	On surface C
$u^h_2 = 0$	$u^h_1 = 0$	$u^h_3 = 0$

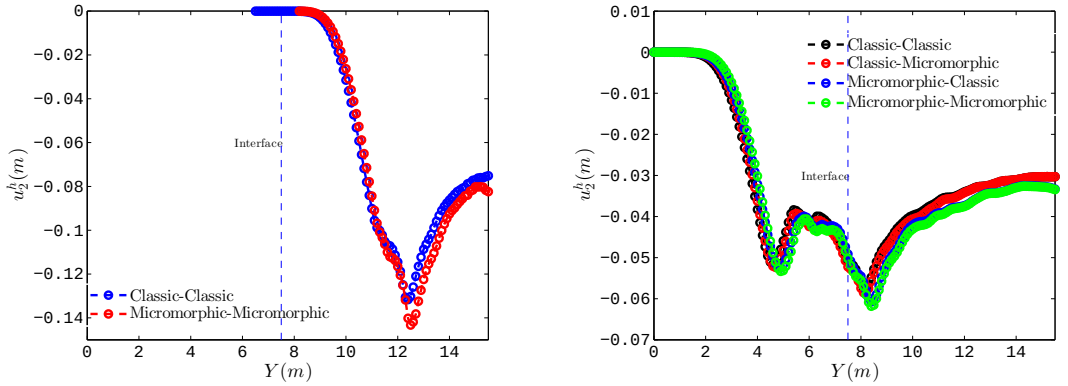

(a) macro-element displacement component u^h_2 at $t = 0.004(s)$.

(b) macro-element displacement component u^h_2 at $t = 0.0085(s)$.

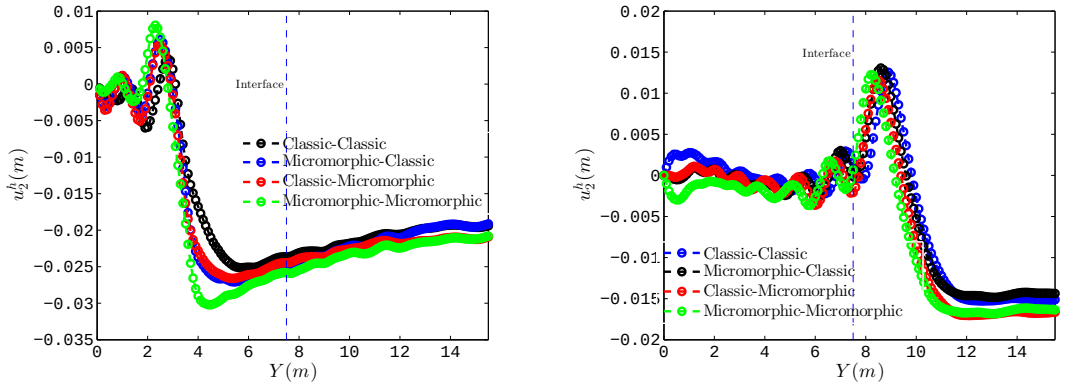

(c) macro-element displacement component u^h_2 at $t = 0.0135(s)$.

(d) macro-element displacement component u^h_2 at $t = 0.0175(s)$.

Figure 5.66. macro-element displacement u^h_2 along width of plate.

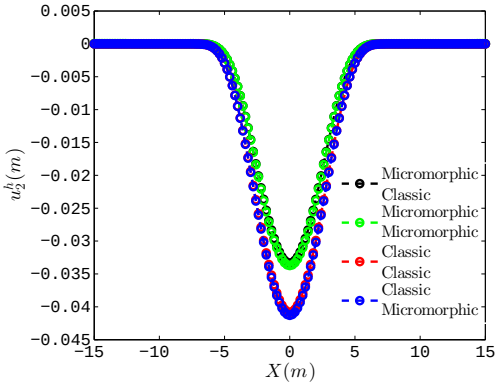

(a) macro-element displacement component u_2^h along interface of micromorphic and classical continuum at $t = 0.006(s)$.

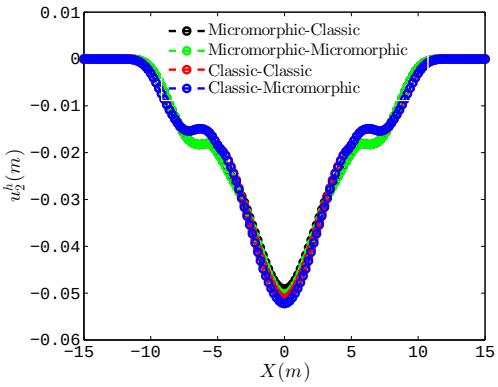

(b) macro-element displacement component u_2^h along interface of micromorphic and classical continuum at $t = 0.0085(s)$.

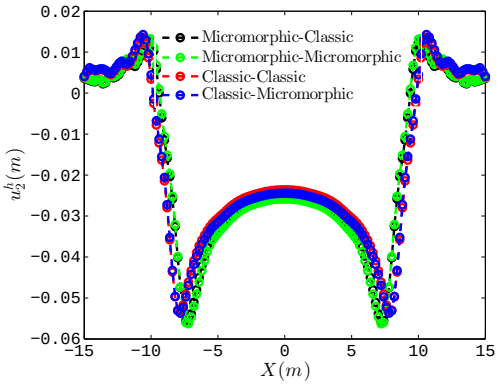

(c) macro-element displacement component u_2^h along interface of micromorphic and classical continuum at $t = 0.0135(s)$.

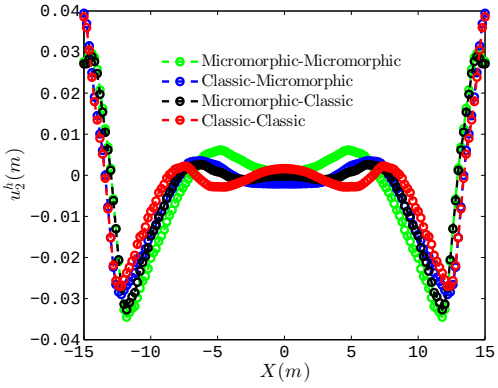

(d) macro-element displacement component u_2^h along interface of micromorphic and classical continuum at $t = 0.0175(s)$.

Figure 5.67. macro-element displacement u_2^h along interface of micromorphic and classical continuum blocks.

Figure 5.66 illustrates the macro-element displacement u_2^h along the width (vertical direction) of the plate. These plots represent the displacement profile along the direction of the longitudinal wave in the plate. These figures show that the difference in the macro-element displacement u_2^h of the four plate models is noticeable. Figure 5.66(a) shows that the micromorphic plate is slightly more flexible than the classical continuum plate. Note that at times $t = 0.004(s)$ and $t = 0.0085(s)$ the longitudinal wave is in the first block of the plate and, therefore, the obtained macro-element displacement component u_2^h of the micromorphic-classic and the classic-micromorphic are overlapped with the micromorphic-micromorphic and the classic-classic plates, respectively. Figure 5.66(b) demonstrates the status of the macro-element displacement u_2^h when the longitudinal wave passed the interface. As mentioned earlier, a small difference in the obtained displacement is noticeable.

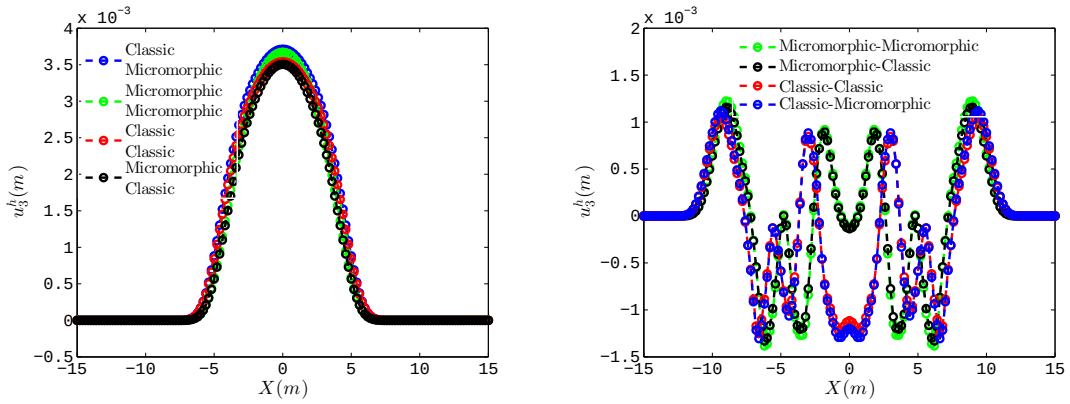

(a) macro-element displacement component u_3^h at $t = 0.004(s)$.

(b) macro-element displacement component u_3^h at $t = 0.0085(s)$.

Figure 5.68. macro-element displacement u_3^h along interface of plate.

It is worth mentioning that in general the profiles of the macro-element displacements u_2^h of the four models are the same. The differences in the longitudinal wave velocities of these models make the displacement profiles of these four models deviate from each other. Figures 5.66(c) and 5.66(d) show the macro-element displacement u_2^h when the wave is reflected from the bottom surface. The differences between the profiles of the macro-element displacement u_2^h of the four models become more evident. Figure 5.67 illustrates profile of longitudinal wave along the interface of the micromorphic and the classical continuum blocks horizontal bold line in Fig.5.65 through plotting

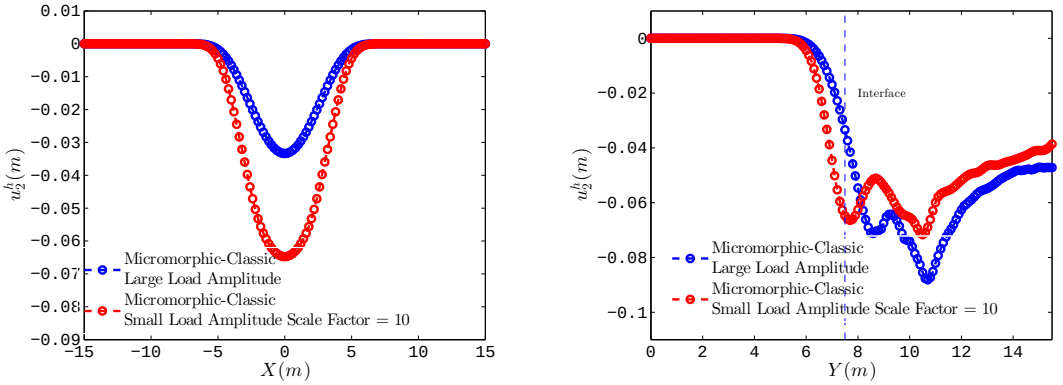

(a) Finite strain analysis versus small strain analysis on macro-element displacement component u_2^h at $t = 0.006(s)$ along interface.

(b) Finite strain analysis versus small strain analysis on macro-element displacement component u_2^h at $t = 0.0085(s)$ along width of plate.

Figure 5.69. Comparison of finite strain and small strain analyses on plate macro-element displacement component u_2^h.

the macro-element displacement component u_2^h. Figure 5.67(a) depicts the longitudinal wave just arrived at the interface. Therefore, the displacement profiles of the micromorphic-classic and the classic-micromorphic plates are similar to those of the micromorphic-micromorphic and the classic-classic plates. This figure shows that the amplitude of displacement in micromorphic continuum is smaller than that of classical continuum; however, it has been observed that (Fig.5.66(a)) for the selected elastic material parameters, deformation in micromorphic continuum for a certain amount of load is larger than that of classical continuum. This is related to the lower micromorphic wave speed and, therefore, the longitudinal wave in micromorphic continuum is behind classical continuum and its displacement amplitude is smaller. Figure 5.67(b) illustrates the longitudinal wave when it arrives at the second block toward the bottom end of the plate. Figure 5.67(c) demonstrates the longitudinal wave when it is reflected off the bottom end of the plate. It can be seen that the macro-element displacement component u_2^h profile is similar for all four models in contrast with that of Fig.5.67(d). Figure 5.67(d) depicts the profile of the macro-element displacement u_2^h when the longitudinal wave passes the interface for the second time. It is noticeable that the macro-element displacement u_2^h starts deviating from each other for all four cases.

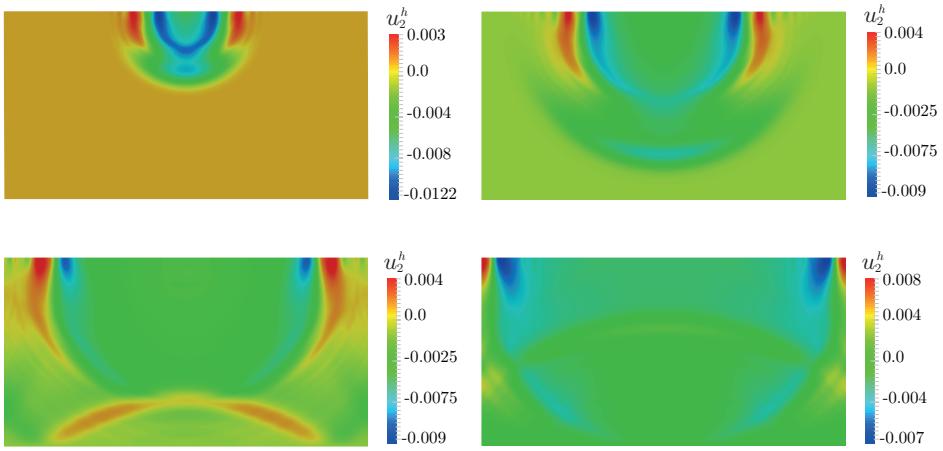

Figure 5.70. Contour plot of macro-element displacement component u_2^h to visualize the longitudinal wave.

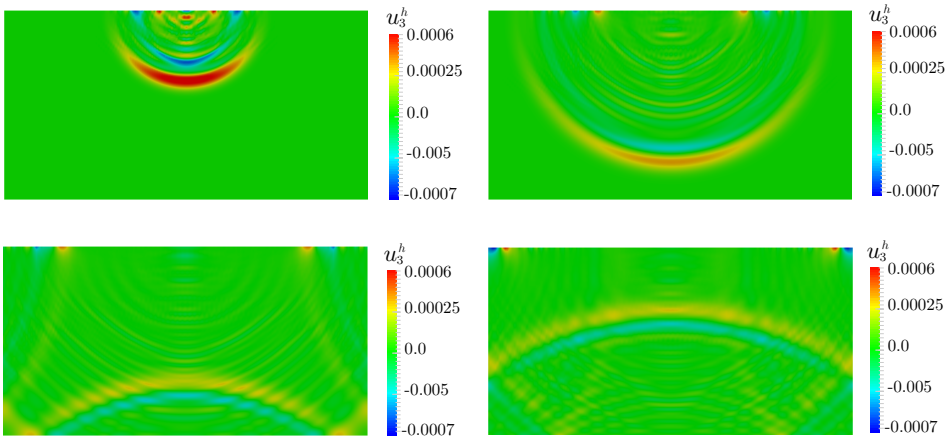

Figure 5.71. Contour plot of macro-element displacement component u_3^h to visualize the transverse wave.

Figure 5.68 depicts the macro-element displacement u_3^h along the interface. Figure 5.68(a) shows the transverse wave along the interface at $t = 0.004(s)$. The profile of out-of-plane macro-element displacement u_3^h is similar in all cases except small differences in the amplitude of the deformations between micromorphic continuum and classical continuum. It can be seen that at time $t = 0.0085(s)$ when the transverse wave passed the interface (Fig.5.68(b)) the profiles of out-of-plane displacement for all the four cases are different. Figure 5.69 show a comparison between the macro-element displacement u_2^h obtained from the finite strain analysis (large load amplitude model) and that of the small load amplitude analysis (small strain analysis). Similar to the previous examples the displacement from the small load amplitude analysis has been scaled to compare with finite strain analysis. The finite strain analysis predicts a larger macro-element displacement component u_2^h in comparison with the scaled small load amplitude model. It is to be noted that the finite strain wave travels at lower speed than the small strain wave. Figures 5.70 and 5.71 show contour plots of the macro-element displacement components u_2^h and u_3^h to visualize the longitudinal and transverse waves for the micromorphic-classic plate model. In these figures, four different times are selected to illustrate the longitudinal and transverse waves propagation in the plate. Figure 5.72 shows the macro-element velocity component $\dot{u}_2^h$ along the interface of the plate at the times $t = 0.006(s)$ and $t = 0.0085(s)$. As mentioned earlier, wave velocity in classical continuum is higher than that of micromorphic continuum. Note that this is not a general conclusion, and it is mainly related to the selected elastic material parameters for micromorphic continuum. In Fig.5.72(a), the velocity profile for all the four plate models are similar, however, their velocity amplitudes are different. Figure 5.72(b) shows that when the longitudinal wave passed the micromorphic and classical continuum interface the profile of velocity changes noticeably when it travels from micromorphic to classical continuum. Figure 5.73 illustrates the second Piola Kirchhoff stress component S_{22}^h along the interface. Similar to what is observed in the macro-element velocity $\dot{u}_2^h$ plots (Fig.5.72), at the time $t = 0.006(s)$ (Fig.5.73(a)), the profile of second Piola Kirchhoff stress component S_{22}^h is similar for all four cases, however, differences in the stress amplitude are noticeable. Figure 5.73 shows that the difference in the profile of the second Piola Kirchhoff stress

S_{22} from the micromorphic-micromorphic and the micromorphic-classic with that of the classic-classic and the classic-micromorphic becomes more evident. Figure 5.74 illustrates the micro-displacement tensor component Φ^h_{22} along the width of the plate. Similar to what is observed in previous examples, when the longitudinal compression wave is traveling, the micro-elements all through the plate start deforming (for the micromorphic-micromorphic case, Φ^h_{22} in Fig.5.74(a) is negative all through the plate) in micromorphic continuum. As the micro-elements are getting compressed at the bottom of the plate, the micro-elements at top of the plate are under tension (Φ^h_{22} turning to positive values) (Fig.5.74(b)). Figures 5.74(c) and 5.74(d) plot Φ^h_{22} when the wave is getting reflected off the bottom surface. Figure 5.75 illustrates the couple stress component M^h_{222} along the width of the plate at the times $t = 0.006(s)$, $t = 0.0085(s)$, $t = 0.0135(s)$, and $t = 0.0175(s)$. As explained in the previous examples, M^h_{222} shows the spatial gradient along the direction 2 of the micro-element stress multiplied by the spatial gradient of the relative position vector. Therefore, when the micro-displacement component Φ^h_{22} has a spatial gradient along the width of the plate, the couple stress component M^h_{222} will be non-zero along the width of the plate. In all the couple stress component M^h_{222} plots in Fig.5.75 there is a peak (either positive or negative) in the M^h_{222} profile along the width of the plate that indicates the peak of spatial gradient of the micro-element stress. Note that the peak in the spatial gradient of micro-element stress can be use as an indication of the location of the wave (no gradient in the micro-element stress of adjacent micro-elements denotes there is no disturbance of wave at that location). Consequently, we have non-zero micro-displacement tensor $\mathbf{\Phi}^h$ at that location.

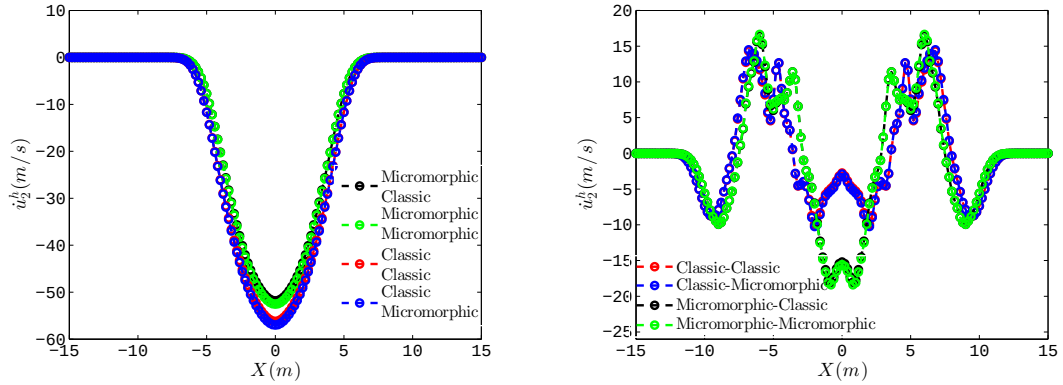

(a) Macro-element velocity component $\dot{u}_2^h$ at $t = 0.006(s)$ along interface.

(b) Macro-element velocity component $\dot{u}_2^h$ at $t = 0.0085(s)$ along interface.

Figure 5.72. Macro-element velocity component $\dot{u}_2^h$.

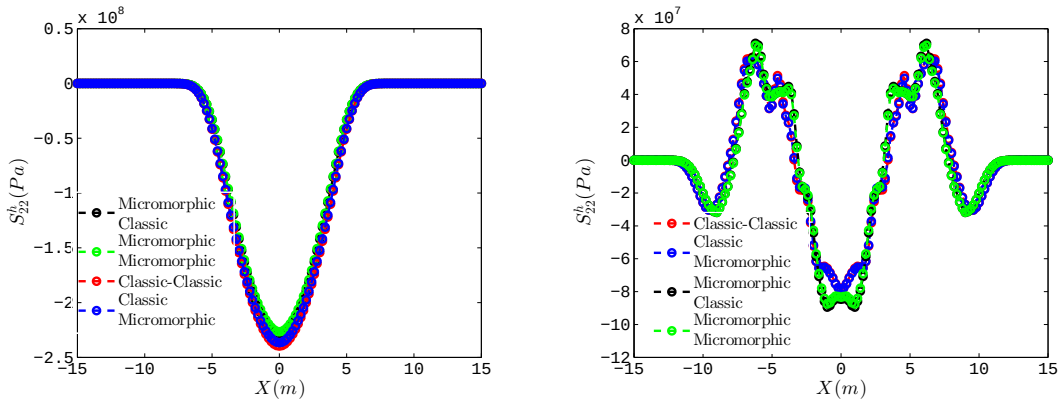

(a) Second Piola Kirchhoff stress component S_{22}^h at $t = 0.006(s)$ along interface.

(b) Second Piola Kirchhoff stress component S_{22}^h at $t = 0.0085(s)$ along interface.

Figure 5.73. Second Piola Kirchhoff stress component S_{22}^h.

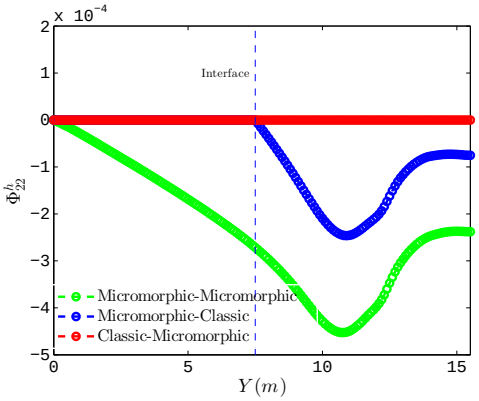

(a) Micro-element displacement component Φ^h_{22} along width of plate at $t = 0.006(s)$.

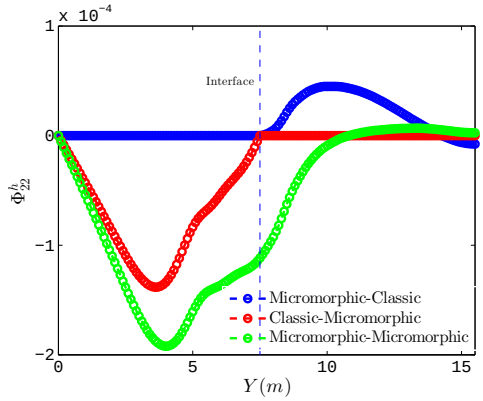

(b) Micro-element displacement component Φ^h_{22} along width of plate at $t = 0.0085(s)$.

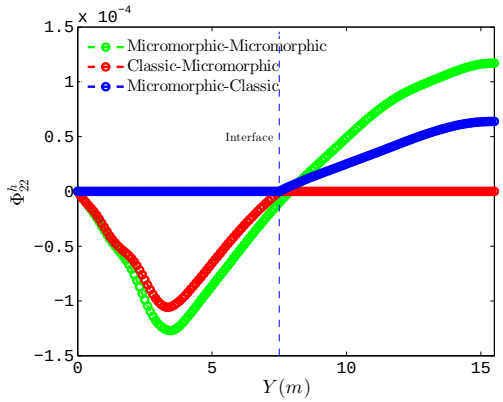

(c) Micro-element displacement component Φ^h_{22} along width of plate at $t = 0.0135(s)$.

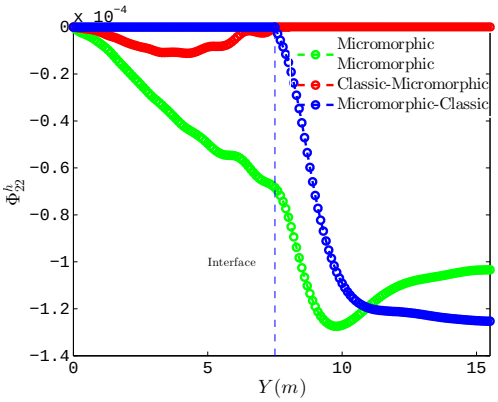

(d) Micro-element displacement component Φ^h_{22} along width of plate at $t = 0.0175(s)$.

Figure 5.74. Micro-displacement tensor component Φ^h_{22}.

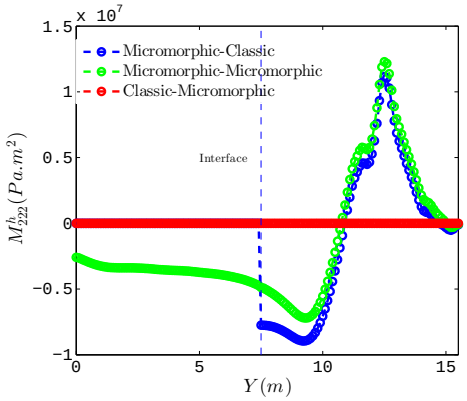

(a) Couple stress component M^h_{222} along width of plate at $t = 0.006(s)$.

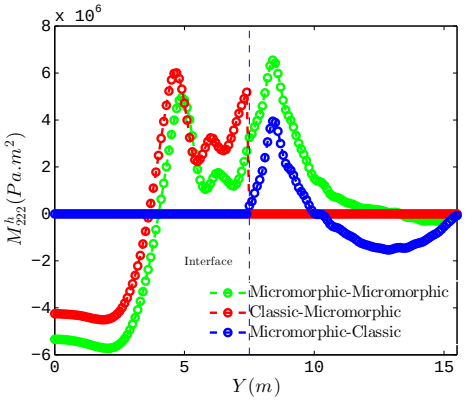

(b) Couple stress component M^h_{222} along width of plate at $t = 0.0085(s)$.

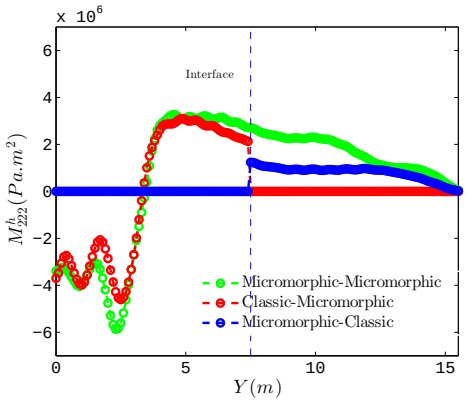

(c) Couple stress component M^h_{222} along width of plate at $t = 0.0135(s)$.

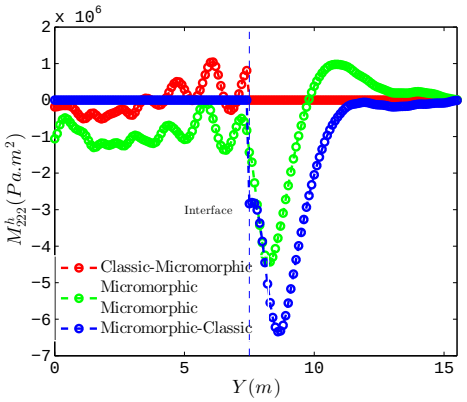

(d) Couple stress component M^h_{222} along width of plate at $t = 0.0175(s)$.

Figure 5.75. Couple stress component M^h_{222}.

Chapter 6

Conclusion, Current and Future Work

The research was devoted to presenting the micromorphic continuum theory (by Eringen) derivations for elasticity, elastoplasticity, and dynamics at finite strain, as well as physical motivation, finite element analysis implementation, and interpretation of the micromorphic micro-structured material modeling. The main focus of this research is on the discussion of the micro-structured material modeling from the perspective of a micromorphic continuum for elasticity, elastoplasticity, and dynamics at finite strain. A three dimensional finite element model has been developed in Tahoe to be able to perform three dimensional micromorphic continuum simulations. To the best of our knowledge, there are no micromorphic finite strain finite element analysis models especially in 3D or analytical solutions in the sense of Eringen in the literature to be comparable with our model. Considering the inhomogeneity in terms of the deformable micro-elements in micromorphic continuum, the macroscopic mechanical response can be different in comparison with the homogenized classical continuum models. The difference is dependent on factors including material parameters (micro-element deformations), the size of micro-elements (the relative position vector family $\boldsymbol{\Xi}^{(\alpha)}$), type of loading (bending and large rotation), and micromorphic BCs. Each of these factors has been investigated through the numerical simulations. The material parameters of micromorphic continuum play the main role in terms of the micro-element stiffness and their deformation under loading. The larger micro-element deformations result into a more noticeable inhomogeneity in the macroscopic mechanical response. The size of micro-element corresponds to

the size of the material's micro-structure in the micromorphic continuum description. Therefore, the results of a material with finer micro-structure is closer to the classical continuum results. Types of loading also affects the macroscopic behavior of the micro-structured materials in comparison with the classical continuum models. Note that in bending and large torsion, the difference in the macroscopic behavior obtained from micromorphic continuum for the micro-structured material with the homogenized classical continuum model is more pronounced in comparison with those of the uniaxial strain column simulation (micromorphic and classical continua are close). It is evident that the boundary conditions on the micromorphic dofs is crucial in terms of defining the micro-element deformations and resulting inhomogeneity added through the couple stress terms. We should keep in mind that the resolution of material modeling through micromorphic continuum is higher than that of classical continuum, but, not as much as that of direct numerical simulations (DNS). Micromorphic continuum theory is established based upon continuum mechanics assumptions. Therefore, the micromorphic continuum picture from the micro-structure is obtained through involving micro-elements and integral averaging over the macro-elements of a continuum body without touching the material micro-structures explicitly. For multi-scale materials modeling, sometimes it is worthwhile working with a micromorphic continuum to pick up more information from an underlying DNS region. However, this may not be the case for all multi-scale modeling problems. The decision can be made through observing the effect of micro-structural deformations obtained from the DNS region and, if the inhomogeneity is pronounced, a micromorphic continuum will provide better resolution for multi-scale material modeling.

6.1 Future Work

The following future work from the view point of finite element analysis can be envisioned such that:

1- Developing micromorphic explicit finite element analysis to overcome numerical instabilities in micromorphic dynamics

2- Developing micromorphic poromechanics to simulate fluid flow through the micromorphic solid skeleton

From the view point of physical motivation and micromorphic continuum application:

1- Calculating micro-deformation tensor $\boldsymbol{\chi}$ and micromorphic strain tensors to plot stress-strain curves based on DNS and micromorphic filter.

2- Calibrating micromorphic constitutive parameters via the calculated micromorphic stress-strain curves.

3- Simulating an integrated model with overlapping regions (DNS/micromorphic filter/micromorphic continuum) and comparing the result with the model entirely simulated by DNS.

4- Applying micromorphic filter on elastoplastic DNS for better failure predictions through micromorphic elastoplasticity.

6.2 Acknowledgements

Funding for this research was provided by ONR MURI grant N00014-11-1-0691. This funding is gratefully acknowledged.

Bibliography

S. Bauer, S. Schafer, P. Grammenoudis, and Ch. Tsakmakis. Three-dimensional finite elements for large deformation micropolar elasticity. Computer Methods in Applied Mechanics and Engineering, 199:2643–2654, 2010.

K. C. Bennet, R. A. Regueiro, and R. I. Borja. Finite strain elastoplasticity considering the eshelby stress for materials undergoing plastic volume change. International Journal of Plasticity, 77: 214–245, 2016.

A. Berezovski, I. Giorgio, and D. Corte. Interfaces in micromorphic materials: wave transmission and reflection with numerical simulations. Mathematics and Mechanics of Solids, 21(1):37–51, 2015.

J. E. Bishop and H. Lim. Continuum approximations. In preparation, 2016.

R. I. Borja and R. A. Regueiro. Strain localization in frictional materials exhibiting displacement jumps. Computer methods in applied mechanics and engineering, 190:2555–2580, 2001.

K. C. Chen and J. Y. Lan. Micromorphic modeling of granular dynamics. International Journal of Solids and Structures, 46:1554–1563, 2009.

B. D. Coleman and M. E. Gurtin. Thermodynamics with internal state variables. The Journal of Chemical Physics, 47:67–115, 1967.

B. D. Coleman and W. Noll. The thermodynamics of elastic materials with heat conduction and viscosity. Archive for Rational Mechanics and Analysis, 13:167–178, 1963.

E. Cosserat and F. Cosserat. Theorie des corps deformables. Hermann, 1909.

R. De Borst, L. J. Sluys, H. B. Muhlhaus, and J. Pamin. Fundamental issues on finite element analyses of localization of deformation. Engineering computation, 10:99–121, 1993.

R. Dingreville, J. Robbins, and T. Voth. Multiresolution modeling of the dynamic loading of metal matrix composites . The Journal of The Minerals, Metals and Materials Society, 65(2):203–214, 2013.

E. Kröner, ed. Mechanics of Generalized Continua. Springer-Verlag, 1968.

A. C. Eringen. Compatibility conditions of the theory of micromorphic elastic solids. National Aeronautics and Space Administration, CR-1236:1–16, 1968.

A. C. Eringen. Theory of micropolar elasticity. in liebowitz, h. Fracture, An advance Treatise, 2: 622–729, 1968a.

A. C. Eringen. Microcontinuum field theories i: foundations and solids. Springer-Verlag, 1999.

A. C. Eringen and E. S. Suhubi. Nonlinear theory of simple micro-elastic solids-1. International Journal of Engineering Science, 2(2):189–203, 1964.

A.C. Eringen. Nonlinear Theory of Continuous Media. McGraw-Hill, 1 edition, 1962.

N. A. Fleck, G. M. Muller, M. F. Ashby, and J. W. Hutchinson. Strain gradient plasticity: theory and experiment. Acta Metallurgica et Materialia, 42:475–487, 1994.

S. Forest. Micromorphic approach for gradient elasticity, viscoplasticity, and damage. Journal of Engineering Mechanics, 135(3):117–131, 2009.

S. Forest and R. Sievert. Elastoviscoplastic constitutive frameworks for generalized continua. Acta Mechanica, 160(1-2):71–111, 2003.

S. Forest and R. Sievert. Nonlinear microstrain theories. International Journal of Solid and Structures, 43(24):7224–7245, 2006.

P. Germain. The method of virtual power in continuum mechanics. part 2: Microstructure. SIAM Journal on Applied Mathematics, 25(3):556–575, 1973.

E. Gheibi and S. L. Gassman. Application of gmpes to estimate the minimum magnitude and peak ground acceleration of prehistoric earthquakes at hollywood, sc. Engineering Geology, 214:60–66, 2016.

P. Grammenoudis, Ch. Tsakmakis, and D. Hofer. Micromorphic continuum. part ii finite deformation plasticity coupled with damage. International Journal of Non-Linear Mechanics, 44:957–974, 2009.

T.J.R. Hughes. The finite element method. Prentice-Hall: New Jersey, 1987.

Mahmoud I Hussein and Romik Khajehtourian. Nonlinear elastic waves in solids: Deriving simplicity from complexity. Bulletin of the American Physical Society, 60, 2015.

MI Hussein, R Khajehtourian, and MH Abedinnasab. Finite-strain bloch wave propagation by the transfer matrix method. arXiv preprint arXiv:1412.2131, 2014.

V. Isbuga. Finite strain micromorphic finite element analysis of elastoplastic geomaterials. PhD thesis, University of Colorado at Boulder, 2012.

V. Isbuga and R. A. Regueiro. Three-dimensional finite element analysis of finite deformation micromorphic linear isotropic elasticity. International Journal of Engineering Science, 49:1326–1336, 2011.

M. M. Khabiri, A. Khishdari, and E. Gheibi. Effect of tyre powder penetration on stress and stability of the road embankments. Road Materials and Pavement Design, 18:1–14, 2016.

R Khajehtourian and MI Hussein. Dispersion characteristics of a nonlinear elastic metamaterial. AIP Advances, 4(12):124308, 2014.

J. D. Lee and Y. Chen. Constitutive relations of micromorphic thermo-plasticity. International Journal of Engineering Science, 41(3-5):387–399, 2003.

Shaofan Li and Qi Tong. A concurrent multiscale micromorhic molecular dynamics. Journal of Applied Physics, 117:154303–(1–14), 2015.

A. Madeo, P. Neff, I. D. Ghiba, L. Placidi, and G. Rosi. Wave propagation in relaxed micromorphic continua: modeling metamaterials with frequency band-gaps. Continuum Mechanics and Thermodynamics, 27:551–570, 2015.

G. A. Maugin. Mechanics of generalized continua, one hundered years after Cosserats. Springer, 2010.

R. Mindlin. Micro-structure in linear elasticity. Archs ration. Mech Analysis, 16:51–78, 1964.

B. Moran, M. Ortiz, and C. F. Shih. Formulation of implicit finite element methods for multiplicative finite deformation plasticity. International Journal of Numerical Methods and Engineering, 54:5135–5145, 1990.

P. Neff, I. D. Ghiba, A. Madeo, L. Placidi, and G. Rosi. A unifying perspective: the relaxed linear micromorphic continuum. Continuum Mechanics and Thermodynamics, 26(5):639–681, 2014.

S. Ramezani, R. Naghdabadi, and S. Sohrabpour. Analysis of micropolar elastic beam. European Journal of Mechanics A/Solids, 28:202–208, 2009.

I. Rapti, A. Modaressi-Farahmand-Razavi, A. Foucault, F. Lopez-Caballero, and F. Voldoire. Coupled s-p wave propagation in nonlinear regularized micromorphic media. Computers and Geotechnics, 77:106–114, 2016.

R. A. Regueiro. Finite strain micromorphic pressure-sensitive plasticity. Journal of Engineering Mechanics, 135(3):178–191, 2009.

R. A. Regueiro. On finite strain micromorphic elastoplasticity. International Journal of Solid and Structure, 47(6):786–800, 2010.

R. A. Regueiro and V. Isbuga. Length scale effects in finite strain micromorphic linear isotropic elasticity: finite element analysis of three-dimensional cubical microindentation. Proceedings of the institution of Mechanical Engineers, Part N: Journal of Nanoengineering and Nanosystems, 2011.

R.A. Regueiro. Nonlinear micromorphic continuum mechanics and finite strain elastoplasticity. ARL-CR-0659, Army Research Laboratory, 2011.

R.A. Regueiro and Z. Duan. Static and dynamic micropolar linear elastic beam finite element formulation, implementation, and analysis. ASCE J. Eng. Mech., 141(8):1–18, 2015.

R.A. Regueiro, B. Zhang, and F. Shahabi. Micromorphic continuum stress measures calculated from three-dimensional ellipsoidal discrete element simulations on granular media. In K. Soga, editor, IS-Cambridge 2014, pages 1–6, 2014.

C. Sansour. Unified concept of elastic-viscoplastic cosserat and micromorphic continua. Journal De Physique. IV, 8(8):341–348, 1998.

C. Sansour, S. Skatulla, and H. Zbib. A formulation for the micromorphic continuum at finite inelastic strain. International Journal of Solid and Structures, 47:1546–1554, 2010.

I. Sasanakul, S. Gassman, W. Pierce, C. Ovalle, R. Starcher, E. Gheibi, and M. Rahman. Dam failures from 1000-year rainfall event in south carolina. Geo-Frontier, 227:114–124, 2017.

A. C. Smith. Inequalities between the constants of a linear micro-elastic solid. International Journal of Engineering Science, 6(2):65–74, 1968.

J. S. Stolken and A. G. Evans. A microbend test method for measuring the plasticity length scale. Acta Materialia, 46:5109–5115, 1998.

E. S. Suhubi and A. C. Eringen. Nonlinear theory of micro-elastic solids-ii. International Journal of Engineering Science, 2:389–404, 1964.

S. Timoshenko and J. N. Goodier. Theory of elasticity. McGraw-Hill, 1969.

P. A. Vermeer and R. de Borst. Non-associated plasticity for soils, concrete, and rock. Heron, 29(3):3–64, 1984.

F. Vernerey, W. Liu, and B. Moran. Multi-scale micromorphic theory for hierarchical materials . Journal of the Mechanics and Physics of Solids, 55(12):2603–2651, 2007.

S. Wu and X. Wang. Mesh dependence and nonlocal regularization of one-dimensional strain softening plasticity. Journal of engineering mechanics, 136(11):1354–1365, 2010.

Z. H. Zhang, Y. Zhuang, Z.and Gao, Z. L. Liu, and X. M. Nie. Cyclic plastic behavior analysis based on the micromorphic mixed hardening plasticity model. Computational Materials Science, 50:1136–1144, 2011a.

Z. L. Zhang, Z. H.and Liu, Y. Liu, X. M.and Gao, and Z. Zhuang. Wedge indentation of a thin film on a substrate based on micromorphic plasticity. Acta Mechanica, 221:133–145, 2011b.